The Alliance of Laboratories in Europe for Research and Technology

ALERT Doctoral School 2012

Advanced experimental techniques in geomechanics

Editors:

Gioacchino Viggiani

Stephen A. Hall

Enrique Romero

Editorial

The twenty-second session of the European Graduate School 2012 (called usually ALERT Doctoral School) entitled *Advanced experimental techniques in geomechanics* is organized by Cino Viggiani, Steve Hall and Enrique Romero. It belongs to the events taking place regularly during the annual meeting of the ALERT Geomaterials association in Aussois. Created in 1989 by Félix Darve, Roberto Nova, Manuel Pastor, Ian Smith, Pieter Vermeer and Olek Zienkiewicz, the ALERT association has become a highly acknowledged platform for the scientific exchange and education in the field of geomaterials. Its 27 members from European universities (and also two non-European Academic institutions) possess a strong potential for the research and scientific development focused on the mechanical behaviour of soils, rocks and concrete. More details can be found at `http://alertgeomaterials.eu`.

In 2011, Manolo Pastor was elected as a new president of the ALERT Geomaterials, following the prominent era of Félix Darve. The newly composed ALERT Bureau introduced some modifications of the ALERT traditions. One of them regards the book of the ALERT school. Over many years, the book was printed as a special number of the *European Journal of Environmental and Civil Engineering* published by *Lavoisier*. Although the cooperation with *Lavoisier* was very good, ALERT have decided to produce the book by its own in the future. In this way, the publication can be made freely available in an electronic form and thus accessible to anybody all over the world.

On behalf of the ALERT Board of Directors and of all the members of ALERT, I would like to thank the organizers of this School 2012 for their intensive work invested into the preparation of the published volume and the oral presentations during the event in the Paul Langevin Centre in Aussois.

Ivo Herle
Director of ALERT Geomaterials
Technische Universität Dresden, Germany

Contents

Advanced experimental techniques in geomechanics: Foreword

Geomaterials exhibit complex mechanical behaviors that are coupled across a range of scale lengths and across many different physical mechanisms. Such couplings come in part from the nature of the materials, being multi-phase (solid plus fluids) and having structures ranging from granular building blocks to fracture or layer separated units. The requirement to consider these couplings also comes from the range of engineering fields in which these natural materials are implicated, meaning that material behaviors often have to be understood over a range of different conditions involving, for example, the presence of different stored or circulating fluids, with potential chemical interactions, and different pressure conditions, relating to near surface conditions or those of deeply buried formations. Furthermore, geomaterials are, by nature, not homogeneous, neither in their "virgin" state nor in their mechanical responses to load. Many different depositional structures, for example, can lead to heterogeneity at different scales, plus, as these materials deform, they generally exhibit some form of localized behavior in the form of strain localization or fracture. Together these different factors lead to a set of materials and phenomena that are very challenging to model.

Various advanced modeling approaches have been proposed to describe the mechanics of geomaterials, including: higher-order continuum approaches to characterize, for example, strain localization; multi-scale approaches involving homogenization of explicitly modeled micro-scale mechanics; discrete element models that attempt to model granular systems from the grain-scale upwards; thermo-chemo-hydro-mechanically coupled models. However, such models require experimental results, at the appropriate scales with the appropriate sensitivities and under the appropriate environmental conditions, to identify and characterize the important mechanisms controlling the material responses, to provide ground truth and to identify model input parameters. Unfortunately, traditional experimental methods often fall short of providing the necessary data for the increasingly ambitious modeling approaches. To address such shortcomings, new (advanced) experimental methods have been under development in recent years. The papers in this volume have been specifically prepared to summarize some of the key developments in this area and specifically to serve as lecture notes for the students and researchers attending the 2012 ALERT doctoral school on "Advanced experimental techniques in geomechanics".

One of the main drawbacks of traditional experimental approaches is that they provide information relating to macro-scale, "averaged" responses and no details on internal structural evolution and deformation mechanisms, e.g., shear band development. In the first paper of this volume, an historical perspective and current trends in ***full-field measurements in experimental geomechanics*** *describes a range of experimental methods, including optical and x-ray methods, that permit micro- and meso-scale material behaviors and heterogeneous responses to be more correctly characterized. The following paper discusses one of these methods in more detail, namely* ***Digital Image Correlation (DIC)****, which has, in recent years become a key tool in experimental mechanics in general and is increasingly popular in geomechanics. In the third paper of this volume, another full-field method is described:* ***ultrasonic tomography****, which provides measurements that complement stress-strain measures.*

As discussed above, geomaterial behaviors, and the geomechanical/geotechnical challenges in which they are concerned often, entail coupled processes involving different thermo-chemo-hydro-mechanical couplings operating at different time and space scales. The second set of three papers of this volume discusses new advanced ***experimental multiphase geomechanics*** *approaches that are now available for laboratory investigation of these key coupled processes.*

The four papers on low-perturbation geophysical measurements place emphasis inherent soil characterization challenges and explore the geotechnical significance of ***elastic, electromagnetic and thermal*** *properties.*

We would like to thank all the contributors to this volume and hope that the papers collected herein will provide a good overview of the current (and future) possibilities in experimental geomechanics as a complement to the lectures given at the doctoral school.

Cino Viggiani
Steve Hall
Enrique Romero

Full-field measurements in experimental geomechanics: historical perspective, current trends and recent results

Gioacchino Viggiani[1] and Stephen A. Hall[2]

[1]UJF-Grenoble 1, Grenoble-INP, CNRS UMR 5521, Laboratoire 3SR, Grenoble, France
[2]Formerly 3SR, now: Division of Solid Mechanics, Lund University, Lund, Sweden and European Spallation Source AB, Lund, Sweden

Full-field measurement is a rapidly growing subject in experimental mechanics. Over the past few years, we have presented a couple of state-of-the-art papers on the application of such methods to experimental geomechanics ([Vig08], [HaD12]). This paper, which is essentially an updated version of [Vig08], four years later, provides an overview of different available methods, and discusses their application to laboratory geomechanics. A selection of examples from the authors' experience with both soils and rocks is presented to illustrate the variety of methods available and the kind of information these methods provide. The examples include measurement of 2D and 3D kinematics, ultrasonic tomography and x-ray tomography, in-situ 3D x-ray diffraction and in-situ, spatially-resolved neutron diffraction. The combination of two full-field methods (x-ray tomography and 3D digital image correlation) is also shown. The aim of the paper is to present the tremendous possibilities now available and the new avenues opening up for research in geomechanics. These methods provide new data on the mechanics of geomaterials at different scales, including continuum measures of strain, porosity, and fabric plus discrete measures of particle kinematics and, one day, possibly even force transmission. Therefore, results of such measurements might be used as a guide to develop higher-order or multi-scale models for the mechanical behavior of geomaterials.

1 Introduction

During the last two decades, so-called non-contact measurement techniques have become increasingly popular in laboratory experimental mechanics (see, *e.g.*, [Hil12]). Such techniques are often referred to as full-field in contrast to more con-

ventional measurement techniques, which are based on the use of transducers positioned at the specimen boundaries. Full-field techniques provide what even multiple local measurements cannot, that is, the measurement of a field of data over the entirety of the specimen (*e.g.*, deformation, density, temperature, etc.) as opposed to point-wise data.

In conventional material testing, specimen response is characterized only globally. Under such conditions, with no information between measurement points, the measured response can at best be seen to represent an overall, averaged material response. Consequently, only in the case of a perfectly homogeneous material undergoing perfectly uniform deformation will the response measured from the test reflect true material (*i.e.*, constitutive) behavior. Obviously, neither are materials truly homogeneous at the scale of a laboratory specimen, nor are boundary conditions perfect. Furthermore, even when starting from "perfectly" homogeneous conditions, specimen deformation can eventually localize into more or less narrow zones (shear and compaction bands, tensile and shear cracks or fractures) at some stage of a test. In the presence of localized strains, it is clear that the meaning of stress and strain variables derived from boundary measurements of loads and displacements is only nominal, or conventional. Measuring the full field of deformation in the specimen is in this case the only way in which test results can be appropriately interpreted.

As far as experimental geomechanics is concerned, the use of full-field measurements in the laboratory is in fact not completely new. For instance, x-ray radiography was used already in the early 1960s in Cambridge as a non-invasive technique for measuring strain field in soil [Ros63, Ros70]. The technique was initially conceived with the purpose of following the positions of lead markers during a test on plane strain soil models. The underlying idea was that displacements of a grid of markers from one radiograph to the next can be interpreted as indications of a continuum displacement field and, through differentiation, a corresponding strain field. However, the radiographs revealed other, extremely interesting effects associated with local changes in the soil itself. In fact, local and relatively confined density changes, if sufficiently marked, produce corresponding contrasts in absorption of x-rays which can be seen on the radiographs. Such density variations allowed direct observation of narrow dilation bands forming in the soil models (*e.g.*, Figure 1). Other pioneering examples of the use of full-field measurement in experimental geomechanics include the method of False Relief Stereophotogrammetry (FRS), first used in soil mechanics by Butterfield and co-workers [But70] and then extensively applied and developed in the 1980s to capture non-homogeneous deformation throughout tests under plane strain conditions (*e.g.*, [Des84, DeD84]; see [DeV04] for an overview). In essence, FRS is based on the analysis of successive pairs of photographs of the side of a specimen deforming under load and allows direct measurement of (incremental) deformations and determination of strain fields throughout a test. As we will present later, FRS provided unprecedented insight for localization studies in geomaterials. However, due to recent, major technological development and rapid proliferation of alternative techniques making use of digital image analysis, FRS has been superseded by Digital Image Correlation (DIC) methods.

Outside of geomechanics, there have been many significant developments in the area of full-field measurements. This is exemplified by the increasing number of

journal publications and conferences specifically devoted to this subject. As an example, the motivating statement for the "Photomechanics 2008" conference was: "Classical procedures used in experimental solid mechanics have been significantly modified by recent advances in optical measurement methods, image processing and infrared thermography. These full-field measurement techniques lead to high resolution displacement, strain and temperature maps which open new and attractive fields of investigation" (http://www.lboro.ac.uk/departments/mm/conferences/ photomechanics//). While geomechanics was certainly pioneering some aspects of full-field measurements some forty years ago, it seems that more recently we are lagging behind our colleagues in solid mechanics – who use such techniques for "simple" materials such as metals and metallic alloys. However, materials such as sand, clay, sandstone, granite, etc., are the quintessential heterogeneous, multi-scale materials. This paper aims to make the point that a wider use of full-field measurement in laboratory geomechanics not only is possible (and exciting), but also it is the only way to significantly advance our understanding of the mechanics of soils and rocks, especially in the hot topics of strain localization and fracture.

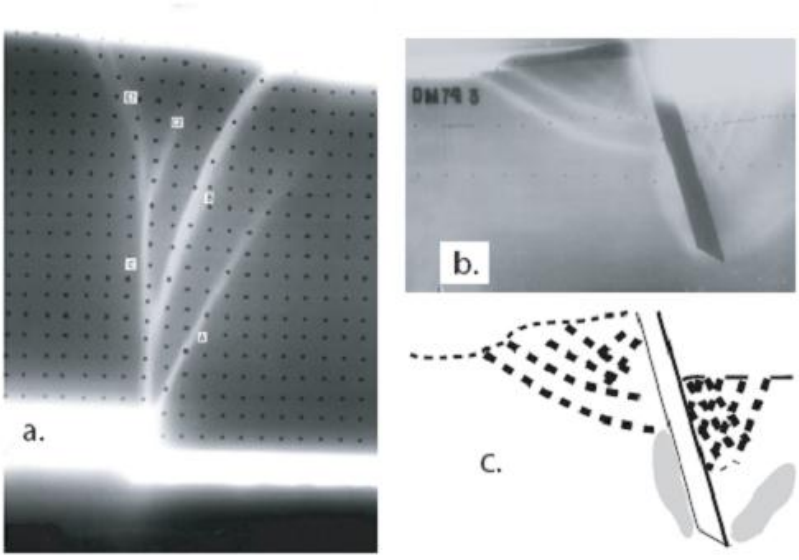

Figure 1. (a) Dilation bands in dense sand over a displacing trapdoor; (b), (c) dilation bands and zones of dilation around a rotating blade in dense sand ((b) radiograph from Cambridge University archive; (c) interpretation of (b), after [Mui02]).

The structure of this paper is as follows. The next section gives an overview of different available full-field laboratory methods, and discusses how they might significantly improve the experimental support to geomechanics. Some selected examples are then presented, which illustrate the application of different full-field methods to a variety of geomaterials. It is important to note that we have deliberately chosen to present examples only from our personal experience. Obviously, in so doing, we do

not pretend that these are necessarily the best or the most advanced examples available, they are just those that we are most familiar with. Although not exhaustively, we have tried to provide a few references to both classic and more or very recent work on each of the methods. The first examples we present are based on our experience with the measurement of 2D kinematics in plane strain tests (using FRS and DIC) on soils (Sect. 3) and rocks (Sect. 4). The application of ultrasonic tomography is then discussed in Sect. 5, with examples concerning a stiff clay and a sandstone. Section 6 discusses the use of x-ray tomography to study the internal structure and deformation processes in a variety of geomaterials. In Sect. 7, we show the power of combined x-ray tomography and 3D DIC for quantitative analysis of the evolution of localized deformation; this is illustrated for a clay rock and then for a fine sand under triaxial compression. For granular geomaterials (*i.e.*, sand), an alternative to DIC is represented by Particle Tracking in 3D; this is discussed in Sect. 8. Finally, in Sect. 9 we present some (very preliminary) results recently obtained using coherent elastic neutron and x-ray diffraction. Through all these examples our aim is to present the tremendous possibilities now available and the new avenues opening up for research in geomechanics. The paper concludes with some discussion about how these emerging full-field methods might be practically employed in a "standard" geomechanics laboratory, *i.e.*, the extent to which large investments are required.

2 OVERVIEW OF METHODS

Several types of full-field techniques have been used in material characterization in the last decades. The fields that are measured concern a range of physical variables, which may be scalars (*e.g.*, temperature), vectors (*e.g.*, displacement) or even tensors (*e.g.*, strain). For each of such variables, many different techniques exist. For example, a displacement field, which is the most common field measured, can be obtained with a number of methods including speckle, speckle interferometry, geometric moiré, moiré interferometry, holographic interferometry, image correlation and the grid method (see [Gré04]) and references therein). It is obvious that once displacements have been measured, a strain field can be derived simply by applying continuum mechanics. However, strain can also be determined directly, *e.g.*, with shearography (again, see [Gré04]).

Displacement field measurements and subsequent strain field calculations can provide a complete picture of the deformation process throughout an experiment, including the effects of pre-existing structure or defects, and any loss of homogeneity during the test (*e.g.*, strain localization). Field information during a test can thus allow tracking of the evolution (from onset to complete development) of specific features of deformation such as individual shear bands or more complex patterns, which might be otherwise hidden.

Kinematics is only one aspect of full-field measurement. In fact, a number of methods exist that provide full-field data on properties such as temperature, density, ultrasonic velocity, or electrical conductivity. These methods, which are often not direct (in that they involve some form of inverse analysis), allow to quantify property variations in time and space. For example, one can derive maps of ultrasonic

velocities in a deformed soil or rock sample and infer from these maps the consequences of deformation, such as compaction and related porosity reduction, or grain crushing. Later in this paper we will discuss in more detail ultrasonic and x-ray tomography, but other methods are also available, *e.g.*, Magnetic Resonance Imaging (MRI, *e.g.*, [She03]), Electrical Resistivity Tomography (ERT, *e.g.*, [Com08] and neutron tomography (*e.g.*, [Sol03], [Mas04], [HaH10]). MRI, ERT and, particularly, neutron tomography are well suited to study fluid motion in porous media in 3D. Measurement of temperature fields (infrared thermography) has potential for experimental studies of fracture onset and development in brittle geomaterials, *i.e.*, rock and concrete (*e.g.*, [Luo90], [WuL06]). The possible interest of thermography for soil mechanics has also been recently shown by [Luo07]. However, whilst these published examples are interesting, MRI, ERT, neutron tomography and thermography are not further discussed in this paper.

Whatever the field measured, all these techniques represent a substantial advance on conventional methods in experimental mechanics, in that they allow qualitative and quantitative characterization of heterogeneities in both material properties and processes during a test. Full-field measurements are particularly attractive for geomechanics, because heterogeneity (at different scales) is the rule rather than the exception when dealing with soils and rocks.

In practice, full-field measurements can be useful for soil and rock testing in a number of ways: (i) material characterization and specimen inspection; (ii) assessment of actual test boundary conditions; (iii) tracking of heterogeneous response during a test; (iv) validation and identification of models. The first possible use is in a sense similar to other techniques for soil or rock characterization (*e.g.*, microscopy), in that images are processed to obtain various properties of the material. However, in the context of full-field measurement the objective is to specifically identify any heterogeneity initially present in the specimen to be tested (defects, inclusions, etc.). This is not just for quality control (avoiding to test "defective" samples) but also, and more importantly, as a powerful means to better interpret test results (*e.g.*, why localized deformation appeared where it did, why was the measured value of permeability higher/lower than expected, etc.). Very much like geomaterials are never homogeneous, imposed test boundary conditions are never perfect. This is the second use of full-field measurement, *i.e.*, to directly measure and thus assess any deviation of the actual from the envisaged conditions. For example, the deformation of the testing apparatus can be measured and its effect removed much more effectively than any standard calibration for system compliance. The third usage of full-field measurement, tracking of heterogeneous response during a test (*e.g.*, strain localization and pattern development), has been introduced already and will be illustrated by a number of examples in the following sections. The final reason why measuring a full-field is of interest is related to the development of constitutive models. If a measured field from a test is available (most commonly, the strain field), this can be in some way compared to an equivalent field obtained using a given constitutive model. The parameters of the model can be then identified (*i.e.*, the inverse problem solved), provided that they play a role in defining the field. The availability of identification strategies enabling the extraction of the constitutive parameters is the key issue, as, in general, no closed-form solutions exist that direct-

ly link the measurements to the unknown model parameters. A few "simple" inversion approaches have been proposed (*e.g.*, the so-called "Virtual Fields Method", [Gré89], [Gré06]), but they are of limited interest for geomaterials, being generally restricted to relatively simple constitutive relations. Another identification strategy has been recently suggested by [Rou08], which directly integrates DIC measurements into a Finite Element formulation that includes a damage law for the material. However, geomaterials require more complex, inelastic models, for which numerical methods (*e.g.*, FEM) must be used to derive the field that is to be compared to the measured data. In general, how the model parameters are extracted from such a comparison remains an open challenge.

3 STRAIN LOCALIZATION IN SOILS STUDIED BY 2D OPTICAL METHODS

3.1 False Relief Stereophotogrammetry (FRS)

The most popular – and possibly obvious – full-field methods in experimental geomechanics involve optical tools to measure the complete surface displacement field of a specimen deforming under applied load. As a first example, a few selected results by Desrues and coworkers will be shown herein, which were obtained using False Relief Stereophotogrammetry (FRS) to capture non-homogeneous deformation in sand specimens throughout the duration of plane strain compression tests. FRS is based on the comparison of photographs taken from a fixed viewpoint at different times during the loading process. An essential feature of FRS is that the deformation is directly perceived as a fictitious relief (hence the name of the method) by using the well-known stereoscopic effect on successive pairs of photographs. The relief observed is due to the (plane) deformation taking place in the time interval between the two photographs, not to a real 3D geometry of the object. In this application of FRS, the photographed image is the side of a sand specimen deforming under load, and the source of the differences between successive images is the deformation process undergone by the specimen. When two photographs are viewed in stereo, displaced regions appear elevated, with the elevation proportional to the magnitude of displacement. In the presence of a shear band, the deforming specimen appears as two planes of different elevation connected by a slope. For a given pair of photographs and thus a given increment of the global axial strain, a shear band can therefore be completely characterized, in terms of both width and orientation.

Figures 2 through 4 show the results of four plane strain compression tests performed on Hostun sand (a fine-grained, angular siliceous sand) in the biaxial apparatus at the Laboratoire 3SR in Grenoble (see [DeV04] for full details). The specimens were all initially dense (relative density $D_r \geq 90\%$). These tests were carried out either dry or under drained conditions at confining effective stress (σ'_3) of 80 to 100 kPa, and deviatoric loading was applied under displacement control. Figure 2 shows, for each test, the stress-strain response in terms of effective stress ratio t/s'

vs. global axial strain, where the deviatoric stress $t = (\sigma_1 - \sigma_3)/2$ and the mean effective stress $s' = (\sigma'_1 + \sigma'_3)/2$ are the Roscoe planar stress measures (with σ_1 and σ_3 the major and minor principal stress, respectively). The numbers noted on each curve are the photograph numbers (see Figures 3 and 4).

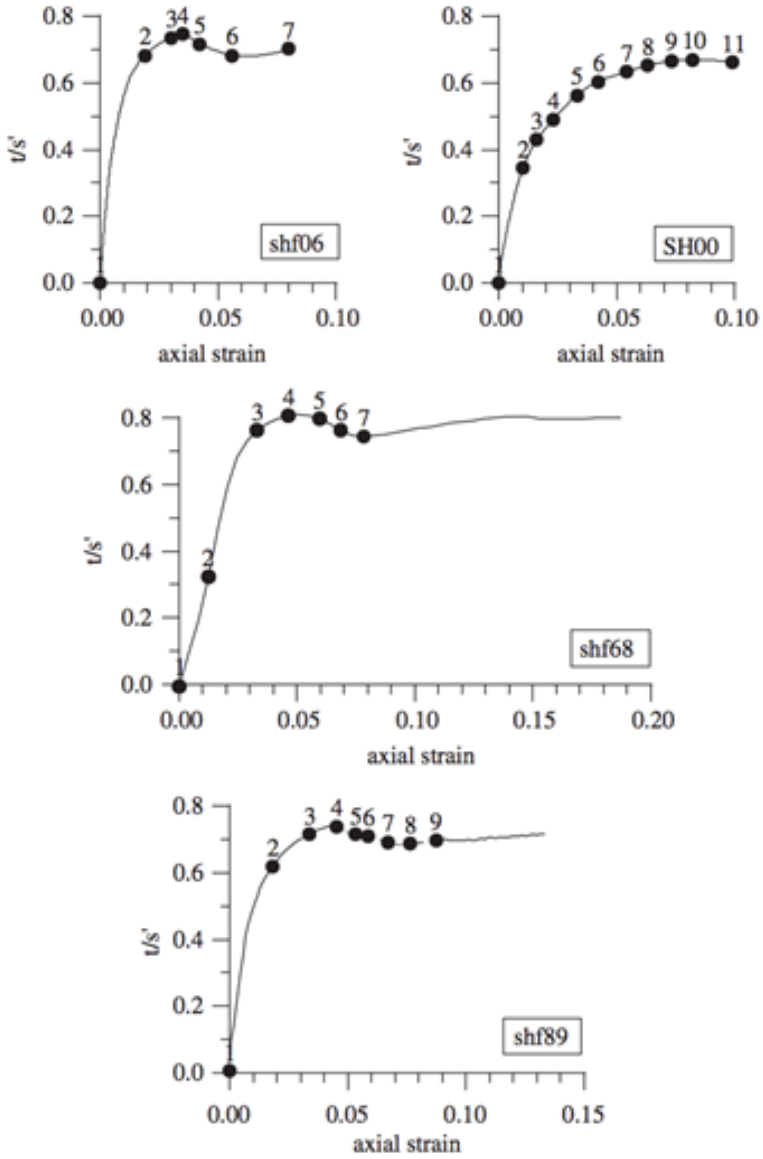

Figure 2. Stress-strain response obtained from plane strain compression tests shf06, SH00, shf68 and shf89 (adapted from [DeV04]).

Figures 3 and 4 show, for each increment, maps of FRS-derived shear strain, $\varepsilon_s = (\varepsilon_1 - \varepsilon_3)/2$, and volumetric strain, $\varepsilon_v = (\varepsilon_1 + \varepsilon_3)$, where ε_1 and ε_3 are the major and minor principal strains, respectively. The size of the symbols is proportional to the value of the relevant quantity (note that symbol scale is different for each increment). As far as volumetric strain is concerned, square symbols are for dilatancy and hexagons for contractancy. Figure 4 also shows the measured displacements from which the (incremental) strain fields have been derived.

In the first example (Figure 3a), shear strain fields indicate that two parallel zones of strain localization form in the middle portion of the specimen in the increment 3–4, *i.e.*, shortly prior to the peak of the stress ratio. Note that shear strains are always larger in the left shear band, which is the only one that is maintained throughout the test and finally intersects the entire specimen, whereas the other shear band eventually disappears. While no bands of localization were observed before photograph 3, shear strain fields suggest a somewhat non-homogeneous deformation already during increment 2–3 if not, to a lesser extent, from the beginning of the test (increment 1–2). Volumetric strain fields essentially reflect the same picture, showing a consistent dilative behavior in the localized regions. Also in the second example (Figure 3b) strain localization occurs shortly before the peak of the stress ratio. The shear strain fields indicate two "conjugate" shear bands first appearing during increment 8–9, which are maintained thereafter (herein the word conjugate is used to mean that the two directions are almost symmetrically reflected about the vertical). This X-shaped pattern of localization is not as evident in the volumetric strain fields. Note that both contractive and dilative behaviors are exhibited inside the regions of localized deformation, especially in the increment 10–11. Figure 4 illustrates another example of patterns of shear band propagation observed: shear band reflection at a rigid boundary. This is the dominant mode of propagation in tests shf68 and shf89, both performed on specimens with low slenderness ratios (about 0.5 and 1, respectively). The results in Fig. 4a show a quite complex pattern of deformation, starting from increment 4–5, when the peak of the stress ratio is attained. Multiple shear bands are observed, forming an array of two conjugate directions that further develops in the post-peak portion of the test. By then, the deformation clearly consists of nearly undeformed portions of the specimen sliding over each other. Similar complex mechanisms involving the progressive development of crossing and parallel bands are shown for another test in Figure 4b.

Since a FRS-derived strain map captures all the deformations within an increment between two photographs, strain that has occurred in different regions at different times within the given increment may appear as if it has occurred simultaneously. Therefore, it is difficult to assess to what extent these complex patterns actually result from progressive development (propagation) of strain localization within the specimen. A different (yet not necessarily alternative) interpretation would be that of an early organization of the strain field into a defined pattern, followed by a progressive increase of strain within the pre-developed pattern. Indeed, it seems that the aspect ratio of the specimen plays a crucial role in deciding to what extent the pattern is pre-defined. More precisely, it makes a difference whether the short dimension of a specimen is between the two sides on which a kinematic condition is imposed (such as in Figure 4a), or between the two sides on which a stress (the cell

pressure) is imposed (such as in Figure 3). In the former case, a complex pattern has to develop in order for a complete localization scheme to emerge, whereas this is not the case in the latter. Figure 4b represents the intermediate case.

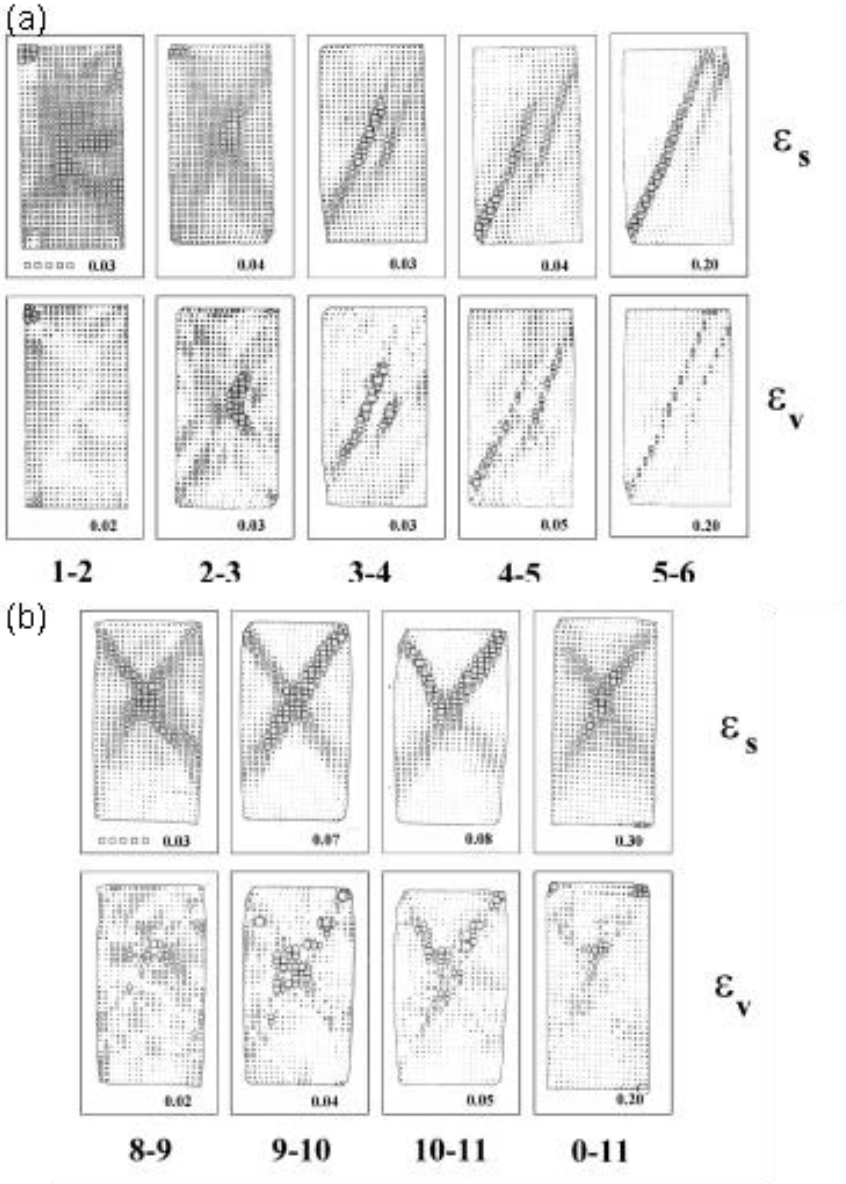

Figure 3. FRS-derived incremental fields of shear strain (ε_s) and volumetric strain (ε_v) in tests (a) shf06 and (b) SH00; note that for test SH00 no localized deformation was revealed prior to photograph 8 (after [DeV04]).

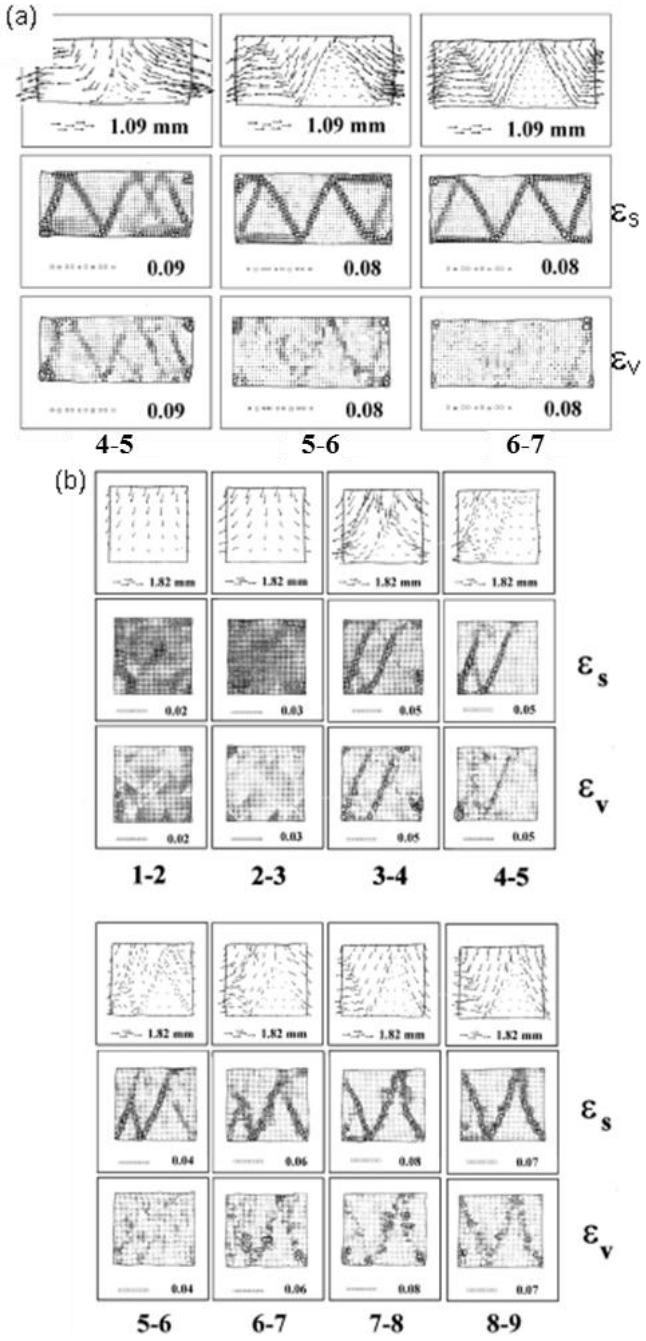

Figure 4. FRS-derived incremental displacements and incremental fields of shear strain (ε_s) and volumetric strain (ε_v) in tests (a) shf68 and (b) shf89 (after [DeV04].

Overall, these few examples illustrate that, depending on the boundary conditions and slenderness of the specimen, various patterns of localization can be observed, including parallel and crossing shear bands, as well as temporary, or "non-persistent" modes of localization, *i.e.*, localized regions which form during the test and eventually "disappear". Many other FRS-derived results on shear banding in sand can be found in [DeV04], as well as in other published studies (*e.g.*, [Fin96], [Fin97]). However, the four examples described above are sufficient to convey the message that a full-field method (FRS, in this case) can provide information that is just inaccessible through conventional measurements.

As a second demonstration of FRS for studying strain localization in soils, we present a few selected results from an experimental program carried out in Grenoble on an overconsolidated stiff clay (Beaucaire marl). Samples were tested in plane strain conditions (again in the Grenoble biaxial apparatus), both drained and undrained.

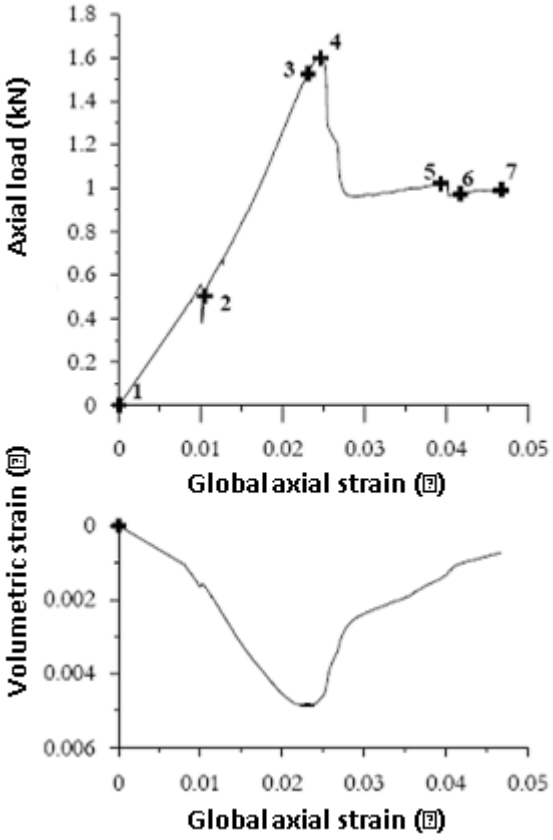

Figure 5. Response obtained from a drained plane strain compression test on stiff Beaucaire marl: (a) axial load *vs*. axial strain, (b) volumetric strain *vs*. axial strain (after [Vig04]).

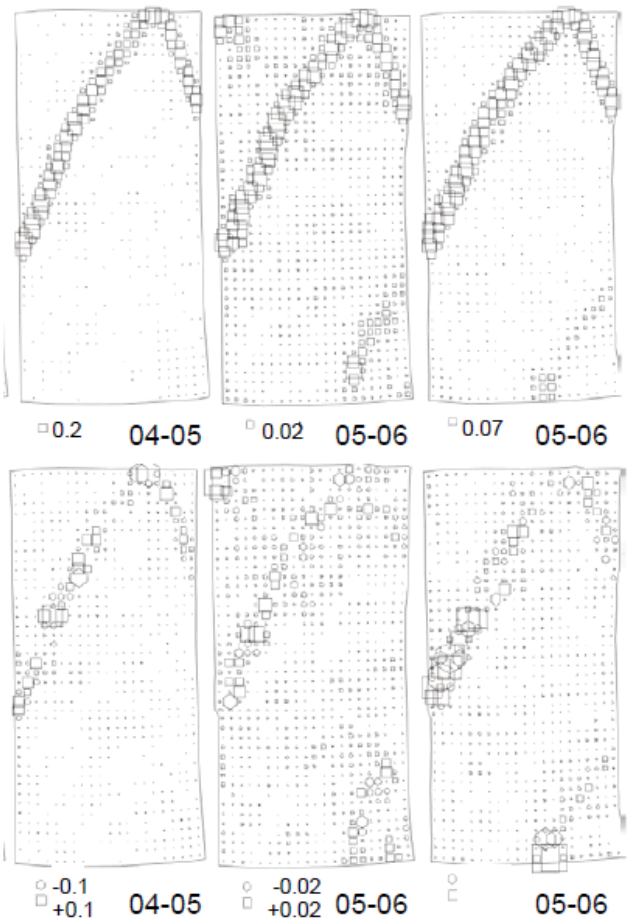

Figure 6. FRS-derived incremental fields of shear strain (top row) and volumetric strain (bottom row) for a drained plane strain compression test on stiff Beaucaire marl as presented in Figure 5 (after [Vig04]

Contractive and dilative behaviors were observed in the experiments, depending on the initial value of mean effective stress. Results from just one drained test are presented here, which is typical of a dilative behavior. Figure 5 shows the curves of axial load and volumetric strain vs. axial strain. The load monotonically increases until a peak is attained, whereupon it sharply drops and then levels off. Two minor load drops can also be observed in the pre- and post-peak regime. A contractive behavior is observed until shortly prior to the load peak, followed by a dilative behavior thereafter. The rate of (global) dilatancy is quite high while the load is dropping, whereas it gets much smaller as the load levels off.

The progression of strain localization in the test is shown in Figure 6 through FRS-derived fields of shear and volumetric strain (using the same representation as in

Figures 3 and 4). The photograph numbers are noted on the curves in Figure 5a. While no strain localization is observed before the load peak (photograph 4), a pair of shear bands form in the specimen in increment 4-5. These bands intersect the top boundary and might be interpreted as one of the two reflecting as another band. In increment 5-6, another band forms in the lower portion of the specimen. Volumetric strain is consistently localized in the same bands as shear strain. Note that although the post-peak behavior is globally dilative, the FRS-derived incremental strains indicate that both contractive and dilative behaviors are exhibited inside the localized regions.

In all the plane strain tests performed on Beaucaire marl, shear bands were always observed to form (for both contractive and dilative global responses). However, the patterns varied from one test to another. A further example is shown in Figure 7, in which multiple parallel zones of strain localization were observed to develop, eventually reducing to a pair of conjugate shear bands as deformation progressed.

3.2 Digital Image Correlation (DIC)

Major developments in digital photography coupled with the (apparent) simplicity of digital image analysis, have recently and rapidly led to the proliferation of techniques alternative to FRS that allow the same type of full-field measurement. These new methods, which may be grouped under the general name of Digital Image Correlation (DIC), make use of digital rather than analogue photographs, and therefore benefit from all the advantages of computer technology, including key aspects such as availability and affordability. In effect, any research group can easily acquire the necessary equipment and computer programs for performing DIC. This was not the case for FRS, which required special equipment in order to be used as a quantitative tool (including a stereocomparator, which is an advanced tool for 3D-photogrammetric measurements).

DIC techniques have been used increasingly over the last 20 years or so in a range of disciplines, including amongst others: solid and fluid mechanics (where the procedure is often referred to as Particle Image Velocimetry, PIV), medicine, animation and film special effects, and image registration. In recent years, the application of DIC to experimental mechanics has literally exploded. For example, [Ort09] noted more than 350 journal papers dealing with DIC-based measurements in the field. An historical reference is provided by [Sut86]. As far as geomaterials are concerned, the use of digital image analysis for characterizing soil fabric and its evolution under load is not new (*e.g.*, [Kuo96], [Muh97]). The application of digital image correlation is increasingly common for the monitoring of deformation in geomechanics laboratory experiments (*e.g.* [Gul99], [Whi03], [Rec04], [Liu04], [Gud04], [Bha05], [Bor08], [HaB10], [Hal10], [Ngu11], [ChH11], [Dau11], [Nie11], [Son12], [Vit12]).

DIC is essentially a mathematical tool for assessing the spatial transformation (including translations and distortions) between two digital images. In practice, DIC is implemented as a computer program that allows regions of a photographed object to be tracked automatically from one digital image to the next, from which displacements can be deduced. This is achieved without specific markers and without manu-

al intervention, provided there is some clear fabric or texture visible across the image. A number of commercial and academic codes exist to carry out DIC, although the implementation to develop in-house software is not too challenging. Whichever computer software is used, the basic idea of DIC remains the same, i.e., to determine the displacements, and perhaps deformations, to map one image onto another. A number of basic steps are generally involved: (i) definition of nodes distributed over the first image; (ii) definition of a region about each node (the correlation window); (iii) calculation of a correlation coefficient for each displacement of the correlation window within an area (the search window) about the target node in the second image; (iv) definition of the discrete displacement (integer number of pixels) given by the displacement with the best correlation; (v) sub-pixel refinement (because the displacements are rarely integer numbers of pixels), which may also involve more complex transformations than simply rigid-body translation; (vi) calculation of the deformation based on the derived displacements. Each DIC implementation has its variations and additions to this general methodology. In particular, there are different approaches for the sub-pixel refinement after the initial discrete estimate of the nodal displacements has been made (based on the displacement in the search window of the correlation window that returned the maximum cross-correlation value). Perhaps the most straightforward approach is to use a functional description of the local correlation field (*e.g.*, for 2D, describing the variation in correlation over the 9 positions within a 3x3, +/-1 pixel, search range about the best integer shift value) and some algorithm to find the maximum of this local cross-correlation surface. Alternatively the sub-pixel refinement can be carried out through iterative optimization of the transformation parameters with interpolation of the "gray-level" to reconstruct the image for each transformation and minimizing the misfit of the first and (transformed) second images. It should be noted that sub-pixel refinement, whichever method is used, is an essential step in DIC, especially when subsequently calculating strains from the displacements. Without sub-pixel refinement only integer numbers of pixel displacements can be resolved, which results in "stepped" displacement maps and strain images with very large strains corresponding to these steps and no strain between. The paper by [Hal12] in this volume presents the basic concepts of DIC for both surface and volume analysis, including technical details on both the data acquisition and the methodology.

As a demonstration of the interest of DIC over FRS, Figure 8 shows results obtained using the DIC software 7D developed at the Université de Savoie (*e.g.*, [Vac99]) for the same photographs used to derive the FRS results in Figure 7. By comparing the maps in Figures 7 and 8, it is clear that DIC provides much more detailed information about the features of strain localization. More shear bands can be identified, including minor conjugate bands in the last increment which are not visible with FRS. This is a result of FRS being based on a manual picking of measurements, which means that the number of data points is understandably limited and definitely less than the number achieved by an automated process like DIC. However, like for any automated procedure, there is a risk of local aberrations in the results (*e.g.*, the exaggerated squares of strain values in the last image to the right of Figure 8), not to speak of any sensitivity to underlying mathematical assumptions in the algorithm. In this respect, FRS has the advantage that the information is filtered by the operator,

and it does not involve any algorithm or associated hypothesis. Despite these advantages, it is clear that DIC is far more practical and versatile than FRS, which is the reason why the latter is less and less used.

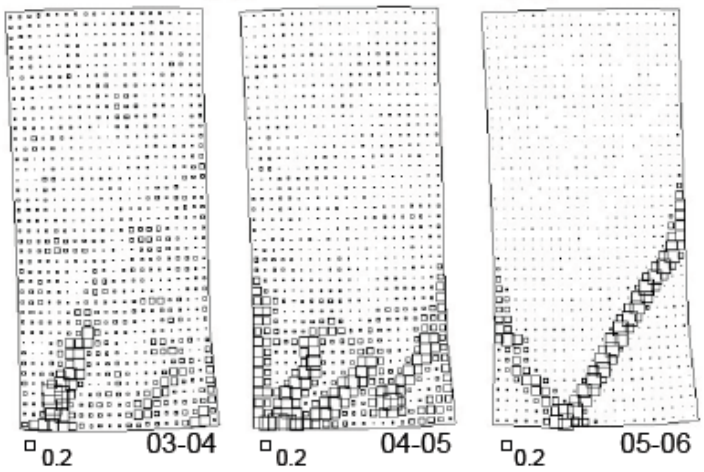

Figure 7. FRS-derived incremental fields of shear strain for another drained plane strain test on Beaucaire marl (after [Vig04]).

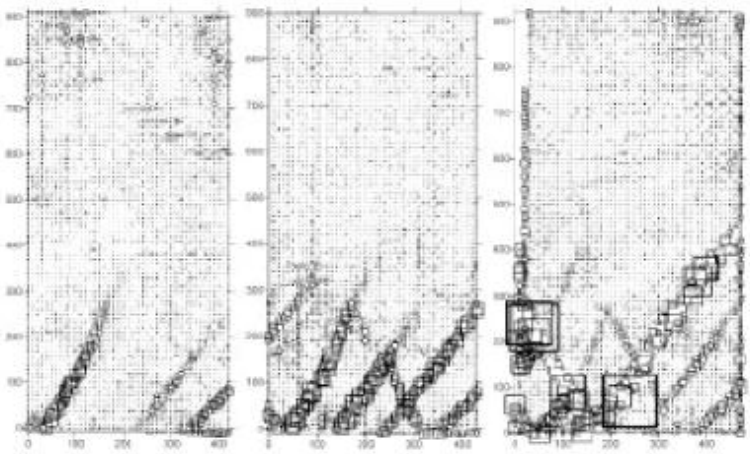

Figure 8. DIC-derived incremental fields of shear strain for the same test as in Figure 7 (after [Vig04]).

A further example of the effectiveness of DIC to reveal the evolution of strain localization throughout the duration of a test is presented in Figure 9, this time for a sensitive soft clay (Norwegian quick clay) tested in plane strain, again in the Grenoble biaxial apparatus (Thakur 2007). The DIC results were obtained using the commer-

cial software DaVis 6.0 (LaVision). Shear strain maps for different increments are shown in the figure, together with the stress deviator versus axial strain curve. A quite complex pattern of deformation is observed, which involves a single shear band forming well before the peak, and a second shear band emerging in the post-peak regime.

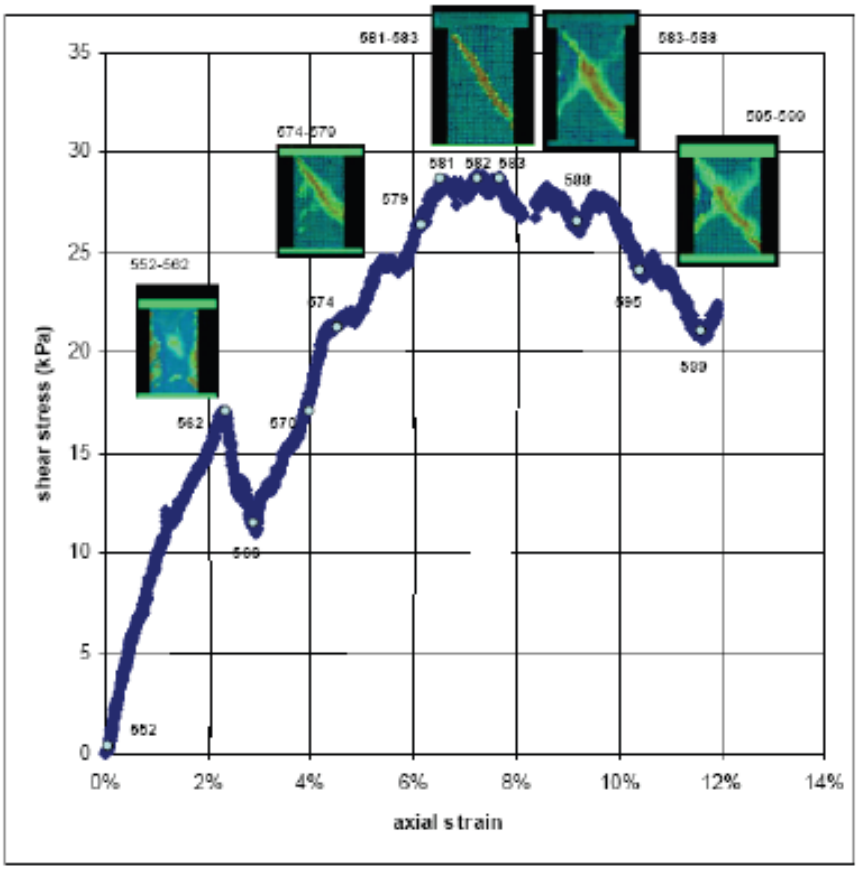

Figure 9. Evolution of strain localization revealed using DIC at different increments through the duration of a plane strain test on Norwegian quick clay (after [Tha07]. The figure shows the stress deviator *vs*. axial strain curve and the DIC-derived maximum shear strain maps.

A note of caution should be mentioned for the two previous examples, which concerned a stiff and a soft clay, *i.e*., fine-grained geomaterials. In fact, for such materials it has long been accepted that the "bands" of localized deformation have a width on the order of some tens of microns (*e.g*., [Mor67]). For the results presented, it should be kept in mind that the photographed specimens were enveloped in a latex

membrane, which follows the specimen deformation but inevitably smoothes the deformation field and likely makes the thickness of any band of localized deformation to appear larger than it is in reality. Therefore, even relative sliding, *i.e.*, a shear crack, would appear in the results of image correlation (either FRS or DIC) as a shear band with finite thickness.

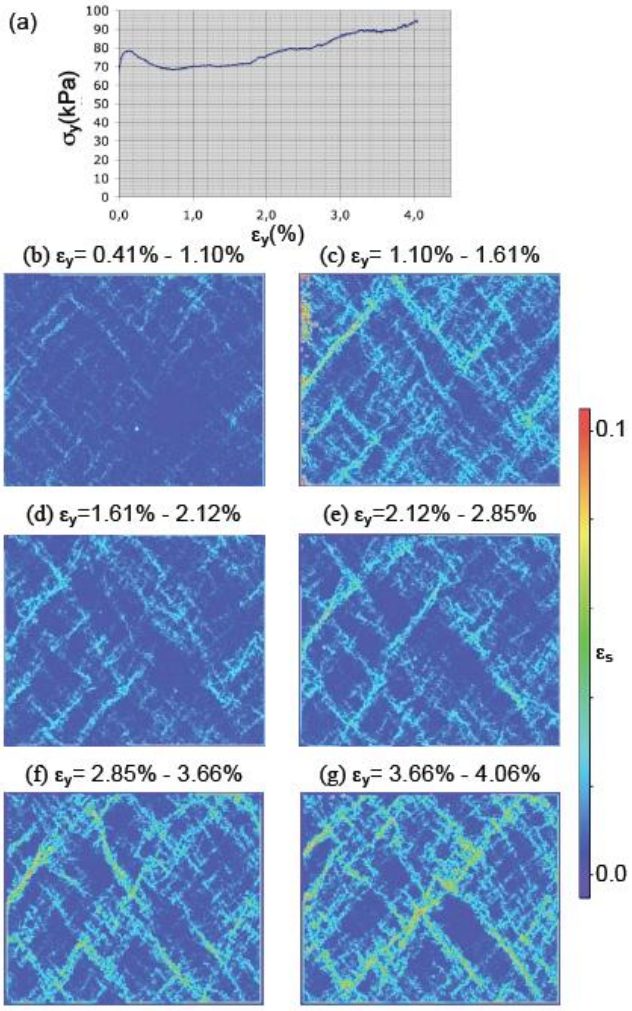

Figure 10. DIC observations of the evolution of emergent structuring of localized deformation in laboratory tests on a two dimensional analogue granular "Schneebeli" material of PVC rods. The images cover roughly the complete sample (about 600 x 500 mm). Stress-strain response is shown (a), while (b)-(g) show the results of DIC-derived maximum shear strain for six consecutive increments of strain after the end of the initial biaxial loading (there was no strain localization observable before the first strain increment shown) (after [Hal10].

As a final example, we present some DIC observations of the evolution of emergent structuring of localized deformation in laboratory tests on a two dimensional granular material. The test described here comes from a series performed in the 1γ2ε shear apparatus in Grenoble (see [Ibr10] and [Hal10], for details on the experiments and more complete results). The 1γ2ε apparatus was developed to apply general stress or strain conditions to a two dimensional analogue granular material (the so-called Schneebeli material), in this case formed of a combination of three different diameters (1.5, 3 and 3.5 mm) of 60 mm long PVC rods. The apparatus consists of a containment parallelogram enclosing the analogue material, with the two vertical sides that are able to rotate, whilst the other two sides always remain horizontal; and all four sides are able to extend or contract (see [Joe92] and [Joe98] for details on the device). The initial dimensions of the rectangular sample were about 600 mm x 500 mm, *i.e.*, the ratio of sample dimension to particle size was around 150-200.
For the test presented here, the sample was isotropically compressed up to $\sigma_x = \sigma_y =$ 65 kPa, and then loaded following a linear strain path with imposed dilatancy. The stress-strain response is shown in Figure 10a, while Figures 10b-g show the results of DIC analysis for six increments of strain. The DIC analysis was carried out using the code PhotoWarp developed at Laboratoire 3SR, which represents a 2D version of a code originally developed for 3D DIC for time-lapse analysis of hydrocarbon reservoirs under production based on 3D seismic images (see [Hal06]). DIC allows quantification of deformation in the Schneebeli material, and reveals patterns of localization that are otherwise hidden (i.e., invisible in the photographs). Only the incremental shear strain images are presented hereafter as the features are seen most clearly in such plots, but the geometry of the features is essentially the same whichever strain quantity is considered. The patterns might be characterized by the orientations of the localized strain features and by the dimensions (thickness/spacing) between the features, both of which are seen to evolve to some extent through the loading, even if the general patterns are established early. However, analysis of total, as opposed to incremental strains, at each stage in fact indicates that the localized bands are not stationary but rather migrate slowly in space resulting in an almost saturated map of total strain at the end of the test (which is not shown here).

4 FRACTURE IN ROCK STUDIED BY 2D DIGITAL IMAGE CORRELATION

Figure 11 presents an example of DIC analysis results (derived using PhotoWarp) from an experimental program to study fracture propagation and coalescence in a soft rock (Neapolitan fine-grained tuff); see [Had06] for more details. In these tests, prismatic rock specimens with configurations of pre-existing cuts were loaded under uniaxial plane strain compression (with a constant axial strain rate). Photographs of the main face of the specimens were acquired through the loading, which allowed the timing and locations of crack initiation and their subsequent propagation to be identified (to some extent). In some cases, it was even possible to see cracks that develop but later close and could not be identified in the specimen after the test.

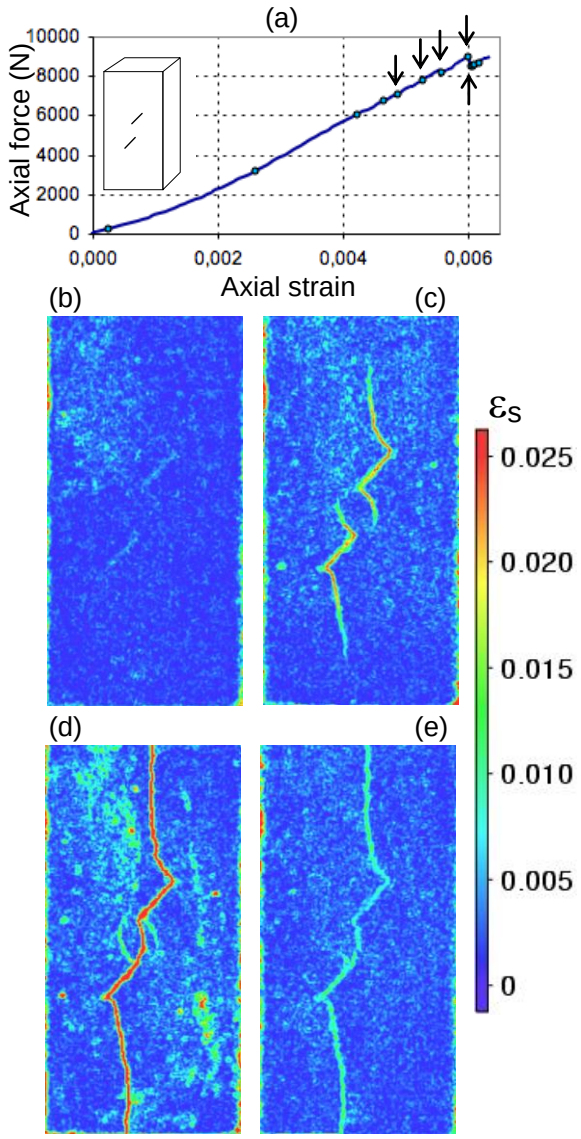

Figure 11. DIC analysis results for fracture propagation and coalescence in prismatic rock specimen of the Neapolitan fine-grained tuff loaded under uniaxial plane strain compression. DIC was carried out on photos of the front face with the zero-strain axis as its normal (dimensions 100 x 50 mm). The sample had two pre-existing cuts (see inset in (a)). (a) Axial stress-strain curve; (b)-(e) DIC-derived maximum shear-strain maps for the intervals between photos taken at the times indicated by the arrows in (a). (No strain localization was discernable before first map shown) (after Had06).

The actual timing of the fracture initiation and the true position of a propagating tip, plus assessment of whether a fracture is actually active at any particular increment, cannot be seen in the photographs and is only revealed by DIC. In fact, even by zooming into the image the small-scale fracture displacements are not evident, especially for fractures propagating in shear (*i.e.*, mode II). In this example, using DIC we were able to observe that cracks initiated at all four tips at the same time (see Figure 11b), but the external wing cracks developed more rapidly than the inner ones (see Figure 11c). When the external wing cracks propagated significantly towards the boundaries of the specimen, the internal cracks either connected across the rock bridge or another failure mode was initiated (which was the case of this test; see Figure 11d), which lead to the final sample failure (Figure 11e).

It should be noted that these results were acquired in a relatively "conservative" fashion, *i.e.*, only a limited number of photographs were acquired with large time steps between some images, with a risk of acquiring an image only after key events had happened. However, with the advances in memory card storage it is now easy to acquire many more images and so reduce the delay between them. This means that it is less likely to miss the key phenomena, which can often happen rapidly and without warning (one wishes to have images just before and just after key events). The subsequent analysis can then be carried out on any or all of the acquired images.

A key issue to consider here is that DIC in its standard form is essentially a continuum-type analysis, *i.e.*, it is inherently assumed that the object under consideration shows no strong discontinuities (*i.e.*, discontinuities of displacement) between the acquisitions of consecutive images. The examples in the previous sections have really only considered weak discontinuities, *i.e.*, discontinuities of strain, either shear bands or cracks smoothed out by the membrane. In the case of a fracture, either opening or shearing, the continuum condition is clearly violated. Therefore, whilst DIC provides a correct analysis of the displacement and strain of blocks around the developing fractures, the actual deformation calculated in the region of the fractures will be meaningless. This will arise due to the two following reasons. The first is of fundamental nature: fractures are discontinuities of the displacement field that cannot be properly described in terms of strain. The second reason is more technical and concerns the image distortion produced by the development of a fracture (in terms of a large strain, for sliding cracks, or in terms of an open zone, for opening cracks), which has the implication that a good image match may not exist. For a qualitative analysis of fracturing, neither of these issues represents a real problem, as fairly good images of fracture traces can be derived based on the zones of high strain (as in Figure 11) or unresolved correlation. Recently, different approaches have been suggested to overcome the challenges of using DIC by accounting for strong discontinuities. For example, [Rhé078] proposed a DIC algorithm that makes use of extended finite elements (XFEM) principles. Another approach has been suggested by [Hel08], in which an automatic procedure allows identification of cracks and their exclusion from the DIC analysis

In Grenoble, a special method of data processing was developed by [Des95] in which the discontinuous nature of the local displacement field is retained, rather than smearing it in a necessarily nonobjective local strain concentration. For FRS, an adequate data acquisition strategy that follows observed cracks was suggested that

allows the displacement jump across a discontinuity to be computed and represented. A DIC implementation of this idea was proposed by [Hal07] and then fully exploited by [Ngu11]. The method proposed by [Ngu11] allows both *automatic* tracing of discontinuities (fractures) and their quantification in terms of the (normal and tangential) displacement jumps along their length. The analysis of spatial and temporal fracture evolution using this method enhances the understanding of the phenomena in that it provides experimental quantification of fracture mode (opening/closing and shearing). A detailed description of the method is given elsewhere in this volume [Hal12], along with a few selected results from the study of [Ngu11] on Neapolitan fine-grained Tuff (the same rock studied by [Had06]).

5 ULTRASONIC TOMOGRAPHY

The above examples have shown how full-field displacement measurements, and subsequent strain field calculations, can be useful in the study of non-homogeneous deformation. However, as stated in the introduction, kinematics is only one aspect of full-field measurement. Full-field data on material properties rather than displacements are also available. Here we shortly describe one such method, which allows quantification of property variations that result from deformation. This method, ultrasonic tomography, might be of interest as a complementary approach to the experimental study of localized deformation in geomaterials. The paper by [HaT12] in this volume provides an overview of ultrasonic tomography and its application as a full-field measurement tool in experimental geomechanics plus provides demonstration of the power of the method with two examples.

Elastic waves (such as ultrasonic waves) can be used to assess, in a non-destructive fashion, the evolution of elastic properties, *e.g*., as a result of deformation. The term "elastic" is used here since the waves propagate without causing any permanent deformation. Elastic wave propagation is controlled by the velocity (a function of the elastic properties and density) and the attenuation in the medium, plus the frequency of the applied dynamic solicitation (wave). In geomaterials, wave propagation is a function of the constituent mineral grains and pore-filling fluids, the grain organization (contacts, porosity etc.) and the presence of cracks or fractures (see for example the overviews by [San96] or [San01], for soils, and [Mav98], for rocks). Thus, in the laboratory, measurements of travel-times and amplitudes of ultrasonic signals propagated across a sample, plus variations with frequency, allow detection of variations in elastic properties (and their development) and so eventually, the characterization of deformation.

Ultrasonic measurement has a relatively long history in laboratory soil and rock mechanics for the study of changes in elastic properties with loading. In soil mechanics, the key focus has been the measurement of soil stiffness at very small strains (i.e., in the "elastic regime") in the laboratory, *e.g*., using the well-known bender elements ([Shi78] and [Vig95] amongst others). Because the elastic waves have very small amplitude they induce very small strains. Therefore bender elements allow elastic properties to be measured throughout a mechanical test, and so are now an essential component of advanced laboratory testing devices (*e.g*., the review by

[Shi05] and references therein). In laboratory rock mechanics and geophysics, the main interest has been non-linear elastic changes under loading, usually attributed to the presence of cracks (*e.g*, [Nur69], [Kin95], [Gue03], amongst many others) and the evolution of damage (*e.g*., [Sta03]). Another key interest has been the assessment of elastic anisotropy and its evolution through the use of either multi-axial ultrasonic measurements or the combination of P-waves and two perpendicular shear wave measurements (the latter especially applicable when using bender elements); *e.g*., [Lin00], [Kin95], [Gue03], [Hal08]. However, even for the multi-axial case, most of the examples of analysis of ultrasonic data have been based on measurements over a limited number of directions (normally acquired just along the sample axis). The problem with such limited measurements is that they may not give a representative picture of the overall sample properties, especially when there is localized deformation. Furthermore, such measurements clearly do not have equivalent sampling to the loading measurements, to which they are frequently compared.

In the fields of acoustics and seismic imaging, data acquisition strategies allow for more advanced elastic-wave imaging approaches. Such approaches can be adapted to provide characterization of elastic property fields in laboratory geomechanics. Seismic or acoustic tomography is such a method. This involves inverse analysis of data from measurements along multiple crossing propagation paths that pass through the studied medium. At the "real-world" scale this might be between two boreholes, whereas in the laboratory the measurements would involve pairs of ultrasonic transducers placed on the surface of the sample. In general two types of ultrasonic tomography are considered, travel-time and attenuation. The theory is similar for both and involves attributing the measured data, *e.g*., the total travel-time along a "ray-path" between pairs of emitting and receiving transducers (often referred to as the time-of-flight or travel-time), to the summation over the path-lengths within all the grid cells traversed by the ray (see Figure 12a). The combination of many such measurements, for a set of intersecting ray-paths between emitting and receiving transducers placed at different locations over the sample, allows, by inversion, a map of the variations in propagation velocity in the sample to be determined (in a least-squares sense). A map of the velocities (or attenuation) over the imaged area is derived by inversion of a system of simultaneous equations, which relates the travel-time data to the velocities in each grid-cell. Encouraging ultrasonic tomography results have been presented for imaging of large inclusion heterogeneities in soils [Dai05] plus for localized deformation in rocks ([Fal92], [Deb99], [Sco04], [Ste07]) and soils ([Lee05], [Hal05]), although further work is required to better apply the technique and to interpret the results. Below we present a few results from the latter and some recent advances made in Grenoble.

Figure 12 shows an example of the application of ultrasonic tomography to a dry, tabular sample of stiff clay (Beaucaire marl), which was previously deformed under plane strain compression [Hal05]. In this case, travel-time tomography (also referred to as velocity tomography) was carried out, but it should be noted that similar procedures could be employed with amplitude data to derive full-field measures of attenuation. The travel-time data used in the tomographic inversion were acquired using just two transducers placed on opposite sides of the sample at different offset positions so as to achieve measurements along a series of crossing ray-paths (as

indicated in Figure 12a). The resultant data are waveforms, as shown in Figure 12b for the measurements between transducers directly opposite each other across the sample. From these data the arrival of the P (compression) -wave at each receiving transducer can be seen clearly as when there is the first significant deviation of the traces from the horizontal. The point of this deviation is taken as the travel-time from source to receiver. If the travel-times for each source-receiver pair are determined in such a way, then a system of equations can be constructed to relate these data to the distance traveled in each grid cell (as indicated in Figure 12a) via the velocity "field" (the unknowns in the inverse procedure). The path-lengths in each cell are usually determined by ray-tracing. Thus inversion of this system of equations provides the velocity in each grid cell, which can be presented as a map as in Figure 12c (clearly this is a simplified explanation and the reader is referred to the many texts in the geophysical literature on the subject, *e.g.*, [San04], as well as [HaT12] in this volume). In the example shown (Figure 12) it can be seen that a localized shear band shows up in the velocity-tomography map as a zone of increased velocities, which is consistent with the expected compaction associated with localization for this test sample. Some variability is also seen in the band, which may represent varying degrees of compaction. However, these results are potentially affected by artifacts of the tomography technique, for example the band offset from the real position in space (marked by the dashed line) and the high velocity zones in the corners at the ends of the band.

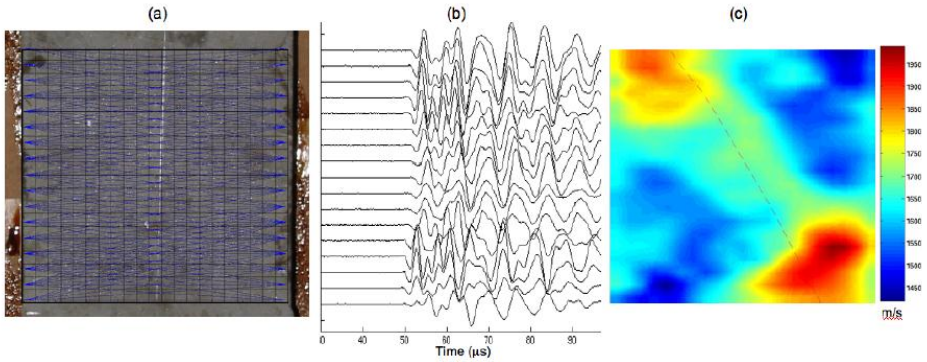

Figure 12. Ultrasonic tomography analysis on a tabular sample of Beaucaire Marl (stiff clay) that had been deformed under plane-strain conditions such that a localised (shear) deformation band developed diagonally across the sample (from top left to bottom right in (a). (a) Photograph of the front face of the sample with the tomography inversion grid and (straight) raypaths between each source and receiver over which travel-times were determined. (b) Example of the data acquired for each source-receiver pair, in this case just for the raypaths for transducer positions directly opposite each other across the sample. (c) Final ultrasonic velocity map from the 2D tomography analysis, which shows a band of higher (increased) velocities that roughly coincides with the trace of the localised deformation zone indicated by the dotted line. (after [Vig08]).

The ultrasonic tomography example presented above is an approach that might be carried out in any laboratory, given an ultrasonic signal generator, a data acquisition system (*e.g.*, a digitizing PC card) and two ultrasonic transducers, plus some patience (displacement of the transducers to each new position and acquiring the data is a fairly tedious task, especially if a high resolution, *i.e.*, a large number of ray-paths are desired). More recently in our group we have started using arrays of ultrasonic transducers (so-called "barrettes"), which allow much more efficient and accurate acquisition of a large number of ray-paths. Such transducer arrays are more common in non-destructive testing applications, but are perhaps more well-known for their use for "scans" of pregnant women. In this work we are using two arrays of 64 transducer elements yielding data over 64x64 intersecting ray-paths, which provides unprecedented (for geomaterials) ultrasonic tomography resolution. So far, this has been done for post-mortem analysis of sandstone specimens deformed under triaxial compression. This technique has been first used by [Res08] and a number of results have been obtained in the doctoral work of E/M. Charalampidou ([Cha11], [ChH11]). Questions remain about the spatial resolution and the presence of artifacts in the velocity images. Thus, on-going work aims to increase the spatial resolution and reduce the artifacts, *e.g.*, through the use of sensitivity kernels and full-waveform inversion techniques – this is done in the context of the PhD thesis of E. Tudisco (publication expected in 2013). One example of the results one can obtain using "barrettes" is shown in the paper by [HaT12] in this volume.
Finally, it should be noted that, in addition to the "active" ultrasonic measurements described above, "passive", acoustic emission (AE), measurements are very useful in identifying locations and mechanisms of damage and fracture (*e.g.*, [Loc77], [LoB77], [Fal92], [Zan98], [Sta03], amongst many others; in our group, AE measurements have been performed for studying localized deformation and damage in different geomaterials, including Neapolitan fine-grained Tuff [Ngu11] and Vosges sandstone [ChH11]). AE monitoring involves listening, with the same transducers as for ultrasonic measurements, for noise associated with damage formation (*e.g.*, cracking). If a number of transducers are used the cracking events may be located in space and details of the rupture process (*e.g.*, shear or opening) can be inferred. Although acoustic emission is quite often used in experimental geomechanics (especially for rock), it is not properly a full-field method and therefore will not be further discussed.

6 3D FULL-FIELD METHODS: X-RAY COMPUTED TOMOGRAPHY

We recalled already in the introduction that the use of x-ray imaging in experimental geomechanics dates back to the 1960s. Figure 1 showed a few examples of radiographs obtained in Cambridge by Roscoe and coworkers, which allowed the detection of bands of localized dilation in granular soil. Similar observations were made by other authors, *e.g.*, for triaxial compression [Kir68], simple shear [Sca82], direc-

tional shear ([Art77], [Art82]), plane strain compression [Var82], thick-walled hollow cylinders [Als92], as well as for flowing sand masses in hoppers ([Bra75], [Mic90]). In all these examples, x-rays were used to obtain radiographs, *i.e.*, 2D images produced by x-ray radiation on photographic plates. Radiographs represent maps of attenuation accumulated through the complete soil mass in the direction perpendicular to the image, which is related to soil density.

The above studies provided valuable qualitative information on localization patterning in sand specimens and sand box models. However, they all suffered from two major limitations: (i) lack of quantitative data on the observed density changes, and (ii) limitation to 2D images. Both limitations are overcome by x-ray Computed Tomography (CT). The principle of CT measurement consists of recording x-ray radiographs of a specimen at many different angular positions around the object. From these different projections, a three dimensional image of the object can be reconstructed with appropriate algorithms (usually based on a back projection principle); see for example [Bar00] for a thorough description of the technique. X-ray CT is therefore a non-destructive imaging technique that allows quantification of internal features of an object in 3D. First developed for medical imaging, x-ray CT is now widely used in material sciences and proved its interest in various domains of geosciences, including geomechanics (*e.g.*, [Mee03], [Ota04], [Des06], [Als10].

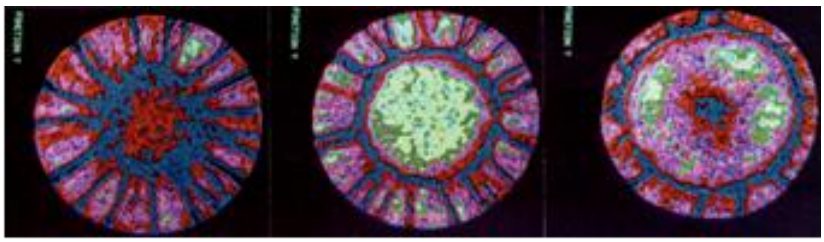

Figure 13. Horizontal slices through a CT image volume of a triaxial compression specimen of dry dense Hostun sand showing complex patterns of density variations (image was acquired near the end the test) (Image courtesy of J. Desrues).

As far as applications of x-ray CT to soil mechanics experiments are concerned, a pioneering contribution is due to [Art71]. At that time x-ray CT was not truly available yet, but tomographic images were obtained by using a special moving source and photographic plate set up. The technique appeared extremely promising and strongly motivated subsequent studies by Desrues and coworkers in Grenoble, who started from the early 1980s to use x-ray CT as a quantitative tool for experimental investigation of strain localization in sand ([Des84], [Col88], [Des96]); see [Des04] for a review. As an example, Figure 13 shows horizontal slices through a three dimensional CT image of a specimen of dry dense Hostun sand (at a stage towards the end of a triaxial compression test). Patterns of localized density variations are revealed as different intensities of the recorded x-ray radiation. The 3D mechanism that appears has some clear structure, which would be otherwise hidden (*i.e.*, invisible from just looking at the specimen, which to external viewing just had a barrel shape at the end of the test). Similar structures are shown in Figure 14, obtained

from another triaxial test on Hostun sand [Des96]. The localization pattern in this case involves a cone and multiple sets of planes associated in pairs, each pair intersecting along a diameter at the top of the specimen. Figure 14b shows Desrues' interpretation of these patterns of localization, including a cross-section close to the top platen, and a section parallel to the axis (compare with Figure 14a).

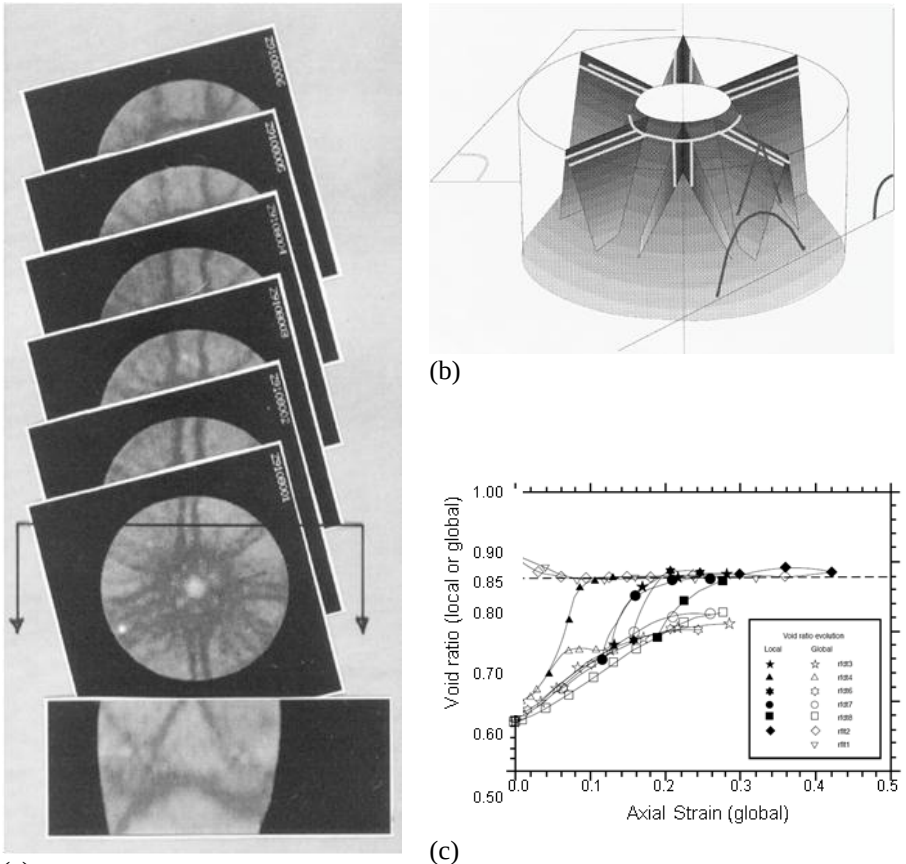

Figure 14. (a) patterns of localized density variations revealed in slices through a CT image volume of a specimen of dry dense Hostun sand near the end of a triaxial compression test (note this is a different test to Figure 13). (b) suggested 3D interpretation of the patterns of localization in Figure 14a. (c) local (solid symbols) and global (open symbols) variation of void ratio in loose and dense specimens of Hostun sand during triaxial compression with 60 kPa effective confining pressure (from [Des96]).

Using x-ray tomography in a quantitative way requires a calibration of CT values to obtain absolute values of density or void ratio. With such a calibration, Desrues was able to show that global measurements of volume change in such tests only give an

averaged picture, and in fact density variation (dilation for dense sand) occurs predominantly within the zones of localized shear. These quantitative analyses of density changes provided experimental confirmation that, for a given stress level, a unique limit void ratio is in fact reached, irrespective of the initial density of the sand being tested (the well-known concept of a critical state, as conjectured already by [Cas38]). However, this is only true locally, *i.e.*, within the shear zones (see Figure 14c).

As a second example of the application of x-ray CT, we refer to the post-mortem (*i.e.*, after the test) observations of strain localization in a granular rock, a sandstone from the Vosges Mountains (France) [Bés00]. Figures 15 and 16 show CT images obtained for two specimens that had been tested in triaxial compression at 30 MPa and 50MPa confinement, respectively. For the 30 MPa specimen (Figure 15), the shear band appears as a black region, *i.e.*, it has a higher porosity than the material outside the band, whereas the shear band is lighter, *i.e.*, denser, for the 50 MPa specimen. In neither case is the shear band a plane, plus there is some density variation along the band itself. Note that the shear band is less well defined for the 50 MPa case. In fact, in this test a number of conjugate bands were visible on the specimen surface. CT tomography revealed also a density inhomogeneity in both the specimens, the denser zone being the bottom half in one case (Figure 15d), and the top half in the other (Figure 16d). This was not due to deformation, but rather was preexisting in the specimens. Strain localization was consistently observed to occur in the less dense portion of the specimen, which likely has lower shear strength.

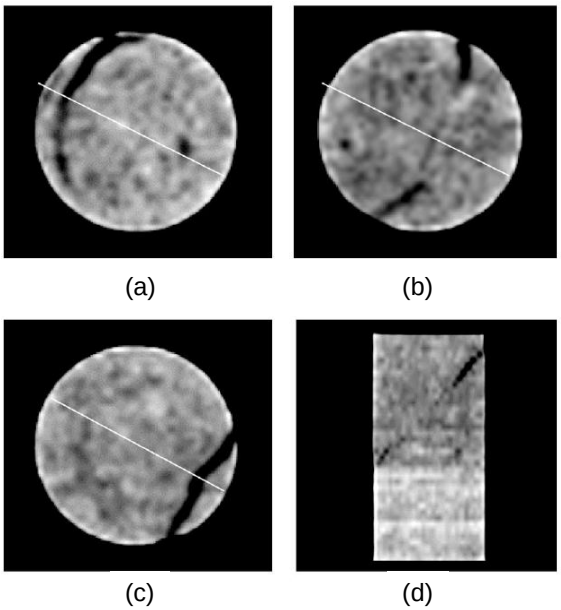

Figure 15. Localization of density variation in a specimen of the Vosges sandstone tested under triaxial compression at 30 MPa confining pressure. White lines in (a), (b) and (c) show the position of the plane in (d) (From [Bés00]).

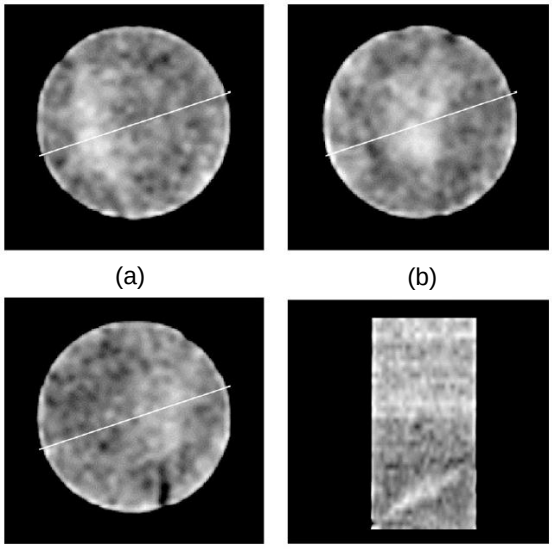

Figure 16. Localization of density variation in a specimen of the Vosges sandstone tested under triaxial compression at 50 MPa confining pressure. White lines in (a), (b) and (c) show the position of the plane in (d) (From [Bés00]).)

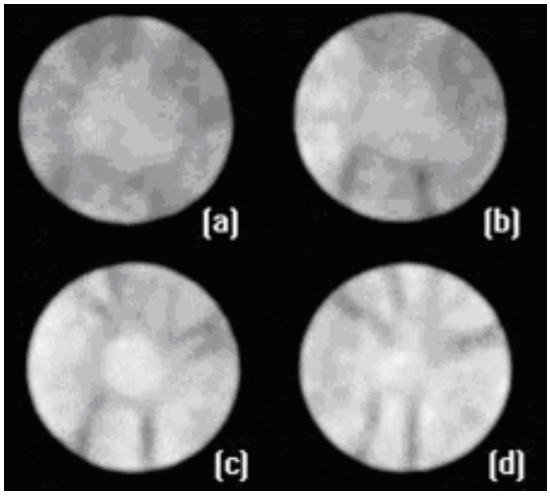

Figure 17. X-ray CT slices revealing patterns of localization in a specimen of Rothbach sandstone, which closely resemble those shown in Figures 13 and 14 for Hostun sand (From [Bés03]).

[Bés03] presented another example of strain localization in rock observed through post-mortem x-ray CT. Figure 17 shows CT images of Rothbach sandstone tested at 5 MPa effective confining pressure from this work. Interestingly, patterns of localized deformation observed in horizontal sections closely resemble those obtained by [Des96] in experiments on Hostun sand (Figures 13 and 14). Together with microstructural analyses, such CT images allowed Bésuelle and co-workers to investigate the features of localized damage (including shear and compaction bands) across the transitional regime from brittle faulting to cataclastic ductile flow in this sandstone.

The above examples clearly show that direct 3D observation of the internal structure of a specimen (be it a soil or a rock) can provide substantial advances in the understanding of strain localization in geomaterials. In particular, accessing the internal structure of a specimen during the test, *i.e.*, while it deforms under applied load (as was done by [Des96]), allows the entire deformation process to be followed: prior to, at, and after the onset of strain localization. However, performing a test properly and x-ray scanning at the same time (*i.e.*, *in-situ* tomography) is extremely challenging for geomaterials due to their specific testing requirements (confining pressure, pore pressure control, etc.). This has been achieved by a number of authors, including [Ray89], [Vin91], [Kaw99], [Ota00], [Ota02], [Als00], [Als08].

It should be noted that all the aforementioned in-situ studies have been performed using more or less "conventional" medical and industrial Computed Tomography (CT) systems. Another, much more powerful source of x-rays can be provided by synchrotron radiation, for which the x-ray beam is a thousand billion times "brighter" than the beam produced by a hospital x-ray machine (like the one used by [Des96]). The higher energy and photon flux of synchrotron radiation allow for a much higher resolution, down to the micrometric scale. Such a resolution may be unnecessary for coarse-grained geomaterials such as sand, in which the width of a shear band is known to be roughly 10 to 20 times the mean grain diameter size (*i.e.*, a few millimetres), unless one wishes to make observations at the scale of the grains. However, increased resolution is crucial for characterizing strain localization in fine-grained materials such as clays and clayey rocks, in which shear bands are much thinner, and in fact are often described as displacement discontinuities or slip surfaces [Vig04]. This is apparent from the relatively poor quality of the (few) available tomographic images of shear zones in fine-grained geomaterials obtained so far ([Ota00], [Til92], [Hic94]).

In the following, a few examples are shown from recent experimental studies, by our team, of strain localization in clay soils, clay rocks and sand. These testing programs were all carried out at the European Synchrotron Radiation Facility (ESRF) in Grenoble, making use of x-ray micro tomography at beamline ID15A. The tests were conducted using a specifically built setup that could be placed in the x-ray beam, so that the specimens were scanned under load (in situ). Synchrotron x-ray radiation was selected because it is the only one that can provide, thanks to its high photon flux, a combination of both fast scanning and high spatial resolution. The former is desired to minimize axial load relaxation, while keeping the specimen at constant axial strain during scanning (the acquisition of an entire specimen required four to six sections and in the most recent tests took 12 to 15 minutes). High spatial resolu-

tion allows fine detail on the deformation process to be obtained (a voxel size of 14 μm was achieved for specimens 10 to 20 mm in diameter).
Figure 18 shows the *in-situ* experimental setup, which included a triaxial apparatus and a loading system. The former is practically the same as a conventional triaxial testing system, except for its much smaller size and the shape of the confining cell. The cells were made from Plexiglas or polycarbonate to be as transparent to the x-rays as possible. Contrary to a conventional system, the tensile reaction force is carried by the cell walls and not by tie bars, which provides a clear path to the specimen for the x-ray beam, free of any obstacle (apart from the cell walls). The axial load and hence the deviator stress are applied using a motor-driven screw actuator. The loading system is placed in the x-ray beamline without interfering with the tomographic scans. See [Len06] for further details.

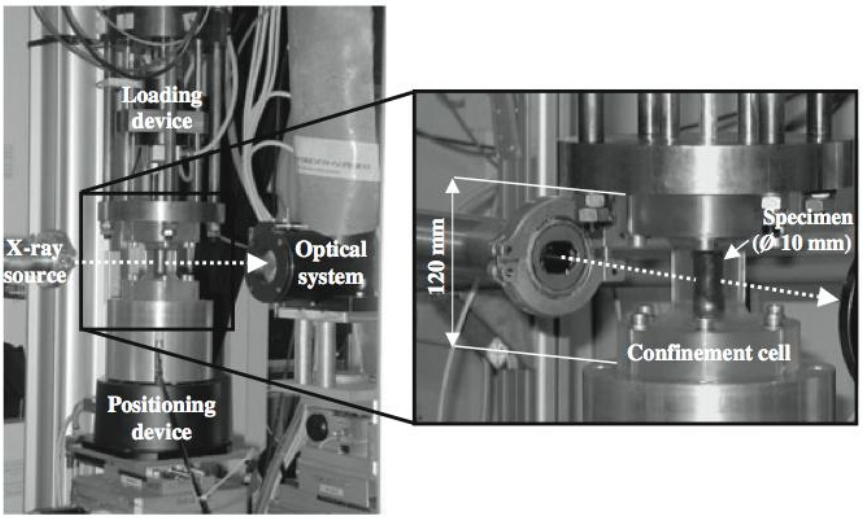

Figure 18. Experimental setup for *in-situ* triaxial x-ray tomography experiments: the complete set-up on the beamline (left) and zoom on the specimen inside the triaxial cell (right) (From [Len07]).

Results from a drained compression test on a 20 mm diameter specimen of Beaucaire marl are presented in Figure 19 [Vig04]. A single shear band formed in the specimen during the test, which could be clearly observed by eye at the end of the test. Two cross-sectional tomographic slices at mid-height of the specimen are shown in the figure, both taken in the post-peak regime. While no localization was observed in prior scans (a) and (b), scan (c) reveals some narrow regions of localized deformation, in which the soil is dilating (see zoom). These bands have a thickness of the order of 40 to 50 μm and include a few segments which can be interpreted as open cracks (black indicates no solid matter) a few pixels wide. At the end of the test (scan (d)), the localization looks like non-continuous cracks, connected by very thin shear bands (see zoom). More generally, the results from a suite of tests on

Beaucaire marl showed that the process of localization involves more than one, non-planar, shear zone, and a varying degree (in time and space) of dilatancy and/or crack opening. Furthermore, no density gradient could be observed (within the resolution of the method) around the zones of localization, which indicates that, whatever its nature (crack or dilating shear band), localization in Beaucaire marl is absolutely sharp in space. As an aside, it is worth noting that, despite the high quality of the reconstruction at the ESRF, the results are not immune from the well-known "ring artifacts", which appear as circular arcs in the images of Figure 19.

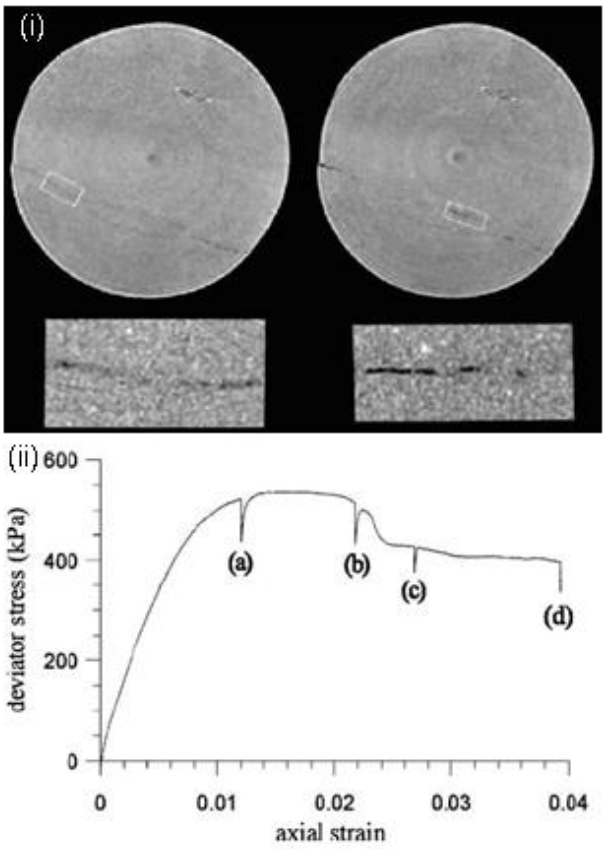

Figure 19. In situ x-ray CT tomography for a drained triaxial test on Beaucaire marl: (i) CT cross-section slices at mid-height of the specimen, at times (c), left and (d), right (sample is 20 mm diameter and the zooms are magnified by 6); (ii) stress-strain response (adapted from [Vig04]).

A second example of recent results from micro tomography at the ESRF has been presented by [Bés06] and [Len07]. The tested material was the Callovo-Oxfordian argillite issued from the ANDRA Underground Research Laboratory in France at approximately 550 m below the ground surface. This sedimentary rock is composed

of particles of calcite and quartz in a clay matrix, with a clay fraction of 40–45%. At the investigated depth, the material has an extremely low permeability (10^{-20}–10^{-22} m^2), a porosity of 15%, and a water content of 6%. The uniaxial compressive strength is about 20 MPa. Figure 20 shows the stress-strain response obtained from an undrained triaxial compression test on a 10 mm diameter specimen at 10 MPa confining pressure. The specimen was scanned at different steps: before and right after applying the confining pressure (steps 0 and 1, respectively), at different levels of axial strain during deviatoric loading (steps 2-7), and finally after removal of the confining pressure (step 8). Figure 21 shows four horizontal CT slices at different steps. The slices at steps 1, 3, 7 and 8 have been selected following a set of material points which were visible at step 1 and could be found on all subsequent images. At step 8, two open cracks can be seen at the specimen edges. Comparison of the images at steps 7 and 8 clearly indicates that crack opening in this test was essentially due to the removal of the confinement pressure. At the earlier step 3, which corresponds to the peak stress, no localized deformation is evident – even knowing where the cracks are eventually opening up later in the test. Furthermore, no visible difference can be seen between steps 1 and 3. In fact, localization becomes just visible in the CT images at step 4 (not shown in the figure - see [Bés06]).

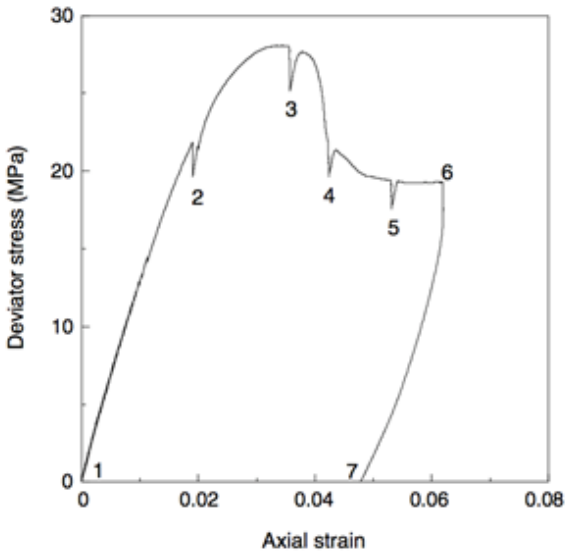

Figure 20. Load curve (deviator stress versus axial strain response) for the discussed triaxial compression test on the Callovo-Oxfordian argillite at 10 MPa confining pressure. The numbers indicate the times at which CT images were acquired (From [Len07]).

Interestingly, the existence of distinct calcite inclusions in the argillite was particularly helpful to highlight relative displacement in the specimen otherwise invisible in the CT images. Figure 22a shows an example of one such inclusion, having an elon-

gated vein shape and a length of a few millimeters. Figure 22b shows the same inclusion (in yellow) and the open fracture (in red) at step 8, *i.e.*, at the end of the test. Figures 22c-h illustrate how, upon loading, this inclusion was severely strained by the localization. Shearing of the inclusion is apparent starting from step 5, which becomes more and more pronounced for increasing deformation (steps 6 through 8). However, this intense shearing is not accompanied by a variation of density measurable within the resolution of the x-ray CT. This indicates that the region of localized deformation in the central part of the specimen is undergoing shear without substantial volume changes, whereas crack opening can be observed towards the edge of the specimen.

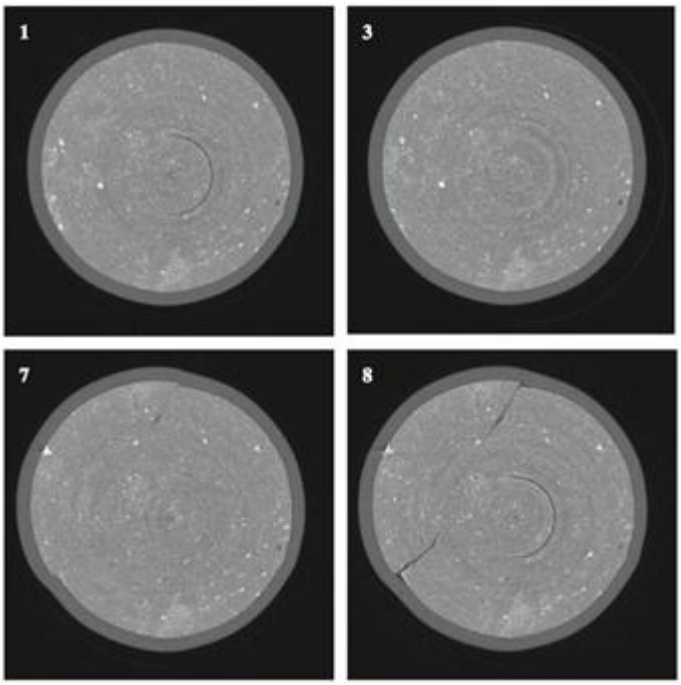

Figure 21. Horizontal slices through the CT image volume of the Callovo-Oxfordian argilite specimen (ø = 10 mm) at four different time steps (see Fig. 20) (From [Len07]).

As a final example from our ESRF experiments, Figure 23 shows vertical CT slices from a triaxial compression test performed on an 11 mm diameter dry specimen of Hostun sand, under a confinement of 150 kPa [Hal08]. The gain in spatial resolution with respect to the results presented earlier in this section from a medical scanner (Figures 13 and 14) is apparent. We are now able to see the individual grains (here the voxel is a cube of side 14 μm, whereas mean grain size, D_{50}, is about 300 μm). This vastly increased resolution opens up new possibilities for understanding the mechanics of granular media (in three dimensions), as we can analyze individual

grain kinematics and grain-grain interactions throughout the volume of a specimen and through the duration of a test. Similar results have been presented by [Mat06] and [Mat07] based on experiments at the SPring-8 synchrotron in Japan. However, the "small" disadvantage of such improved resolution is that one "cannot see the wood for the trees", *i.e.*, those patterns that were evident in the medical scanner images (again, see Figures 13 and 14) are much less apparent. For example, looking at the three vertical slices in Figure 26 (acquired before, at, and after the load peak), one can hardly discern the developing shear band, which is possibly more evident in the third image, going from the bottom right to the top left of the specimen.
Finally, Figure 24 shows one of the first 3D images of Hostun sand obtained using the multi-scale tomographic equipment that was installed at our laboratory in early 2008. Note that a similar spatial resolution is achieved as for the ESRF example above. However, the acquisition time is significantly longer for the same specimen size and spatial resolution, due to the much lower photon flux.

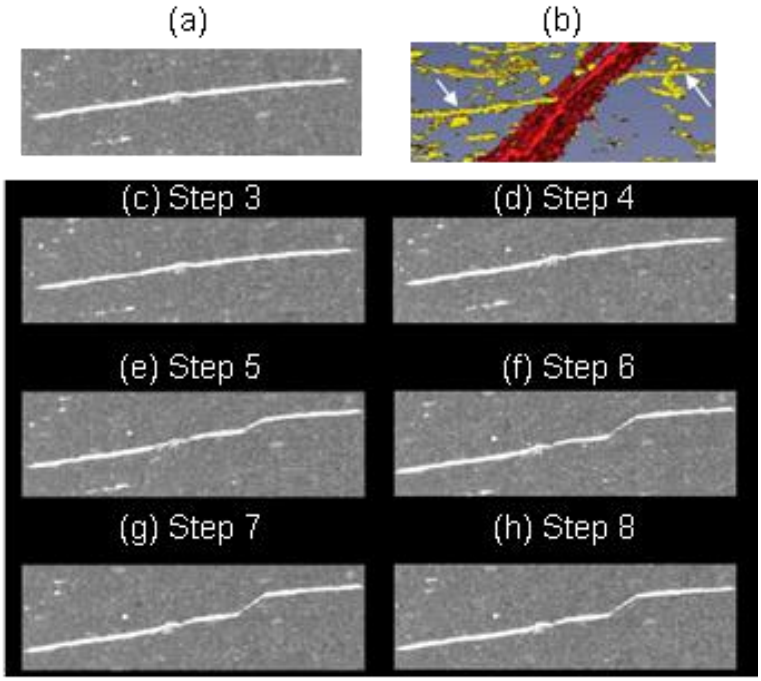

Figure 22. (a) An inclusion in the Callovo-Oxfordian argilite at the start of the test (the image is a small vertical section extracted from the x-ray tomogram and the inclusion is a few millimeters long). (b) 3D view of the same inclusion (yellow) and cross-cutting open fracture (red) at step 8 (the end of the test) highlighted through thresholding and false-coloring of the gray-scale image. (c)-(h) the inclusion at different stages through the test showing increasing shearing (From [Bés07]).

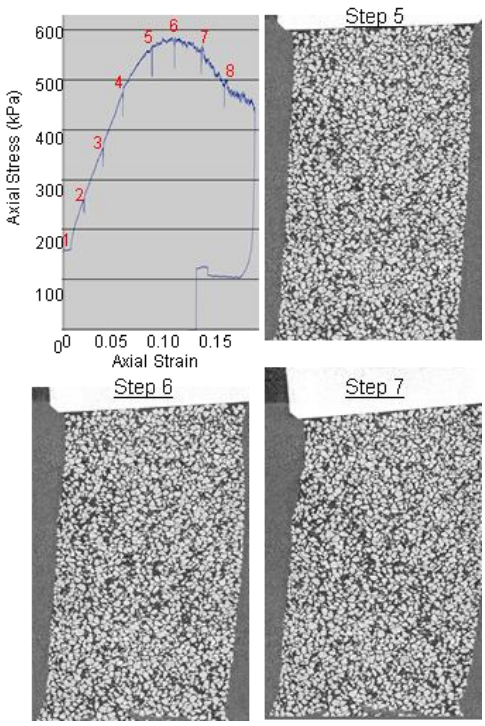

Figure 23. Results from a triaxial compression test (150 kPa confinement) on a dry Hostun sand specimen (11 mm diameter). (a) Axial stress-strain curve with CT-scan times indicated. (b) Vertical CT slices acquired before, at, and after the load peak (voxels are cubes of side 14 μm and the mean grain size is about 300 μm).

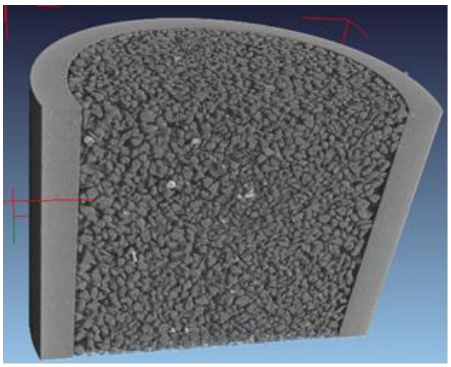

Figure 24. 3D cut-out view of an x-ray CT image of dry Hostun sand in a plastic tube (about 11 mm diameter) acquired using the multi-scale tomographic equipment at Laboratoire 3SR (image courtesy of N. Lenoir).

7 COMBINING X-RAY TOMOGRAPHY AND 3D DIC

The discussion in the previous section concerning CT observation of localized strain in clay rocks, illustrates a fundamental difficulty with experimental detection of strain localization through the use of x-ray CT, which is associated to the very nature of localized strain. The issue is that while localization can sometimes induce large volumetric deformation – either dilatancy (or crack opening) or compaction (compaction bands), depending on the material and loading conditions, in general volumetric strain in a shear band is small compared to the shear strain. Unfortunately, CT images only represent local mass density fields. If the material inside the region of localized deformation dilates (or contracts), then local mass density variations can be an effective means to track the regions of localized deformation. This was the case with the studies of shear banding in sand from Desrues presented in the previous section. However, for the experiments on the argillite, this was only the case with open cracks, where voids are created between the crack edges that are clearly visible on the tomographic images (*e.g.*, step 8 in Figure 21). If the localized deformation is isochoric (no volume change), *e.g.*, it consists of closed, shearing cracks, then it is invisible in CT images (except for the "lucky" cases where the shear cuts markers such as the inclusion in Figure 22).
The limitation of x-ray tomography to studying only phenomena with significant density changes can be overcome by complementing x-ray CT with 3D digital image correlation, which is an extension of 2D DIC discussed in section 3.2. 2D DIC has previously been applied to x-ray radiographs ([Rus89], [Syn99]). More recently, applications of DIC in three dimensions have been presented by *e.g.*, [Bay99], [Smi02], [Ver04], [Bor04], [For04]. See [Hal12] in this volume for further details, references and examples.

7.1 Example 1: localized deformation in a clay rock

The first example comes from an experimental study on a clay rock ([Bés06], [Len07]). A few results are shown in the following that demonstrate how correlation of 3D digital images from x-ray tomography provides a means to detect (within a given accuracy) localized deformation, independent of its nature (shear or volumetric strain). These results were obtained for the test on Callovo-Oxfordian argillite already presented in the previous section (Figures 20 to 22). The details of the 3D DIC method used are thoroughly discussed elsewhere ([Len07]). Herein it will be sufficient to bear in mind that each 3D image is decomposed into several cubical subsets, each of them containing 20^3 voxels. Due to the small deformation experienced by the argillite specimens, for this study the transformation between two images was assumed to be a rigid translation without any rotation or distortion.
Figures 25 and 26 show vertical and horizontal cuts through the DIC-derived (incremental) shear strain field volumes. In the pre-peak increment (2–3, see Figure 20)

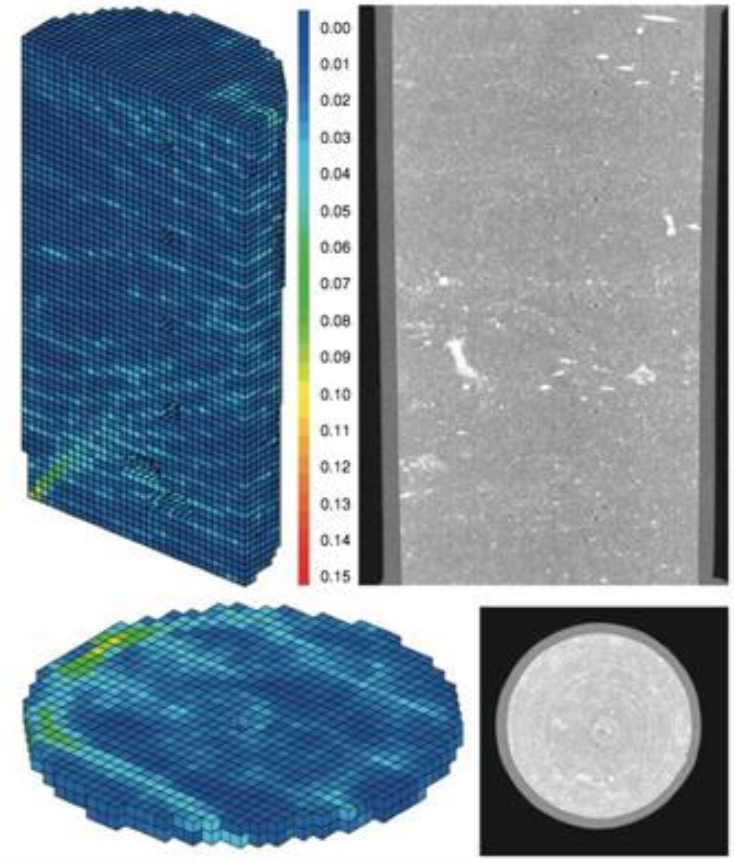

Figure 25. DIC-derived deformation maps for load increment 2-3 (before peak load - see Fig. 20) of the triaxial test on the Callovo-Oxfordian argillite (ø = 10 mm). Top and bottom right: vertical (along the specimen axis) and horizontal (close to the bottom of the specimen) sections through the CT volume image at step 3. Top and bottom left: incremental maximum shear strain maps for the equivalent sections (color scale is [0, 0.15]) (from [Len07]).

the onset of strain localization is visible at the bottom left corner of the vertical cut through the shear strain map (Figure 25). The horizontal cut in Figure 25 suggests that during this increment the localization developed with a conical shape. Note that the x-ray sections of the specimen at the end of the increment do not reveal any trace of localized deformation. In the post-peak increment (3–4, see Figure 20), a fully developed shear band through the specimen can be observed (Figure 26). As compared to the pre-peak increment, the zone of localized deformation is more planar both in the vertical and in the horizontal cuts. In fact, the post-peak localization band partly coincides with the pre-peak cone of localized deformation in the lower region, suggesting that the later shear zone evolved from the initial one. As for the previous increment, no clear sign of strain localization is visible in the x-ray sections of the

specimen at the end of the increment. It is worth noting that the thickness of the shear bands in these strain volumes is exaggerated with respect to real size. This is due to the lower limit to resolvable thickness dictated by the dimensions of DIC subsets (280 μm side length), whereas CT images indicate that the thickness of the localization zones (be these dilating shear bands or open cracks) in the tested specimens was typically less than 70 μm.

One of the key conclusions from this study is that, through 3D DIC, it was shown that localized shear had initiated in the specimen already prior to the stress deviator peak. In fact, this was possibly the case also for the test on Beaucaire marl discussed earlier (see Figure 19). In other words, the important general message here is that the DIC analysis of 3D images from x-ray tomography can reveal patterns of deformation that could not be observed using only the gray scale images, in which they may remain hidden (if they do not involve significant volume changes); this is even with high resolution synchrotron micro tomography.

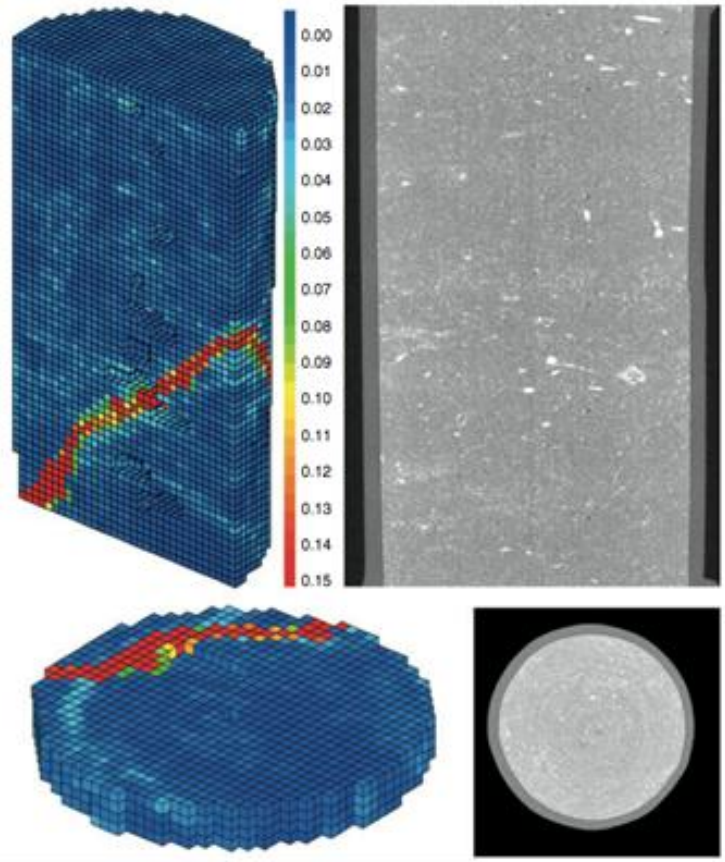

Figure 26. As Figure 25 but load increment 3-4, i.e., after peak load (from [Len07]).

7.2 Example 2: localized deformation in sand

As a second example, a few results are shown in the following that show how correlation of 3D digital images from x-ray tomography provides extra information about localized deformation in sand. These results were obtained for the test on Hostun sand already presented in the previous section (Figure 23). Here the aim was to both observe the material evolution with grain-scale resolution and to image the deformation processes. To this end 3D DIC is employed to assess the 3D displacement and strain fields in the sample. To our knowledge this study, results of which have been published in [Hal09], [HaB10] and [Vig09], was the first application of 3D DIC to granular media.

The test described hereafter was carried out at the ESRF in Grenoble on beamline ID15A, using a setup very similar to the one described in the previous section for the experiments on the clay rock. Triaxial compression was performed on a dry specimen of S28 Hostun sand, under a confining pressure of 100 kPa. Deviatoric loading was strain controlled, with a screw driven piston descending at 60μm/min, which corresponds to quite a low strain rate (0.05 %/min for a 11 mm high specimen). In this test, the sample was 11 mm in diameter and 22 mm high and had an initially dense packing. It should be noted that despite the small sample size (in comparison to standard triaxial tests on sands), the sample can be considered to be sufficiently large such that it remains mechanically pertinent (*i.e.*, its response can be considered representative of that of a larger mass of the material); in fact the sample comprises roughly 50000 grains. These reduced dimensions were imposed by the x-ray imager width, which was just 14 mm (the sample needed to be smaller than this to not risk passing out of the field of view, although this does occur by the end of the test; see later). X-ray tomography scans were carried out at key moments throughout the test, which are marked by (small) relaxations in the loading curve in Figure 27b. The sample stress-strain response shows a roughly linear initial trend followed by a curvature to the peak stress at around 11% nominal axial strain, after which the stress drops, to what is probably the beginning of a plateau, after which the test was stopped and the sample unloaded.

Figure 27c shows a series of vertical slices through the x-ray tomography image volumes at different stages in the test (see Figure 27b). These slices are roughly perpendicular to the "plane" of localization that developed during the test. The voxel size of these images is 14x14x14 μm^3, which represents a spatial resolution far greater than was previously possible with medical or laboratory scanners. As such it is possible to clearly identify the individual grains (recall that the mean grain size is around 300 μm or 21 voxels). These *in-situ* images show that the sample starts to lean to the right and there is a rotation of the upper platen in the latter part of the test, but there is no clear evidence of localized deformation. Porosities have been calculated from the images for each step based on overlapping cubic windows of side 61 voxels (854 μm) throughout the sample volume (see Figure 27d); these represent the accumulated porosity evolution from the start of the test. From these porosity fields an evolving inclined zone of localized dilation can be seen.

3D volumetric DIC has been carried out on consecutive pairs of 3D image volumes to provide the incremental displacement and strain fields (the results are thus aver-

ages over the given time interval). The key parameters in the DIC are the distance between the calculation nodes and the correlation window size; in this analysis these were, respectively, 20 voxels (or 280 μm) and a cube with sides of 21 voxels (or 294 μm) reduced to 11 voxels (or 154 μm) for the sub-pixel derivation. Results from this DIC analysis indicate that, despite the granular nature of the material, smooth and relatively continuous displacement fields are measured. The evolved localization is evident as a band bounded by two "weak" discontinuities, *i.e.*, strain are discontinuous, not the displacements. Figure 27e shows median projections of the 3D field of maximum shear strain $(\varepsilon_1 - \varepsilon_3)/2$ (where ε_1 and ε_3 are the major and minor principal strains) for increments 3-4, 4-5, 5-6 and 6-7. These strain images clearly show the evolution of a localized band that traverses the sample diagonally from left to right. It is important to note the zones of near zero strain away from the localized zone as these indicate that the DIC is clearly working well and the localization is real.

It is worth noting that the DIC strain analysis provides an incremental analysis, *i.e.*, it indicates the deformation active in each strain increment. This is different from what can be seen with accumulated porosity changes shown in Figure 27d. As such it is seen from these incremental maps that the localization initiated in the increment 4-5, *i.e.*, well before the peak load, and before this becomes clear in the porosity images. Furthermore, the localization is revealed to start as a broad zone that thinned with loading. In increment 6-7, the zone has a width of about 5 mm (*i.e.*, about 17 D_{50}). It is also clear that the localized zone is not uniform, showing a degree of structure. The width of the band is in fact difficult to define. It appears that in places the shear band contains a narrower internal core of much higher strain. The DIC results show that the localized band is not uniform and, whilst it is well defined (and quite planar), there are aligned zones of either reduced or elevated strains at an angle "conjugate" to the main band. The orientations of these zones are similar to those of “columns” of aligned grains identified by [Oda04] in a shear band in sand. Therefore, the shear-strain structures might indicate the presence of columnar structures in the grain assemblage and motivate the use of discrete image analyses.

We have already noted earlier in the paper (Section 4) that standard implementations of DIC assume a continuous displacement field, at least within each subset. When deriving strain from the displacements of separate subsets, continuity between adjacent subsets is assumed. For this reason, we refer to such DIC analysis as ‘continuum DIC’ (or in this case piece-wise continuous). An alternative DIC approach for granular materials that recognizes the granular character both of the images and the mechanical response was recently proposed by M. Bornert and presented in [HaB10] and [Pan10]. This approach is a ‘discrete DIC’ procedure with the specific aspect that the regularly shaped and spaced subsets are replaced by subsets centered on individual grains, with a shape following the actual shape of the grain. If the grains are assumed to be rigid, then the transformation of each subset is a rigid motion involving a three-component translation vector plus a three-component rotation.

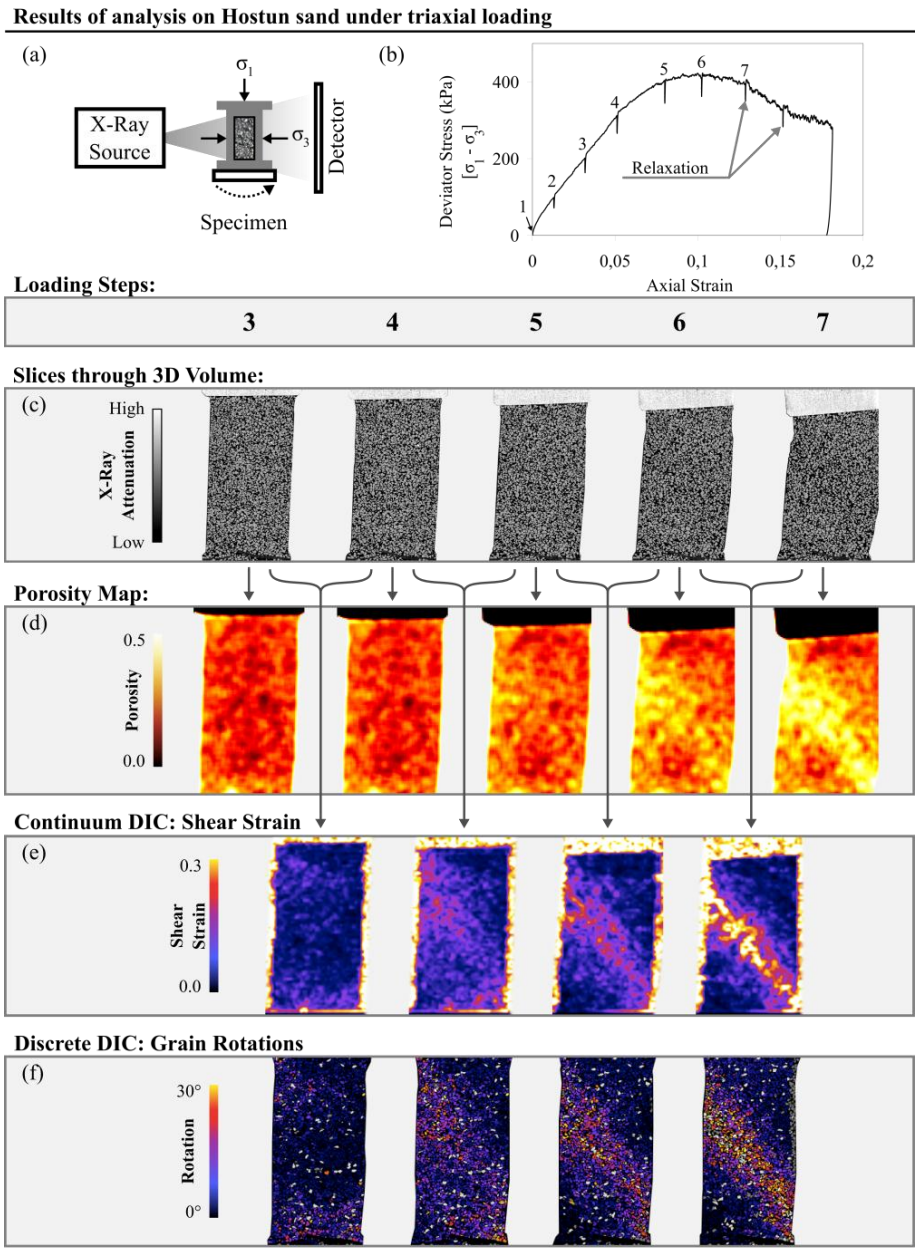

Figure 27. (a) Data acquisition; (b) stress-strain curve indicating also the image acquisition times; (c)-(f) vertical slices through the image volumes of x-ray tomography, porosity, shear strain and individual grain rotations (note that the grains in the final image are represented in their initial configuration).

Discrete DIC was applied by [HaB10] to the x-ray tomography images from the test on Hostun sand to provide incremental analysis of the kinematics of each grain (3D displacements and rotations). Grain displacements agree with the continuum DIC results with relatively continuous fields of displacements, even in the presence of strain localization, which explains why continuum DIC performed well. However, locally (between grains) the kinematics can be discontinuous. As an example, Figure 27f presents the magnitude of rotation for each grain about its rotation axis (which is specific for each grain). These results indicate that grain rotations become progressively more intense into a zone that roughly corresponds to where shear strain localizes, showing that the shear strain is due, at least in part, to grain rotations at the micro-scale.

8 TRACKING INDIVIDUAL SAND GRAINS

As seen in the previous section, x-ray micro-tomography allows 3D imaging at sufficiently high spatial resolution to "see" all the individual grains in a sample of sand of appropriate dimensions.

The x-ray images can be binarized into grains and pores then "segmented" to identify and label individual grains. This can be performed by using a 3D watershed algorithm (in our group, we typically use the algorithm from the image-processing package VISILOG ©Noesis, http://www.noesisvision.com/). The output from this procedure is an image volume in which each grain is assigned a unique label (number) such that they can subsequently be identified and characterized to give their geometrical characteristics. In addition, once the grains are separated and labeled, contacts between grains can be identified as described by [HaL10] to give binary or labeled volumes of contacts. In principle, quantification of contact statistics and geometries can thus be carried out, *e.g.*, in terms of orientation distribution functions, contact density fields and grain coordination numbers. Contact density distributions can also be derived, see [HaL10]. The orientation of a contact, however, is difficult to measure because the typical spatial resolution of the scans (10 to 15 μm) is not enough to accurately resolve the surfaces of the grains in contact. Measured contact orientations are therefore highly dependent on the type of watershed method used to split the grains apart (creating the contact areas by removing voxels at the interface between grains); this has been recently shown by [AnH12]. More advanced segmentation techniques, as well as the calculation of contact orientations based on grain topology around the contact are currently being investigated, see [AnH12].

Once each grain is assigned a unique label, one can in fact recognize individual grains based on their geometrical characteristics through a series of *in-situ* 3D tomography images. This is the very idea of *Grain Tracking*, which has been recently suggested as a possible alternative to the discrete DIC approach discussed above. This concept was originally proposed by [HaL08], and it has been recently implemented in a method called ID-Track – see [And12]. This method allows the quantification of individual grain kinematics (displacements and rotations) of large quantities of sand grains (tens of thousands) in a test sample undergoing loading. With ID-Track, grains are tracked between images based on some geometrical feature(s) that

allow their unique identification and matching between images. This differs substantially from Digital Image Correlation (DIC), which makes measurements by recognizing patterns between images. Since ID-Track does not use the image of a grain for tracking, it is significantly faster than DIC; however, it suffers in the measurement of rotations when compared with Discrete DIC.

The ID-Track technique, which is fully detailed in [And12], has been applied to the analysis of grain kinematics in several experiments on different granular materials. In this paper, results from two such tests (triaxial compression) are presented to illustrate the method one on the angular Hostun sand and one on the rounded Caicos Ooids; see [And12] for further details.

The results presented in Figure 28 are vertical slices through the labeled volume of grains in the reference state for the two tests considered; the slices have been oriented in order to contain both the axis of the sample and the normal to the shear band that eventually forms. Each grain that has been tracked for a given increment is colored either according to its displacement (the norm of the displacement vector) or according to its value of rotation (the axis of rotation is not shown). Grains that are not tracked are left blank. The sample is compressed from the bottom upwards, so that displacement in the axial direction is imposed as 0 at the top of the sample. It is immediately apparent (especially in the displacements) that the overall kinematics of the sample are characterized by smooth fields – as previously shown with continuum DIC [HaB10]. At the end of both tests, a highly localized pattern of deformation in the form of a single shear band occurs. More complex patterns of localization are often observed when shearing dense sand in triaxial compression (*e.g.*, [Des96]), but these are unlikely to occur in the very small specimens (with respect to grain size) tested in this work. In any case, a single shear band is the localization mode expected for a dense sand sheared with standard conditions (sample with slenderness ratio of 2 and non-lubricated ends) – see, for example, [Des96].

The displacement field in the first increment of loading for the test on Hostun sand (Figure 28, top) appears to be smooth, although there are some grains that are not tracked (6 to 8% per increment), which correspond to blank grains – *i.e.*, holes in the image. Furthermore, there are occasional grains that are incorrectly tracked (grains with displacements very different to their neighbors can sometimes be seen). The overall behavior is, however, clear: over the first strain increment, there is an almost smooth incremental displacement, from 0 at the top of the sample (imposed) to 0.4 mm at the bottom (also imposed). A slight lack of verticality in the sample at the beginning of the test (sample axis tilted by 1.4° in the slices shown) manifests itself as an ‘‘inclined’’ displacement field relative to the direction of loading. In continuum mechanics, this would correspond to a strain field that is not wholly uniform, yet without strong gradients. In the following increment (2–3), before the peak in the overall sample response, the gradient of the displacement field is oriented perpendicular to the direction of the band that eventually forms. These discrete observations support the theoretical idealization of a shear band as a region of localized deformation bounded by *weak* discontinuities, *i.e.*, discontinuities in the gradient of displacement.

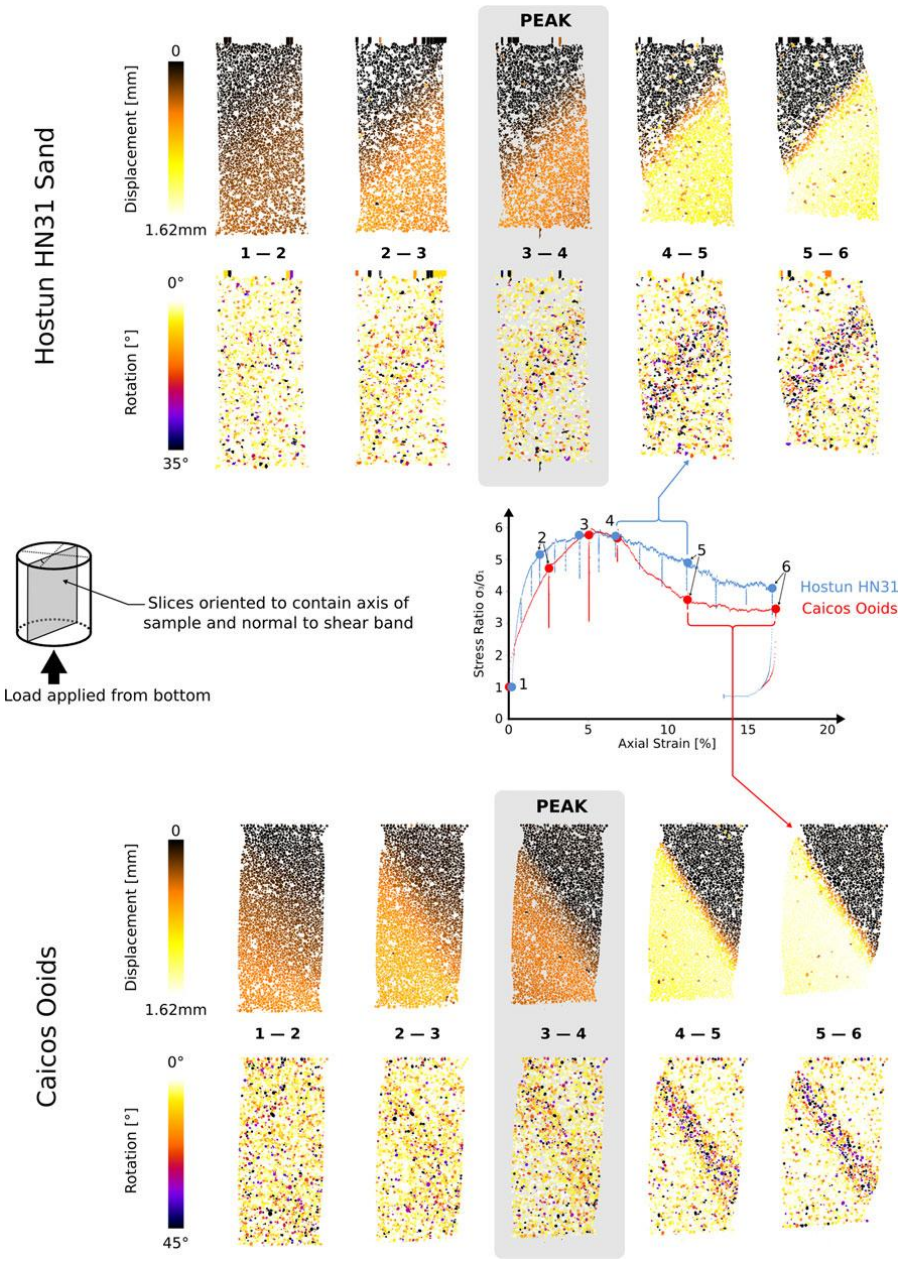

Figure 28. Results of ID-Track on five strain increments for TXC on Hostun Sand and Caicos Ooids. Results are shown as slices oriented in order to contain both the axis of the sample and the normal to the shear band that eventually forms; tracked grains are colored by the norm of their displacement vector or value of rotation (axis of rotation not shown) (from [And12]).

The displacements progressively concentrate into a band 7 to 8 grains thick by the last increment (5–6, see Figure 29 top left for a zoom into the displacement field). The band appears to be oriented at about 47° from the horizontal. Up until the peak, rotations appear to be disorganized in space. After the peak, when the band is fully developed, the rotations are clearly concentrated in space. In the increment that lies over the peak (3–4), some concentration of rotations can be discerned. Initial indications of this concentration might exist in increment 2–3. The rotations are concentrated in the same band as indicated by displacement, although the width of concentration appears to be larger (10–12 grains thick, see Figure 29, bottom left). ID-Track also provides the axis of rotation for each grain, which is not necessarily orthogonal to the slices shown. It is of interest to look at the component of rotation occurring in the plane of the slices, *i.e.*, the component of rotation around an axis orthogonal to the plane of the slices (which might be termed rolling in the ‘‘steepest direction’’, if the shear band is imagined as a plane on which grains are rolling). It appears that grains inside the band do not show any more evident concentration of rotation when measured with this component – from which we can conclude that rotations clearly concentrate in the band, but apparently not in the ‘‘steepest direction’’.

For the test on Caicos Ooids presented in Figure 28 (bottom), it can be seen that grains are tracked more successfully, with only 1 to 3% lost grains. The improved success rate, over that of the Hostun example, is due to a higher quality of segmentation – the watershed algorithm works better on the more spherical grains of this material. In terms of displacement, a similar phenomenon to the Hostun sand can be seen to occur – the major differences are that the band appears slightly more concentrated (6 to 7 grain diameters, see Figure 29, top right) and steeper relative to the horizontal (54°). Note that, as with the Hostun sample, the displacement field is slightly inclined from the very beginning of the test. Also, as with Hostun, rotations are disorganized in space and therefore not localized in the first increment. Rotations start to concentrate after the peak, again with hints visible over the peak, and possibly already in the preceding increment (2–3). The band as measured by rotation is thicker than that measured by displacement, but considerably less so than with Hostun sand (7 to 8 grain diameters, Figure 29, bottom right). It should be noted that although the sphericity of the grains results in a higher quality segmentation, the grains are not so spherical that their orientation cannot be well defined by their moment of inertia tensor. As with Hostun, the rotations localize, but the directions of rotation apparently do not.

One tentative explanation for the difference between the relative width of the shear band as measured by displacement or rotation for these two sands is based on the grain shape: the shear band (which is inherently a 2D phenomenon at the sample scale) causes grains to move differentially while it is trying to develop in a 3D material. The development of the band causes a region with a thickness of about 7 grains to displace differentially (the bottom ‘‘block’’ of grains moves almost as a rigid body). However, in order to displace differentially, the grains in the shear band must also rotate around each other. In a rounded material these rotations are not strongly transmitted into the rest of the sample due to the lower level of interlocking between grains, whereas in the angular material, a ‘‘cog’’ effect may occur, explaining why

the band measured in rotations is so much thicker for Hostun sand. The greater number of grains involved in the rotations may also explain the higher residual stress of the angular sample, since sliding in the band (necessarily causing rotation in 3D) is ‘‘resisted’’ more strongly.

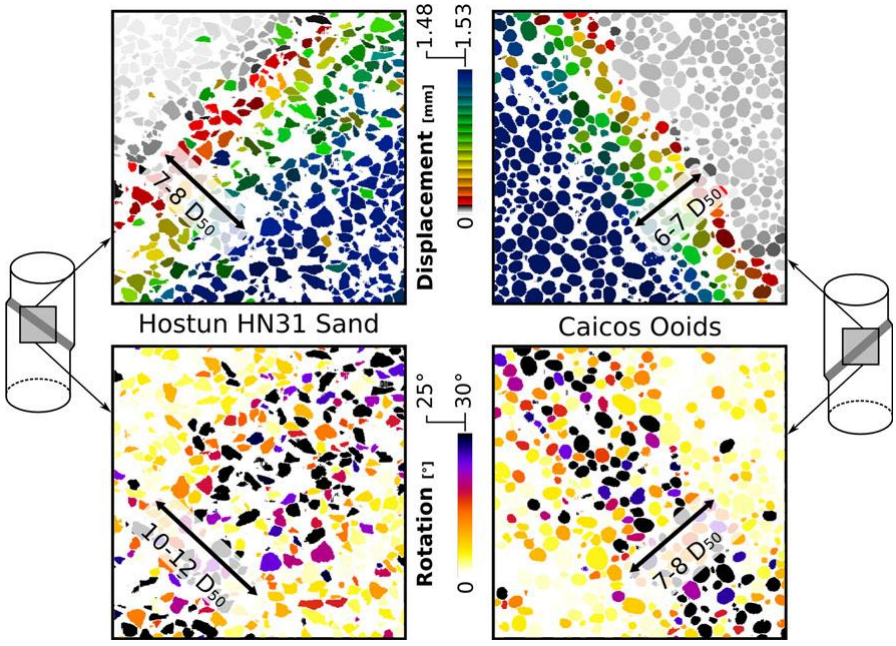

Figure 29. Zoom into shear band for the two tests, at the last strain increment 5–6 in Figure 28 (from [And12]).

From a computational point of view, it should be reported that, given the calculated grain IDs and their positions and orientation vectors in space for a reference and a deformed configuration, tracking takes only a few minutes on a powerful laptop. This is a major advantage relative to the reported tens of hours for an increment of Discrete DIC. However, as mentioned above, ID-Track suffers in the measurement of rotations when compared with Discrete DIC. For this reason, a new hybrid, grain-based image-correlation approach has been recently developed, which matches images of the grains between configurations (the images of the grains contain several thousand data points rather than two 3-component vectors), in the style of [HaB10]. This approach skips the computationally expensive searching of the grains by image correlation, and instead uses the results of ID-Track to find the images of a grain in reference and deformed configurations, which are then copied into padded cubic arrays. The reference image is rotated and displaced in 3D by transforming its original coordinates and looking them up in a specifically written trilinear interpolation of the reference image. The search for the 3 rotation and 3 displacement components yielding the highest similarity between the rotated and translated reference image and the deformed image is then led by an optimization algorithm – see [AnH12] for further details.

9 INTRA-GRANULAR MEASUREMENTS: COHERENT ELASTIC NEUTRON AND X-RAY DIFFRACTION

The understanding of mechanics of granular materials could be aided by measures of force distribution, in addition to the grain kinematics and structural evolution. Unfortunately, forces cannot be measured; however they might be inferred from strains in the supporting grains. To this end [Hal11] recently presented first results of neutron and x-ray diffraction measurements of changes in crystallographic lattices of sand grains (which are quartz crystals) in samples of many grains under load. These approaches exploit the concept of coherent elastic scattering, which is the interaction of x-rays with the electron cloud around an atom, or of a neutron with the nucleus of an atom, leading to diffraction. Constructive and destructive interference of the diffracted x-rays or neutrons leads to patterns of 'Bragg peaks' that are characteristic of the arrangement of atoms in the scattering crystals and, in particular, the spacing between the atomic planes (the so-called "d-spacing"). The diffraction angle (2θ) of the Bragg peaks can change if the d-spacings between crystallographic planes change. Measurement of changes in Bragg peak positions can thus be used to determine strains in different directions in the diffracting crystals such that each grain can act as a local 3D strain gauge or, for elastic grain deformations, a force gauge. Two spatially resolved diffraction techniques, with different space and strain resolutions, are described below.

9.1 *In-situ* Neutron diffraction

The monochromatic neutron diffraction instrument SALSA, at the Institut Laue-Langevin, France (see [Pir06]) allows very precise measures of crystal strains over small gauge volumes on the assumption that, within the volume, there is a continuous orientation distribution function of crystals (an assumption of "powder" diffraction). [Hal11] presented results of neutron diffraction measurements using SALSA for sand under 1D (oedometric) compression (using an aluminum oedometer of internal diameter 30 mm). Loading was carried out *in-situ*, *i.e.*, whilst mounted in the diffraction set-up, over a load-unload-load cycle of $0 \rightarrow 35 \rightarrow 1 \rightarrow 35$ kN. At each 1 kN loading step the force was held whilst a diffraction measurement was performed for a gauge volume of 4 x 4 x15 mm^3 in the center of the sample (average sand grain diameters were about 250 μm); the large gauge volume produced stronger scattering thus allowing faster measurements over a range of loads, at the expense of spatial resolution. A Bragg peak at $2\theta \approx 86.8°$ ($\lambda = 1.64$ Å) was measured with a Q-vector (strain measurement direction) along the sample axis.

Figure 30 shows the loading-piston displacement (indicating macro-strain) and the axial 2θ values (indicating grain-strain averages over the gauge-volume) as functions of the applied axial force. Globally, the grain-strain follows a remarkably similar trend to the macro-strain. However, the grain-strain at first increases more slowly, than the macro-strain, until about 10 kN, after which the gradient increases; this

appears to correspond to a reduction in the macro-curve gradient (*i.e.*, a stiffer response). These trends perhaps indicate a change in the general deformation mechanism from porosity reduction to grain strain.
There is a significant non-recovered macro-strain as would be expected due to porosity reduction, but there is also a significant residual grain-strain. This suggests that the grains remain confined between themselves ("locked") after removal of the load. The significant variation of the grain-strain variations around the trend is not thought to be just noise, but rather might indicate the occurrence of load transfer in and out of this volume; this hypothesis is being tested with 3D mapping and smaller gauge volumes.

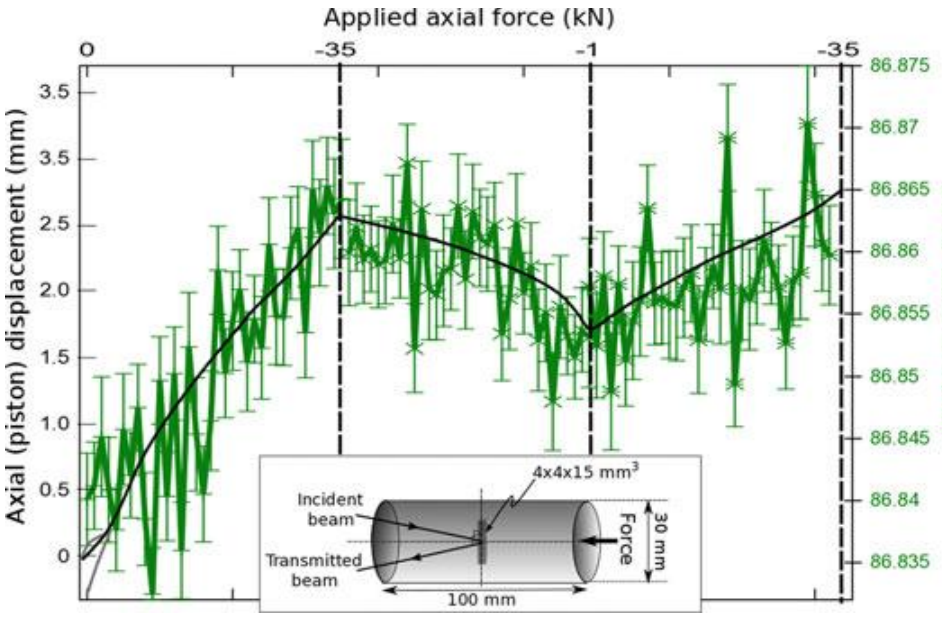

Figure 30. Neutron diffraction results: macroscopic axial displacement and change in 2θ, indicating grain-strain in the axial direction (average over the gauge volume see in-set), as functions of the applied axial force. Inset: measurement and loading set-up (from [Hal11]).

9.2. *In-situ* 3DXRD

The measurements presented above using neutron diffraction are measures of crystallographic strain averaged over a volume. Whilst the technique is being extended to use smaller gauge volumes and 3D mapping, it will remain a "continuum" intragranular measure. Similar gauge-volume techniques exist for x-rays, but with the fine focusing possible at synchrotron facilities other, more refined, approaches can be considered. 3DXRD (3D x-ray diffraction) is a technique that can provide grain-

by-grain measures of 3D grain-strains, albeit for reduced numbers of grains; this has mostly been applied for metals, see [Pou04].
However, 3DXRD for sands has been presented by [Hal11]. Measurements were carried out at the ESRF using beamline ID11 where grain-strain resolution of about 10^{-4} can be expected. This was the first such application to geomaterials, and involved 1D compression *in-situ* in the 3DXRD setup using quartz-glass oedometers (internal diameter 10 mm) and sand grains of average diameters of about 720 μm. The early results presented in [Hal11] demonstrated that diffraction patterns could be measured and assigned to individual grains. Furthermore, there were good indications that quantitative measures of individual grain-strains plus grain and sub-grain kinematics (rotations and intra-granular crack opening) could be made. The analysis of these data is still on-going and individual grain strains over a range of loads are now being determined.
The possibility of inferring forces at different scales provides another new dimension to the experimental analysis and thus new understanding for modeling. One might imagine eventually being able to access all aspects of the mechanical behavior of granular materials, *i.e.*, kinematics (displacements, strain) and statics (forces, stress). Such measures will also improve the understanding of the mechanisms, *e.g.*, how are the forces transmitted, do just a few grains support the load and, if so, what is the configuration of the load-carrying grains and what are the characteristic distances? Additionally, what are the processes that lead to failure? If force-chain buckling is key to failure, as has been suggested (*e.g.*, [Oda04]), one must be able to measure this experimentally, which requires some experimental determination of force (rather than just relying on geometrical considerations) – the diffraction measures discussed, might well permit this in the future for real sands (as opposed to numerical experiments or idealized experiments on photoelastic materials). The example given above using neutron diffraction also highlights key issues relating to the partitioning of strain in the granular material – whilst at low strain it is the porosity reduction that is important, at higher (but not so high) strain, the grains themselves do deform (this result will clearly depend on packing). These results can also illuminate issues relating to the phenomenon of granular locking.

10 CONCLUDING REMARKS

In this paper we have endeavored to provide an overview of available full-field laboratory methods and to show their interest in geomechanics. Although this paper only discusses laboratory applications, it should be noted that full-field methods are used also in the field, *i.e.*, out of the laboratory (in fact, some of them were originally applied at the field scale, *e.g.*, in geophysics and remote sensing).
While the examples presented concern a variety of geomaterials (sand, clay, and rock), they are predominantly focused on the study of strain localization and localized failure, which is a direct consequence of our specific research interests. However, full-field measurement techniques have a wider range of application in laboratory geomechanics. In laboratory testing perfection is impossible: boundary conditions can never be perfectly prescribed, and even far from failure geomaterial specimens

are never truly homogeneous.. Therefore, any experiment on soil or rock is essentially a "boundary value problem", as opposed to a "single-element" test, and so one should consider the distribution of stress and strain in the specimen in order to extract constitutive information. Full-field measurements are a means to achieve this, in that they allow the effects of pre-existing or test-induced anomalies, inhomogeneities and imperfections of various kinds to be identified and thus accounted for in the interpretation of test results. In addition, there is an increasing interest in testing configurations that deliberately lead to heterogeneous stress/strain fields. For example, this is necessary for calibration of constitutive models based on higher order continuum mechanics (e.g., [ChR11], which requires comparison of computed and measured fields with significant stress/strain gradients.

One major complexity of the behavior of geomaterials is related to the loss of homogeneity of the deformation process during loading. Strain localization, which precedes and leads to global failure, operates at a micro-scale that is characteristic of the material. The central role played by grain-scale mechanisms in the onset and evolution of shear bands in granular materials has been a subject of study and debate in geomechanics for decades. On the modeling side, one way to handle strain localization is to incorporate a micro-scale. In Grenoble this has been approached in different ways, for example by using higher-order continua (*e.g.*, second gradient models, see [ChR11]), or multi-scale computations (in which a micro-scale is explicitly simulated, *e.g.*, [Nit11] and [And11]). In order to inform these models, the mechanisms involved with strain localization need to be experimentally investigated at the microscale – in the case of sand, the scale of the grain. The results shown in this paper show how this is now possible thanks to x-ray tomography, combined with either 3D DIC or Particle Tracking. With such tools, the evolution of the 3D microstructure of a small sample of sand can be followed while it deforms, individual grains can be distinguished in the time-lapse 3D images, and analyzed to give the full 3D kinematics of all the grains.

A crucial issue is practicality: clearly all these methods are of interest, but which can reasonably be used in a "standard" geomechanics laboratory and which require large investments? A single digital camera is certainly affordable and provides immediate access to field data from a test. Performing 2D digital image correlation with these field images only requires some (easily available) DIC software. In effect, 2D field measurement of displacements and strain can be considered accessible to virtually any geomechanics research group. Things become more complicated if one wishes to see inside a deforming specimen, *i.e.*, using 3D x-ray images. However, access to 3D surface field data is also possible by simply using two cameras, which allows measurements of the 3D surface displacement field of any 3D object (stereovision). Using stereovision together with DIC leads to the so-called digital image stereocorrelation technique (DISC), often also referred to as "3D DIC". This technique is now widely used in experimental solid mechanics and has been recently reviewed by [Ort08] (who provides a substantial list of references). [Rec03] and [Rec07] presented an interesting application of DISC to triaxial compression tests on sand; see [Med06] for full details. These results indicate that DISC is affordable and easy to implement, whilst providing significant added value to otherwise standard geomechanics experiments.

On the other extreme to affordable digital cameras, one can mention neutron tomography, which has significant potential for full 3D (volume) imaging of fluid distribution in rocks and soils, yet is not easily accessible (there are only twenty or so neutron sources around the world, including the ILL in Grenoble). As far as x-ray imaging is concerned, synchrotron facilities are also limited in number (about forty, including the ESRF in Grenoble). However, in recent years there has been a rapid proliferation of laboratory x-ray imaging facilities of ever increasing quality and decreasing cost (not to mention the medical scanners, which exist at essentially every university hospital). These state-of-the-art laboratory x-ray equipment allow spatial resolutions that rival the synchrotrons', albeit with significantly slower scanning times. As an example, we have been extensively using the x-ray scanner installed at Laboratoire 3SR in Grenoble since 2008, and have experimentally investigated the patterns of (localized) deformation and failure in a variety of geomaterials; besides the examples already shown in this paper, one can mention bio-cemented sand [Tag11], sandstone ([Cha11], [ChH11]) and, more recently, partially saturated sand ([Rie11], [Rie12]).

It seems fair to say that the tremendous possibilities now available with imaging technology make it relatively easy to obtain impressive 2D or 3D images. Such images can effectively illustrate the spatial distribution and temporal evolution of important quantities such as deformation, density, temperature, etc. during a test. While this allows hidden features of the investigated processes to be revealed, there remains significant work to be done to extract quantitative information. As an illustrative example, producing a 3D x-ray tomography image is now relatively straightforward, but translating this into a quantitative map of local sample density is not trivial for heterogeneous materials (because x-ray absorption not only depends on porosity, but also on mineralogy).

In summary, it is our opinion that full-field measurement techniques have opened up new avenues for research in geomechanics, and will continue to do so especially when different full-field acquisition methods and quantitative analysis tools are used in conjunction, as exemplified by the combination of DIC (or Particle Tracking) and x-ray tomography presented in this paper.

ACKNOWLEDGEMENTS

We would like to thank all the members of our team GDR at Laboratoire 3SR (especially Pierre Bésuelle, Pascal Charrier, Jacques Desrues, Jack Lanier and Nicolas Lenoir), who are the hidden co-authors of most aspects of this paper in terms of both technical development and general philosophy. A number of our PhD and masters students should also be acknowledged, including Edward Andò, Elma Charalampidou, Lam Nguyen, Laura Restaino, Francesco Tagliaferri, Vikas Thakur and Erika Tudisco. Results from 1γ2ε were obtained in collaboration with Erdin Ibraim and David Muir Wood of Bristol University. The help of Philippe Roux (LGIT, Grenoble), with the ultrasonic measurements, and Pierre Vacher (Université de Savoie), with some of the DIC work, is also gratefully acknowledged. We are very grateful to Marco Di Michiel and Jon Wright for their invaluable contribution to the experi-

mental programs at ESRF. Certain results presented in this paper were obtained within the contexts of the French CNRS research network “GDR 2519 – Mesure de champs et identification en mécanique des solides”, the ANR project µModEx (contract ANR-05-BLAN-0192), and the Ph.D. thesis by N. Lenoir funded by the French agency ANDRA.

References

[Als08] Alshibli, K.A. and Hasan, A. (2008) – Spatial variation of void ratio and shear band thickness in sand using X-ray computed tomography. Géotechnique, Vol. 58, No. 4, 249–257.

[Als10] Alshibli, K.A. and Reed, A. (Editors) (2010) - Advances in Computed Tomography for Geomaterials: GeoX 2010. ISTE, Wiley, 425 pages.

[Als00] Alshibli, K.A., Sture, S., Costes, N.C., Franck, M.L., Lankton, M.R., Batiste, S.N. and Swanson, R.A. (2000) – Assessment of localized deformation in sand using X-ray computed tomography. Geotechnical Testing Journal, Vol. 23, 274–299.

[Als02] Alsini, A., Vardoulakis, I. and Drescher, A. (1992) – Deformation localization in cavity inflation experiments on dry sand. Géotechnique, Vol. 42, No. 1, 395–410.

[And12] Andò, E., Hall, S.A., Viggiani, G., Desrues, J. and Bésuelle, P. (2012) – Grain-scale experimental investigation of localised deformation in sand: a discrete particle tracking approach. Acta Geotechnica, 7, No. 1, 1-13.

[AnH12] Andò, E., Hall, S.A., Viggiani, G., Desrues, J. and Bésuelle, P. (2012) – Experimental micromechanics: grain-scale observation of sand deformation. Géotechnique Letters, on-line.

[And11] Andrade, J.E., Avila, C.F., Hall, S.A., Lenoir, N. and Viggiani, G. (2011) – Multiscale modeling and characterization of granular matter: from grain kinematics to continuum mechanics. Journal of the Mechanics and Physics of Solids, 59, 2, 237-250.

[Art71] Arthur, J.R.F. (1971) – New techniques to measure new parameters. Proceedings of Roscoe Memorial Symposium on Stress–Strain Behaviour of Soils, Cambridge, G.T. Foulis & Co., 340–346.

[Art82] Arthur, J.R.F. and Dunstan, T. (1982) – Rupture layers in granular media. Proceedings of IUTAM Conference on Defects and Failure in Granular Media, Balkema, 453–459.

[Art77] Arthur, J.R.F., Dunstan, T., Al-Ani, Q.A.J.L. and Assadi, A. (1977) – Plastic deformation and failure in granular media. Géotechnique, Vol. 27, No. 1, 53–74.

[Bar00] Baruchel, J. (2000) – X-ray Tomography in Materials Science. Paris, Editions Hermes.

[Bay99] Bay, B.K., Smith, T.S., Fyhrie, D.P. and Saad, M. (1999) – Digital volume correlation: three-dimensional strain mapping using X-ray tomography. Experimental Mechanics, Vol. 39, No. 3, 217–226.

[Bha05] Bhandari, A.R. and Inoue, J. (2005) – Strain localization in soft rocks – a typical rate-dependent solid: experimental and numerical studies. International Journal for Numerical and Analytical Methods in Geomechanics, Vol. 29, 1087–1107.

[Bés00] Bésuelle, P., Desrues, J. and Raynaud, S. (2000) – Experimental characterisation of the localization phenomenon inside a Vosges sandstone in a triaxial cell. International Journal of Rock Mechanics & Mining Sciences, Vol. 37, 1223–1237.

[Bés03] Bésuelle, P., Baud, P. and Wong, T. (2003) – Failure mode and spatial distribution of damage in Rothbach sandstone in the brittle-ductile transition. Pure and Applied Geophysics, Vol. 160, No. 5-6, 851–868.

[Bés11] Bésuelle, P. and Hall, S.A. (2011) – Characterization of the strain localization in a porous rock in plane strain condition using a new true-triaxial apparatus. Springer Series in Geomechanics and Geoengineering, 11:345–352.

[Bés06] Bésuelle, P., Viggiani, G., Lenoir, N., Desrues, J. and Bornert, M. (2006) – X-ray Micro CT for Studying Strain Localization in Clay Rocks under Triaxial Compression. In: Advances in X-Ray Tomography for Geomaterials, J. Desrues et al. Eds, ISTE, London, 35–52.

[Bor04] Bornert, M., Doumalin, P., Maire, E. and Moulinec, H. (2004) – Full 3D investigation of the local strain field in particulate metal matrix composites. Proc. 12th Int. Conf. on Experimental Mechanics ICEM12, Bari, Italy, 1-8.

[Bor08] Bornert, M., Valès, F., Gharbi, H. and Nguyen Minh, D. (2008) - Multiscale full-field strain measurements for micromechanical investigations of the hydromechanical behaviour of clayey rocks. Strain, International Journal for Experimental Mechanics, 46, 33–46..

[Bra75] Bransby, P.J. and Blair-Fish, P.M. (1975) – Deformation near rupture surfaces in flowing sand. Géotechnique, Vol. 25, No. 2, 384–389.

[But70] Butterfield, R., Harkness, R.M., and Andrawes, K.Z. (1970) – A stereophotogrammetric method for measuring displacements fields", Géotechnique, Vol. 20, No. 3, 308–314.

[Cas38] Casagrande, A. and Watson, J.D. (1938) – Compaction tests and critical density investigations of cohesionless materials for Franklin Falls Dam, Merrimack Valley flood control. Corps of Engineers, U.S. Army Engineering Office, BII-7.

[ChR11] Chambon, R. (2011) – Instability and Bifurcation for Inelastic Geomaterials. Advances in Bifurcation and Degradation in Geomaterials, Springer, 1-7.

[Cha11] Charalampidou E.M. (2011). Experimental Study of Localised Deformation in Porous Sandstones. PhD thesis, Heriot Watt University, Edinburgh and Université de Grenoble, Grenoble.

[ChH11] Charalampidou, E.M., Hall, S.A., Stanchits, S., Lewis, H. and Viggiani, G. (2011) – Characterization of shear and compaction bands in a porous sandstone deformed under triaxial compression. Tectonophysics, 503, 1-2, 8-17.

[Col88] Colliat-Dangus, J.L., Desrues, J. and Foray, P. (1988) – Triaxial testing of granular soil under elevated cell pressure. In: Advanced triaxial testing for soil and rocks, R.T. Donaghe et al. Editors, STP977, ASTM, 290–310.

[Com08] Comina, C., Festa, C., Foti, S. and Musso, G. (2008) – Monitoring 3D diffusion processes with high-speed electric tomography. The Leading Edge, 468–471.

[Dai05] Daigle, M., Fratta, D., and Wang, L.B. (2005) – Ultrasonic and X-ray Tomographic Imaging of Highly Contrasting Inclusions in Concrete Specimens. GeoFrontier 2005 Conference. Austin, TX.

[Dau11] Dautriat, J., Bornert, M., Gland, N., Dimanov, A. and Raphanel, J. (2011) – Localized deformation induced by heterogeneities in porous carbonate analysed by multi-scale digital image correlation. Tectonophysics, 503, 100–116.

[Deb99] Debski, W. and Young, R.P. (1999) – Enhanced Velocity Tomography: Practical Method of combining Velocity and Attenuation Parameters. Geophysical Research Letters, Vol. 26, No. 21, 3253–3256.

[Des84] Desrues, J. (1984) – La localisation de la déformation dans les matériaux granulaires. Thèse de Doctorat es Science, USMG and INPG, Grenoble, France.

[Des95] Desrues, J. (1995) – Analyse stéreophotogrammétrique de la fissuration progressive. Photomécanique 95, Y. Berthaud et al. Editors, Éditions Eyrolles, Paris, 149–162.

[Des04] Desrues, J. (2004) – Tracking Strain Localization in Geomaterials Using Computerized Tomography. Proc. Of the International Workshop on X-ray CT for Geomaterials, Kumamoto, Japan, November 6-7, 2003, Balkema, Lisse, The Netherlands, 15-41.

[Des96] Desrues, J., Chambon, R., Mokni, M. and Mazerolle, F. (1996) – Void ratio evolution inside shear bands in triaxial sand specimens studied by computed tomography. Géotechnique, Vol. 46, No. 3, 527–546.

[DeD84] Desrues, J. and Duthilleul, B. (1984) – Mesure du champ de déformation d'un objet plan par la méthode stéréophotogrammétrique de faux relief. Journal de Mécanique Théorique et Appliquée, Vol. 3, No. 1, 79–103.

[DeV04] Desrues, J. and Viggiani, G. (2004) – Strain localization in sand: an overview of the experimental results obtained in Grenoble using stereophotogrammetry. International Journal for Numerical and Analytical Methods in Geomechanics, Vol. 28, No. 4, 279 –321.

[Des06] Desrues, J., Viggiani, G. and Bésuelle, P. (Editors) (2006) – Advances in X-ray Tomography for Geomaterials", ISTE, 452 pages.

[Fal92] Falls, D., Young, R.P., Carlson, S.R. and Chow, T. (1992) – Ultrasonic Tomography and Acoustic Emission in Hydraulically Fractured Lac du Bonnet Grey Granite. J. Geophys. Res., 97, 6867–6884.

[Fin96] Finno, R.J., Harris, W.W., Mooney, M.A. and Viggiani, G. (1996) – Strain localization and undrained steady state of sands. Journal of Geotechnical Engineering, ASCE, Vol. 122, No. 6, 462–473.

[Fin97] Finno, R.J., Harris, W.W., Mooney, M.A. and Viggiani, G. (1997) – Shear bands in plane strain compression of loose sand. Géotechnique, Vol. 47, No. 1, 149–165.

[For04] Forsberg, F. and Sjödahl, M. (2004) – Tomographic 3D-DSP: measurement of internal deformations. Proc. 12th Int. Conf. on Experimental Mechanics ICEM12, Bari, Italy, 217–226.

[Gre89] Grédiac, M. (1989) – Principe des travaux virtuels et identification. Comptes Rendus Acad. Sci., 309, 1–5.

[Gre89] Grédiac, M. (2004) – The use of full-field measurement methods in composite material characterization: interest and limitations. Composites: Part A 35, 751–761.

[Gré06] Grédiac, M., Pierron, F., Avril, S. and Toussaint, E. (2006) – The Virtual Fields Method for Extracting Constitutive Parameters From Full-Field Measurements: a Review. Strain, International Journal for Experimental Mechanics, Vol. 42, 233–253

[Gud04] Gudehus, G. and Nübel, K. (2004) – Evolution of shear bands in sand. Géotechnique, Vol. 54, 187–201.

[Gue03] Gueguen, Y. and Schubnel, A. (2003) – Elastic wave velocities and permeability of cracked rocks. Tectonophysics, 370, 163–176.

[Gul99] Guler, M., Edil, T.B. and Bosscher, P.J. (1999) – Measurement of particle movement in granular soils using image analysis. Journal of Computing in Civil Engineering, ASCE, Vol. 13, No. 2, 116–122.

[Hal06] Hall, S.A. (2006) – A methodology for 7D warping and deformation monitoring using time-lapse seismic data. Geophysics, 71, O21–O31.

[Hal12] Hall, S.A. (2012) - Digital Image Correlation in Experimental Geomechanics. *This volume.*

[HaD12] Hall, S.A., Desrues, J., Viggiani, G., Bésuelle, P. and Andò, E. (2012) - Experimental characterisation of (localised) deformation phenomena in granular geomaterials from sample down to inter- and intra-grain scales. Procedia IUTAM, Vol. 4, 54-65.

[HaB10] Hall, S.A., Bornert, M., Desrues, J., Pannier, Y., Lenoir, N., Viggiani, G. and Bésuelle, P. (2010) - Discrete and Continuum analysis of localised deformation in sand using X-ray micro CT and Volumetric Digital Image Correlation. Géotechnique, 60, 5, 315-322.

[Hal09] Hall, S.A., Lenoir, N., Viggiani, G., Desrues, J., and Bésuelle P. (2009) – Strain localisation in sand under triaxial loading: characterisation by x-ray micro tomography and 3D digital image correlation. Proceedings of the 1st Int. Symp. on Computational Geomechanics (ComGeo), 2009, IC2E, 239-247.

[HaL10] Hall, S.A., Lenoir, N., Viggiani, G., Bésuelle, P., and Desrues, J. (2010) – Characterisation of the evolving grain-scale structure in a sand deforming under triaxial compression. In: Advances in Computed Tomography for Geomaterials, GeoX 2010. Ed. K.A. Alshibi and A.H. Reed, Wiley, & Sons, 34-42.

[Hal05] Hall, S.A., Lewis, H., Viggiani, G. and Lenoir, N., (2005) – Damage assessment in geomaterials using elastic waves. 7th International Workshop on Bifurcation, Instabilities and Degradation in Geomechanics, Chania, Greece.

[Had06] Hall, S.A., de Sanctis, F. and Viggiani, G. (2006) – Monitoring fracture propagation in a soft rock (Neapolitan Tuff) using acoustic emissions and digital images. Pure and Applied Geophysics, Vol. 163, 2171–2204.

[HaH10] Hall, S. A., Hughes, D. and Rowe, S. (2010) – Local characterisation of fluid flow in sandstone with localised deformation features through fast neutron imaging. ICEM 14 – 14th International Conference on Experimental Mechanics, Poitiers, France, Edited by F. Brémand, EPJ Web of Conferences, Volume 6, id.22008.

[Hal08] Hall, S.A., Kendall, J-M., Maddock, J. and Fisher, Q. (2008) – Crack density tensor inversion for analysis of changes in rock frame architecture. Geophys. J. Int., 173, 577–592.

[HaL08] Hall, S.A., Lenoir, N., Pannier, Y., Desrues, J., Bornert, M., Viggiani, G., Bésuelle, P., di Michiel, M. and Otani, J. (2008) – Characterisation of localised deformation in granular geomaterials using x-ray (micro) tomography and 3D-volumetric digital image correlation, Photomechanics 2008.

[Hal10] Hall, S.A., Muir Wood, D., Ibraim, E. and Viggiani, G. (2010) – Localized deformation patterning in 2D granular materials revealed by Digital Image Correlation. Granular Matter, 12, 1, 1-14.

[HaT12] Hall, S.A. and Tudisco, E. (2012) – Full-field ultrasonic measurement (ultrasonic tomography) in experimental geomechanics. *This volume.*

[Hal07] Hall, S.A., Viggiani, G., and Bésuelle, P., (2007) – Analysis of fracture in a soft rock (Neapolitan Tuff) using digital image correlation with displacement discontinuity quantification. Euro-conference of rock physics and geomechanics on "natural hazards: thermo-hydro-mechanical processes in rocks" EMFCSC, Erice, Sicily (Italy) (www.earthprints.org/bitstream/2122/2692/1/Hall.pdf)

[Hal11] Hall, S.A., Wright, J., Pirling, T., Andò, E., Hughes, D.J. and Viggiani, G. (2011) – Can intergranular force transmission be identified in sand? First results of spatially-resolved neutron and x-ray diffraction. Granular Matter, 13, 251-254.

[Hel08] Helm, J.D. (2008) – Digital image correlation for specimens with multiple growing cracks. Experimental Mechanics, Vol. 48, No. 6, 753-762.

[Hic94] Hicher, P.Y., Wahyudi, H. and Tessier, D. (1994) – Microstructural analysis of strain localisation in clay. Computers and Geotechnics, Vol. 16, 205–222.

[Hil12] Hild, F. and Espinosa, H.D. (Editors) (2012) - Full field measurements and identification in Solid Mechanics. Special Issue of IUTAM Procedia, Vol. 4, 1-226.

[Ibr10] Ibraim, E., Lanier, J., Muir Wood, D. and Viggiani, G. (2010) – Strain path controlled shear tests on an analogue granular material. Géotechnique, 60, 7, 545-559.

[Joe92] Joer, H., Lanier, J., Desrues, J. and Flavigny, E. (1992) – 1γ2ε: a new shear apparatus to study the behaviour of granular materials. Geotechnical Testing Journal, Vol. 15, No. 2, 129–137.

[Joe98] Joer, H., Lanier, J. and Fahei, M. (1998) – Deformation of granular material due to rotation of principal axes. Gèotechnique, Vol. 48, No. 5, 605-619.

[Kaw99] Kawakata, H., Cho, A., Kiyama, T., Yanagidani, T., Kusunose, K. and Shimada H. (1999) – Three-dimensional observations of faulting process in Westerly granite under uniaxial and triaxial conditions by X-ray CT scan. Tectonophysics, 313, 293–305.

[Kin95] King, M., Chaudhry, N. and Shakeel, A. (1995) – Experimental ultrasonic velocities and permeability for sandstones with aligned cracks. International Journal of Rock Mechanics & Mining Sciences, Vol. 32, 155–163.

[Kir68] Kirkpatrick, W.M. and Belshaw, D. J. (1968) – On the interpretation of the triaxial test. Géotechnique, Vol. 18, No. 3, 336–350.

[Kuo96] Kuo, C.-Y., and Frost, J.D. (1996) – Uniformity evaluation of cohesionless specimens using digital image analysis. Journal of Geotechnical Engineering, ASCE, Vol. 122, No. 5, 390–396.

[Lee05] Lee, J.S., Fernandez, A.L. and Santamarina, J.C. (2005) – S-Wave Velocity Tomography: Small-Scale Laboratory Application. Geotechnical Testing Journal, Vol. 28, No. 4, 1-9.

[Len06] Lenoir, N. (2006) – Comportement mécanique et rupture dans les roches argileuses étudiés par micro tomographie à rayons X. Ph.D. thesis, Université de Grenoble (http://tel.ccsd.cnrs.fr/tel-00011996).

[Len07] Lenoir, N., Bornert, M., Desrues, J., Bésuelle P. and Viggiani, G. (2007) – Volumetric digital image correlation applied to X-ray micro tomography images from triaxial compression tests on argillaceous rocks. Strain, International Journal for Experimental Mechanics, Vol. 43, No. 3, 193–205.

[Lin00] Lings, M.L., Pennington, D.S. and Nash, D.F.T. (2000) – Anisotropic stiffness parameters and their measurement in a stiff natural clay. Géotechnique, Vol. 50, No. 2, 109–125.

[Liu04] Liu, J. and Iskander, M. (2004) – Adaptive Cross Correlation for Imaging Displacements in Soils. Journal of Computing in Civil Engineering, ASCE, Vol. 18, No. 1, 46–57.

[Loc77] Lockner, D.A., and Byerlee, J.D. (1977) – Acoustic emission and creep in rock at high confining pressure and differential stress. Bull. of the Seismological Society of Amer., Vol. 67, 247–258.

[LoB77] Lockner, D.A., and Byerlee, J.D. (1977) – Hydrofracture in Weber sandstone at high confining pressure and differential stress. J. Geophys. Res., Vol. 82, 2018–2026.

[Luo90] Luong, M.P. (1990) – Infrared thermovision of damage processes in concrete and rock. Engineering Fracture Mechanics, Vol. 35, No. 1–3, 291–301.

[Luo07] Luong, M.P. (2007) – Introducing infrared thermography in soil dynamics. Infrared Physics & Technology, Vol. 49, No. 3, 306–311.

[Mas04] Masschaele, B., Dierick, M., Cnudde,, V., Van Hoorebeke, L., Delputte, S., Gildemeister, A., Gaehler, R., and Hillenbach (2004) – High-speed thermal neutron tomography for the visualization of water repellents, consolidants and water uptake in sand and lime stones. Radiation Physics and Chemistry, 71, 807-808.

[Mat06] Matsushima, T., Uesugi, K., Nakano, T. and Tsuchiyama, A. (2006) – Visualization of Grain Motion inside a Triaxial Specimen by Micro X-ray CT at SPring-8. In: Advances in X-Ray Tomography for Geomaterials, J. Desrues et al. Eds, ISTE, London, 35–52.

[Mat07] Matsushima, T., Katagiri, J., Uesugi, K., Nakano, T. and Tsuchiyama, A. (2007) – Micro X-ray CT at SPring-8 for Granular Mechanics". In: Soil Stress-Strain Behavior: Measurement, Modeling and Analysis, Ling et al. Eds., Springer, Netherlands, 225-234.

[Mav98] Mavko, G., Mukerji, T. and Dvorkin, J. (1998) – The rock physics handbook: tools for seismic analysis in porous media. Cambridge University Press, New York.

[Med06] Medina-Cetina, Z. (2006) – Probabilistic calibration of a soil model. Ph.D. thesis, Johns Hopkins University, Baltimore.

[Mee03] Mees, F., Swennen, R., Van Geet, M., and Jacobs, P. (2003) - Applications of X-ray computed tomography in the geosciences. Geological Society, London, Special Publications; 2003; v. 215

[Mic90] Michalowski, R.L. (1990) – Strain localization and periodic fluctuations in granular flow processes from hoppers. Géotechnique, 40, 389-403.

[Mor67] Morgenstern, M.R. and Tchalenko, J.S. (1967) – Microscopic structures in kaolin subjected to direct shear. Géotechnique, Vol. 37, 309-327.

[Muh97] Muhunthan, B. and Chameau, J.L., (1997) – Void fabric tensor and ultimate state surface of soils. ASCE J. Geotech. GeoEnviron. Engrg. 123, 2, 173–181.

[Mui02] Muir Wood, D. (2002) –Some observations of volumetric instabilities in soils. International Journal of Solids and Structures, Vol.39, No. 13–14, 3429–3449.

[Mui07] Muir Wood, D. (2007) – The magic of sands — The 20th Bjerrum Lecture. Canadian Geotechnical Journal, 44, 11, 1329-1350.

[Ngu11] Nguyen, T.L., Hall, S.A., Vacher, P. and Viggiani, G. (2011) – Fracture mechanisms in soft rock: identification and quantification of evolving displacement discontinuities by digital image correlation. Tectonophysics, 503, 1-2, 117-128.

[Nie11] Niedostatkiewicz, M., Lesniewska, D. and Tejchman, J. (2011) - Experimental analysis of shear zone patterns in cohesionless for earth pressure problems using particle image velocimetry. Strain, International Journal for Experimental Mechanics, 47, 218–231.

[Nit11] Nitka, M., Combe, G., Dascalu, C. and Desrues, J. (2011) – Two-scale modeling of granular materials: a DEM-FEM approach. Granular Matter 13, 3, 277-281.

[Nur69] Nur, A. and Simmons, G. (1969) Stress-induced velocity anisotropy in rock: an experimental study. J. Geophys. Res., 74, 6667–6674.

[Oda04] Oda, M., Takemura, T. and Takahashi, M. (2004) – Microstructure in shear band observed by microfocus X-ray computed tomography. Géotechnique, Vol. 54, 539-542.

[Ort09] Orteu, J.J. (2009) – 3-D computer vision in experimental mechanics. Optics and Lasers in Engineering, Vol. 47, No. 3–4, 282–291.

[Ota00] Otani, J., Mukunoki, T. and Obara, Y. (2000) – Application of X-ray CT method for characterization of failure in soils. Soils and Foundations, Vol. 40, 111–118.

[Ota02] Otani, J., Mukunoki, T. and Obara, Y. (2002) – Characterization of failure in sand under triaxial compression using an industrial X-ray scanner. International Journal of Physical Modelling in Geotechnics, Vol. 1, 15–22.

[Ota04] Otani, J. and Obara, Y. (Editors) (2004) – X-ray CT for Geomaterials – Soils, Concrete, Rocks. Balkema.

[Pan10] Pannier Y., Lenoir N. and Bornert M. (2010 – Discrete volumetric digital image correlation for the investigation of granular type media at microscale: accuracy assessment. In EPJ Web of Conferences: ICEM 14 – 14th International Conference on Experimental Mechanics, EDP Sciences, 6, n°35003.

[Pir06] Pirling, T., Bruno, G. and Withers, P.J. (2006) – SALSA, a new concept for strain mapping at the ILL. Mat. Sci. Eng.; A 437, 139-144.

[Pou04] Poulsen, H.F. (2004) – Three-dimensional X-ray diffraction microscopy: mapping polycrystals and their dynamics. Springer Tracts in Modern Physics, 154 pages.

[Ray89] Raynaud, S., Fabre, D., Mazerolle, F., Géraud, Y. and Latière, H.J. (1989) – Analysis of the internal structure of rocks and characterization of mechanical deformation by a nondestructive method: X-ray tomodensitometry. Tectonophysics, Vol. 159, 149–159.

[Rec04] Rechenmacher, A.L., and Finno, R.J. (2004) – Digital image correlation to evaluate shear banding in dilative sands. Geotechnical Testing Journal, Vol. 27, No. 1, 13–22.

[Rec07] Rechenmacher, A.L. and Medina-Cetina, Z. (2007) – Calibration of Soil Constitutive Models with Spatially Varying Parameters. Journal of Geotechnical and Geoenvironmental Engineering, ASCE, Vol. 133, No. 12, 1567–1576.

[Rec03] Rechenmacher, A.L., Medina-Cetina, Z. and Ghanem, R.G. (2003) - Predictions for Heterogeneous Soil Behavior: Towards a Probabilistic Characterization of Soil Design Parameters. International Workshop LSD2003, Cambridge, Massachusetts.

[Res08] Restaino, F.L. (2008) – Characterizing strain localization in sandstone by full-field measurements. MSc thesis, Université de Grenoble.

[Ret07] Réthoré, J, Roux, S, and Hild, F (2007) – From pictures to extended finite elements: Extended digital image correlation (X-DIC). Comptes Rendus Mécanique, Vol. 335, 131–137.

[Rie11] Riedel, I. (2011) – Characterization and micro-scale analysis of Hostun Sand water retention behavior. MSc thesis, Université de Grenoble.

[Rie12] Riedel, I., Andò, E., Salager, S., Bésuelle, P. and Viggiani, G. (2012) – Water retention behaviour explored by x-ray CT analysis. Proceedings of E-UNSAT 2012, Napoli.

[Ros70] Roscoe, K.H. (1970) – The influence of strains in soil mechanics. Géotechnique, Vol. 20, No. 2, 129–170.

[Ros63] Roscoe, K.H., Arthur, J.R.F. and James, R.G. (1963) – The determination of strains in soils by an x-ray method. Civ. Eng. Public Works Rev., 58, 873–876 and 1009–1012.

[Rou08] Roux, S. and Hild, F. (2008) – Digital Image Mechanical Identification (DIMI). Experimental Mechanics, Vol. 48, No. 4, 495-508.

[Rus89] Russel, S.S. and Sutton, M.A. (1989) – Strain-field analysis acquired through correlation of X-ray radiographs of a fiber-reinforced composite laminate. Experimental Mechanics, Vol. 29, No. 2, 237–240.

[San96] Santamarina, J.C. and Cascante, G. (1996) – Stress anisotropy and wave propagation - A micromechanical view. Canadian Geotechnical Journal, 33,770-782

[San98] Santamarina, J.C. and Fratta, D. (1998) – Introduction to Discrete Signals and Inverse Problems in Civil Engineering", ASCE Press, VA.

[San01] Santamarina, J.C., Klein, K. and Fam, M. (2001) – Soils and Waves., J. Wiley and Sons, Chichester, UK, 488 pages.

[Sca82] Scarpelli, G. and Muir Wood, D. (1982) – Experimental observations of shear band patterns in direct shear tests. Proceedings of IUTAM Conference on Defects and Failure in Granular Media, Balkema, 473–484.

[Sco04] Scott T.E., and Abousleiman Y. (2004) – Acoustical imaging and mechanical properties of soft rock and marine sediments. Final Technical Report #15302, Department of Energy (DOE Award Number: DEFC26-01BC15302).

[She03] Sheppard, S., Mantleb, M.D., Sedermanb, A.J., Johnsb, M.L. and Gladden, L.F. (2003) – Magnetic resonance imaging study of complex fluid flow in porous media: flow patterns and quantitative saturation profiling of amphiphilic fracturing fluid displacement in sandstone cores. Magnetic Resonance Imaging, 21, 365–367.

[Shi05] Shibuya S., Koseki, J., and Kawaguchi, T. (2005) – Recent developments in deformation and strength testing of geomaterials. In: Deformation characteristics of geomaterials, Di Benedetto et al., Eds., Taylor Francis Group, London, 3-26.

[Shi78] Shirley, D.J., and Hampton, L.D. (1978) – Shear-wave measurements in laboratory sediments. J. Acoust. Soc. Am., Vol. 63, No.2, 607–613.

[Smi02] Smith, T.S., Bay, B.K. and Rashid, M.M. (2002) – Digital volume correlation including rotational degrees of freedom during minimization. Experimental Mechanics, Vol. 42, No. 3, 272–278.

[Sol03] Solymar, M., Lehmann, E., Vontobel , P. and Nordlund, A. (2003) - Relating variations in water saturation of a sandstone sample to pore geometry by neutron tomography and image analysis of thin sections. Bull Eng Geol Env., 62, 85–88.

[Son12] Song, A., Medina-Cetina, Z. and Rechenmacher, A.L. (2012) – Local Deformation Analysis of a Sand Specimen Using 3D Digital Image Correlation for the Calibration of a Simple Elasto-Plastic Model. Proceedings of GeoCongress 2012, 2292–2301.

[Sta03] Stanchits, S.A., Lockner, D.A. and Ponomarev, A.V. (2003) – Anisotropic changes in P-wave velocity and attenuation during deformation and fluid infiltration of granite. Bull. Seis. Soc. Am., 93, 1803–1822.

[Ste07] Stevens, D.F. (2007) – Stress redistribution in Berea sandstone samples using acoustic emission tomography in the laboratory. MSC thesis, Virginia Polytechnic Institute and State University.

[Sut86] Sutton, M.A., Cheng, M., Peters, W.H., Chao, Y.J. and McNeill, S.R. (1986) – Application of an optimized digital correlation method to planar deformation analysis. Image and Vision Computing, 4,143–150.

[Syn99] Synnergren, P., Goldrein, H.T. and Proud, W.G. (1999) – Application of digital speckle photography to flash x-ray studies of internal deformation fields in impact experiments. Applied Optics, Vol. 38, No. 19, 4030–4036.

[Tag11] Tagliaferri, F., Waller, J., Andò, E., Hall, S.A., Viggiani, G., Bésuelle, P. and DeJong, J.T. (2011) – Observing strain localisation processes in biocemented sand using x-ray imaging. Granular Matter, 13, 247-250.

[Tha07] Thakur, V. (2007) – Strain localization in sensitive soft clays. PhD thesis, Norwegian University of Science and Technology.

[Til92] Tillard-Ngan, D., Desrues, J., Raynaud, S. and Mazerolle, F. (1992) – Strain localisation in the Beaucaire marl. In: Geotechnical Engineering of Hard Soils–Soft Rocks, Balkema, 1679–1686.

[Vac99] Vacher, P., Dumoulin, S., Morestin, F. and Mguil-Touchai, S. (1999) – Bidimensional strain measurement using digital images. Proceedings Institution of Mechanical Engrs., 213, Part C: 811–817.

[Var82] Vardoulakis, I. and Graf, B. (1982) – Imperfection sensitivity of the biaxial test on sand. Proceedings of IUTAM Conference on Defects and Failure in Granular Media, Balkema, 485–491.

[Ver04] Verhulp, E., van Rietbergen, B. and Huiskes R. (2004) – A three-dimensional digital image correlation technique for strain measurements in microstructures. Journal of Biomechanics, Vol. 37, 1313–1320.

[Vig09] Viggiani, G. (2009) – Mechanisms of localized deformation in geomaterials: an experimental insight using full-field measurement techniques. In: Mechanics of Natural Solids, D. Kolymbas & G. Viggiani (Eds), Springer-Verlag, 105-125.

[Vig95] Viggiani, G., and Atkinson, J.H. (1995) – Stiffness of fine-grained soil at very small strains. Géotechnique, Vol. 45, No. 2, 249–265.

[Vig10] Viggiani, G., Bésuelle, P., Hall, S.A. and Desrues, J. (2010) – Sand deformation at the grain scale quantified through x-ray imaging. Keynote paper, in: Further Advances in X-Ray Tomography for Geomaterials, K. Alshibli et al. Eds, ISTE, London, 1-17.

[Vig04] Viggiani, G., Desrues, J. (2004) – Experimental observation of shear banding in stiff clay. In: Geotechnical Innovations, R.B.J. Brinkgreve et al. Eds., Verlag Glückauf Essen, 649–658.

[Vig08] Viggiani, G. and Hall, S.A. (2008) – Full-field measurements, a new tool for laboratory experimental geomechanics. Keynote paper, in: Deformation Characteristics of Geomaterials, S.E. Burns, P.W. Mayne and J.C. Santamarina Eds, IOS Press, Vol. 1, 3-26.

[ViL04] Viggiani, G., Lenoir, N., Bésuelle, P., Di Michiel, M., Marello, S., Desrues, J. and Kretzschmer, M. (2004) – X-ray micro tomography for studying localized deformation in fine-grained geomaterials under triaxial compression. Comptes rendus Mécanique, Vol. 332, 819–826.

[Vin91] Vinegard, H.J., de Waal, J.A. and Wellington, S.L. (1991) – CT studies of brittle failure in Castlegate sandstone. Int. J. Rock Mech. Min., Vol. 28, 441–448.

[Vit12] Vitone, C., Cotecchia, F., Viggiani, G. and Hall, S.A. (2012) – Strain fields and mechanical response of a highly to medium fissured bentonite clay. International Journal for Numerical and Analytical Methods in Geomechanics, online, DOI: 10.1002/nag.2095.

[Whi03] White, D.J., Take, W.A. and Bolton, M.D. (2003) – Soil deformation measurement using particle image velocimetry (PIV) and photogrammetry. Géotechnique Vol. 53, No. 7, 619–631.

[WuL06] Wu, L., Liu, S., Wu, Y. and Wang, C. (2006) – Precursors for rock fracturing and failure. Part 1: IRR image abnormalities. International Journal of Rock Mechanics & Mining Sciences, Vol. 43, 473–482.

[Zan98] Zang, A., Wagner, F.C., Stanchits, S., Dresen, G., Andresen, R. and Haidekker, M. (1998) – Source analysis of acoustic emissions in Aue granite cores under symmetric and asymmetric compressive loads. Geophys. J. Inter., Vol. 135, 1113–1130.

Digital Image Correlation in Experimental Geomechanics

Stephen A. Hall

Division of Solid Mechanics, Lund University, Lund, Sweden
and European Spallation Source AB, Lund, Sweden

Digital Image Correlation (DIC) is a powerful tool in experimental mechanics that has seen increasing use in recent years. This method provides full-field measurement of kinematics and strain at the surface of, or within, objects during their deformation, which permits a more correct analysis of deformation than traditional approaches and without the need to assume homogeneous behaviour in the interpretation. Therefore heterogeneity, either pre-existing or evolving (e.g., strain localisation), can be correctly addressed; this is essential in the study of geomaterials that are by nature heterogeneous. This paper presents the basic concepts of DIC for both surface and volume analysis, including technical details of both the data acquisition and the methodology. A few specific aspects and examples relating to experimental geomechanics applications are discussed, including the analysis of discontinuous deformation in the form of fractures and granular mechanics.

1 Introduction

Digital Image Correlation (DIC), in its original form, is a method for non-contact full-field kinematics measurement of planar or non-planar surfaces undergoing deformation. This method has been used increasingly over the last 20-30 years in a range of experimental mechanics applications (see for example, [SOS09]; [Wit08]) and recently has seen a massive increase in popularity, as reflected, for example, in more than 350 journal papers using DIC-based measurements in mechanics cited in [Ort09]. The rise of DIC has also been seen in experimental geomechanics (e.g., [GEB99]; [WTB03]; [RF04]; [LI04]; [GN04]; [BI05]; [BVGNM08]; [HBD$^+$10], [HMWIV10]; [NHVV11]; [CHS$^+$11]; [DBG$^+$11]; [NLT11]; [SMCR12]; see also [VH10].

This paper outlines the basic principles of DIC from 2D-surface DIC through to 3D-volumetric DIC plus extensions from continuum analysis to discontinuous and discrete

analyses. A few examples are given, from the authors work (with collaborators) of application of DIC in geomechanics. The structure of the paper is as follows: first the origins of DIC are briefly presented and the different types of DIC are described in a general sense. This is followed by a presentation of the basic DIC methodology, described in the context of the simplest case, i.e., 2D-surface DIC. Subsequently the practicalities of 2D-DIC and 3D-volume DIC are discussed and a few examples are provided. Finally, some extensions of the DIC method to discontinuous deformation (fracture) and discrete (granular media) analysis are discussed. In addition to the overview provided herein, it is noted that good summaries of DIC can be found, for example in [BHmBqFl06], [SOS09] and [Bay08].

1.1 Origins of DIC

Before discussing the DIC procedure and application, it is interesting to note the evolution of the technique since its conception in the early 1980s. Prior to DIC being proposed various different techniques were investigated for full-field kinematics and strain field analysis. The first such example in geomechanics was probably the use of x-ray radiography in the early 1960s to observe plane strain soil models (e.g., [RAJ63]). In these examples, displacements of a more or less regular grid of lead-shots placed within 2D soil models were imaged using x-ray radiography. During the different deformation experiments (including trap-door and moving wall tests) images were acquired and the displacements of the lead-shot markers were traced (manually) from one film to the next and interpreted in terms of continuum displacement fields and strain fields were determined by differentiation. Later, in the 1980s, Desrues et al., in Grenoble, used sterophotogrammetry to analyse, with relatively high spatial resolution, displacement and strain fields in plane-strain tests on soils in ground-breaking studies of localisation phenomena (see, for example, [Des84] and the overview of [DV04]). Elsewhere in experimental mechanics, other techniques were also developed including Moiré fringe analysis and speckle interferometry (see [Gre04]). In the early 1980s Sutton et al., at the University of South Carolina developed correlation based image (not particle) tracking techniques.

The development of DIC by Sutton and co-workers during the 1980s has been outlined by [McN06]. The developments started with single point 2D surface DIC in 1980 in a process requiring significant user interaction and up to a day to get the single point. By 1982 the approach had developed to provide full 2-D fields of points, but this still required user interaction to define a good estimate of an initial point's displacement and the results came out at a rate of about 30 minutes per point. Around this time problems with out-of-plane motion were recognised, which lead to the development of a so-called 3D-DIC approach (termed 3D-surface DIC below) using dual cameras; this involved a complex calibration and about one day of user interaction to calibrate). The first truly practical 3D-surface DIC, included deforming subsets, was produced in the early 1990s. Some of the key references in this development are [PR81], [MSW$^+$83], [SCP$^+$86], [STBC91] and [LSPI93].

The extension of 2D-surface DIC to 3D-volume DIC to measure 3D displacement and strain fields within a volume, e.g., using 3D images acquired by x-ray tomography, is relatively straightforward, but is quite recent; e.g., [BSFS99], [SBR02], [VvRH04], [BCD$^+$04], [FS04]. The use of 3D-volume DIC in geomechanics is even more recent (e.g., [BVS06], [LBD$^+$07] and [HBD$^+$10]). See [Bay08], for an overview of the developments of 3D-volumetric DIC.

The brief history above highlights the quite recent, and rapid, development of DIC as an experimental tool; use in geomechanics is even more recent, but has also been an area of rapid development; including the passage to full 3D-volume analysis.

It should be noted that much of the drive for the rapid development and increased use of DIC as an experimental tool comes from the move to digital cameras since the early 1990s. This has permitted much lower cost and easy to use image acquisition, than traditional imaging methods, at speeds and resolutions that are increasing all the time. Furthermore, significant advances in computer-processing power and computer-based data treatment have allowed ever more elaborate algorithms to be applied and much faster analysis of ever larger images (now it is common place to analyse $>$10 MPx images in a few seconds, where MPx denotes mega-pixels).

1.2 Different types of DIC

DIC and related techniques have been developed in a range of disciplines including, amongst others, solid and fluid mechanics, medicine, animation/film special effects and image registration. In these developments different terms have been used in the different disciplines (and even within the same discipline) for similar (and even for the same) procedures. Below some of the key terms used are clarified.

1.2.1 PTV, PIV and DIC

In fluid mechanics the use of Particle Tracking Velocimetry (PTV) is quite commonplace. This is a method in which individual particles are identified in consecutive images and tracked from one image to another. The tracked particles are generally some form of "seed" particles assumed to faithfully follow the flow dynamics; these seeding particles can be identified, tracked and used to calculate velocity information. The equivalent in solid mechanics would be using tracers (e.g., the lead-shots in the Cambridge radiography work) or by identifying particles such as grains in consecutive images. Particle image velocimetry (PIV) is another technique used in fluid mechanics where, rather than identifying particles and tracking them as in PTV, the correspondence between small segments of consecutive images is determined based on correlation of the "unique" character of the image segments. See, for example, [Adr91] for a discussion of PIV and PTV in fluid mechanics.

PIV and DIC are basically the same and are, in essence, just different names for similar ideas (PIV is the term most commonly used in fluid mechanics where the concept

of a velocity field, rather than simply displacement, is clear). Other names for similar approaches include: image cross-correlation, block or region matching method, surface displacement analysis and sub-region scanning computer vision.

1.2.2 2D/3D-surface and 3D-volume DIC

The term DIC covers a set of methods where the displacements (and deformations) of an object are determined by the correlation of small subsets of digital images of the object. DIC is most commonly applied with photographs, but can be applied to "any" repeated images of objects acquired using "any" 2D or 3D technique. The three main types of DIC used are described in the following:

- 2D-DIC: 1 camera, 2 photos, 2 components of position vector, 2 components of displacement vector; applicable to planar objects with in-plane deformation (i.e., plane-strain biaxial tests) - the study surface must be initially flat and remain so for 2D-DIC to correctly provide the kinematics of the object.
- 3D-surface DIC (stero-vision plus stereo-correlation): 2 cameras (requires special calibration of the two cameras), 2 x 2 photos, 3 components of position vector on the surface, 3 components of displacement vector on the surface, 3D surface deformation (but no "internal depth" - strain tensor can be derived only with assumptions about gradient of displacements in the third, depth, dimension); applicable to the evaluation of non-planar objects and out-of-plane deformations, but still restricted to surface analysis.
- 3D-volumetric DIC (also known as Digital Volume Correlation - DVC): 3D imaging device (e.g., x-ray tomograph), 2 x 3D volume images, 3 components of position vector, 3 components of displacement vector, 3D deformation (full strain tensor determined without any assumptions); applicable to analysis of 3D deformation including internal deformation, but requires that the object has internal "character" that may be followed (correlated) between images.

These three main types of DIC provide increasing information on the displacement gradient tensor ($\mathbf{F}$), as outlined below. 2D-DIC illuminates just the red components, 3D-surface DIC the red and green and 3D-volume DIC illuminates the full tensor (red, green and blue components);

$$\mathbf{F} = \begin{pmatrix} 1+\frac{\delta u}{\delta x} & \frac{\delta u}{\delta y} & \frac{\delta u}{\delta z} \\ \frac{\delta v}{\delta x} & 1+\frac{\delta v}{\delta y} & \frac{\delta v}{\delta z} \\ \frac{\delta w}{\delta x} & \frac{\delta w}{\delta y} & 1+\frac{\delta w}{\delta z} \end{pmatrix}; \tag{1}$$

u, v and w are the displacement components in the space coordinates x, y and z, respectively.

1.2.3 Global and local DIC

In most DIC implementations, image correlation is carried out over small windows of the images, which are treated independently (see the method description in the following section). Such an approach can be thought of as *local*, i.e., the derived image transformation is only determined locally around each analysis node. In other areas of development of DIC-like methods, e.g., image registration in computer vision, approaches that work on the whole image (or at least a region of interest over the whole image) have been developed. In such approaches the image registration, i.e., the transformation from one image to another, is not defined solely by the mapping function of one image subset to another, but also depends on the deformation of the image as a whole, i.e., the transformations of each node are linked to their neighbours. This leads to a problem for which a global solution is sought to maximise the image correlation, whilst also, in some way, minimising the deformation of the mesh that links the nodes of the DIC analysis grid. As such approaches work on the whole images they can be refered to as *global*. [HR12] present a discussion and comparison of these two different strategies for DIC analysis. In general, the following discussions concentrate on the local approach.

2 Background theory and methodology

The principle of DIC is to assess the displacements fields, and thus strains fields (if required), over the surface of a deforming material by comparison of two images acquired at different stages of deformation. The first image is generally referred to as the "reference image" and the second, acquired after some increment of deformation, as the "deformed image". In general, the method starts by defining a grid of analysis points over the reference image; then, a group of pixels, commonly called a "subset", is defined about each node of this grid. Image correlation is performed, for each node, by identifying the most similar subset in the deformed image based on some statistical measure of correlation of the images within each subset and some mapping function between the subsets. In this section more detail on each step of the procedure is provided, from the input data description and acquisition to the DIC analysis and post-processing of the DIC output.

2.1 Image structure

Before describing the methodology of DIC, it is first necessary to note a few issues about the nature of the input images, which will impact on DIC analyses. Digital images are, by nature, discretised both in spatial resolution and in terms of the intensity information that is contained in each point of the image.

The spatial discretisation of a digital images comes from the nature of the detectors (i.e., digital cameras in the case of surface measurement). An imaging detector is not a

continuous object, but is rather made up of a number of small detector pixels. The size of these pixels and their spacing dictates the maximum image resolution that can be attained; however it should be noted that depending on the performance of the detector, the actual resolution can be less than that of a pixel as there can be leakage/cross-talk between neighbouring pixels that blurs the information across an area larger than a single pixel, therefore the true resolution is reduced. In x-ray tomography similar image discretisation exists, although the 3D version of a pixel is known as a voxel. In this case, the discretisation occurs at two levels, first at the level of the detector, which is pixelated as in a digital camera, and secondly at the level of the reconstruction of the tomographic image from the acquired radiography images. As for the 2D case, the voxel size is not necessarily the true image resolution, which is likely lower. The image resolution and pixel-/voxel-isation is important for DIC as this is the highest resolution one can get on displacements without invoking some form of interpolation, as will be discussed later.

Digital images can also be pixelated in their information content at each point; as generally non-colour images are used, this information content is often referred to as the image grey-scale. The discretisation of the grey-scale depends on the image format, for example in 8-bit images only 256 discrete grey-levels can be used and 16-bit images have 65536. This discretisation is applicable between low- and high-end limits below or above of which any values will take the maximum value (or, worse, can cause issues with saturation that can affect the recorded grey-scale in the surrounding pixels). The digitisation of the images and the upper/lower saturation limits, are thus further constraints on the resolution of any subsequent image processing. In general the acquisition parameters (e.g., exposure time) should be defined to maximise the dynamic range of the data (i.e., the number of grey-scale values that contain useful information), whilst avoiding saturation, which can lead to, often unpredictable, non-physical grey-scale variations and changes from one image to the next.

The spatial and grey-scale resolutions can be defined both at acquisition and in subsequent image treatment. Furthermore, care should be taken in the use of different image formats. It might be tempting, for example, to economise on data storage by utilising a jpeg format, but this format involves a compression algorithm that will blur out details in the image and thus degrade later analyses.

2.2 Basic DIC procedure

Figure 1 outlines the different steps to a generic DIC methodology. Whilst various different implementation of DIC exist they generally involve the same set of basic steps: (i) definition of nodes distributed over the first image; (ii) definition of a region centred on each node (the correlation window / motif / subset); (iii) calculation of some measure of similarity (e.g., the correlation coefficient) between the two image subsets for different displacements of the correlation window within an area (the search window) in the second image; (iv) definition of the discrete displacement (integer number of pixels), given by the displacement in (iii) with the best correlation; (v) sub-pixel re-

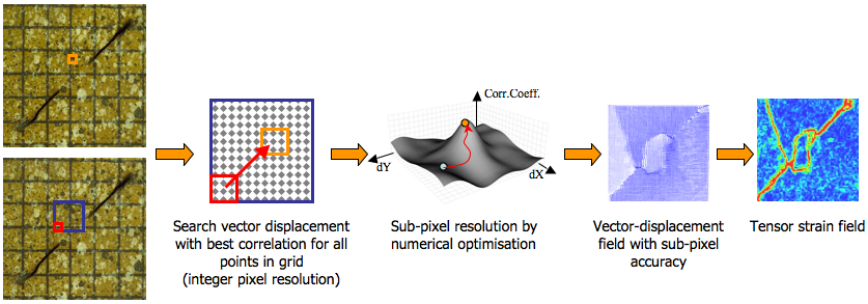

Figure 1: Schematic of a 2D-surface DIC analysis approach

finement (because the displacements are rarely integer numbers of pixels - see below). It is also common, in mechanics, to complete the DIC analysis with calculation of the strains, which is based on the gradients of the derived displacements and a continuum assumption.

3D-surface DIC (see Figure 2) involves some additional steps involving the calibration of the two imaging cameras for their juxtaposition and focal lengths, plus the images from the two cameras must be correlated at each step (this provides the 3D surface shape - a procedure known as stereo-vision) and the image-pairs must also be correlated between steps (stereo-correlation).

Important parameters for DIC are the size of the subset or correlation-window and the spacing between each analysis point. These define the resolution of the DIC analysis and subsequent strain calculations. If the size of the correlation window is large then the resolution on any displacement gradients will be reduced and could even lead to poor correlations if the image varies too much over the window (although this depends on the algorithm used for the correlation - see sections on subpixel analysis and taking displacement gradients into account, below). Conversely, if the correlation window is too small, relative to the image texture and noise level, then poor or erroneous correlations can result due to non-uniqueness of the subset correlation. The spacing between the analysis points (nodes) controls the smoothing of the result (coupled with the correlation window size, this defines the subset overlap, which can provide smoothing similar to a moving average) and also the accuracy/resolution on any subsequent analysis of displacement gradients, e.g., for strain. If the subset spacing is too small, relative to the noise in the displacement measurements, then the gradient of the displacements can be dominated by noise and strain can not be well determined.

Another parameter that should generally be defined is the search region size. Clearly this could be defined to be the whole image, but would not provide an optimal calculation time, plus increases the risk of erroneous image matches. Therefore the search window size is usually restricted based on some assumption of the likely displacements. Some DIC methodologies also use the definition of an initial point (either au-

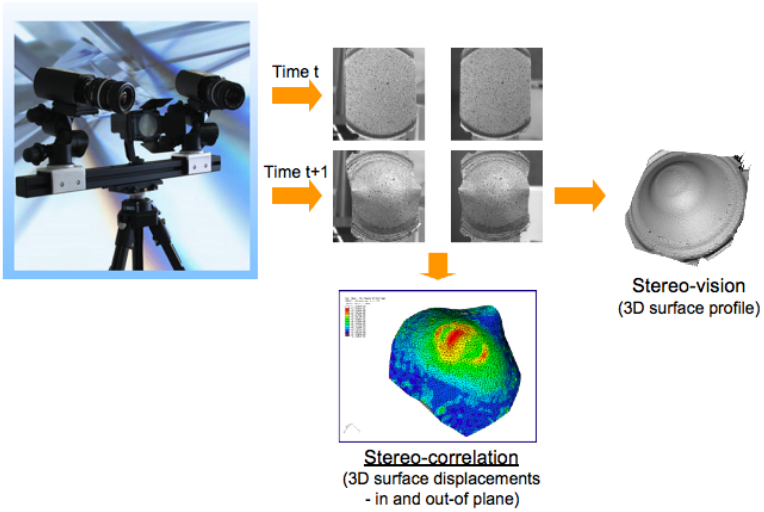

Figure 2: Schematic of a 2D-surface DIC analysis approach (after [Ort])

tomatically or manually defined) for which the displacement is determined and used as the seed for the surrounding pixels. This provides some acceleration of the procedure, as it is not necessary to search over a full search-range at every pixel, the down-side is that it is possible that correlations can not be found based on the seeded guess.

Different measures can be used to assess the degree of similarity of the subset images between photographs. An overview of some of the commonly used criteria is given in [BHmBqFl06], with the key ones being variants of least-squares (LSQ and normalised LSQ) and cross-correlation (CC, normalised CC and zeroed normalised CC):

$$LSQ(u,v) = \sum_{x,y}[I_1(x,y) - I_2(x+u,y+v)]^2; \tag{2}$$

$$NLSQ(u,v) = \frac{\sum_{x,y}[I_1(x,y) - I_2(x+u,y+v)]^2}{\sqrt{\sum_{x,y} I_1(x,y)^2 \sum_{x,y} I_2(x+u,y+v)^2}}; \tag{3}$$

$$CC(u,v) = \sum_{x,y} I_1(x,y) I_2(x+u,y+v); \tag{4}$$

$$NCC(u,v) = \frac{\sum_{x,y} I_1(x,y) I_2(x+u,y+v)}{\sqrt{\sum_{x,y} I_1(x,y)^2 \sum_{x,y} I_2(x+u,y+v)^2}}; \tag{5}$$

$$ZNCC(u,v) = \frac{\sum_{x,y}[I_1(x,y) - \overline{I_1}][I_2(x+u,y+v) - \overline{I_2}]}{\sqrt{\sum_{x,y}[I_1(x,y) - \overline{I_1}]^2 \sum_{x,y}[I_2(x,y) - \overline{I_2}]^2}}. \tag{6}$$

In the above, x and y are the (2D) spatial coordinates, u and v the displacements of a pixel from image 1 (I_1) to a new position in image 2 (I_2). Note that in the case of rigid body displacements of a subset, u and v, will be constant for all (x, y) positions in that subset, but, if there is a displacement gradient taken in to account in the DIC analysis, these values can vary with x and y (i.e., $u = f(x)$ and $v = f(y)$).

It is generally accepted that a normalised similarity measure is optimal for DIC, as it can account for variations in lighting and image contrast that might otherwise lead to erroneous correlations. Zeroed coefficients are also used to address variations between compared images, but this is often not necessary and is best addressed at the image acquisition stage with, for example, adequate lighting of the study object.

To illustrate the calculations, and in particular how the number of operations can easily multiply, the following subsection outlines an example calculation of the correlation coefficient for a single analysis node.

2.2.1 Example calculation

For each node in a DIC analysis, a similarity measure must be calculated. This involves computing the summations in one of equations (2)–(6), for example, for all points in the image subset (summation over x and y positions) plus at all values of u and v in the search range. To demonstrate this procedure, a simple case is described below for a correlation window of size 5x5 such that the correlation calculation involves the summation over positions $(x, y) = (x_0 \pm 2, y_0 \pm 2)$ within each subset in I_1 (where (x_0, y_0) are the centre coordinates of the correlation window). The simple (non-normalised) correlation coefficient (equation 4) is used for brevity.

For the first test displacement $(u, v) = (-2, -2)$ the correlation coefficient is calculated by

$$\begin{aligned} CC(u=-2, v=-2) =& [I_1(x_0-2, y_0-2) I_2(x_0-2-2, y_0-2-2)] \\ &+ [I_1(x_0-2, y_0-1) I_2(x_0-2-2, y_0-1-2)] \\ &+ [I_1(x_0-2, y_0-2) I_2(x_0-2, y_0-2)] \\ &+ [I_1(x_0-2, y_0+1) I_2(x_0-2-2, y_0+1-2)] ... \\ &... + [I_1(x_0+2, y_0+2) I_2(x_0+2-2, y_0+2-2)]. \end{aligned} \tag{7}$$

This calculation must be repeated for each (u, v) in the search range to yield a matrix of correlation coefficients, $CC(u, v)$. From this matrix of $CC(u, v)$ the maximum value defines the best *integer shift* of the subset. This is the maximum resolution possible before some interpolation must be employed to provide *sub-pixel resolution* (the strategies for achieving this are described in the following section). It is clear from above that the number of computations necessary in a DIC analysis can increase rapidly as the dimensions of both the correlation and search windows are increased along each dimension, especially in 3D.

2.2.2 Subpixel resolution

As discussed earlier, digital images are discretised (into pixels / voxels). This implies that the highest resolution on displacements that is possible using the procedure described thus far, is that of a pixel. Whilst this level of resolution might be acceptable in some cases, if the objective is to determine strain-fields, the low resolution can become an issue. Without sub-pixel resolution a stepped displacement field is achieved, as only integer values of displacement can be resolved, this subsequently produces lines of high strain corresponding with the jumps between integer displacement values (see Figure 3). The resultant strain field is thus patterned according to the jumps in displacements (see Figure 4, left column).

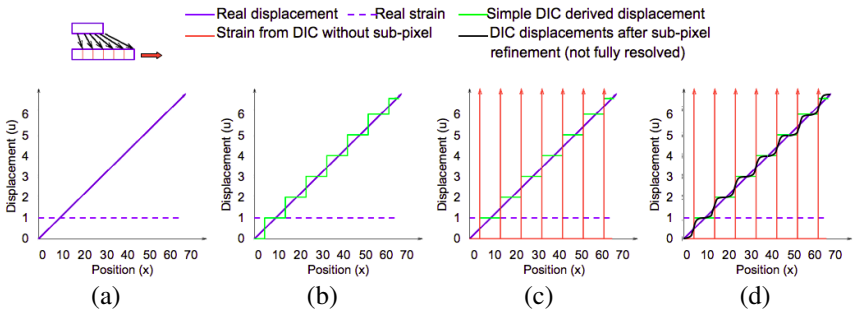

Figure 3: Schematic of the effect of integer-precision in DIC analysis and of subsequent sub-pixel refinement. (a) Imposed displacement and resultant strain; (b) integer resolved displacements; (c) strains resulting from integer resolved displacements; (d) sub-pixel resolved displacements (not fully resolved).

Subpixel resolution can be achieved in DIC using a number of different procedures, which fall into three main categories: (i) resampling of the images to achieve a reduced pixel size; (ii) interpolation of the CC field to find the best correlation; (iii) grey-scale interpolation with cross-correlation (or equivalent) optimisation.

Resampling of the images to achieve a smaller pixel size, and thus increased resolution, can be used within the same DIC framework as already described. However, this is computationally inefficient and does not avoid the discretisation of the images, it just moves it to a smaller scale.

Interpolation of the correlation coefficient involves finding the maximum of the local variation in the correlation coefficient over the neighbourhood of test displacements around the best integer shift displacement. Describing the correlation coefficients corresponding to these integer shifts by some mathematical function provides estimates of the coefficient for all displacements, even for sub-pixel displacements over the region where the interpolation function is valid. The maximum of this function can be found, which gives the sub-pixel resolution displacement. Such an approach is relatively fast, but is only really suited to rigid body translation (higher order deformations

could be analysed, but these would require grey-scale interpolation and thus probably reduces the interest in such an approach over the one described in the following).

The most accurate sub-pixel resolution can be achieved by a grey-scale interpolation and correlation optimisation approach. Such an approach involves interpolation of the "grey level" of the second (deformed) image with optimisation of the transformation that projects the motif of the deformed image on to the initial image (or vice versa). The image transform can be any general transformation, i.e., translation, rotation and/or deformation. The procedure for such a grey-scale interpolation based correlation involves a numerical search for the maximum of the image correlation through some non-linear optimisation approach (e.g., quasi-newton), which generally means finding the set of transformation parameters for which the gradient of the correlation coefficient (as a function of the transformation parameters) is zero.

To illustrate the grey-scale interpolation based refinement concept, the normalised correlation coefficient (equation 4) is written in a more compact form,

$$NCC = \frac{\sum_i (F_i G_i)}{(\sum_i F_i^2 \sum_i G_i^2)^{\frac{1}{2}}}, \tag{8}$$

where F_i is the subset of i pixels in the reference image and G_i is an equivalent subset of the image of the object in its deformed state. For sub-pixel analysis G is replaced by $G' = f(\mathbf{p})$, where $\mathbf{p}$ is the vector of the translation parameters, e.g., $\mathbf{p} = (dx, dy)$ for rigid body motion. A test transformation, $\mathbf{p}$, can thus be made and the correlation, plus its gradient, calculated; where the gradient is,

$$\frac{\partial NCC}{\partial p} = \left[\sum_i F_i^2 \sum_i G_i^2\right]^{-\frac{1}{2}} \sum_i \left(F_i \frac{\partial G_i}{\partial p}\right) - \frac{\sum_i (F_i G_i)}{(\sum_i F_i^2)^{\frac{1}{2}} (\sum_i G_i^2)^{\frac{3}{2}}} \sum_i \left(G_i \frac{\partial G_i}{\partial p}\right). \tag{9}$$

Equation 9 indicates that the gradient of the correlation, as a function of the transformation parameters, involves just the gradient of the interpolation of the second image (G_i'), i.e., the derivative of the interpolation function, which can often be determined analytically, or solved numerically by local partial differences of the image. Optimisation using the gradient of the correlation coefficient can be achieved using some standard non-linear optimisation procedure, e.g., Levenberg-Marquardt, conjugate gradients or Broyden-Fletcher-Goldfarb-Shanno (BFGS). [SBR02] provide a good presentation of such a grey-scale interpolation and optimisation approach (for the 3D-volume case with translation plus rotation).

It should be noted that the subpixel resolution achieved with either of the optimisation approaches described above will never be perfect and there will generally be some residual deviation from the "true" answer. This residual results in the often-called "s-curve" (e.g., [CS97]; [BBD$^+$08]) as indicated in Figure 3, which involves a tendency towards integer values (or for some interpolation functions, half-integer values). In an image these can manifest as "fringe" type patterns similar to (but less severe than) the integer resolution result. The resolution achieved can be controlled, to some extent, through the choice of interpolation function and also the number of iterations or

stopping threshold in the optimisation. Note that common functions used for the grey-scale interpolation are nearest neighbour, bi-(tri-)linear and bi-(tri-)cubic; of these bi(tri)-cubic is the best, but requires greater computation times. Nearest-neighbour interpolation does not provide much increase in resolution and bi-(tri-)linear can also be quite limited. However when going to 3D-volume calculations the processing time cost of a tri-cubic interpolation becomes more of an issue.

Figure 4 presents an example (from [HBD$^+$10]) of the improvements possible in DIC analysis using sub-pixel refinement (in this case the second method was used with searching for the local maximum of the correlation coefficient). Comparison of the two results, with and without sub-pixel resolution, indicates that in the integer-resolution results mostly-nonphysical lines due to the displacement steps are seen. Whilst these patterns do show some organisation that might reflect underlying strain field heterogeneity and strain localisation, it is clear that the result is erroneous, as reflected, for example, in the zero strain zones between the lines. The sub-pixel resolved image shows a much more physically-reasonable result, with clear patterns of strain localisation that do not just fall on lines of steps in the displacement field. It should also be noted that these patterns were robust to changes in the DIC parameters (different search and correlation window sizes), which provides confidence in the validity of the observations (see [HBD$^+$10] for more details).

2.2.3 Taking displacement gradients into account

After derivation of a set of nodal displacement vectors over the study image it is commonplace to derive strain fields from them. Strain field calculations are performed from the displacement vectors using standard continuum mechanics approaches and, in general, the existing DIC node mesh where the displacement vectors are defined. In addition, displacement gradients can be taken into account earlier in the DIC flow by using a more rich transformation vector ($\mathbf{p}$) in the grey-scale optimisation approach described above. However, even if displacement gradients are taken into account in the sub-pixel optmisation stage, it is common to still derive the strain field from the nodal displacement vectors and not to use the gradients from the image correlation transformation function.

2.3 Accuracy, precision and resolution

[BBD$^+$08] provide a detailed analysis of the effect of the different DIC parameters and implementations on DIC accuracy and performance. Furthermore, [WTB03] discuss the issues of DIC accuracy, precision and resolution with respect to geotechnical laboratory experiments, which can be summarised as follows:

- DIC accuracy is a function of the errors associated with the optics of image formation, the image-processing algorithm and the transformation by which image-space coordinates (pixels) are converted into object-space coordinates.

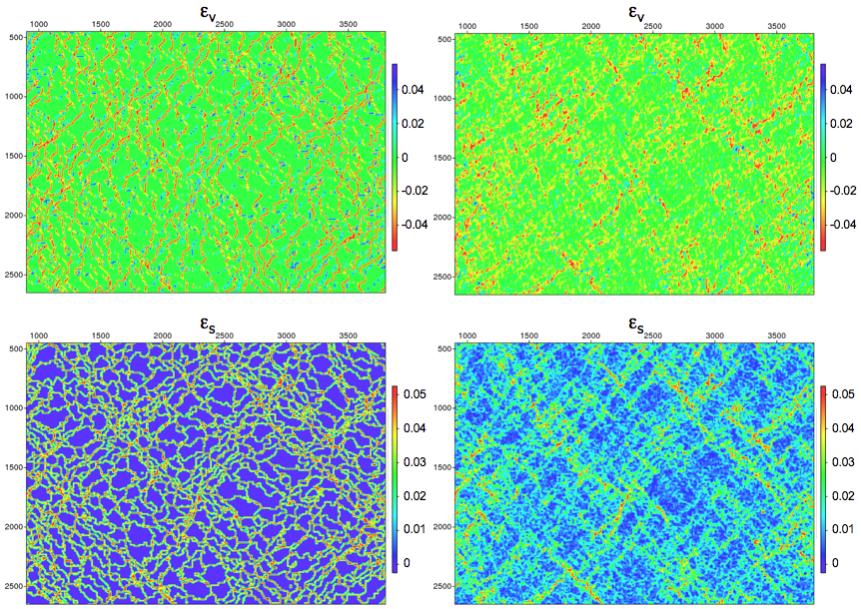

Figure 4: Examples of volumetric and shear strain fields (assuming plane-strain) in 2D deformation experiments on an analogue granular material from [HMWIV10] without sub-pixel refinement (left) and with correlation-coefficient interpolation based sub-pixel refinement (right).

- DIC precision is associated with the precision of the cross-correlation algorithm used, the image texture, i.e., the spatial frequency of the image, the form of the cross-correlation equations and the subpixel refinement/interpolation scheme.
- DIC resolution depends on the input image resolution, the correlation window size and the speckle pattern dimensions/quality.

3 2D-surface DIC

In the following a few specific details and some examples are given concerning the use of 2D-DIC in experimental geomechanics (note that many of the issues raised are also applicable to 3D-surface DIC, although this requires extra calibration and a correlation between the two cameras, as discussed above).

3.1 Data acquisition

The first requirement for surface DIC is clearly that the surface of interest is visible to the camera(s). For un-confined (uniaxial) testing, this is not a problem, although in general this will not give 2D-deformation and 3D-surface DIC should be used. Otherwise it is necessary to have a loading apparatus that ensures plane-strain conditions (and thus a planar 2D surface with displacements only within the 2D plane), such as the plane-strain biaxial apparatuses at Laboratoire 3SR in Grenoble for soils (developed by J. Desrues, eg., [Des84]) and rocks (developed by P. Bésuelle, e.g., [BH11]). These devices impose a plane-strain condition using rigid front and back walls, of which at least one is transparent to allow photography of the sample surface in the plane perpendicular to the plane-strain axis, i.e., in the 2D deformation plane, during loading. For some particular sample geometries near-plane-strain conditions can also be achieved with uniaxial conditions, as in the example given later from [NHVV11]. There have also been examples in geomechanics of the application of 3D-surface DIC to triaxial tests on sand (e.g., [SMCR12]) to assess the heterogeneity of the material response based purely on surface displacements, this, however, remains somewhat limited as there will clearly be displacement gradients into the volume that can not be assessed.

Until the advent of digital photography, film (argentic) cameras were used for imaging experiments (e.g., [Des84]). Such cameras provide very high resolution photographs (without pixelisation), but they are slow in acquisition (due, for example, to the need to change film) and in analysis (images are not directly usable for computer based analysis) plus, in general, the acquisition is limited to small number of images. Digital cameras have revolutionised photography, particularly with regards to DIC. Whilst they have lower spatial resolution than their film counterpart (common scientific cameras are now in the range of 10-20 MPx, although greater resolution cameras are avail-

able (including a 200 MPx one[1])), they permit fast acquisition (especially with rapid cameras that are now capable of several 100s kHz, although resolution reduces with speed) and the number of images is only limited by disk/card storage space. Most importantly, digital cameras provide images that are "easily" analysed on computers, whereas film images must be converted to digital format, which is not necessarily a reliable process (although very high resolutions might be achieved - in one example analysed by the author 600 MPx images were achieved from scanned film photographs).

Whilst image acquisition quality and resolution are important, the object illumination and surface texture are perhaps more important; if there is no texture in the image that might be tracked from one image to another or if the image is too dark to see any texture then the images can be of any resolution, but the DIC will not function well. The first requirement is, therefore, to have good illumination of the study object; good means that the illumination should be homogeneous and static plus should not lead to saturation of the imager. The term "static" refers to no change from one image acquisition to the next as this will mean that homologous parts of the object from one image to the next will not appear to be the same. The second requirement is that the imaged surface has sufficient image texture to differentiate the different parts of the surface and thus ensure the possibility of identifying uniquely each image subset from one image to the next (in an homogeneous image all comparisons would equal so no unique match can be found and it is not possible to define displacement). In some cases the study object might have sufficient natural texture to enable DIC analysis, however it is common, even in such cases, to augment the study object's texture in the images by applying a "speckle pattern". Speckle patterns are spots applied to the object surface to provide image contrast that can be easily identified in the acquired photographs. Such patterns can be applied in a number of ways, with the usual method being using a fine spray with an aerosol spray-paint. Finer speckle can be achieved using spray-guns and for larger objects a sponge or stencil plus spray might be used. Whichever method is used, it is important that there is image contrast at the scale of the measurement and a speckle that can be resolved by the image; i.e., homogenous spots need to be much smaller than the window used in the correlation calculation. It is also very important that the pattern can follow the movement and deformation of the material.

3.2 An example - localised deformation patterning in a 2D granular material

In this section, an example of 2D DIC applied in experimental geomechanics, from [HMWIV10] is presented. The tests concerned were performed on an analogue two-dimensional granular material, consisting of a large number of small PVC rods, in a special laboratory apparatus that allows the application of general stress or strain conditions. DIC was carried out on pairs of consecutive photographs taken during

[1] www.hasselbladusa.com/products/h-system/h4d-200ms.aspx

the tests, which enabled direct observation of internal displacements and localised strain patterning for a series of general strain increments with different orientations of principal strain and different imposed angles of dilation.

Figure 5(a) shows an example of the analysed photographs. In this case no image texture was applied to the surface as sufficient texture existed already due to the variability of the finish of the individual rods. Besides the image resolution (which was approximately 0.19 mm/pixel for each 13.5 Mpixel digital image), the key parameters in this application of DIC were the distance between the calculation nodes, 10 pixels in x and y, and the correlation window size, a square of side 41 pixels, which was reduced to 11 pixels for the sub-pixel derivation. These parameters define correlation windows that overlap slightly for adjacent nodes, which provides some inherent smoothing, but this is small and should not compromise the subsequent strain calculation. These parameters were optimised from extensive testing ([Dop06]). The parameter testing also allowed the stability of the results to be confirmed and to ensure that any patterns observed were not just numerical artefacts of the DIC algorithms adopted. For example, a possible artificial cause of patterning is inaccuracy in the sub-pixel refinement, but this has been ruled out (as presented earlier in Figure 4). Note that the DIC analysis was carried out using the PhotoWarp code of the author.

Figures 5(b, c) show examples of the displacement fields derived from the DIC analysis for the first and last load steps of a loading sequence, as indicated in Figure 6(a). Figure 6(b) presents the maximum shear strain fields for the complete series of strain increments. The strain localisation phenomena can be recognised in the displacement fields of the last load step, but less clearly in the first; note that no evidence of strain localisation could be seen in the photographs alone. The strain fields clearly expose the presence of strain localisation features and their patterning. In fact, the observed evolving structures consist of bands of localised deformation and 'cells' of low deformation between the bands. [HMWIV10] analysed the orientations of identified localised features over a number of tests and this was seen to depend on the applied strain path. Furthermore, characteristic features and dimensions of the localisation features were also approximately determined. Aside from the mechanical implications of the results, this represents a very good example of the power of DIC to reveal inhomogeneous deformation features that were otherwise invisible.

3.3 3D-volume DIC

As discussed in the Introduction, the extension of 2D-DIC to 3D volume images is relatively straightforward. The main challenges relate to the efficient computing of a vastly increased number of correlation and search operations in 3D. However, this is increasingly easy to address with modern computing capabilities.

In geomechanics there have been a few examples of the application of 3D-volume DIC based on the analysis of repeated 3D x-ray tomography imaging, e.g., [BVS06]; [LBD$^+$07]; [HBD$^+$10]; [WLHO10]; [TBDH10]; [CHS$^+$11]. However, whilst appli-

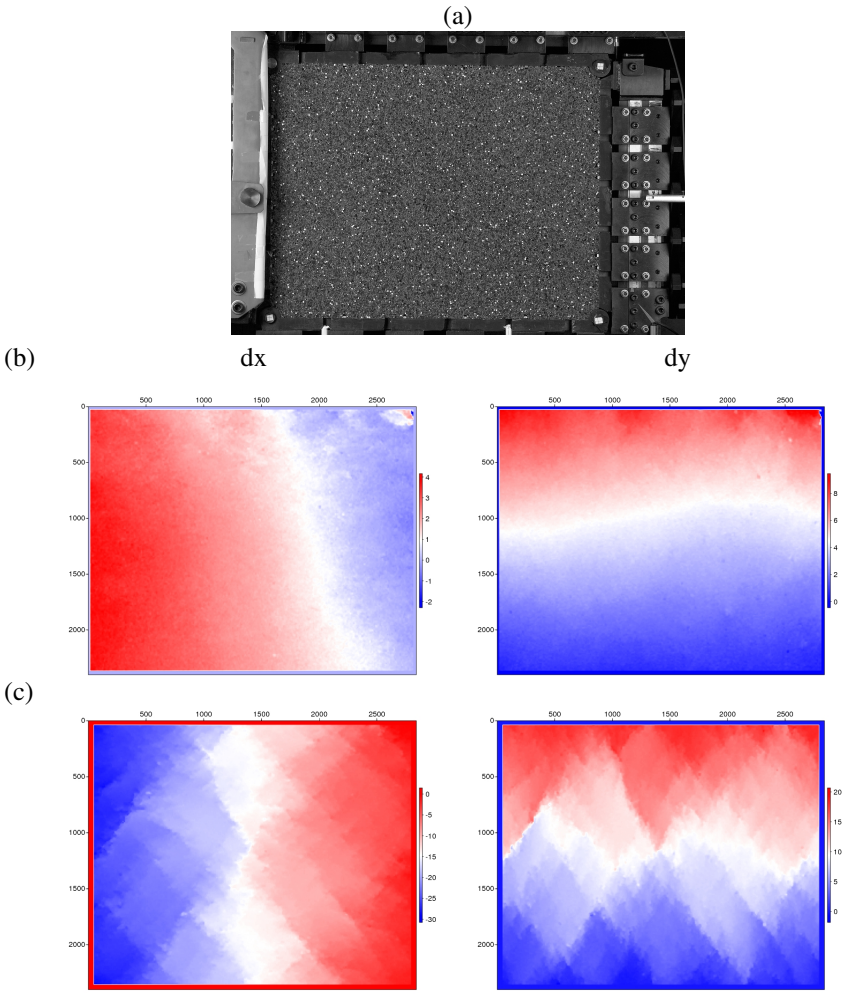

Figure 5: Examples of the displacement fields derived from the DIC analysis for the first and last load steps of the loading sequence indicated in Figure 6 from the Test I65-T0(6.9d) of [HMWIV10] on a 2D analogue granular material.

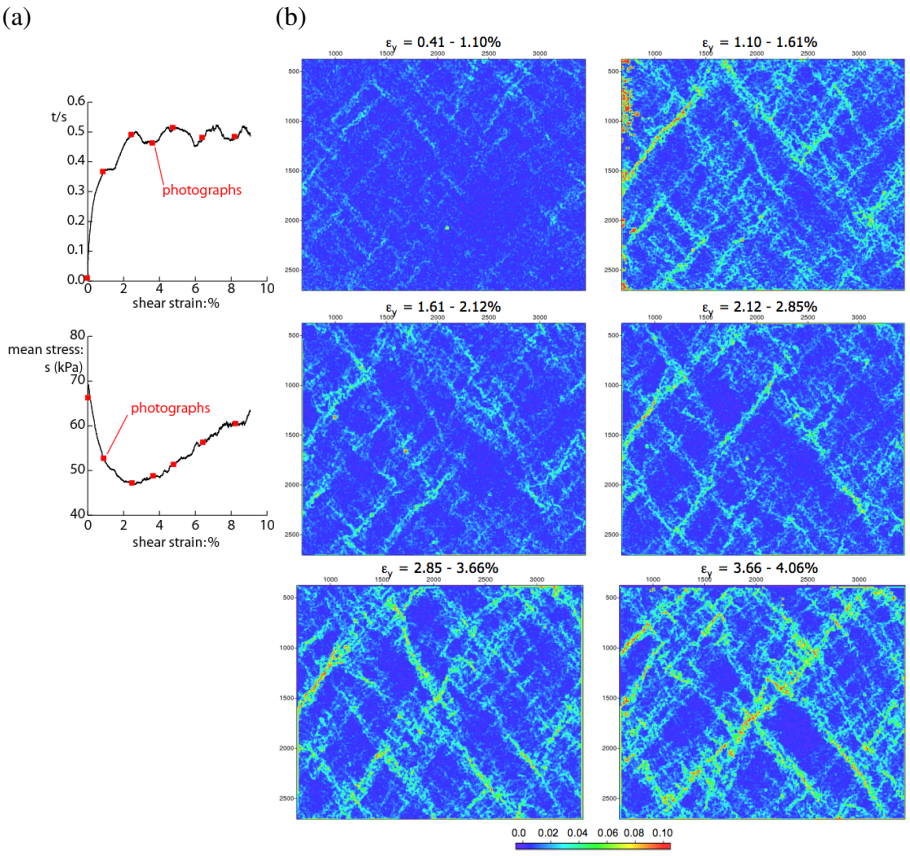

Figure 6: Test I65-T0(6.9d) of [HMWIV10]: (b) incremental internal shear strains for imposed strain increments noted in the loading curve (a).

cations until now have considered 3D x-ray tomography data, there is nothing precluding the use of other 3D images, e.g., from neutron tomography, in fact there have even been examples of 3D-volume DIC applications to geomechanics at a larger scale, i.e., that of subsurface hydrocarbon reservoirs, using 3D seismic imaging data (e.g., [Hal06]). The constraint as to which images might be analysed is the same as for all DIC applications, i.e., repeated imaging with sufficient image texture that can be tracked uniquely from one image to the next. The only difference between 3D-volume DIC and surface DIC is that the texture must, in general, be inherent in the material (although it might be possible to add texture ('markers" / "tracers") by mixing in another material, but this risks altering the mechanics of the study system).

In the following two example of 3D-volume DIC applications in experimental geomechanics are presented, one for analysing localised deformation in a sandstone, using pre- and post-deformation x-ray tomography images, and the other for deformation in sand with "in-situ" x-ray tomography imaging.

3.4 A couple of examples

3.4.1 Pre- post-test analysis of triaxial deformed sandstone

In the context of the PhD thesis of E Charalampidou ([Cha11]) a number of triaxial experiments were run on sandstone samples from the Vosges mountains of north-eastern France. In these studies x-ray tomography images of different resolutions were acquired before and after the triaxial loading tests, which permitted full-field analysis of the total deformation (due to loading and unloading) in the samples and, in particular, the characterisation of any evolved localised deformation features in terms of shear versus volumetric strains. Two examples from this study are summarised in the following, one for a sample deformed at 50 MPa confining pressure and the other for a sample deformed at 130 MPa (see [CHS$^+$11]). In the former, compactant shear bands were expected, based on previous work of [BDR00]. In the latter, more compactant features were expected, although it was not known if they would be in the form of true compaction bands or some hybrid shear-compaction mode.

The 3D images for this study were acquired using the multi-resolution x-ray tomograph at Laboratoire 3S-R in Grenoble. Both "high-resolution" (30 μm voxel width) and "low-resolution" images (90 μm voxel width) were acquired before and after the triaxial loading. The high-resolution images were acquired just over the central part of the specimen and the low-resolution images over the whole specimen. The post-test high-resolution images were first analysed "as is", and in cases where shear-bands were expected (P_c=50 MPa) the localisation features could be distinguished as zones of increased x-ray absorption. For the sample where the localised deformation was expected to be more compactant (P_c=130 MPa) it was difficult (impossible) to identify anything associated with localised deformation in the tomography images.

3D-volumetric DIC analysis was carried out on both the low- and high-resolution pre-

and post-test x-ray tomography images. The TomoWarp code of the author (see, for example, [HLV$^+$09]) was used. This analysis aimed to highlight and quantify the localised deformation that had evolved in the samples during loading. The results of the analysis of the high resolution data are discussed in the following (DIC grid spacing was 5 voxels in each direction and the correlation windows were cubes of side 10 voxels; note that the grain size of the rock was about 300 μm, i.e., about 10 voxels). Full 3D strain tensors were derived over cubic volumes defined by each set of eight neighbouring DIC analysis nodes, therefore the "gauge length" was the node spacing dimension, i.e., 5 voxels (150 μm). The strain tensor is more easily interpreted in terms of its invariant quantities and in particular the first and second invariants, which relate to the volumetric and maximum shear strains respectively, these are presented in Figures 7 and 8.

For the P_c=50 MPa case (Figure 7) localised deformation features can be seen clearly in the shear-strain image (more clearly than in the original post-test x-ray image), and, in fact, two coalescing bands and their coalescence zone are evident. The volume strain image shows that the localised zone contains both dilatant and compactant regions; previously deformation bands formed in this rock at this pressure (50 MPa) were described as being just compactant shear bands ([BDR00]), but these DIC results suggest a more complex scenario. In the other example, for a sample deformed at 130 MPa (see Figure 8), no indication of localised deformation was apparent in the tomography images, yet clear patterns of localised deformation can be seen in the DIC results; this is another strong example of the power of DIC to reveal 'invisible" deformation features. In this case, a number of bands can be seen to have formed and they all show some degree of shear deformation as well as compaction where the bands are aligned orthogonal to the principle stress direction (vertical on these images). As a result these bands were described as shear-enhanced compaction bands [Cha11].

3.4.2 In-situ triaxial testing on sand

The second 3D-volumetric DIC example concerns experimental results from a triaxial compression test performed on a dry specimen of S28 Hostun sand (quartz sand with a mean grain size, D50, of about 300 μm), under a confining pressure of 100 kPa, carried out "in-situ" in an x-ray tomography set-up at beamline ID15A of the European Synchrotron Radiation Facility (ESRF); see [HBD$^+$10]. The sample was 11 mm in diameter and 22 mm high, comprising roughly 50000 grains. Loading was carried out in a triaxial system similar to that described in [LBD$^+$07] and Figure 9b shows the sample stress-strain response; the timing of the 3D imaging coincides with the relaxations in the loading curve (loading was stopped during the measurements). Figure 9a presents vertical slices through the 3D x-ray tomography volumes acquired through the test. These images have a voxel size of 14 x 14 x 14 μm^3; such dimensions were chosen to provide sufficient voxels per grain (about 5500 voxels on average with about 21 voxels across their diameters), which allowed clear identification of individual grains in the 3D images. To assess the evolution of the strain field in the sample during loading and the development of localised deformation (as observed in

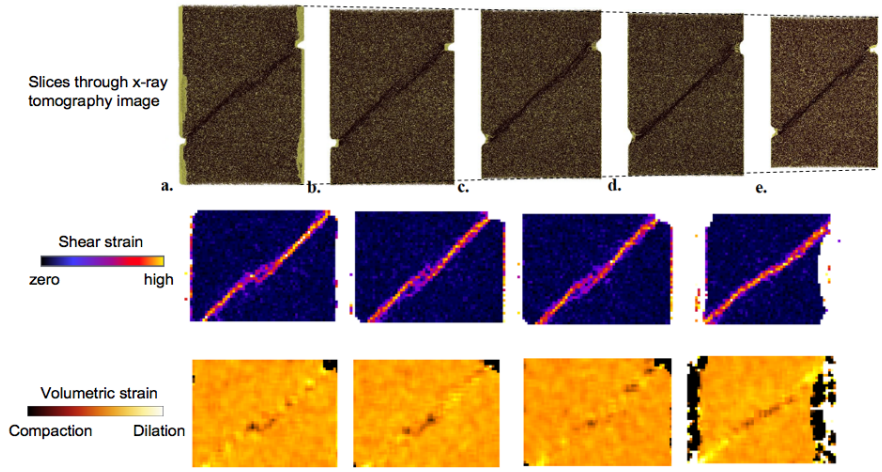

Figure 7: Results from [CHS+11] for 3D-volumetric DIC analysis on a sample of a Vosges sandstone deformed under triaxial compression at 50 MPa confining pressure. Top: vertical slices through the x-ray tomography volume image after triaxial loading at differerent positions in the sample (shown in a "perspective view"). Middle and bottom: vertical slices through the maximum-shear and volumetric strain volume images, respectively, derived from 3D-volumetric DIC analysis of the pre and post-deformation 3D tomography images.

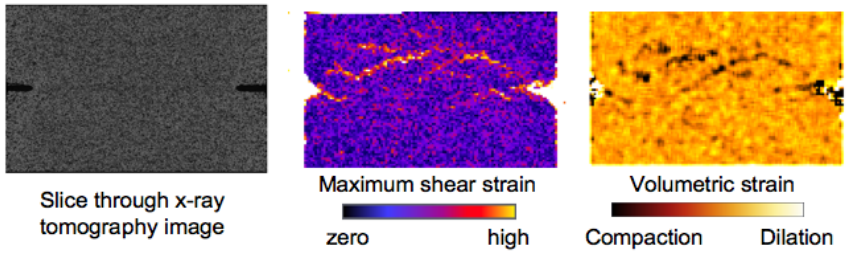

Figure 8: Results from [CHS+11] for 3D-volumetric DIC analysis on a sample of a Vosges sandstone deformed under triaxial compression at 130 MPa confining pressure. Left: vertical slice through the x-ray tomography volume image after triaxial loading. Middle and right: vertical slices, at the same position, through the maximum-shear and volumetric strain volume images, respectively, derived from 3D-volumetric DIC analysis of the pre and post-deformation 3D tomography images.

more standard sized tests), 3D-volumetric DIC was performed (using the TomoWarp code cited earlier). This DIC analysis, carried out on consecutive pairs of the 3D x-ray tomography image volumes, provided 3D displacement and strain fields for each load increment. Figure 9c shows vertical slices through DIC-derived "shear strain" volumes (the second invariant of the strain tensor). As for the tomography images, these vertical slices are cut roughly perpendicular to the "plane" of localisation that developed during the test. These strain images clearly show the evolution of a localised strain band that traverses the sample diagonally from top-left to bottom-right, corresponding to an observed band of porosity increase (see [HBD$^+$10]). This localisation appears to initiate in the increment 4-5, i.e., well before the peak load. Furthermore it can be seen that the band starts as a broad zone and converges towards a narrow band of localised strain in step 6-7 (the zone is around 5 mm, i.e., about 17 D50, at this stage) with a narrower, high strain core. Note that the strain localisation is visible in these maps before it becomes clear in the tomography images or even in derived porosity images (see [HBD$^+$10]). The DIC results also show that the localised band is not uniform and contains structure, including aligned zones of either reduced or elevated strains at angles "conjugate" to the main band direction. The orientations of these zones are similar to those of "columns" of aligned grains identified by [OTT05] in a shear band in sand.

4 Discontinuous deformation

In its standard form, DIC is essentially a continuum-type analysis, i.e., it is inherently assumed that the object under consideration shows no strong discontinuities in displacement between the acquisitions of consecutive images. In the case of fracture, either opening or shearing, the continuum condition is clearly violated. Therefore, whilst DIC provides a correct analysis of the displacement and strain of blocks around developing fractures, the actual deformation calculated in the region of the fractures will be meaningless. This will arise due to the two following reasons. The first is of fundamental nature: fractures are discontinuities of the displacement field that cannot be properly described in terms of strain. The second reason is more technical and concerns the image distortion produced by the development of a fracture (in terms of a large strain, for sliding cracks, or in terms of an open zone, for opening cracks), which has the implication that a good image match may not exist. Similar issues apply to the analysis of other non-continuum systems such as granular media. In the following possible strategies for the treatment of fracture and granular mechanics are briefly discussed with some examples.

4.1 Displacement discontinuities (treatment of fractures)

For a qualitative analysis of fracturing, neither of the issues described above, regarding the use of "continuum" DIC, represents a real problem, as fairly good images of

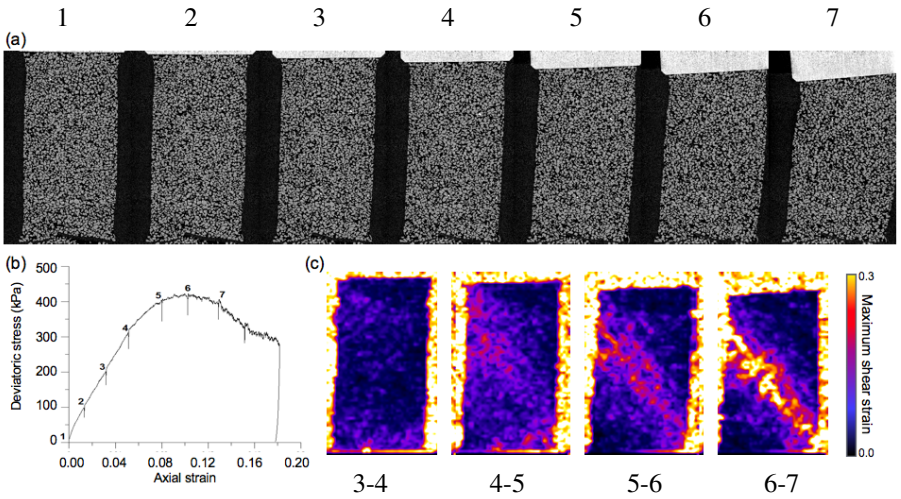

Figure 9: Results from [HBD$^+$10] for 3D-volumetric DIC analysis on a sample of Hostun sand deformed under triaxial compression at 100 kPa confining pressure (the initial sample dimensions were 11 mm in diameter and 22 mm high). (a) Vertical slices through the x-ray tomography volume images acquired during triaxial loading at differerent stages of deformation, as indicated by the stress-relaxations in the load curve in (b). (c) Vertical slices through the incremental maximum-shear strain volume images derived from 3D-volumetric DIC analysis of consecutive pairs of 3D tomography images (only the results for increments 3-4, 4-5, 5-6 and 6-7 are shown here).

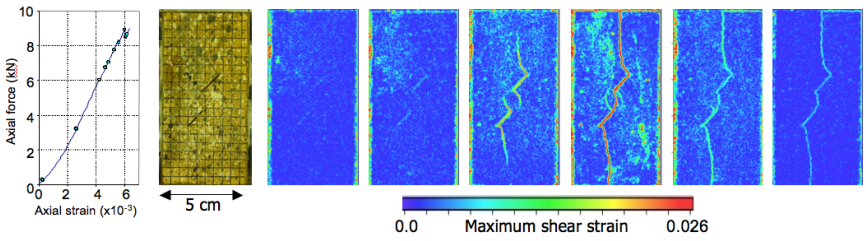

Figure 10: DIC results of [HVB07] based on the study by [HdSV06] on the evolution of fractures from pre-existing flaws in a soft rock (Neapolitan Yellow Tuff). The first two images show the loading curve and a photograph of the sample at the end of the test, whilst the remaining images are the incremental maximum shear strain fields derived by 2D-DIC analysis of consecutive image pairs acquired at the stains indicated in the loading curve.

fracture traces can be derived based on the zones of high strain or unresolved correlation (see Figure 10) and, in fact, fractures can generally be identified much earlier in their evolution using such images than they can be directly from the photographs themselves. However, correct, quantitative, treatment of fractures in DIC requires adaptations to the DIC procedure or the analysis of the results. For example, [RRH07] and [RRH08] proposed a DIC algorithm that makes use of extended finite elements (XFEM) in the context of a global DIC approach to allow for discontinuities in the displacement field during the DIC computation. Another approach has been suggested by Helm (2008), in which an automatic procedure allows identification of cracks and their exclusion from the DIC analysis. Furthermore, [NHVV11] recently proposed a method in which standard (local) DIC analysis is employed and the displacement discontinuities are addressed in a correct post-processing procedure; this approach is discussed in more detail in the following.

4.1.1 Example: fracture analysis based on DIC post-processing ([NHVV11])

The method of [NHVV11] for treatment of fractures (analysis of fracture initiation, propagation and coalescence) was inspired by the earlier work of [Des95] on the analysis of displacement discontinuities in displacement field images from False Relief Stereophotogrammetry. Initial application of such a method to DIC data was presented by [HVB07] and this approach was extended and formalised (including automated fracture-trace identification) by [NHVV11]. The method proposed by [NHVV11], based on standard DIC analysis, provides: (i) automatic tracing of the lines of displacement discontinuities (fractures); (ii) quantification of the normal and tangential displacement jumps along the length of the traced fractures. The fracture traces are identified as cells in the DIC that show large jumps in displacement between the included nodes, these are grouped into fractures by an algorithm that follows lines of

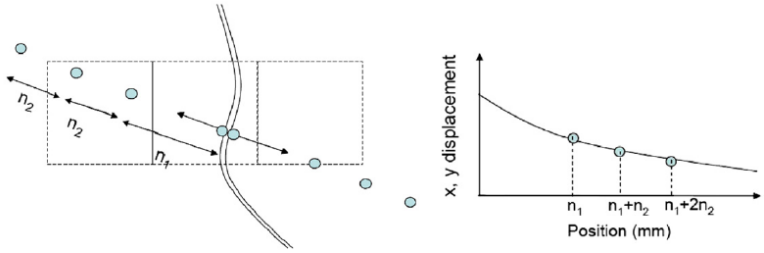

Figure 11: Schematic of the displacement discontinuity analysis approach of [NHVV11] after the fracture traces have been identified indicating the process for the interpolation and extrapolation of the displacements on either side of the fracture back to the fracture line.

high discontinuity values. Subsequently the displacement jumps are derived across the fracture lines, along their whole length by extrapolation of the displacement field back to the fracture line along fracture-orthogonal paths, using points on either side of the fracture (see Figure 11). With this method, the tip, length and geometry of the displacement discontinuities are more easily identified and traced through a test. The relative movement between the two sides of each crack can be quantified and, based on the well-defined geometry, decomposed into normal and tangential components relative to the local fracture trajectory. Thus a quantitative analysis of fracture evolution processes is achieved.

Figure 12 shows an example displacement field from the analysis of [NHVV11] of fracture evolution from pre-existing inclined flaws in a soft rock (Neapolitan Yellow Tuff) deformed under plane-strain uniaxial compression. (In this case the 7D code of P. Vacher was used; see [VDMMT99].) The clear discontinuities in displacement, both across the pre-existing flaws and across the evolving "wing cracks" that formed from the flaw tips, can be seen; in a strain map these would appear (erroneously) as lines of high strain. Figure 13 shows the traced fracture lines and displacement discontinuity "maps" for different stages of the fracture evolution.

4.2 Granular materials and discrete DIC

Another situation where continuum analyses can be inappropriate is in the study of granular mechanics. In the example given earlier for 3D-volumetric DIC applied to in-situ triaxial testing on sand, the granular nature of the material, and of the images, was ignored and the material was considered as being (piece-wise) continuous. However, whilst the DIC results from this analysis appear to represent well the deformation that occurred and no significant discontinuities in displacement can be observed, it is to be expected that the displacement field would be locally continuous, within each grain, but discontinuous between the grains. The challenge was therefore to develop an

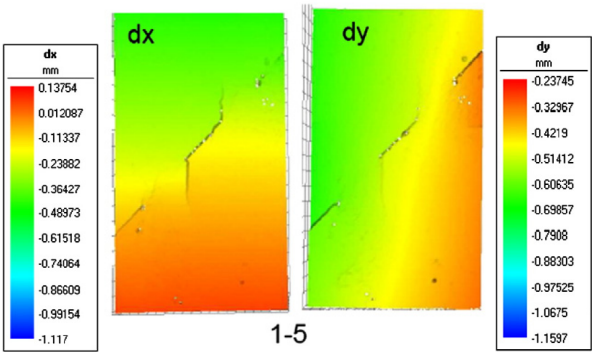

Figure 12: Example of the displacement fields from one of the tests of [NHVV11] where the initiation, propagation and coalescence of fractures from pre-existing flaws in a soft rock (Neapolitan Yellow Tuff) was studied (in this case there were three, aligned pre-exsiting flaws cut in the sample). These images show for the total displacement field from the start of the test (image 1) to the 5th image after some propagation of the wing cracks.

adapted "discrete" DIC technique to derive the kinematics of all the individual grains. An approach to address this challenge is described below, based on the work presented in [HBD+10].

In standard implementations of DIC there is an inherent assumption of a continuous displacement field, at least within each subset. When deriving strain from the displacements of separate subsets, continuity between adjacent subsets is also assumed. For this reason, such DIC analysis might be referred to as "continuum DIC" (or, perhaps, piece-wise continuous DIC). An alternative DIC approach for granular materials, that recognises the granular character both of the images and the mechanical response, was proposed by M. Bornert (Institut Navier) and presented in [HBD+10] and [PLB10]. This approach is a "discrete DIC" procedure with the specific aspect that the regularly shaped and spaced subsets are replaced by subsets centred on individual grains, with a shape following the actual shape of the grain and including only a single grains (cubic subsets will generally cover more than a single grain especially if distributed over a regular, as opposed to grain-centred, arrangement). If the grains are assumed to be rigid, then the transformation of each subset will a rigid motion involving a three-component translation vector plus a three-component rotation. The method is described in full in the cited papers, but the key results are summarised below.

In the analysis of [HBD+10], discrete DIC was applied to provide quantification of the incremental kinematics of each grain (3D displacements and rotations) in the sand specimen loaded in triaxial compression described earlier (see [HBD+10]). The derived grain displacements agreed well with the continuum DIC results and show relatively continuous fields of displacements, even in the presence of strain localisation.

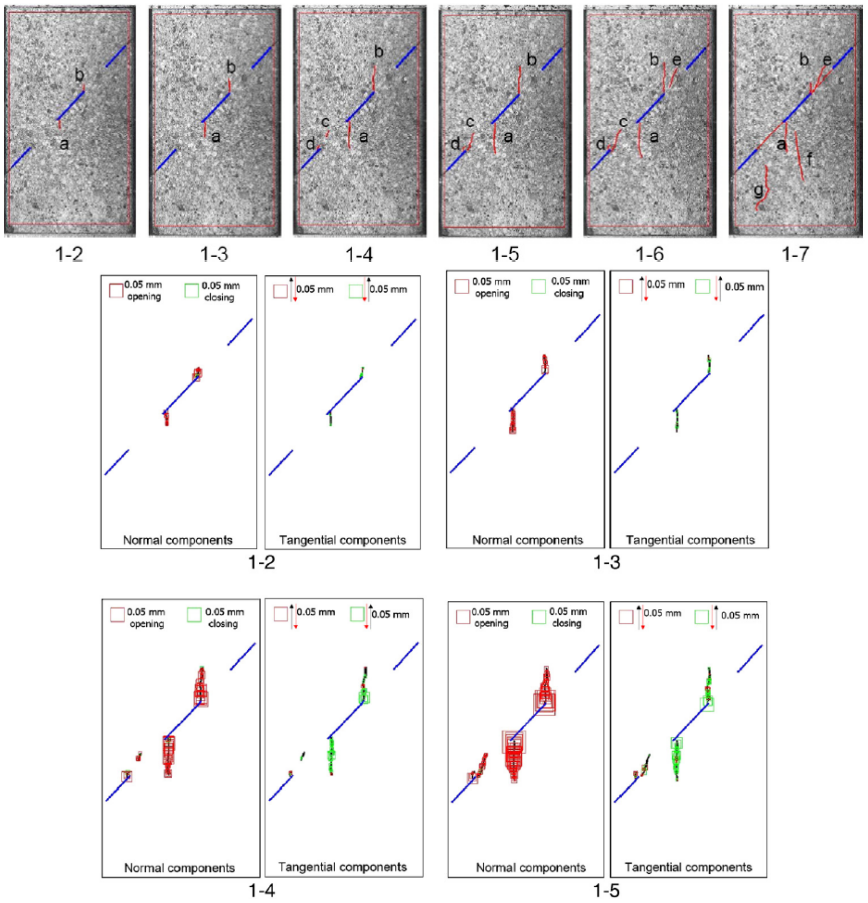

Figure 13: Results from the study of [NHVV11] on the initiation, propagation and coalescence of fractures from pre-existing flaws in a soft rock (Neapolitan Yellow Tuff). Upper: the analysed photographs with automatically traced fractures overlain. Lower: quantified displacement jumps across the traced fractures for four example load levels; in each case the displacement jumps have been decomposed in to the local, normal and tangential components.

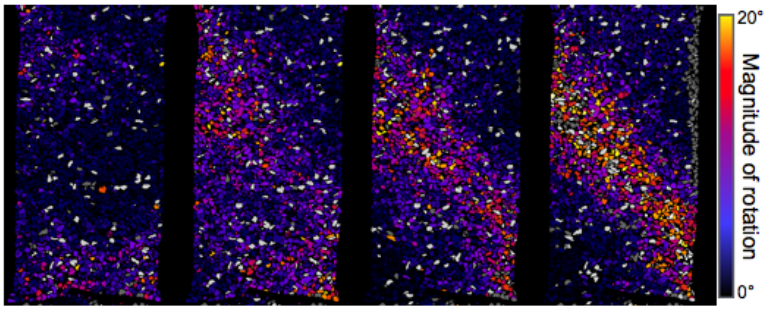

Figure 14: Results from [HBD+10] for discrete 3D-volumetric DIC analysis corresponding to the continuum DIC results in Figure 9. Here just the magnitude of the incremental rotation of each grain (about their own individual rotation axes) are plotted for loading increments 3-4, 4-5, 5-6 and 6-7. A clear localisation of the rotations in to the shear band highlighted by the continuum analysis can be seen.

This explains why a continuum DIC approach performed well. However, locally (between grains) the kinematics were seen to be discontinuous (this could be analysed on a contact-by-contact basis to determine the contact kinematics). A key contribution of the discrete DIC approach is that it provides the full kinematics of each grain. These data revealed more detail about the micro-mechanics underlying the evolution of the localised deformation zone, which at the meso-scale of the continuum DIC manifested as a shear-band. For example, Figure 14 presents the magnitude of rotation for each grain about its rotation axis (which is specific for each grain). These results indicate that grain rotations become progressively more intense into a zone that roughly corresponds to where shear strain localises (see Figure 9). This indicates that the meso-scale shear strain is due, at least in part, to grain rotations at the micro-scale. Further development of this methodology and data analysis is ongoing in the context of the PhD thesis of E. Andò at Laboratoire 3SR in Grenoble (publication expected in 2013).

5 Parameter identification from DIC

In the preceding discussions and example applications, DIC has been presented as a measurement tool primarily for the full-field characterisation of deformation mechanisms through quantification of spatial and temporal variations in the kinematics or strain at the surface of, or within, deforming objects. However, such data represent a very rich set of measurements that might be exploited in inverse procedures to more accurately derive material model parameters, either for the material as a whole (on the assumption of global properties) or for the local variations in the material. The most evident of such approaches is perhaps the use of a optimisation procedures comparing

numerical and real experiments, where the misfit between the simulated and the measured (from DIC) displacement fields is minimised through optimisation of the model parameters. However, a number of other strategies have also been proposed. Such aspects are beyond the scope of this paper, but good overviews of the different DIC *parameter identification* procedures can be found in [HR06] and [ABB$^+$08].

6 Conclusions

Digital Image Correlation, DIC, is a powerful tool in experimental mechanics that has seen a significant increase in use in recent years, including within geomechanics. This method provides full-field measurement of kinematics and strain at the surface of or within objects during their deformation. This permits a more correct analysis of deformation than traditional approaches without the need to assume homogeneous behaviour in the interpretation. Therefore heterogeneity, either pre-existing or evolving (e.g., strain localisation), can be correctly addressed; this is essential in the study of geomaterials, which are by nature heterogeneous.

This paper has presented the basic concepts of DIC for both surface and volume analysis, including technical details on both the data acquisition and the methodology. A few more specific aspects relating to geomaterials have also been discussed, i.e., the analysis of discontinuous deformation in the form of fractures and granular mechanics. These topics plus the identification of model parameters from DIC are likely to be significant areas of future development in geomechanics over the coming years. It is also likely that the use of DIC will become standard, although there are, in many cases, still technical challenges to be overcome to permit visualisation of test specimens during loading without compromising the experiment boundary conditions.

References

[ABB$^+$08] S. Avril, M. Bonnet, A-S. Bretelle, M. Grédiac, F. Hild, P. Ienny, F. Latourte, D. Lemosse, S. Pagano, E. Pagnacco, and F. Pierron. Overview of identification methods of mechanical parameters based on full-field measurements. *Experimental Mechanics*, 48:381–402, 2008.

[Adr91] R.J. Adrian. Particle-imaging techniques for experimental fluid mechanics. *Annual Review in Fluid Mechanics*, 23:261–304, 1991.

[Bay08] B.K. Bay. Methods and applications of digital volume correlation. *Journal of Strain Analysis*, 43:745–760, 2008.

[BBD$^+$08] M. Bornert, F. Brémand, P. Doumalin, J.-C. Dupré, M. Fazzini, M. Grédiac, F. Hild, S. Mistou, J. Molimard, J.-J. Orteu, L. Robert, J.-J. Surrel, P. Vacher, and B. Wattrisse. Assessment of digital image

correlation measurement errors: Methodology and results. *Experimental Mechanics*, 3:353–370, 2008.

[BCD+04] M. Bornert, J. M. Chaix, P. Doumalin, J. C. Dupré, T. Fournel, D. Jeulin, E. Maire, M. Moreaud, and H. Moulinec. Mesure tridimensionnelle de champs cinématiques par imagerie volumique pour l'analyse des matériaux et des structures. *Instrumentation, Mesure, Métrologie*, 4:43–88, 2004.

[BDR00] P. Bésuelle, J. Desrues, and S. Raynaud. Experimental characterization of the localization phenomenon inside a vosges sandstone in a triaxial cell. *International Journal of Rock Mechanics and Mining Science*, 37:1223–1237, 2000.

[BH11] P. Bésuelle and S.A. Hall. Characterization of the strain localization in a porous rock in plane strain condition using a new true-triaxial apparatus. *Springer Series in Geomechanics and Geoengineering*, 11:345–352, 2011.

[BHmBqFl06] P. Bing, X. Hui-min, X. Bo-qin, and D. Fu-long. Performance of sub-pixel registration algorithms in digital image correlation. *Measurement Science and Technology*, 17:1615–1621, 2006.

[BI05] A.R. Bhandari and J. Inoue. Discrete and continuum analysis of localised deformation in sand using x-ray micro CT and volumetric digital image correlation. *International Journal for Numerical and Analytical Methods in Geomechanics,*, 29:1087–1107, 2005.

[BSFS99] B.K. Bay, T.S. Smith, D.P. Fyhrie, and M. Saad. Digital volume correlation: three-dimensional strain mapping using x-ray tomography. *Experimental Mechanics*, 39:217–226, 1999.

[BVGNM08] M. Bornert, F. Vale's, H. Gharbi, and D. Nguyen Minh. Multiscale full-field strain measurements for micromechanical investigations of the hydromechanical behaviour of clayey rocks. *Strain, International Journal for Experimental Mechanics*, 46:33–46, 2008.

[BVS06] A. Bauer, E. Verhulp, and S. Schoofs. Measuring local strains in sandstones under stress with microcomputed tomography. In J. Desrues, G. Viggiani, and P. Bésuelle, editors, *Advances in x-ray tomography for geomaterials*, pages 247–253. ISTE, 2006.

[Cha11] E.-M. Charalampidou. *Experimental Study of Localised Deformation in Porous Sandstones*. PhD thesis, Heriot Watt University, Edinburgh and Université de Grenoble, Grenoble, 2011.

[CHS+11] E. M. Charalampidou, S. A. Hall, S. Stanchits, H. Lewis, and G. Viggiani. Characterization of shear and compaction bands in a porous sandstone deformed under triaxial compression. *Tectonophysics*, 503:8–17, 2011.

[CS97] S. Choi and S. Shah. Measurement of deformations on concrete subjected to compression using image correlation. *Experimental Mechanics*, 37:307–313, 1997.

[DBG+11] J. Dautriat, M. Bornert, N. Gland, A. Dimanov, and J. Raphanel. Localized deformation induced by heterogeneities in porous carbonate analysed by multi-scale digital image correlation. *Tectonophysics*, 503:100–116, 2011.

[Des84] J. Desrues. La localisation de la déformation dans les matériaux granulaires. Thése de doctorat es science, USMG and INPG, Grenoble, France, 1984.

[Des95] J. Desrues. Analyse st!ereophotogramm!etrique de la fissuration progressive. In Y. Berthaud et al., editor, *Photomécanique 95*, pages 149–162. Éditions Eyrolles, 1995.

[Dop06] M. Dopff. Digital image correlation, rapport de stage, Laboratoire 3S-R, Grenoble, 2006.

[DV04] J. Desrues and G. Viggiani. Strain localization in sand: an overview of the experimental results obtained in grenoble using stereophotogrammetry. *Numerical and Analytical Methods in Geomechanics*, 28:279–321, 2004.

[FS04] F. Forsberg and M. Sjödahl. Tomographic 3D-DSP: measurement of internal deformations. In *Proc. 12th Int. Conf. on Experimental Mechanics ICEM12, Bari, Ital*, pages 217–226, 2004.

[GEB99] M. Guler, T.B. Edil, and P.J. Bosscher. Measurement of particle movement in granular soils using image analysis. *Journal of Computing in Civil Engineering, ASCE*, 13:116–122, 1999.

[GN04] G. Gudehus and K. Nübel. Evolution of shear bands in sand. *Géotechnique*, 54:187–201, 2004.

[Gre04] M. Grediac. The use of full-field measurement methods in composite material characterization: interest and limitations. *Composites: Part A*, 35:751–761, 2004.

[Hal06] S.A. Hall. A methodology for 7D warping and deformation monitoring using time-lapse seismic data. *Geophysics*, 71:O21–O31, 2006.

[HBD+10] S.A. Hall, M. Bornert, J. Desrues, Y. Pannier, N. Lenoir, G. Viggiani, and P. Bésuelle. Discrete and continuum analysis of localised deformation in sand using x-ray micro CT and volumetric digital image correlation. *Géotechnique*, 60:315–322, 2010.

[HdSV06] S.A. Hall, F. de Sanctis, and G. Viggiani. Monitoring fracture propagation in a soft rock (Neapolitan tuff) using acoustic emissions and digital images. *Pure and Applied Geophysics*, 163:2171–2204, 2006.

[HLV+09] S.A. Hall, N. Lenoir, G. Viggiani, J. Desrues, and Bésuelle P. Strain localisation in sand under triaxial loading: characterisation by x-ray micro tomography and 3D digital image correlation. In *Proceedings of the 1st International Symposium on Computational Geomechanics (ComGeo I), Juan-les-Pins, Cote d'Azur, France, April 29–May 1st, 2009*, 2009.

[HMWIV10] S.A. Hall, D. Muir Wood, E. Ibraim, and G. Viggiani. Localised deformation patterning in 2D granular materials revealed by digital image correlation. *Granular Matter*, 12:1–14, 2010.

[HR06] F. Hild and R. Roux. Digital image correlation: from displacement measurement to identification of elastic properties – a review. *Strain, International Journal for Experimental Mechanics*, 42:69–80, 2006.

[HR12] F. Hild and R. Roux. Comparison of local and global approaches to digital image correlation. *Experimental Mechanics*, DOI: 10.1007/s11340-012-9603-7, 2012.

[HVB07] S.A. Hall, G. Viggiani, and P. Bésuelle. Analysis of fracture in a soft rock (Neapolitan tuff) using digital image correlation with displacement discontinuity quantification, Euro-conference of rock physics and geomechanics on "natural hazards: thermo-hydro-mechanical processes in rocks", EMFCSC, Erice, Sicily (Italy) (www.earth-prints.org/bitstream/2122/2692/l/hall.pdf, 2007.

[LBD+07] N. Lenoir, M. Bornert, J. Desrues, Bésuelle P., and G. Viggiani. Volumetric digital image correlation applied to x-ray micro tomography images from triaxial compression tests on argillaceous rocks. *Strain, International Journal for Experimental Mechanics*, 43:193–205, 2007.

[LI04] J. Liu and M. Iskander. Adaptive cross correlation for imaging displacements in soils. *Journal of Computing in Civil Engineering, ASCE*, 18:46–57, 2004.

[LSPI93] Y.J. Luo, P.F.and Chao, M.A. Sutton, and W.H. Peters III. Accurate measurement of three-dimensional deformations in deformable and rigid bodies using computer vision. *Experimental Mechanics*, 33:123–132, 1993.

[McN06] S. McNeill. University of South Carolina: http://www.me.sc.edu/fs/lyons/emch361/06s/dic-mcneill.pdf, 2006.

[MSW+83] S.R. McNeill, M.A. Sutton, W.J. Wolters, W.H. Peters, Ill, and W.F Ranson. Determination of displacements using an lmproved digital correlation method. *Image and Vision Computing*, 1:1333–1339, 1983.

[NHVV11] T.L. Nguyen, S.A. Hall, P. Vacher, and G. Viggiani. Fracture mechanisms in soft rock: identification and quantification of evolving displacement discontinuities by extended digital image correlation. *Tectonophysics*, 503:117–128, 2011.

[NLT11] M. Niedostatkiewicz, D. Lesniewska, and J. Tejchman. Experimental analysis of shear zone patterns in cohesionless for earth pressure problems using particle image velocimetry. *Strain, International Journal for Experimental Mechanics*, 47:218–231, 2011.

[Ort] J.J. Orteu.

[Ort09] J.J. Orteu. 3-D computer vision in experimental mechanics. *Optics and Lasers in Engineering*, 47:282–291, 2009.

[OTT05] M. Oda, T. Takemura, and M. Takahashi. Microstructure in shear band observed by microfocus x-ray computed tomography. *Géotechnique*, 54:1–4, 2005.

[PLB10] Y. Pannier, N. Lenoir, and M. Bornert. Discrete and continuum analysis of localised deformation in sand using x-ray micro CT and volumetric digital image correlation. In *EPJ Web of Conferences: ICEM 14 – 14th International Conference on Experimental Mechanics*, number 35003. EDP Sciences, 2010.

[PR81] W.H. Peters and W.E Ranson. Digital imaging techniques in experimental stress analysis. *Optical Engineering*, 21:427–432, 1981.

[RAJ63] K.H. Roscoe, J.R.F. Arthur, and R.G. James. The determination of strains in soils by an x-ray method. *Civ. Eng. Public Works Rev.*, 58:873–876 and 1009–1012, 1963.

[RF04] A.L. Rechenmacher and R.J. Finno. Digital image correlation to evaluate shear banding in dilative sands. *Geotechnical Testing Journal*, 27:13–22, 2004.

[RRH07] J. Réthoré, S. Roux, and F. Hild. From pictures to extended finite elements: Extended digital image correlation (X-DIC). *Comptes Rendus Mécanique*, 335:131–137, 2007.

[RRH08] J. Réthoré, S. Roux, and F. Hild. Extended digital image correlation with crack shape optimization. *International Journal for Numerical Methods in Engineering*, 73:248–272, 2008.

[SBR02] T.S. Smith, B.K. Bay, and M.M. Rashid. Digital volume correlation including rotational degrees of freedom during minimization. *Experimental Mechanics*, 42:272–278, 2002.

[SCP+86] M.A. Sutton, M. Cheng, W.H. Peters, Y.J. Chao, and S.R. McNeill. Application of an optimized digital correlation method to planar deformation analysis. *Image and Vision Computing*, 4:143–150, 1986.

[SMCR12] A. Song, Z. Medina-Cetina, and A.L. Rechenmacher. *Local Deformation Analysis of a Sand Specimen Using 3D Digital Image Correlation for the Calibration of a Simple Elasto-Plastic Model*, pages 2292–2301. 2012.

[SOS09] M.A. Sutton, J-J. Orteu, and H. Schreier. *Image Correlation for Shape, Motion and Deformation Measurements: Basic Concepts, Theory and Applications*. Springer, 2009.

[STBC91] M.A. Sutton, J.L. Turner, H.A. Bruck, and Z.A. Chae. Representation of the discretely sampled surface deformations for displacement and strain analysis. *Experimental Mechanics*, 31:168–177, 1991.

[TBDH10] D. Takano, P. Bésuelle, J. Desrues, and S.A. Hall. Deformation in fractured argillaceous rock under seepage flow using x-ray CT and digital image correlation. In K.A. Alshibli and A.H. Reed, editors, *Advances in Computed Tomography for Geomaterials, GeoX 2010*, pages 222–229. Wiley & Sons, 2010.

[VDMMT99] P. Vacher, S. Dumoulin, F. Morestin, and S. Mguil-Touchal. Bidimensional strain measurement using digital images. *Journal of Mechanical Engineering Science C*, 213:811–817, 1999.

[VH10] G. Viggiani and S. A Hall. Full-field measurements, a new tool for laboratory experimental geomechanics. In S.E. Burns, P.W. Mayne, and J.C. Santamarina, editors, *Proc. 4th Int. Symp. Deformation Characteristics Geomater.*, pages 3–26. IOS Press, 2010.

[VvRH04] E. Verhulp, B. van Rietbergen, and R. Huiskes. A three-dimensional digital image correlation technique for strain measurements in microstructures. *Journal of Biomechanics*, 37:1313–1320, 2004.

[Wit08] P. Withers. Strain measurement by digital image correlation. *Strain, International Journal for Experimental Mechanics*, 44:421–422, 2008.

[WLHO10] Y. Watanabe, N. Lenoir, S.A. Hall, and J Otani. Strain field measurements on sand under triaxial compression using x-ray ct data and digital image correlation. In K.A. Alshibi and A.H. Reed, editors, *Advances in Computed Tomography for Geomaterials, GeoX 2010*, pages 76–83. Wiley & Sons, 2010.

[WTB03] D.J. White, W.A. Take, and M.D. Bolton. Soil deformation measurement using particle image velocimetry (PIV) and photogrammetry. *Géotechnique*, 53:619–631, 2003.

Full-field ultrasonic measurement (ultrasonic tomography) in experimental geomechanics

Stephen A. Hall[1] **and Erika Tudisco**[2]

[1] *Division of Solid Mechanics, Lund University, Lund, Sweden and European Spallation Source AB, Lund, Sweden*
[2] *Grenoble-INP / UJF-Grenoble 1 / CNRS UMR 5521, Laboratoire 3SR, Grenoble, France and Università di Roma Tor Vergata, Rome, Italy*

Whilst ultrasonic wave measurements have been used for a relatively long time as a non-destructive method in laboratory soil and rock mechanics. However, such measurements can have significant limitations in the presence of heterogeneities, either pre-exisiting or evolving in the form of deformation structures, which are common in geomaterials. With heterogeneity, measurement of wave propagation along just a few directions in a sample can not provide a good characterisation of a material's elastic properties nor of the changes in them associated with deformation; only averages along the (limited number of) propagation paths can be described. Ultrasonic tomography provides the possibility to assess the spatial, and eventually temporal, variations in ultrasonic velocity (and attenuation) within geomechanics test specimens and thus overcome the spatial sampling limitations of standard approaches. This paper provides an overview of ultrasonic tomography and its application as a full-field measurement tool in experimental geomechanics plus provides demonstration of the power of the method with two examples.

1 Introduction

Ultrasonic wave measurements have been used for a relatively long time as a non-destructive method in laboratory soil and rock mechanics. In such studies, ultrasonic data have generally been used to provide some form of global/average measurements of the ultrasonic wave propagation velocity in test specimens to understand, for example, the small strain stiffness and elastic anisotropy evolution in soils (e.g., [VA95]; [LPN00]; [YHS05]; [SKTK05]; [ISF05]) and to assess the evolution of elastic prop-

erties and anisotropy in rocks under load (which is often attributed to micro-crack or layer opening/closing), e.g., [NS69], [KCS95], [MS07], [SK95], [Say02], [GS03], [HKFM08], [SAM+89], [SVD06], [FGS07]. In such applications the ultrasonic measurements are generally made between a small number of transducer positions (most often just two transducers placed at either end of a cylindrical specimen). Although, measurements might also include P-wave and S-wave transducers to provide greater insight into both the compression and shear moduli plus anisotropy of the material.

Problems can arise with the standard ultrasonic practises described above in the presence of heterogeneities, either pre-exisiting or evolving in the form of deformation structures (deformation in geomaterials is rarely uniformly distributed and is often localised, e.g., in to shear-bands or fractures). With heterogeneity, measurement of wave propagation along just a few directions in a sample can not provide a good characterisation of a material's elastic properties nor of the changes in them associated with deformation; only averages along the (limited number of) propagation paths can be described. As with many other measurements, a full, more pertinent material characterisation requires full-field measurement (see [VH08], for a discussion on the need for, and use of, full-field measurements in geomechanics).

Ultrasonic tomography might overcome some of the limitations of standard ultrasonic measurements, when it comes to characterising heterogeneity, as it is a "full-field" measurement method that can provide a field of ultrasonic velocity measurements over a whole sample. With this in mind, a small number of ultrasonic tomography studies of geomaterials have been presented, including for imaging of large inclusion heterogeneities in soils ([DFW05]) and of localised deformation in rocks ([FYCC92], [DY99], [TY04], [Ste07], [CHS+11]) and soils ([LFS05], [HLVL05], [HVC+07]).

This paper provides an overview of ultrasonic tomography and its application as a full-field measurement tool in experimental geomechanics. First the background theory and general method are outlined before some practical aspects are discussed and subsequently a couple of examples are provided. The reader is also referred to the many texts in the geophysical literature for a presentation of tomography methods as well as inverse theory in general (e.g., [Gub04] and, for an example oriented towards engineering, [SF05]).

2 Theory and method

Ultrasonic tomography involves inverse analysis of data measurements along many crossing propagation paths that pass through the studied medium. At the 'real-world" scale this might be between two boreholes, whereas in the laboratory the measurements would be made using ultrasonic transducers placed on the surface of the sample. The theory and data processing/analysis methods are, however, essentially the same.

In general two types of elastic-wave tomography can be considered, involving inversion of travel-time or amplitude data to provide maps of velocity and attenuation,

respectively. The theory is similar for both, involving (for ray-based tomography) "back-projection" of the measured data along "ray-paths" between pairs of emitting and receiving transducers, such that the recorded travel-times/amplitudes are assigned proportionally to the grid cells of the inversion model traversed by each ray with a weighting given by the relative path-lengths within the respective cells. The combination of many such measurements, for a set of intersecting ray-paths between emitting and receiving transducers placed at different locations over the sample, allows a map of the propagation velocity (or attenuation) in the sample to be determined (in a least-squares sense) by inversion. Therefore ultrasonic tomography can provide access to the spatial variations of the elastic properties in a test sample and, potentially, their evolution in time.

This section outlines the background theory and methodology for ray-based ultrasonic travel-time tomography before a brief discussion on extensions to such methods and the presentation of two illustrative examples.

2.1 Travel time tomography

As discussed above, travel time tomography involves the inversion of travel time data from many intersecting paths through a medium to define a velocity model over the imaged area. The first requirement in such a procedure is to have some model that can describe how the ultrasonic energy traverses the study material, in order to correctly attribute the variations in the measurements to specific regions in space. The most common approach to achieve this is to use raypaths to define the trajectory of the ultrasonic pulses through the study material. The representation of the wave propagation using ray paths is based on an assumption that the data are of high frequency, i.e., the wavelength is at least several times smaller than the spatial variations of the velocity model. The following presentation of ultrasonic tomography utilises this approach, but some of the short-comings and possible solutions are discussed in a subsequent section.

In the context of a ray-based travel-time tomography procedure, the traveltime measurements, t, for a given source-receiver pair, are connected to the model, i.e., the velocity field, v, via the travel time integral with respect to the distance, l, along the raypath connecting the source and receiver;

$$t = \int_{raypath} \frac{1}{v(x,z)} dl. \tag{1}$$

The term $v(x,z)^{-1}$, i.e., the inverse of the velocity, is usually denoted as the *slowness*, $s = v(x,z)^{-1}$.

The representation in (1) supposes a continuous velocity field (which is generally the reality), but in order to construct a system of equations for an inversion procedure, it is necessary to define a discretised representation of the velocity field consisting

of elements of constant velocity. This model discretisation normally involves partitioning the model space (i.e., the area over which the velocity model is to be defined and which is illuminated by the recorded data) into a regular grid of, usually square, cells (although the grid need not be defined as such, this just facilitates the inversion procedure).

Once a model grid is defined, the travel time equations (1) for each raypath between all sources and receivers can be written as the sum of the travel time within each grid cell through which the rays pass; i.e., the travel time integral reduces to a summation of weighted slownesses, where the weight is the segment length of the rays in each cell. Therefore, if the segment length of the ith ray in the jth cell, with slowness s_j, is denoted l_{ij}, then the travel time, t_i, is given as,

$$t_i = \sum_j l_{ij} s_j. \tag{2}$$

Equation 2 can be written in matrix form as $\mathbf{d} = \mathbf{Am}$, where $\mathbf{d}$ is the data vector containing the travel times, $\mathbf{A}$ is the MxN raypath segment matrix, with element values equal to l_{ij}, and $\mathbf{m}$ is the model vector containing the slowness values for each grid cell. (As the rays will not pass through all of the cells of the velocity grid, many of the elements of $\mathbf{A}$ are zero.) The objective of the tomographic inversion is now to find a solution, $\mathbf{m}$, to this system of equations, that minimises the error between the data, $\mathbf{d}$, and the modelled times given by $\mathbf{Am}$.

If the number of measurements (travel times) is equal to the number of cells in the velocity model, then $\mathbf{A}$ will be square and so a solution to the linear set of equations can be found by inverting $\mathbf{A}$, i.e., $\mathbf{m} = \mathbf{A^{-1}d}$. However, in most cases there are many more equations than unknowns (i.e., more data than cells in the velocity model) so a least-squares solution is sought using $\mathbf{m} = (\mathbf{A^T A})^{-1}\mathbf{A^T d}$ (see Appendix). Unfortunately such a solution usually gives a poor result, in terms of its representation of a physically realistic velocity field. In fact, whilst the inverse problem appears to be over-determined, the number of independent data are less than it appears (as discussed later) plus, due to the sparsity of $\mathbf{A}$, the system of equations is ill conditioned. Therefore, a damped or regularised solution method must be used based on a perturbation from some initial guess of the expected velocity field.

If an initial guess of the slowness model is defined then $\mathbf{d}$ and $\mathbf{m}$ can be replaced by $\delta\mathbf{d}$ and $\delta\mathbf{m}$ the differences of the measured data and the predicted data based on the initial guess velocity model. Therefore the set of equations is rewritten as,

$$\delta\mathbf{m} = (\mathbf{A^T A} + \epsilon\mathbf{I})^{-1}\mathbf{A^T}\delta\mathbf{d} = \mathbf{m} - \mathbf{m_0}, \tag{3}$$

where $\delta\mathbf{d} = \mathbf{d} - \mathbf{A}(\mathbf{m_0})$ and the damping is given by $\epsilon\mathbf{I}$, for $\mathbf{I}$ the identity matrix and ϵ some small positive scalar.

If the starting model is very close to the actual model so that the travel time equations can be considered to be linear (see below), then $\mathbf{m} + \delta\mathbf{m}$, from equation (3), is the

final answer. However, this is not the normal case and it is usually necessary to iterate through several passes of the inversion using the new model as the starting model at each iteration with an updated model produced each time. This procedure is repeated until convergence in the model is, in some way, deemed to have been reached.

An additional complication arises from the fact that the propagation paths of the ultrasonic waves through the medium, defined here by the raypaths, depend on the velocity field. In the above, the system of equations has been written in a linear form, however in reality this is a non-linear problem as the raypaths are generally unknown *a priori* because they depend on the (unknown) model, therefore the problem has to be linearised (see Appendix). In homogeneous media rays will be straight paths from source to receiver, but in inhomogeneous media the rays will follow some curved trajectory. In general, the initial guess velocity field is homogeneous, therefore, at the first iteration, the linearisation is given by straight-ray paths, but since the resultant "inverted" field will (probably) be heterogeneous, it is generally necessary to redefine the (non-straight) raypaths at each iteration. This is called relinearisation and is based on the premise that a small change in the velocity model does not change the traveltimes (Fermat's principle).

2.1.1 Iterative inversion procedure

A basic "recipe" for the inversion procedure can be defined as follows:

1. Define initial guess, $\mathbf{m_0}$ and damping parameter ϵ.
2. Calculate $\delta\mathbf{d} = \mathbf{d} - \mathbf{A}\mathbf{m_0}$ and $\mathbf{A} = f(\mathbf{m_0})$ ((re)linearisation step).
3. Invert for $\delta\mathbf{m} = (\mathbf{A^T}\mathbf{A} + \epsilon\mathbf{I})^{-1}\mathbf{A^T}\delta\mathbf{d}$.
4. define $\mathbf{m} = \mathbf{m_0} + \delta\mathbf{m}$.
5. Iterate over steps 2-4, replacing the initial guess, $\mathbf{m_0}$ by the updated model vector, $\mathbf{m}$, until a stable solution is found.

In such a procedure, the initial guess velocity field is generally taken to be homogeneous (e.g., the average of all the ray-path velocities), but if other information can be used to define a model that is closer to the actual field, this should aid the inversion procedure. If the velocity field is not homogenous, as will be the case after the first iteration from an homogeneous model, then the definition of $\mathbf{A} = f(\mathbf{m_0})$ will require some method to trace the raypaths through the new velocity model; strategies for this are briefly outlined in the following.

2.1.2 Ray-tracing

Key to the above outlined procedures is the knowledge of the ray-paths for each source-receiver measurement through the model. For an homogeneous material the raypaths will be straight and therefore the raytracing is trivial, but then so will be the

inversion. If the velocity variations are small, a reasonable approximation can still be achieved with straight rays (which means that no relinearisation is necessary), although with some loss in spatial resolution of the result. However, in general, it is necessary to numerically determine the trajectories of each ray through the velocity model at each relinearisation stage in the iterative procedure described above.

Ray-tracing can be performed in a number of ways and there is extensive literature on the subject (a good discussion of the options can also be found in [SF05]; pages 284-290). There are three main strategies that can be adopted, other than straight rays: bending rays, curved rays and (Eikonal or Huygens) finite-difference travel time map minima tracing. These are all based on the fulfilment of Fermat's principle of minimum travel time. The first involves fixing the source and receiver position and perturbing an initial ray path until a travel time minimum is achieved (this can be quite computationally intensive and may converge into a local, rather than global, minimum, but will always find a solution). The second, involves a ray-shooting approach where the source position is fixed and different take-off angles are tested, and refined, until the ray arrives at the target receiver position (this approach will not always succeed in finding a solution and the result and efficiency often depends on the closeness of the initial guess take-off angle to the actual angle; the method is however relatively easy to implement). Another approach to ray-tracing is to use finite difference approximations of the Eikonal equation (e.g., [Vid88]; [AO93]) or Huygen's principle (e.g., [SF01])to produce travel time maps to each source and receiver from all points in the medium. The summation of the travel time maps for each source-receiver pair allows the minimum travel time path (the ray path) to be easily identified (such approaches are quite computationally expensive, but are more robust than the other ray-tracing approaches, especially in the presence of large velocity gradients).

2.1.3 Regularisation and damping

In the above discussion it has been stated that damping is generally necessary in the tomographic inversion. However, damping is normally only needed in inverse problems that are under-determined (i.e., there are less data than unknowns). In ultrasonic tomography, this is does not generally appear to be the case. However, having a lot of measurements (ray paths) does not necessarily imply that the problem is over-determined (more data than unknowns) as many of the ray-paths cover similar parts of the model and thus provide much the same information, therefore the number of independent data are reduced. Furthermore different parts of the model can have very different illuminations (density of rays traversing each grid cell), with some parts having very low data coverage. Therefore, damping or regularisation are generally required.

The damping described in equation (3) controls the amount of deviation of the inverted velocity model from the prior model and is the same for each cell. Different strategies can be adopted with the damping, e.g., to have a damping that is linked to the ray density of each cell so that a cell with greater data coverage is less damped

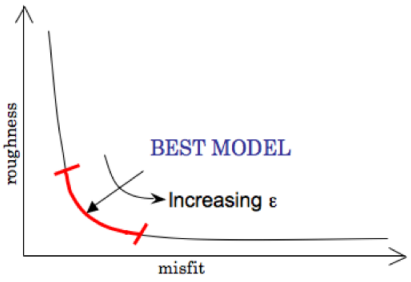

Figure 1: Schematic of a trade-off curve where the model misfit is plotted against the model roughness for different values of the damping/regularisation parameter ϵ.

than one with little data constraint. Alternatively, regularisation can be used to apply a spatial constraint on the model to, avoid non-physical local fluctuations in the velocity field. One possible strategy is the minimisation of the second derivatives of the velocity model, which can be achieved by replacing the identity matrix in (3) by $\mathbf{R^T R}$, where $\mathbf{R}$ is a "regularisation" matrix as described in [SF05](pages 213-215). An alternative approach is provided by [PC92] using an A-matrix "augmented" to contain the regularisation matrices.

When using regularisation or damping, there is a parameter, here denoted ϵ, that controls the amount of damping or regularisation in the model. The definition of this parameter is, however, not clear. Larger ϵ implies more damping (i.e., a model that is closer to the initial guess) or more regularisation (i.e., a smoother model) and in both cases this will generally mean a larger misfit in the inversion. To choose the best value for ϵ the concept of the trade-off curve is often invoked, this is a curve that plots the misfit of the model against the roughness of the model as a function of the smoothing parameter, as in Figure 1. The best solution (i.e., the best compromise between model roughness and model misfit) is at the knee of this trade-off curve (although this can be difficult to define, as a clear "knee" may not exist in the curve).

2.1.4 Anisotropy

Until now the discussion has considered just isotropic inversion, as this is the simplest case. However, anisotropy is common in geomaterials and so including anisotropic velocities in an inversion could improve the resolution of the velocity field as well as providing greater insight into the material properties. [CP92] and [PC92] provided a possible means to achieve this. However, this is not discussed in detail herein, but is of clear interest for future evolution of the method. (It is noted that the inclusion of anisotropy in the model vastly increases the number of model parameters and requires a greater illumination, particularly angular illumination, of the material.)

2.2 Limitations of ray-based approaches and beyond ray-based tomography

The use of ray theory in tomography is based on an assumption that the wavelength is at least several times smaller than the spatial variations of the velocity field. For many of the cases of interest in laboratory geomechanics, this will not be a fully valid assumption. Therefore, whilst reasonable results can often be achieved using ray-based inversion, improvements may be possible using approaches that are not limited by the high-frequency approximation of ray-based methods.

[SF05] provide a short discussion on the validity and wavelength/resolution limitations of ray-tracing stating that the key limitation arises from assumptions made in the use of the Eikonal equation, which is the basis of ray-tracing, as an approximation to the wave equation (a more thorough discussion can be found in [PW93]). This assumption breaks down for velocity changes occurring over distances smaller than a wavelength and so features of dimensions smaller then the first Fresnel zone would not be well imaged with ray-based methods. [PW93] thus give the dimension of the smallest features that may be imaged as being of the order of $\sqrt{L\lambda}$, where L is the propagation distance and λ the wavelength, although they also state that this might be a conservative limitation. However, [Sch96] states that, for a crosswell-type geometry (as used in the later examples), this resolution is just the vertical resolution and the horizontal resolution is also constrained by the aperture of the imaging, i.e., the angular illumination between the source and receiver arrays; the horizontal resolution is thus given as $(4x_0/l)\sqrt{3x_0\lambda/4}$, where x_0 is half the distance between the two transducer arrays and l the length of the arrays.

Alternatives to the use of ray-base tomography have been proposed that do not consider the propagation of the energy to be within an infinitely small volume (the ray) and thus avoid some of the high frequency assumptions. Of these, the simplest concept is the use of "wavepaths" (e.g., [Woo92]; [VM93]), which is based on the idea that, whilst ray-based approaches attempt to map all sensitivity onto the infinitely thin rays through the medium, wavepath approaches consider that the traveltime is sensitive to changes in the Fresnel zone volume, which is more physically reasonable. Therefore, instead of using rays to fill out the $\mathbf{A}$ matrix the first Fresnel zone around the ray is used over which the travel time residuals are smeared with weighting based on the wavepath coverage (an area instead of a line) of each traversed cell. These Fresnel volume wavepaths can be calculated, in a similar way to described above for Eikonal-solver based ray-tracing, by using a finite difference solution to the Eikonal equation to produce travel time maps to the sources and receivers, which, when added together, can be used to define the Fresnel volume as described by [VS94]. A more complete version of the wavepath concept is provided by the use of full sensitivity kernels to describe the sensitivity of each travel time measurement to any perturbation in the velocity field, e.g. [DHVDH05].

Finally, the most well resolved and complete tomographic approach that has recently been gaining in popularity (in part due to the now available computer processing

power) are "full waveform inversion" (FWI) approaches. Such approaches attempt to consider the full information contained in the waveform data (or at least a windowed part of it) without reducing it down to a set of travel time or amplitude values. In such approaches the waveform data are compared to a full numerical simulation of the wave propagation through the study medium and the inversion proceeds by comparing the simulated and real waveform data and updating the velocity model to minimise the misfit between the two. A good summary of FWI and key references can be found in [VO88].

3 Ultrasonic tomography data acquisition

3.0.1 Input data

The input data to travel time tomography are the arrival times of the ultrasonic signal from each source to each receiver. These arrival times must be determined from the recorded time series data at each receiver (which is usually time-synchronised with the source pulse); see Figures 2b and 3b for examples of such data. In general it is desirable to pick the "first arrival" time, which corresponds to the moment at which the first energy arrives at a receiver, however this can often be difficult to determine consistently between receivers, even using automatic picking procedures such as implementations of Aikake's Information Criterion, for example. Therefore, the time to the first peak or trough might be used if there is no velocity dispersion (note that the travel times and measurement system should be calibrated against measurements on materials of known velocity). It is also quite common to use cross-correlation of Fourier-shift-theory approaches to track the arrivals from one source-receiver pair to the next; this assumes only small changes in the waveforms and so is not always completely reliable.

An approach that can lead to more robust arrival picking through increased signal:noise and separation of multiple arrivals is "double-beamforming". This approach is a form of optimally-oriented local data stacking technique that can enhance the waveform signals and thus aid the data picking, which is being investigated for experimental geomechanics applications in context of the PhD thesis of E. Tudisco (publication expected in 2013).

3.0.2 Illumination

A key data constraint on the viability of tomographic inversion is that there is sufficient illumination of the study region by the ultrasonic data. In the context of ray-theory, this relates to a sufficient ray coverage in each cell of the model, which requires simply that sufficient measurements are made over a range of source and receiver positions. Furthermore, it is desirable to have uniform coverage of the model and isotropic illumination (i.e., sources and receivers placed all around the study area). Uniform data

coverage is difficult to achieve, and in fact will also be dictated by the velocity field in the material. A non-isotropic coverage, i.e., data acquired over a limited range of illumination angles, will generally result in some smearing in the directions of the better illumination. The best data coverage can be achieved, for 2D tomography, with cylindrical samples and a "fan" acquisition for sources and receivers placed all around the specimen. However, experimental and geometrical constraints normally dictate the possible acquisition. In the two examples given later a "cross-hole" type geometry is used, which places sources and receivers on opposing sides of the specimen. The resultant inversions show some clear artefacts relating to the ray coverage, which might have been reduced if it had also been possible to use transducers placed at the ends of the specimens. See, for example, [SF05](pages 282-284) for further discussion on these aspects.

4 A couple of examples

In the following, ultrasonic tomography results are presented for two examples, the first for a stiff clay and the second for a sandstone, both exhibiting localised deformation. In the first example, for the stiff clay, a simple acquisition procedure was performed involving two transducers placed accurately at a number of different positions along the side-walls of the sample (see [HVC$^+$07]) to yield a number of intersecting raypaths (see Figure 2a). In the second example, for the sandstone, the acquisition was made using two arrays of 64 transducer elements yielding 64x64 intersecting raypaths in a single acquisition (see Figure 3), which provides an unprecedented (for geomaterials) data coverage for the ultrasonic tomography.

4.0.3 Ultrasonic tomography to image localised deformation in a stiff clay

Figure 2 shows an example, from [HVC$^+$07], of the application of ultrasonic tomography to a dry, tabular sample of stiff clay (Beaucaire marl), which had been deformed under plane strain compression resulting in the evolution of a single localised shear-band feature. In this case, the travel-time data used in the tomographic inversion were acquired using just two transducers placed on opposite sides of the sample at different offset positions so as to achieve measurements along a series of crossing ray-paths (as indicated in Figure 2a). The map of ultrasonic velocities from a ray-based tomographic inversion of these data is shown in Figure 2c and the localised shear band shows up as a zone of increased velocities, which is consistent with the expected compaction associated with the strain localisation for this test sample. Some variability is also seen in the band, which may represent varying degrees of compaction. However, these results are potentially affected by artefacts of the tomography technique, for example the band offset from the real position in space (marked by the dashed line) and the high velocity zones in the corners at the ends of the band.

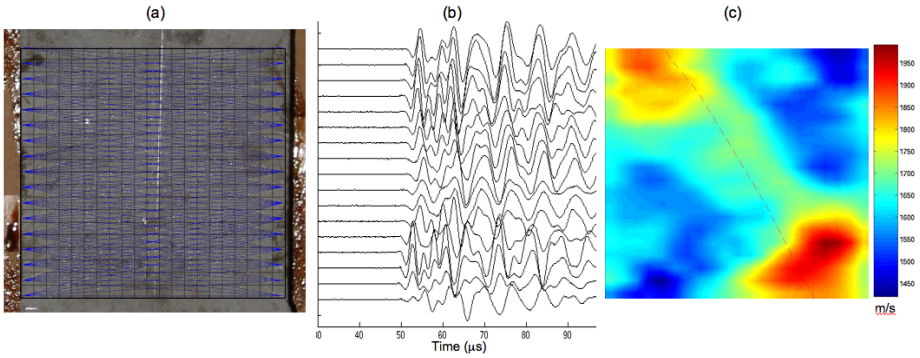

Figure 2: Ultrasonic tomography analysis on a parallelpipedic sample of Beaucaire Marl (stiff clay) that had been deformed under plane-strain conditions such that a localised (shear) deformation band developed diagonally across the sample (from top left to bottom right in (a). (a) Photograph of the front face of the sample with the tomography inversion grid and (straight) raypaths between each source and receiver over which travel-times were determined. (b) Example of the data acquired for each source-receiver pair, in this case just for the raypaths for transducer positions directly opposite each other across the sample. (c) Final ultrasonic velocity map from the 2D tomography analysis, which shows a band of higher (increased) velocities that roughly coincides with the trace of the localised deformation zone indicated by the dotted line.

4.0.4 Ultrasonic tomography to image localised deformation in a sandstone

As a second example of laboratory ultrasonic tomography, results are presented for a "post-mortem" analysis of a Vosges sandstone specimen deformed under triaxial compression at 20 MPa (from the work of [Res08] and [Cha11]; the latter reference contains further examples of the analysis of same rock deformed at different confining pressures). The studied specimen was a cylinder with two opposite flattened faces to provide contact surfaces for the ultrasonic transducer arrays (see Figure 3). Notches were made in these flattened faces to enforce the expected shear bands to develop in the middle of the sample and in the direction perpendicular to the velocity measurements. After the triaxial compression test the sample exhibited an inclined shear-band between the two notches (visible at the surface by eye and within the sample in x-ray tomography images, the latter indicating a zone of increased density).

Ultrasonic measurements were made before and after the triaxial loading using two arrays of 64 piezoelectric transducer elements and a source/receiver recording system with 64 independent A/D channels (courtesy of P. Roux at Laboratoire ISTERRE, Grenoble), which provide data over 64x64 intersecting raypaths in a single, fast measurement. The 64 transducer elements of each array were contained within single casings (see Figure 3) and distributed over a height of 48 mm at a spacing of .75 mm; each element has a width of 20 mm. This gives in effect a 2D array that is well focussed in the direction perpendicular to the face in contact with the specimen, but divergent in the plane parallel to this direction. Therefore a large range of propagation directions can be imaged in one plane with a good signal energy, but an assumption that the medium is "2D" perpendicular to the contact face has to be made.

Figure 3 shows example waveforms for propagation between transducer elements directly opposite each other across the sample, which might be compared to the data presented in Figure 2b; in this case, the data acquisition is much denser than in the previous example. If the sample were homogeneous this "plane wavefront" would be expected to show equal arrival times and similar waveforms for each recording. However, some variability can be seen in the wavefront, including in the arrival times; in particular, later arrivals are observed around the two positions that correspond to the notches, which indicates reduced velocities in these areas. The recorded full-waveform data for all the source-receiver pairs were analysed to provide first-arrival times and inverted using ray-based travel-time tomography to yield a 2D velocity field for the given specimen.

Figure 4 shows the inverted velocity field for specimen. This velocity field, as with others for similar tests, indicates the resolution of the localised shear-band as a zone of reduced velocity. X-ray tomography images of this sample indicate that these zones are more dense than the surrounding less-deformed rock, which might suggest that higher ultrasonic velocities would be expected (due to reduced porosity). However, the reduced velocities seem to indicate that the damage phenomena likely involved the creation of a high density of new cracks/contacts, possibly associated with micro-cracking through destructuration (cement breakage) - grain crushing is unlikely at this

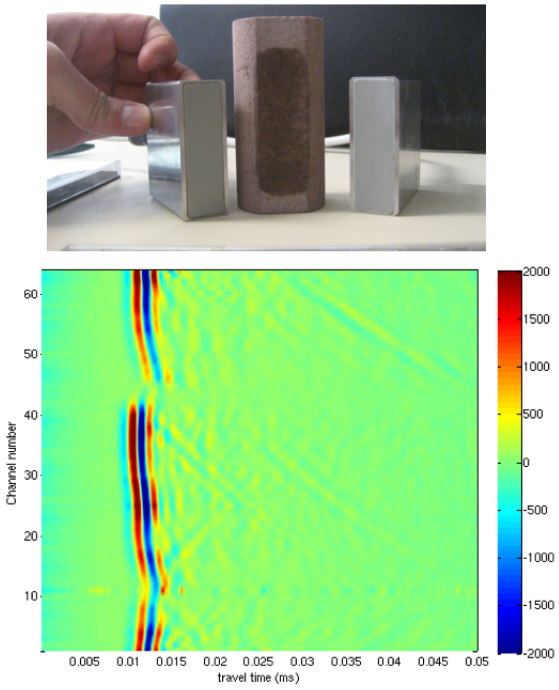

Figure 3: Upper image: Example of the sandstone specimens used in the study of ultrasonic imaging of localised deformation (the specimen is about 80 mm high) and the ultrasonic transducer arrays used for the measurements (each one has 64 transducer elements distributed over the height at 0.75 mm vertical spacing). Lower image: Example of the data acquired for each source-receiver pair (for the raypaths for transducer positions directly opposite each other across the sample). These data are equivalent to those in Figure 2b, but with waveforms plotted in colour corresponding to the amplitude. The vertical positions of the two "notches" (see main text) correspond to the lower amplitude zones and variations in velocity can be seen in the arrival time differences.

level of confining pressure -, and the porosity reduction effect is small. Whilst the low-velocity zone in Figure 4, which corresponds to the localised deformation band, appears to be well resolved, it is in fact much wider than the band identified on the corresponding x-ray tomography images. On the one hand this could indicate the greater sensitivity of the elastic waves to the damage processes (only quite strong density changes can be resolved in the x-ray images) and so damage away from the concentrated deformation zone in the core of the shear band might also be detected. However, there is also the spatial resolution of the ultrasonic tomography that should be considered. In this case the dominant recorded frequency was around 800 kHz, which for a velocity of 1800 m/s corresponds to a wavelength of about 2.25 mm ($\lambda = v/f$: wavelength = velocity/frequency). Based on the resolution limits of ray-based tomography (given earlier) this would give a resolution in the centre of the specimen of about 6 mm, which is only slightly larger than the "expected" shear-band width of around 5 mm, but, as discussed, this is possibly a conservative estimate. Therefore further investigation is required to better interpret such results in terms of potential smearing versus the good sensitivity of the velocity measurements to even small degrees of damage.

5 Conclusions

Ultrasonic tomography provides the possibility to assess the spatial, and eventually temporal, variations in ultrasonic velocity (and attenuation) within geomechanics test specimens. This paper has outlined different theoretical and practical aspects of ultrasonic tomography plus has demonstrated the power of the method with two examples. However, as a tool for experimental geomechanics, ultrasonic tomography is still in its infancy, but there is good potential for future development. Good results have been presented in [CHS$^+$11] and [Cha11], but questions remain about the spatial resolution and the presence of artefacts in the velocity images. On-going work aims to increase the spatial resolution and reduce the artefacts, including through the use of sensitivity kernels and full-waveform inversion techniques in the context of the PhD thesis of E. Tudisco (publication expected in 2013). Furthermore, this work is considering the use of ultrasonic tomography during loading and differential tomography to study the evolution of the velocities, which might be combined with full-field strain data from digital image correlation to provide much greater insight into the mechanics of the studied materials. Other advances that would be of significant interest for experimental geomechanics are the inclusion of anisotropy in the inversion and the use of both compressional (P) and shear (S) wave data; together such data could provide a quite complete characterisation of the elastic properties (and their evolution) in a material. The other key remaining challenges relate to the interpretation of the data in terms of the underlying mechanics, which must involve integration of different (full-field) techniques that are sensitive to different aspects of the mechanics, e.g., the combination with digital image correlation.

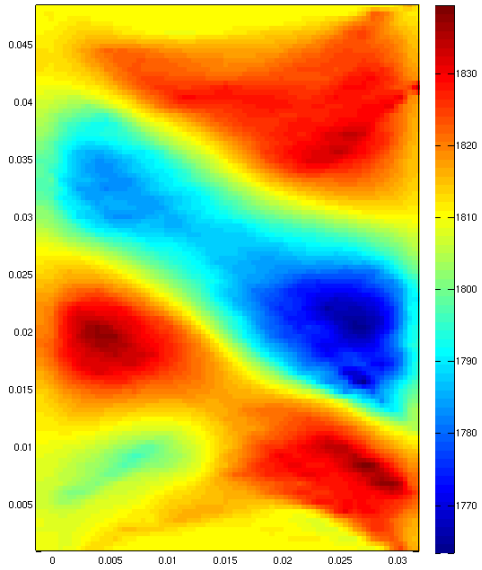

Figure 4: Result of the 2D ultrasonic velocity tomography over the central zone of a sample of a Vosges sandstone deformed under 20 MPa confining pressure (colourbar indicates velocities in m/s and the distances on the x and y axes are in m). A band of low velocities is seen crossing diagonally across the sample corresponding to the location of the localised shear deformation feature that developed during loading between the notches (the notches are at the edges of the specimen near the upper and lower extremities of the low velocity band).

References

[AO93] D.F. Aldridge and D.W. Oldenberg. Two dimensional tomographic inversion with finite difference traveltimes. *Journal of Seismic Exploration*, 2:257–274, 1993.

[Cha11] E.-M. Charalampidou. *Experimental Study of Localised Deformation in Porous Sandstones*. PhD thesis, Heriot Watt University, Edinburgh and Université de Grenoble, Grenoble, 2011.

[CHS+11] E. M. Charalampidou, S. A. Hall, S. Stanchits, H. Lewis, and G. Viggiani. Characterization of shear and compaction bands in a porous sandstone deformed under triaxial compression. *Tectonophysics*, 503:8–17, 2011.

[CP92] C.H. Chapman and R.G. Pratt. Traveltime tomography in anisotropic media – II. Theory. *Geophysical Journal International*, 109, 1992.

[DFW05] M. Daigle, D. Fratta, and L.B. Wang. Ultrasonic and x-ray tomographic imaging of highly contrasting inclusions in concrete specimens *geofrontier 2005 conference*, Austin, TX, 2005.

[DHVDH05] M. V. De Hoop and R. D. Van Der Hilst. On sensitivity kernels for 'wave-equation' transmission tomography. *Geophysical Journal International*, 160:621–633, 2005.

[DY99] W. Debski and R.P. Young. Enhanced velocity tomography: Practical method of combining velocity and attenuation parameters. *Geophysical Research Letters*, 26:3253–3256, 1999.

[FGS07] J. Fortin, Y. Gueguen, and A. Schubnel. Effects of pore collapse and grain crushing on ultrasonic velocities and v_p/v_s. *Journal of Geophysical Research*, 112:B08207, 2007.

[FYCC92] D. Falls, R.P. Young, S.R. Carlson, and T. Chow. Ultrasonic tomography and acoustic emission in hydraulically fractured lac du bonnet grey granite. *Journal of Geophysical Research*, 97:6867–6884, 1992.

[GS03] Y. Gueguen and A. Schubnel. Elastic wave velocities and permeability of cracked rocks. *Tectonophysics*, 370:163–176, 2003.

[Gub04] D. Gubbins. *Time Series Analysis and Inverse Theory for Geophysicists*. Cambridge University Press, 2004.

[HKFM08] S.A. Hall, J-M. Kendall, Q. Fisher, and J. Maddock. Crack density tensor inversion for analysis of changes in rock frame architecture. *Geophysics Journal International*, 173:577–592, 2008.

[HLVL05] S.A. Hall, H. Lewis, G. Viggiani, and N. Lenoir. Damage assessment in geomaterials using elastic waves. In *Proceedings 7th International*

Workshop on Bifurcation, Instabilities and Degradation in Geomechanics, Chania, Greece, 2005.

[HVC+07] S.A. Hall, G. Viggiani, E. Charalampidou, P. Bésuelle, and C. Rousseau. Caractérisation de léndommagement localisé dans les géomatériaux ł'aide des ondes ultrasonores en conditions de laboratoire. In *Proceedings 18ème Congrès Français de Mécanique*, pages 163–176, 2007.

[ISF05] M.A. Ismail, S.S. Sharma, and M. Fahey. A small true triaxial apparatus with wave velocity measurement. *Geotechnical Testing Journal*, 28:1–10, 2005.

[KCS95] M. King, N. Chaudhry, and A. Shakeel. Experimental ultrasonic velocities and permeability for sandstones with aligned cracks. *International Journal of Rock Mechanics and Mining Science*, 32:155–163, 1995.

[LFS05] J.S. Lee, A.L. Fernandez, and J.C. Santamarina. S-wave velocity tomography: Small-scale laboratory application. *Geotechnical Testing Journal*, 28:1–9, 2005.

[LPN00] M. L. Lings, D. S. Pennington, and D.F.T. Nash. Anisotropic stiffness parameters and their measurement in a stiff clay. *Géotechnique*, 50:109–125, 2000.

[MS07] C. MacBeth and H. Schuett. The stress dependent elastic properties of thermally induced microfractures in aeolian rotliegend sandstone. *Geophysical Prospecting*, 55:323–332, 2007.

[NS69] A. Nur and G. Simmons. Stress-induced velocity anisotropy in rock: an experimental study. *Journal of Geophysical Research*, 74:6667–6674, 1969.

[PC92] R.G. Pratt and C.H. Chapman. Traveltime tomography in anisotropic media – II. Application. *Geophysical Journal International*, 109, 1992.

[PW93] Williamson P.R. and M.H. Worthington. Resolution limits in ray tomography due to wave behavior: Numerical experiments. *Geophysics*, 58:727–735, 1993.

[Res08] F.L. Restaino. Characterizing strain localization in sandstone by full-field measurements, MSc thesis, Université Joseph Fourier - Grenoble INP, 2008.

[SAM+89] P.R. Sammonds, M.R. Ayling, P.G. Meredith, S.A.F. Murrell, and C. Jones. A laboratory investigation of acoustic emission and elastic wave velocity changes during rock failure under triaxial stresses. In V. Maury and D. Fourmaintraux, editors, *Rock at great depth*, pages 233–240. A.A. Balkema, 1989.

[Say02] C. Sayers. Stress-dependent elastic anisotropy of sandstones. *Geophysical Prospecting*, 50:85–95, 2002.

[Sch96] G.T. Schuster. Resolution limits for crosswell migration and traveltime tomography. *Geophysical Journal International*, 127:427–440, 1996.

[SF01] P. Sava and S. Fomel. 3-D traveltime computation using Huygens wavefront tracing. *Geophysics*, 66:883–889, 2001.

[SF05] J.C. Santamarina and D. Fratta. *Introduction to Discrete Signals and Inverse Problems in Civil Engineering*. ASCE Press, 2005.

[SK95] C.M. Sayers and M. Kachanov. Microcrack-induced elastic wave anisotropy of brittle rocks. *Journal of Geophysical Research*, 100:4149–4156, 1995.

[SKTK05] S. Shibuya, J. Koseki, and T. T. Kawaguchi. Recent developments in deformation and strength testing of geomaterials. In Di Benedetto et al., editor, *Deformation Characteristics of Geomaterials*, pages 3–28. Taylor & Francis Group, 2005.

[Ste07] D.F. Stevens. Stress redistribution in Berea sandstone samples using acoustic emission tomography in the laboratory, MSc thesis, Virginia Polytechnic Institute and State University, 2007.

[SVD06] S. Stanchits, S. Vinciguerra, and G. Dresen. Ultrasonic velocities, acoustic emission characteristics and crack damage of basalt and granite. *Pure and Applied Geophysics*, 5–6:975–994, 2006.

[TY04] Scott T.E. and Abousleiman Y. Acoustical imaging and mechanical properties of soft rock and marine sediments, *final technical report #15302*, Department of Energy (DOE, award number: DEFC26-01BC15302), 2004.

[VA95] G. Viggiani and J.H. Atkinson. Stiffness of fine grained soil at very small strains. *Géotechnique*, 45:249–265, 1995.

[VH08] G. Viggiani and S. A Hall. Full-field measurements, a new tool for laboratory experimental geomechanics. In S.E. Burns, P.W. Mayne, and J.C. Santamarina, editors, *Proc. 4th Int. Symp. Deformation Characteristics Geomater.*, pages 3–26. IOS Press, 2008.

[Vid88] J.E. Vidale. Finite-difference calculation of traveltimes. *Bulletin of the Seismological Society of America*, 78:2062–2076, 1988.

[VM93] D.W. Vasco and E.L. Majer. Wavepath traveltime tomography. *Geophysical Journal International*, 115:1055–1069, 1993.

[VO88] J. Virieux and S. Operto. An overview of full-waveform inversion in exploration geophysics. *Geophysics*, 74:WCC127–WCC152, 1988.

[VS94] M. Van Scaack. Calculating Fresnel zones for crosswell tomography. *Stanford Tomography Project*, 5:paper C, 1994.

[Woo92] M.J. Woodward. Wave-equation tomography. *Geophysics*, 57:15–26, 1992.

[YHS05] S. Yamashita, T. Hori, and T. Suzuki. Effects of fabric anisotropy and stress condition on small strain stiffness of sands. In Di Benedetto et al., editor, *Deformation Characteristics of Geomaterials*, pages 187–194. Taylor & Francis Group, 2005.

A Appendix: linear and linearised inverse theory

Linear inverse theory is a method for finding a model given some data and a set of linear equations relating the data to the model parameters, which in matrix form would be,

$$\mathbf{d} = \mathbf{A}\mathbf{m}, \tag{4}$$

where $\mathbf{d} = \{y_1^{obs}, y_2^{obs}, ..., y_N^{obs}\}$ are the data, $\mathbf{m}$ is a vector containing the model variables (e.g., $\mathbf{m} = (a, b)^T$, for a straight line) and $\mathbf{A}$ is some matrix relating the two (this can be thought of as the matrix describing the "physics" of the problem). For the simple, even-determined, case of a straight-line and two data points ($\mathbf{d} = \{y_1, y_2\}$, $\mathbf{x} = \{x_1, x_2\}$ and $\mathbf{m} = \{a, b\}$), Equation (4) would be written

$$\begin{pmatrix} y_1 \\ y_2 \end{pmatrix} = \begin{pmatrix} x_1 & 1 \\ x_2 & 1 \end{pmatrix} \begin{pmatrix} a \\ b \end{pmatrix} \tag{5}$$

In this case it is straight-forward to determine the inverse problem, $\mathbf{m} = \mathbf{A^{-1}}\mathbf{d}$;

$$\begin{pmatrix} a \\ b \end{pmatrix} = \frac{1}{x_1 - x_2} \begin{pmatrix} 1 & -1 \\ -x_2 & x_1 \end{pmatrix} \begin{pmatrix} y_1 \\ y_2 \end{pmatrix}. \tag{6}$$

Thus from the above

$$a = \frac{y_2 - y_1}{x_2 - x_1}, b = \frac{x_2 y_1 - x_1 y_2}{x_2 - x_1}. \tag{7}$$

If there are more data (i.e., if the problem is over-determined) then the same procedure can be followed, e.g., for $\mathbf{y} = y_1, y_2, y_3$ such that (4) would be written

$$\begin{pmatrix} y_1 \\ y_2 \\ y_3 \end{pmatrix} = \begin{pmatrix} x_1 & 1 \\ x_2 & 1 \\ x_3 & 1 \end{pmatrix} \begin{pmatrix} a \\ b \end{pmatrix}. \tag{8}$$

In this case there is no solution as $\mathbf{A}^{-1}$ does not exist. Instead the aim is to find the "best-fit" model, i.e., to minimise the "prediction error of the solution" in a *least squares* sense. The prediction error is defined as

$$r_i = y_i^{obs} - y_i^{model}(m), \tag{9}$$

so

$$\mathbf{r} = \mathbf{d} - \mathbf{Am}. \tag{10}$$

The least squares error is

$$\phi(\mathbf{m}) = \sum_{\mathbf{N}} (\mathbf{y_i^{obs}} - \mathbf{y_i^{model}}(\mathbf{m}))^{\mathbf{2}} = \mathbf{r^T r} = (\mathbf{d} - \mathbf{Am})^{\mathbf{T}}(\mathbf{d} - \mathbf{Am}), \tag{11}$$

which is to be minimised. Thus the least-squares solution is given by the model vector $\mathbf{m}$ that gives a zero gradient of $\phi(\mathbf{m})$,

$$\nabla\phi(\mathbf{m}) = -\mathbf{A^T}(\mathbf{d} - \mathbf{Am}) = \mathbf{0}. \tag{12}$$

Therefore the least squares solution is given by

$$\mathbf{m} = (\mathbf{A^T A})^{-\mathbf{1}}(\mathbf{A^T d}). \tag{13}$$

Here the *normal equations* can be defined: $(\mathbf{A}^T\mathbf{A})\mathbf{m} = (\mathbf{A^T d})$.

A.1 Weighted least squares solution

If there is some understanding of the uncertainty of each measurement it is important to include this in the inverse solution. This can be achieved by "weighting" each data point by its standard deviation. In this situation (11) becomes, for data with independent and normally distributed noise,

$$\phi(\mathbf{m}) = \sum_{\mathbf{N}} (\frac{\mathbf{y_i^{obs}} - \mathbf{y_i^{model}}(\mathbf{m})}{\sigma_\mathbf{i}})^{\mathbf{2}} = \mathbf{r^T C_d^{-1} r}, \tag{14}$$

and so the normal equations become

$$(\mathbf{A}^T C_d^{-1}\mathbf{A})\mathbf{m} = (\mathbf{A^T C_d^{-1} d}), \tag{15}$$

and the solution is clearly,

$$\mathbf{m} = (\mathbf{A^T C_d^{-1} A})^{-\mathbf{1}}(\mathbf{A^T C_d^{-1} d}), \tag{16}$$

where $\mathbf{C_d} = diag[\sigma_1^2, \sigma_1^2, ..., \sigma_N^2]$ (or, if the noise is not independent, $\mathbf{C_d}$ is the covariance matrix of the data). The weighted solution will thus be most sensitive to the data with the lowest uncertainties.

A.2 Damped least squares solution

If the number of model parameters is greater than the number of data there will be a combination of model parameters which have no effect on the data, i.e., the data do not "illuminate" these parts of the model. These actually correspond to eigenvectors

of $\mathbf{A}^T {\mathbf{C_d}}^{-1}\mathbf{A}$ with zero eigenvalues and result in a singular matrix in the inversion. In this case the aim is to find the "*minimum length solution*" through *damping* and to minimise both the misfit and the complexity (roughness) of the model. In this situation, the normal equations become

$$(\mathbf{A}^T {\mathbf{C_d}}^{-1}\mathbf{A} + \mathbf{W})\mathbf{m} = (\mathbf{A^T} {\mathbf{C_d}}^{-\mathbf{1}}\mathbf{d}), \tag{17}$$

and $\mathbf{W}$ is the damping matrix that generally a diagonal matrix, such that it might be given as $\mathbf{W} = \epsilon\mathbf{I}$, where $\mathbf{I}$ is the identity matrix and ϵ is some small positive scalar.

B Non-linear inverse theory: linearised inverse problems

In many problems the function relating the data and the model is not linear, therefore the approaches outlined above can not be used as $\mathbf{A}$ can not be simply defined. If the model is weakly non-linear, i.e., if it can be linearised, the solution to the problem is relatively straight-forward.

For $\mathbf{d} = \mathbf{F}(\mathbf{m}) + \mathbf{e}$, we can write

$$\delta\mathbf{d} = \frac{\delta\mathbf{F}}{\delta\mathbf{m}}\delta\mathbf{m} + \mathbf{e}. \tag{18}$$

Therefore,

$$\delta\mathbf{d} = \mathbf{A}\delta\mathbf{m}, \tag{19}$$

where $A_{ij} = \frac{\delta F_i}{\delta m_j}$. This can be solved iteratively, as described in the main text, given that $\delta\mathbf{d} = \mathbf{d} - \mathbf{F}(\mathbf{m_0})$ and

$$\delta\mathbf{m} = (\mathbf{A^T}\mathbf{A})^{-\mathbf{1}}\mathbf{A^T}\delta\mathbf{d} = \mathbf{m} - \mathbf{m_0}. \tag{20}$$

Note that this will only work if the problem is convergent and also risks getting stuck in local minima; therefore the initial guess is often very important.

Experimental techniques for multi-scale description of soil fabric and its dual pore network

Enrique Romero*-Guido Musso-Cristina Jommi*****

** Universitat Politècnica de Catalunya*
Department of Geotechnical Engineering and Geosciences
c/ Jordi Girona, 1-3, Campus Nord UPC, Building D-2
08034 Barcelona, Spain
enrique.romero-morales@upc.edu

***Politecnico di Torino*
Dipartimento di Ingegneria Strutturale, Edile e Geotecnica
Corso Duca degli Abruzzi, 24
10129 Torino, Italy

****Politecnico di Milano*
Dipartimento di Ingegneria Strutturale
piazza Leonardo da Vinci, 32
20133 Milano, Italy

Fabric affects many aspects of soil mechanical behaviour. When transport processes are of concern, its dual, the pore network, is the key aspect ruling the soil properties of interest. In this chapter, a review of a few widely used techniques, currently adopted to analyse the pore network at increasing scale, is presented, namely mercury intrusion porosimetry, environmental scanning electron microscopy and electrical resistivity tomography. Details on the techniques, their advantages and limitations, are first covered, followed by the presentation of selected test results. The results highlight how these techniques provide an insight into the pore network, and how they can be usefully exploited in the understanding of different hydro-electro-mechanical processes ordinarily observed at the phenomenological scale. Attention is focused on unsaturated soils with reference to water retention properties, micro / macrostructure interaction, and role of sample heterogeneity.

1 Introduction

Multi-scale studies associated with pore network properties are increasingly used to improve understanding of behaviour features and multiphase flow properties in porous media at the phenomenological scale, where the latter term is used to identify the scale of a standard laboratory test on a representative *homogeneous* volume element. These include distribution of pores space –micropore / macropore-, connectivity, constricted porosity by throats, hysteresis, fluid occupancy during multiphase flow displacement processes, wettability. Pore network rules liquid and gas permeability properties, as well as water retention, and electro-chemical transport. Dually, it affects mechanical properties, among which volumetric stiffness may be mentioned. As will be shown in the next chapter, flow and deformation properties are therefore coupled, and influence each other.

The pore network is studied at the microstructure scale, by means of techniques at the particle / aggregation scale (usually below <100 μm) capable of analysing the arrangement and distribution of particles and pores –and their contacts and connectivity– [Del96, Mit05, And12]. Among various available techniques used to study porous geomaterials at the microstructural scale, mercury intrusion porosimetry (MIP) and scanning electron microscopy (environmental ESEM with digital image analysis) are given special attention in the present chapter. The former technique has been frequently used to describe pore network properties affecting coupled hydro-chemo-mechanical processes (see, for instance, [AlM96, Rom99, Mus03, Kol06b, Rom11]). The latter is a quantitative technique with minimal sample preparation requirement, and which allows subjecting the sample to hydraulic paths during observation [Mon03a, Mon03b, Rom08, Air10].

Mesostructural scanning techniques, based on time-domain reflectometry, near-infrared spectroscopic measurements, electric impedance/resistivity tomography, neutron tomography, X-ray computed tomography, dual-energy gamma-ray technique, among others, allow increasing the scale of observation, therefore appreciating the role of heterogeneous elements, such as inclusions or cracks, in the engineering behaviour of porous media [Bak90, Bor05, Des06, And12]. Applications of these mesostructural techniques in saturated and unsaturated soils have been devoted to the monitoring of hydro-chemo-mechanical processes [Com08, Com10, Dam09, Cos12], to the detection of desiccation cracks [Geb06, Muk06, Sen09], to the visualisation of diffusion and multiphase transport processes, as well as fluid retention and permeation properties [Rol05, Van05, Rod06, Car06, Kol06a, Pir07, Kar07, Man12, Rie12]. Higher resolution mesostructural techniques, together with improved image processing, have recently allowed moving to micrometric scale, narrowing the gap between meso and microstructural techniques [Bri98, Jac02, Bés06, Tak06, And12].

Among the latter mesostructural technique, electrical resistivity tomography (ERT) is described in detail in this chapter. The technique turns out to be remarkably useful when studying coupled hydro-chemo-mechanical phenomena in which the pore network arrangement, and not only the pore size distribution, plays a relevant role.

The spatial resolution of ERT as a mesostructure tool is slightly above 10 mm. At this resolution, and with reference to geomaterials testing, it can be classified as a semi-quantitative technique, since it provides a good general electrical picture of the sample, while accuracy in estimating electrical conductivity can be lost if sharp gradients exists. With respect to other techniques mentioned before, an essential advantage of ERT is that it can be easily implemented in modified laboratory cells for mechanical and hydraulic testing. Sequences of maps of electrical resistivity (potentially 3D), taken while performing hydro-chemo-mechanical tests, can then be used to visualize transport and mechanical processes occurring inside the sample. Appropriate data treatment may be exploited to back-analyse transport parameters, as shown in the last chapter.

2 Mercury intrusion porosimetry and environmental scanning electron microscopy

2.1 Mercury intrusion porosimetry

Mercury intrusion porosimetry (MIP) is one of the most commonly used techniques for analysing the pore size distribution (PSD) of geomaterials with interconnected porosity. The interested reader may refer to [Web97, Del96, Sim04, Rom08]. With this technique an absolute pressure p is applied to a non-wetting liquid (mercury) in order to enter the empty pores. Washburn equation may be adopted to provide a relationship between the applied pressure and a characteristic size of the intruded pores [Dia70, Jua86]. For ideal pores of cylindrical shape or parallel infinite plates (fissure-like pores), the equation reads:

$$p = -\frac{n\,\sigma_{Hg}\cos\theta_{nw}}{x} \tag{1}$$

where σ_{Hg} is the surface tension of mercury (σ_{Hg}=0.484 N/m at 25°C), θ_{nw} the contact angle between mercury and particles surface, and x the entrance or throat pore diameter ($n = 4$) or the spacing width between parallel plates ($n = 2$). The value $n = 4$ is often used in MIP, as the cylindrical model is most frequently adopted. The contact angle is usually taken between 139° and 147° for clay minerals [Dia70], although higher values have been reported on kaolinitic clay [Pen00].

Sample preparation requires emptying the sample of water that prevents the penetration of mercury. Samples can be dehydrated using controlled relative humidity-drying, oven-drying, freeze-drying or critical-point-drying techniques [Del84b]. For heat and dry sensitive materials, freeze drying is preferred [Ahm74]. Freeze drying process involves temperature (fast cooling) and pressure conditions (sublimation of

ice) to avoid surface tension forces caused by air-water interfaces [Ahm74, Del82, Del84b, Del96, Pen00].

A constant contact angle at equilibrium is assumed in the elaboration of MIP data, irrespective of the actual penetration flow conditions, in spite of Equation (1) being valid only with reference to equilibrated states, at null penetration velocity of mercury. In fact, the contact angle varies as a function of the dynamic flow of the advancing interface, as shown by [Hof75, Aït04]. For this reason, sufficient time lapse must be left in pressure rising and mercury ejection to allow for quasi-static state conditions to be reached at any step. Usually, an imposed mercury pressure is held constant until penetration ceases or falls below a specified rate.

The main limitations of MIP are: a) completely isolated pores enclosed by surrounding solids are not measured –this enclosed porosity is not significant in soils, but can play increasing role in low-porosity geomaterials-; b) pores that are accessible only through smaller ones, hence constricted porosity by throat effect, are not detected until the smaller entrance pores are penetrated; c) the apparatus may not have enough capacity to enter the smallest pores of the sample (non-intruded porosity with entrance pore sizes below 7 nm); and d) the minimum pressure which can be applied practically by the apparatus limits the maximum detected pore size (non-detected porosity with entrance pore sizes larger than 400 μm). Alteration in the pore geometry during pressure application is also of concern. It has been reported that the soil structure is not affected during high-pressure intrusion [Sil73, Law78 and Ree79], due to the fact that most of the pore network is already filled with incompressible mercury during penetration. However, this is not the case before penetration starts and at low applied pressure, for compressible materials. Occurrence of substantial initial volume change due to isotropic compression in clayey samples prior to intrusion was reported by [Pen00]. Deformation of the sample holder system during mercury pressure changes is another factor which can induce interpretation errors, and which should be accounted for in data elaboration [Sim04].

The pore-size distribution can be deduced by mercury intrusion, by relating the volume of intruded pores to the pressure required for intrusion. The intrusion stage can be followed by an extrusion stage, which can be accomplished by decreasing the applied pressure. The cumulative intruded volume data along an intrusion-extrusion cycle highlights that not all the mercury intruded during the penetration stage is recovered when the pressure is released. An amount of mercury remains permanently entrapped in the constricted porosity by throat effects. Various theories explaining the causes of MIP hysteresis and entrapment have been discussed and examined in detail by [Mat95, Abe99 and Mor02]. A second intrusion will follow approximately the same extrusion path, thus identifying that part of porosity which is not affected by throat effects. The latter is assumed to coincide with the non-constricted or free porosity. Delage & Lefebvre [Del84] and Delage *et al*. [Del96] assumed that the small intra-aggregate pores, pores inside soil aggregates, display a non-constricted or free porosity, while the large inter-aggregate pore space between the aggregates corresponds to the entrapped porosity. The extrusion data can thus be exploited also

to provide additional information on the multiscale arrangement of the microstructure pore network.

Data from mercury intrusion can be complemented, for pore sizes below 60 nm, with nitrogen desorption isotherms (although the use of the adsorption branch is also possible. Data from the latter technique are interpreted using BJH model [Bar51], based on which emptying of pores from condensed adsorptive at decreasing relative nitrogen pressure is re-interpreted by Kelvin equation [Sil73, Web97]. The model is based on the assumption that pores have cylindrical shape and that the pore radius is equal to the sum of the Kelvin radius and the thickness of the film adsorbed on the pore wall.

Results of MIP technique may be better reported as pore size density function, PSD, i.e. the log differential intrusion curve *vs*. entrance or throat pore size, which aids visual detection of the dominant pore modes. Figure 1 shows the cumulative intruded pore ratio (volume of intruded pores / volume of solids) for dense clay phyllite (void ratio around 0.34), as well its corresponding PSD, obtained by MIP and BJH desorption data [Gar10]. According to MIP data, the dense material displays a single dominant pore mode at around 15 nm. PSD based on the analysis of the nitrogen desorption branch is not always straightforward, since an intense spike at around 4nm is sometimes present that reflects an artefact (associated with the spontaneous evaporation of metastable pore liquid, [Low04]). In such cases, a more realistic PSD can be obtained from the analysis of the adsorption branch [Low04].

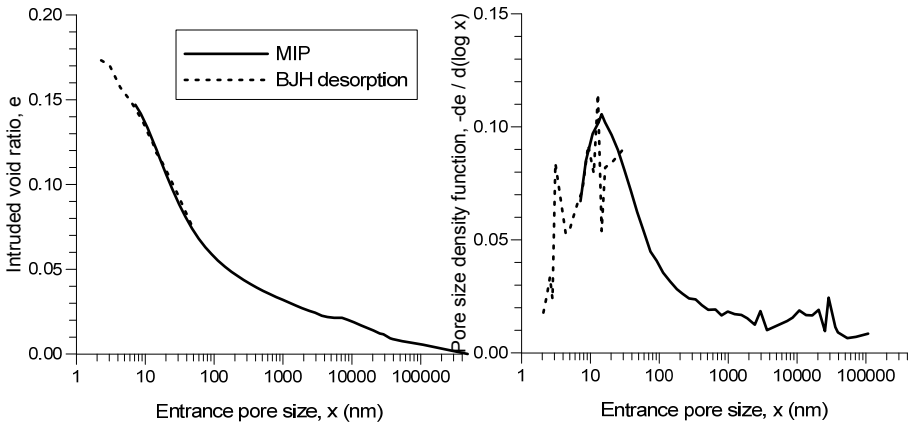

Figure 1: Left: Evolution of intruded void ratio with entrance pore size by MIP and BJH desorption of natural phyllite. Right: Pore size density functions [Gar10].

Further insight into the pore structure may be provided by the interpretation of MIP data in terms of the fractal character of the porous medium, admitting self-similarity of the hierarchical pore network. For the calculation of the surface fractal dimension

D_s, the following expression written as a function of the mercury pressure p, has been usually adopted [Kor92, Mey94, Fad96], where V is the intruded pore volume:

$$\log\left(\frac{\mathrm{d}V}{\mathrm{d}p}\right) \propto (D_s - 4)\log p \tag{2}$$

Intervals of self-similarity of the different pore types can be experimentally obtained from the linear sections of the corresponding log-log plot, the slope of which gives the values of D_s, as shown in Figure 2. In the figure, one pressure range is identified for the high-density soil with a characteristic fractal dimension of D_s=3.09, which reflects a more space-filling volumetric pore structure. On the contrary, two pressure regimes can be identified in the low-density sample: a low-pressure regime exhibiting a fractal dimension D_s=1.88, which corresponds to a fissure-like structure, and a high-pressure regime for pore sizes lower than 300 nm presenting again a volumetric structure (D_s = 3.04). Fractal concepts related to porosimetry studies have been used by [Fad96, Gim97, Jom03], as a complementary tool to detect microstructural changes and differences in pore geometry at various structural levels. It is worth noting that fractal dimension analysis also allows detecting anomalies in MIP data, such as the initial compression before mercury penetration takes place.

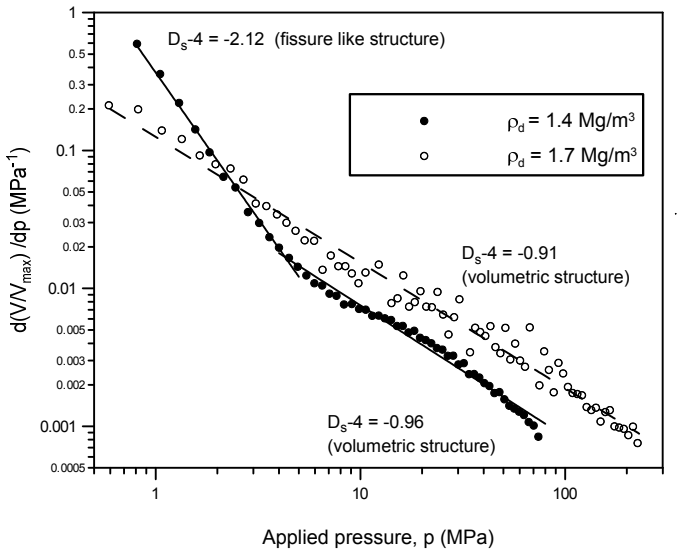

Figure 2: Fractal description of the pore network for two dry densities of a kaolinitic-illitic clay [Rom08].

As MIP data depend on pore sizes and pore network connectivity, they can be usefully exploited to derive quantitative water retention properties of geomaterials [Pra85, Rom99, Aun01, Sim01, Sim02]. The non-wetting mercury penetration at intrusion pressure p is assumed to be equivalent to air-intrusion at matric suction s during a drying path for the same diameter of pores x being intruded:

$$s = \frac{4\sigma \cos\theta_w}{x} \;;\; p = -\frac{4\sigma_{Hg} \cos\theta_{nw}}{x} \;;\; s = -\frac{\sigma \cos\theta_w}{\sigma_{Hg} \cos\theta_{nw}} p \approx 0.196\, p \qquad (3)$$

where σ is the surface tension of water and $\cos\theta_w$=1 the wetting coefficient for the air-water interface (refer to Equation (1) for σ_{Hg} and θ_{nw}).

The volume of pores not intruded by mercury –assuming a non-deformable soil– is used to evaluate the water content w or degree of saturation S_r corresponding to the equivalent applied matric suction. Derivation of the matric suction – saturation relationship from MIP data should be limited to the low-suction range, in which capillarity dominates water retention. In fact, water is generally held due to capillarity at low suctions (usually < 2 MPa), and by adsorption on particle surfaces and in clay inter-layers at higher suctions [Cas92, Rom99]. Moreover, to correctly estimate the water content, data must be corrected for the non-intruded porosity, which can be assimilated to a residual water content w_r [Rom08]:

$$S_{r\,nw} + S_r = 1 \;;\quad (w - w_r) = (w_{sat} - w_r)(1 - S_{r\,nw}) \qquad (4)$$

where w_{sat} is the water content at S_r=1, and $S_{r\,nw}$ the complementary non-wetting degree of saturation intruded by mercury.

In comparing MIP elaboration with direct water retention data, attention must be paid to the evolution of the pore size distribution during hydraulic paths for active soils [Sim01, Sim05, Rom11]. In principle, the PSD measured on a soil sample gives the water retention curve corresponding to the end of a water retention curve test, after volume changes have ceased. Figure 3 presents a comparison of water retention results on drying of a clayey silt, with the information deduced from MIP using freeze-dried samples.

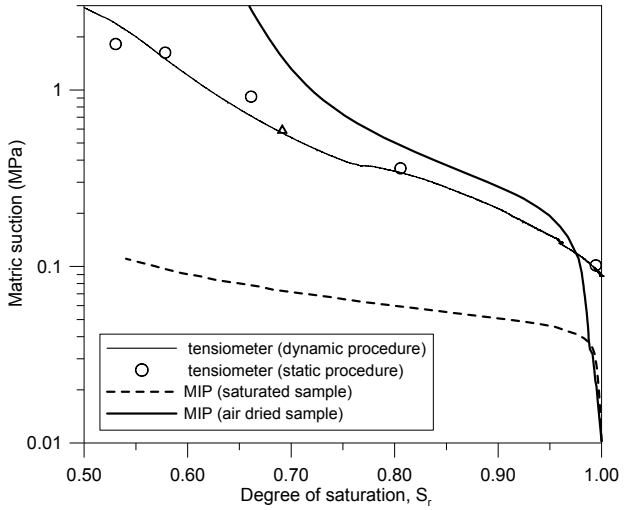

Figure 3: Water retention results on drying of clayey silt compared to deduced data from MIP using freeze-dried samples [Rom08].

'Dynamic' and 'static' procedures refer to the measurement of matric suction using high-range tensiometers during a continuous drying process and at static equilibrium under constant water content, respectively. The figure shows good agreement in the determination of the air-entry value using MIP, when the sample has been previously air-dried and undergone shrinkage. In this case, the denser state reached on drying is associated with a higher air-entry value, which matches the tensiometer results with a distribution of pores that evolve with suction. On the contrary, deduced water retention results from MIP starting from saturated conditions, reflect a lower air entry value, which is in agreement with the *frozen* higher porosity of the saturated state.

MIP results have been successfully used on an extended range (up to 41 MPa) to determine water retention properties of low-porosity claystone (void ratio e=0.12), which does not undergo important volume changes on drying. Figure 4 shows the cumulative intruded void ratio using MIP and BJH adsorption information up to e=0.10. The PSD function obtained from MIP displays one dominant pore mode at approximately 16 nm. The air entry value corresponding to the dominant pore mode can be determined from Laplace's equation, giving a value of 18 MPa. Figure 4 also shows the estimated water retention curve based on MIP deduced data, together with psychrometric measurements.

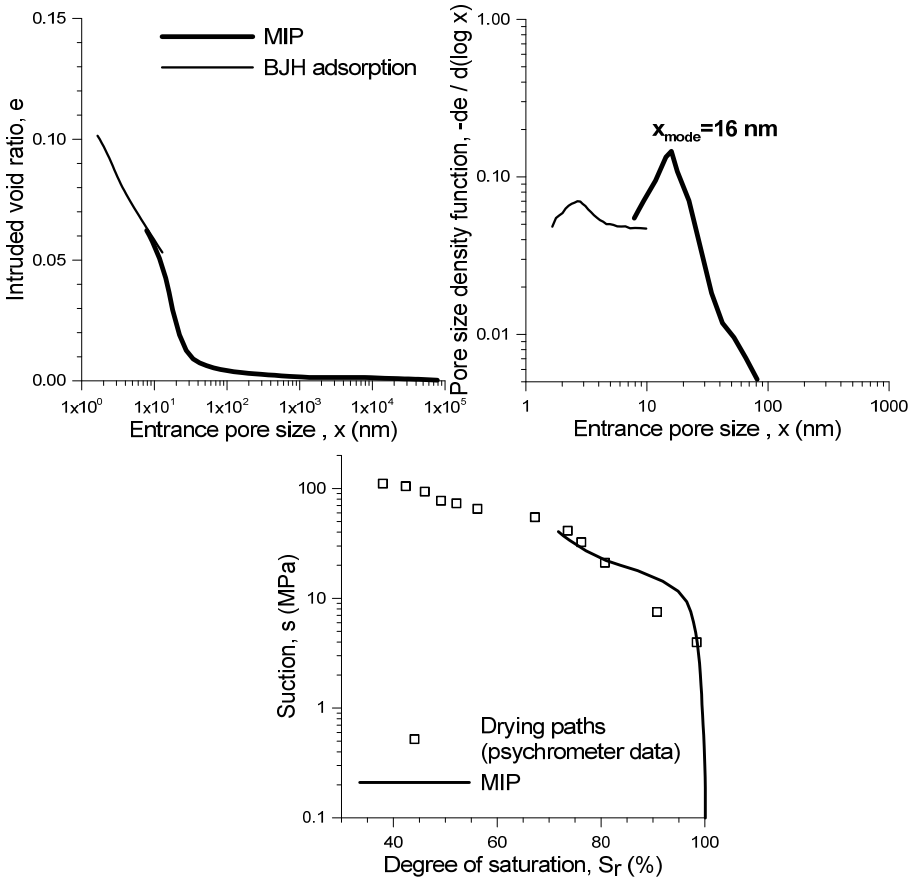

Figure 4: Top left: Cumulated intruded void ratio on low-porosity claystone. Top right: Pore size density function with dominant pore mode. Bottom: Deduced water retention data from MIP results compared to psychrometer readings [Rom12].

2.2 **Environmental scanning electron microscopy**

As already described, MIP analysis is performed on a dried sample, therefore having *frozen* PSD and pore network during the test. On the contrary, the pore network of active soils evolves, together with aggregate swelling and shrinking, when in contact with water. This evolution may be observed by means of Environmental scanning electron microscope (ESEM). The latter is a special type of SEM that works under controlled environmental conditions and requires no conductive coating on the specimen. The technique enables examining wet samples and preserving their natural characteristics for further testing [Dan93, Bak95, Kom99, Mon03a, Rom08, Air10, Rom11].

The equipment presents a sample chamber at a higher pressure and separated from increasing vacuum chambers by pressure-limiting apertures (electron gun chamber is at 10^{-5} Pa). Water vapour is the most commonly used chamber gas, which is controlled with an electronic servo system at absolute vapour pressures between 0.13 and 2 kPa. The microscope is also equipped with a Peltier cooling / heating system (working within 20°C above or below ambient temperature) installed underneath the sample stub to control sample temperature. Accordingly, the examination of the sample can be continuously done at different vapour pressures and temperatures, hence at different relative humidity, making it a suitable equipment to study the gradual effects of wetting and drying stages at microstructural scale. A certain degree of resolution is compromised when using this equipment, especially at elevated relative humidity of the sample chamber.

Montes-H *et al*. [Mon03a, Mon03b] used ESEM jointly with a digital image analysis program to estimate at aggregate scale the swelling–shrinkage behaviour of bentonite at different total suctions. More recently, [Rom08, Air10, Rom11] used the same technique to study the effects of total suction changes on the volumetric behaviour at microstructural level of different clays. Airò Farulla *et al*. [Air10] changed temperature and vapour pressure conditions to perform a suction cycle according to the wetting and drying paths outlined in Figure 5. The cycle started at point B, where the sample (initially at point A), was let to equilibrate for 15 min at RH=30% (total suction around 160 MPa), by applying a vapour pressure of 0.65 kPa at 20°C. A photomicrograph was taken at each stage (different points in Figure 5) and after an equalisation time of 10 minutes. Two procedures for digital image analysis were used to isolate aggregates and calculate area variations due to relative humidity changes. The first procedure, shown in Figure 6, consisted in defining the aggregate contour on the inverse image, in transforming it into a binary image, and in counting the white pixels. Aggregate area variations were calculated with reference to the initial condition (point B, Figure 5). The second procedure used an automatic digital image analysis [Abr04], which consisted in using a threshold filter, in selecting a region of interest and in applying an automatic segmentation algorithm. Aggregate areal deformations (negative in expansion) measured during the wetting and drying cycle and using the two aforementioned procedures are plotted against total suction in Figure 7.

Romero *et al*. [Rom11] used the same procedure to study aggregate volume changes along a wetting and drying cycle on two different clays. A consistent picture of volume change behaviour was obtained by these authors on different clays, when comparing microstructural ESEM results with MIP data and with phenomenological (at larger scale) results. They finally exploited these data to complement the description of evolutionary water retention properties of active clays.

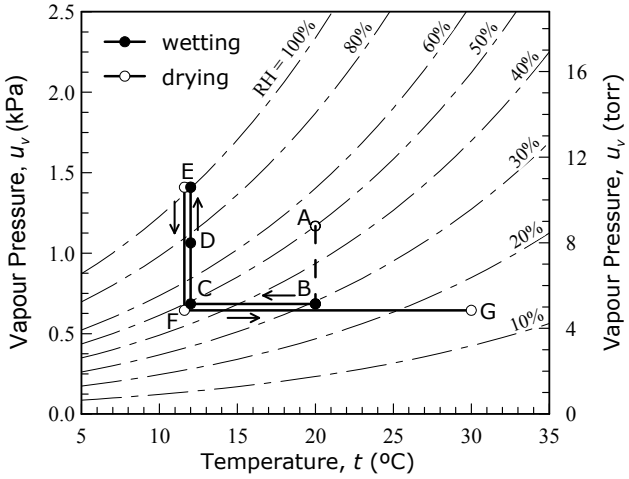

Figure 5: Wetting and drying paths followed by a clayey aggregate in the ESEM [Air10].

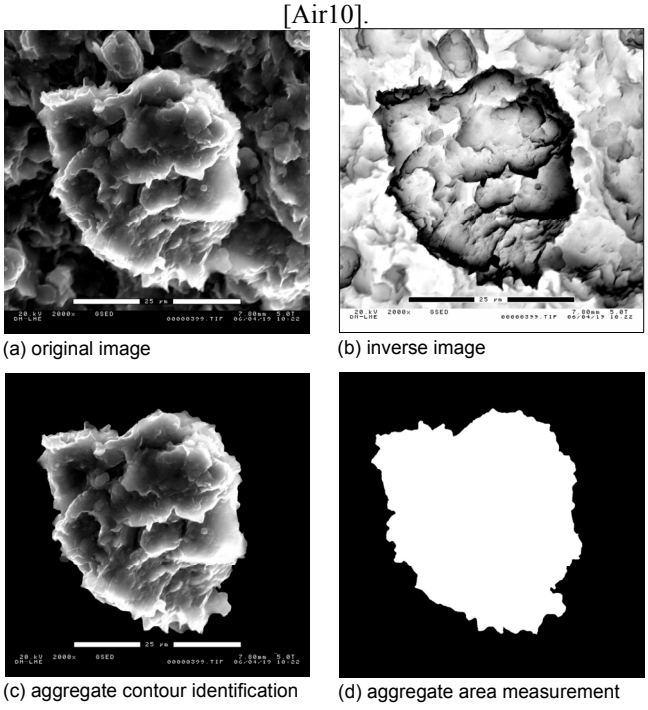

Figure 6: Manual digital image treatment to measure changes in aggregate area. [Air10].

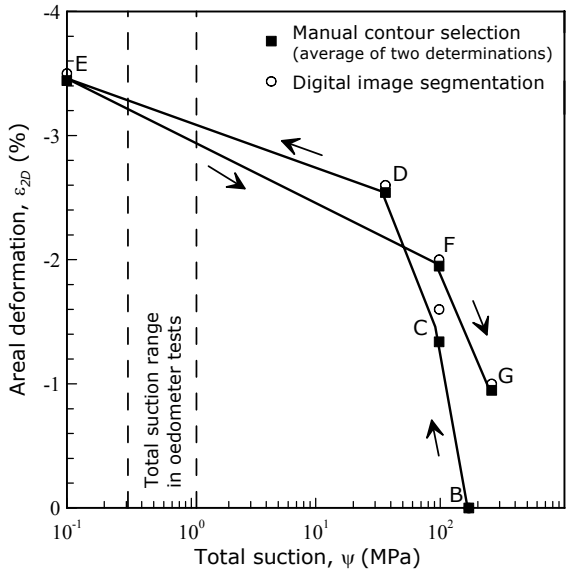

Figure 7: Areal deformation of the aggregate versus total suction in wetting-drying path [Air10].

3 Electrical Resistivity Tomography (ERT)

3.1 Introduction

Electrical resistivity tomography (ERT) allows increasing the scale of observation of the role of pore network on the phenomenological behaviour of soils. Usefulness of electrical measurements in the characterisation of geomaterials at the laboratory scale is enhanced by its association to the tomography technique. A single electrical measurement implicitly introduces the assumption that the investigated body is homogeneous. A great number of measurements, all referring to the same volume but taken from different points, permits the relaxation of the homogeneity assumption. Joint analysis of several measurements allows then an insight into the distribution of electrical properties within the studied body.

Thanks to this scale of observation, ERT may found different applications, among which developments for medical diagnosis are of outmost relevance. As for the literature related to geosciences, the synthetic study from [Lyt78] proved that the technique could be applied as an experimental procedure to detect heterogeneities of rock cores. Since then, the numerical algorithms used have been improved, increasing accuracy in the evaluation of local values of conductivity and resolution in the reconstruction of shapes.

The technique can be applied at different scales (from laboratory mesostructural investigations to stratigraphic characterisation) and the resolution varies from about one millimetre to the order of meters.

In petroleum engineering electrical tomography has been implemented commercially with names such as FMS (Formation MicroScanner) and FMI (Fullbore Formation MicroImager). It is used to obtain 'image logs', or electrical pictures of the wellbore that are quite effective to recognize and detect mechanical failures and naturally occurring fractures. A comparison between information recovered through visual inspection of the core and information from FMS images is available in [Kho12]. The technique is used also to recover stratigraphic information in shallow environments.

In near surface geophysics, early studies included identification of aquifers systems and sources of pollutions [Whi94, Osi95, Bev91]: then attention switched towards imaging of subsurface fluid movement in porous and fractured media [Dai92, Sla97]. Later studies, associated to further improvements of the inversion technique, deal with quantitative assessment of transport characteristics in soils and rocks.

In the following, equipment, operational principles and data elaboration are presented, to highlight the multiscale potentialities of ERT, together with its resolution limitations at the different scales of observation. Microresistivity for fabric studies, which complement the previous techniques, are then introduced. Examples of quantitative application of the technique for multiphase flow are postponed to the last chapter.

3.2 Principles of ERT

In ERT several pairs of electrodes are attached to the surface of the object: two electrodes apply the electrical current, and other pairs of electrodes measure the induced electrical potential differences (as in the four electrodes terminals). Either the pair of electrodes applying current or the pair electrodes measuring the potential drop are changed from measurement to measurement. A forward model is separately built to calculate the electrical potential differences that would be measured if the electrical conductivity within the object had a certain distribution. Finally an inverse model is used to estimate the distribution of electrical conductivity that minimizes the scatter between experimental measurements and predictions of the forward model [Bor05].

ERT reconstruction: forward model

The solution of the forward problem links the voltage measurements to the object conductivity. Most reconstruction codes implement the forward model with a Finite

Element solver [Vau97, Bor02, Pol02], discretising both domain Ω and conductivity distribution.

Assuming that the conductivity χ of the object under measurement is isotropic, that the electric and magnetic fields are slowly varying and neglecting capacitance effects, it follows that the governing equation of the problem is the balance of electrical charge in stationary conditions:

$$\nabla \cdot \left(\chi \nabla \phi \right) = 0 \tag{5}$$

where ϕ is electric potential inside the body.

The presence of the electrodes is taken into account via appropriate conditions at the boundaries of the object, ∂Ω, as with the complete electrode model [Som92]. The model assumes that the potential is homogeneous over the electrode space and that overpotential phenomena occur at the interface between the electrode and the object under measurement. The following relation holds for each electrode *l = 1, ..., L*:

$$V_l = \phi + z_l \chi \frac{\partial \phi}{\partial \vec{n}} \quad on \quad \partial\Omega_l, \quad l = 1,..,L \tag{6}$$

where V_l is potential of the l^{th} electrode, z_l is contact impedance of the l^{th} electrode, $\partial \vec{n}$ is the outwards normal to $\partial\Omega$ and $\partial\Omega_l$ is the portion of $\partial\Omega$ underneath electrode *l*.

Electrical stimuli are accounted for by specifying for each electrode that:

$$\int \chi \frac{\partial \phi}{\partial \vec{n}} = I_l \quad on \quad \partial\Omega_l, \quad l = 1,..,L \tag{7}$$

where I_l is current injected into the l^{th} electrode. Equation (6) and (7) apply to the portions of ∂Ω that fall underneath each electrode. To the remaining parts of ∂Ω (inter electrode gaps), the following relationship applies:

$$\chi \frac{\partial \phi}{\partial \vec{n}} = 0 \tag{8}$$

as no current density is crossing the free surface of the object under measurement. Equations (6) to (8) specify the model for the electrodes, voltages on the electrodes are however specified to within an arbitrary additive constant as no reference potential has been specified. As this is an arbitrary choice, usually the model is complemented with the additional condition:

$$\sum_{l=1}^{L} V_l = 0 \tag{9}$$

that allows the unique determination of all V_l.

ERT reconstruction: inversion

Field reconstruction is formulated as non-linear least-squares problem, where the conductivity of the forward model is varied until a satisfactory match between the measurements simulated by the forward model and the real measurements is met. The reconstruction procedure searches for a discretised conductivity $\mathbf{s}_{rec}$:

$$\mathbf{s}_{rec} = \arg\min \left\| h(\mathbf{s}) - \mathbf{v} \right\|_2^2 \tag{10}$$

where h is the nonlinear forward operator from model space to measurements space, $\mathbf{s}$ is the discrete conductivity, $\mathbf{v}$ is the vector of measured voltages and $\| \ \|_2^2$ indicates the squared 2-norm. The reconstruction problem, both in its continuous form and in its discrete form (Equation 10), is ill-posed in the sense that small perturbations in the measured data can cause arbitrarily large errors in the estimated conductivity [Syl87]. Then, regularisation techniques are needed to obtain a stable solution. In practical terms, ill-conditioning arises from certain patterns of conductivity for which the corresponding measurements are extremely small [Bre90], so being affected by measurement noise. Such patterns of conductivity, for which the observations are unreliable, corrupt the reconstruction. Regularisation techniques are adopted in order to prevent such problem. Commonly Equation (10) is solved using the Tikhonov regularisation, formulating the reconstruction as:

$$\mathbf{s}_{rec} = \arg\min \left\| h(\mathbf{s}) - \mathbf{v} \right\|_2^2 + \alpha F(\mathbf{s}) \tag{11}$$

where $F(\mathbf{s}) > 0$ is the regularisation function, and α a positive scalar called Tikhonov factor. F acts as a penalty term, by taking large values corresponding to distributions $\mathbf{s}$ that are to be prevented in the reconstructed profile. The effect of F on the reconstructions can be adjusted by varying the value of α. The conductivity being discrete, the regularisation function is usually expressed as:

$$F(\mathbf{s}) = \left\| L\mathbf{s} \right\|_2^2 \tag{12}$$

where L is the regularisation matrix. The reconstruction is therefore formulated as:

$$\mathbf{s}_{rec} = \arg\min \left\| h(\mathbf{s}) - \mathbf{v} \right\|_2^2 + \alpha \left\| L\mathbf{s} \right\|_2^2 \tag{13}$$

Regularisation methods mostly achieve the stability of the inversion by penalizing sudden variations in the conductivity, hence offering a trade-off between stability of the reconstruction and sharpness of image. Thorough discussions on the choice of α and on regularisation techniques in ERT can be found in [Kol01] and [Bor02].

ERT testing cell: geometry, size and disposition of electrodes

Spatial resolution and accuracy of ERT reconstructions are constrained from computational aspects (type of algorithm and refinement of the mesh of the numerical models) and from experimental set ups (number, size, geometry and spacing of electrodes used).

[Com08] reports that the total number of independent measurements N of a tomographic reconstruction is:

$$N = \frac{n(n-1)}{2} \tag{14}$$

where n is the number of available electrodes.

A trade off in the design of ERT cells concerns the size of the electrodes [Dam09]. Better definition of the electrical problem is achieved when injecting electrodes have a large surface, generating an even current density, and measuring electrodes are small, providing punctual measurements. Since in ERT electrodes work in turn to inject current and to measure voltage, a compromise is needed. For 2D ERT reconstructions of cylindrical bodies, [Lee10] suggests dimensionless ratios:

$$\frac{W}{D} \approx \frac{\pi}{2n} \text{ and } \frac{L}{D} \approx 0.4 \tag{15}$$

where W is the width of the electrode, D is the diameter of the cell and L is the length of the electrode. These ratios were evaluated based on Finite Element Method simulations of synthetic problems. Anyway, it could be not so strictly necessary to comply rigorously with all of them, also depending on the characteristics of the software used for inversion / reconstruction (e.g. if this introduces complete electrode model [Som92] and if it can model steep gradients).

Finally, measurement protocol can rely on different configuration. Two of them are: (i) the adjacent electrode scheme and (ii) the opposing electrode scheme [Vau97]. Figure 8 shows the current lines obtained with these two configurations under the hypothesis of a homogeneous body. The adjacent electrode configuration, confining

the current towards the cell walls, is more sensitive along the boundaries and loses sensitivity at the centre of the cell. The opposing electrode configuration, providing a more homogenous distribution of electrical current, has a more homogeneous sensitivity.

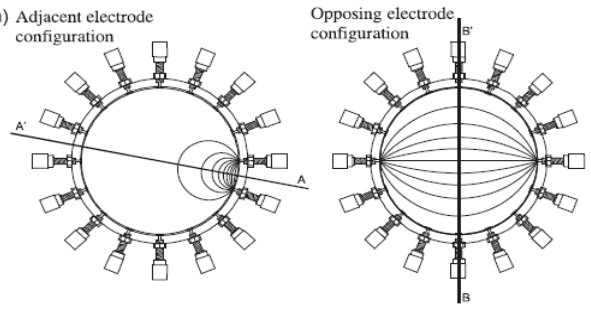

Figure 8: Adjacent electrode and opposing electrode configuration, applied to a cylindrical sample [Dam09].

Even with the opposite electrode configuration, sensitivity of the reconstruction is generally low when anomalies are located towards the centre of the cell [Dam09]. In many cases [Bor05, Lov05, Com08, Dam09] the image of the object is satisfactorily reproduced, but the electrical conductivity values found are not necessarily correct. This depends both on the regularisation technique used and on the ERT system geometry [Dam09]: actually, some very good quantitative results can be obtained if variations of the electrical conductivity in space are not too dramatic. From a practical perspective, quantitative evaluations are easier to be achieved in the case of variations of porosity than in the case of fractures.

ERT testing cell: components

An ERT testing cell is made of a Personal Computer (PC), a data acquisition system, an inverter and a measuring cell. Figure 9 refers to the system used in [Bor05]. A digital direct synthesiser is used for the generation of the AC waveform, which is then fed to a voltage controlled current source and applied via a multiplexer to the pair of driving electrodes. High output impedance of the current source is desirable to drive currents in very resistive media. The injected current intensity is measured on a shunt resistor in series with the driving pair, which ensures accurate measurement of the applied current. A second multiplexer connects the electrodes to an Analogical Digital Converter (ADC), for voltage measurement. The output signals are processed by an on-board Digital Signal Processor which separates in phase and out of phase components. The instrument is controlled by a PC to implement the measurement scheme and to gather the results.

Figure 10 shows the double mesh used in the inversion of tests used in [Com05a] and [Bor05]. A coarse mesh (Figure 10a) has been used to represent the discrete conductivity, while a second finer mesh has been used to represent the electric potential. The number of elements of the coarse mesh coincided with the number of unknowns of the reconstruction process; hence it was chosen considering the number of available measurements in the light of sensitivity and non uniqueness issues. Since such a mesh is not appropriate for an accurate solution of the forward problem, a second and finer mesh was used for the computation of simulated voltages at the electrodes: the fine mesh (Figure 10b) is an adaptive refinement of the coarse mesh.

Further details concerning the experimental set up and the implementation of ERT to laboratory geotechnical studies in available in [Com05a].

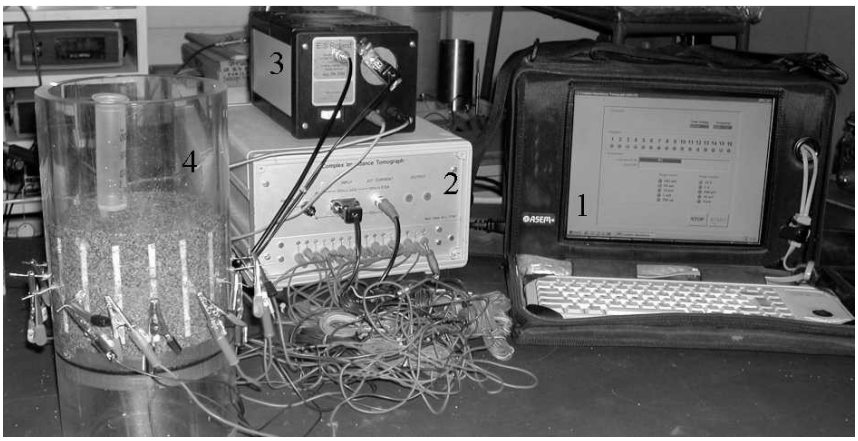

Figure 9: 2D ERT testing cell: 1 Personal Computer 2 Data acquisition system 3 Inverter 4 Measuring Cell [Bor05].

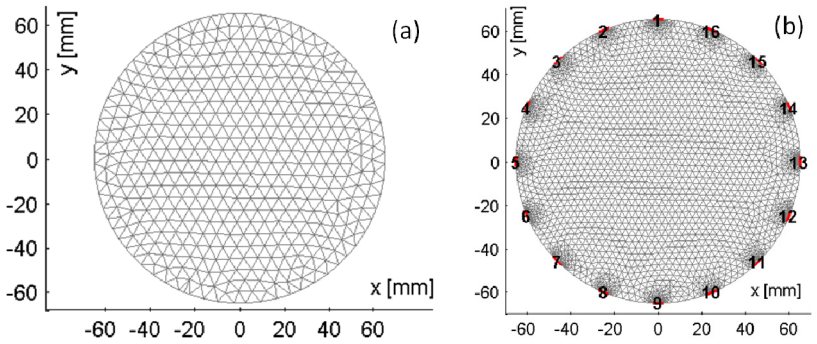

Figure 10: Double mesh used by [Bor05]: (a) mesh of the discrete conductivity (b) refined mesh for the accurate solution of the forward problem.

3.3 Selected ERT studies

Different geometries and spacings between electrodes have been adopted, depending of the desired scale of investigation (see Table 1). It emerges that in some studies ERT ('microresistivity') has been applied to recover information concerning the fabric of the specimens, while in others, with lower resolution, mostly to check local porosity variations or possibility to track transport of fluid or salt.

Table 1: Selected applications of resistivity tomography in the laboratory

Study	Electrodes/ Geometry	Resolution/ measurements per image (m.p.i.)	Objective / Results
[Jac90]	64 sprung gold plated electrodes 5 mm diam / 10 mm spacing	5 mm	Investigating meso structure and fractures. Comparison with down – hole electrical imaging tools.
[Bri98]	2880 electrode grid 5 mm spacing	5 mm	Comparison with X ray radiographs. Investigation of fabric/tortuosity through back analysis of the formation factor F^*
[Jac02]	576 electrodes 10 mm length 5 mm penetration all electrodes on one side of the sample	5 mm 2000 m.p.i. (2D) 8000 m.p.i. (3D)	Comparison with X ray radiographs. Investigation fabric/tortuosity through back analysis of the formation factor F^*
[Lov05]	Injecting electrodes on opposite sides of sample / measuring electrodes on sample surface	5 mm same as down-hole electrical imaging tools	Investigation of depth of fractures / fracture distribution.
[Bin96]	12 equally spaced electrodes on the sidewall of a 320 mm diameter column 4 planes	25 mm (1% total area) 400 m.p.i	Qualitative tracement and flow path of tracer in an undisturbed soil column. Detection of area with higher clay content and of small stones.
[Bor05]	16 electrodes on the circumference of a 130 mm column Electrodes 5 mm wide and 100 mm long.	≈ 10 mm (pixel side) 96 m.p.i.	Validation of the technique. Detection of heterogeneities due to spatial variations of porosity and of composition of the solid phase (cm scale).
[Dam09]	16 electrodes on circumference of 139 mm diameter tube. Electrodes are 7 mm wide and 70 mm long.	≈ 10 mm Sensitivity depends on position of anomalies (decreases if anomaly is at the sample centre)	Validation of the technique / diffusion from a punctual source.
[Com10]	3D EIToedometer 16 electrodes on the sample circumference 13 electrodes on the base 13 electrodes on the top	≈ 5 mm (voxel side) 788 m.p.i.	Changes in water content. Local changes in porosity during mechanical consolidation.

Studies focusing on material fabric have been conducted mostly using electrodes placed over planar surfaces with spacing of about 5 mm. Studies focusing on material heterogeneity and on transport processes have been dome on larger samples, with electrodes usually placed on the external circumference of the sample at spacing of the order of 20-30 mm.

Microresistivity for fabric studies

[Bri98] and [Jac02] showed interesting applications of microresistivity to characterise the fabric of seafloor sediments and rock cores. The heterogeneity of samples of sediments and carbonate rocks was investigated by joint use of X-radiography and microresistivity tomography. In these works resolution of the two techniques was different (0.43 mm / pixel for the Xray, 5 mm / pixel for the microresistivity): data were transformed to an intermediate scale of 1 mm/pixel to make them comparable [Bri98]. X-radiographs underwent nearest-neighbor resampling. Microresistivity data were formed into 1mm/ pixel scale by Kriging.

X radiographs were interpreted to provide density maps (Figure 11a) and microresistivity data were interpreted to provide maps of the formation factor (Figure 11b).The formation factor F^* was evaluated as:

$$F^* = \frac{\chi_w}{\chi_t} \tag{16}$$

where χ_w is the electrical conductivity of the pore water and χ_t is the local electrical conductivity of the sample as estimated by microresistivity.

Knowing the specific density allows deriving porosity maps from density maps (Figure 11c) and information from the two techniques is finally merged to define a map of Archie's exponent m (Figure 11d). This last step is obtained introducing Archie's law:

$$F^* = n^{-m} \tag{17}$$

Archie's exponent reflects the effects on the electrical conductivity of the medium that cannot be explained simply by porosity. Then m can be related to tortuosity [Bri98] or to pore shape and structure [Jac02].

For instance [Bri98] related zones where m is close to one (layer B in Figure11d) to a pelletised volumetric pore structure (see section 2.1) with well-developed connectivity in the direction current flow during electrical measurements. This structure is associated to development of biogenic gas after sediment deposition that migrated in vertical direction. Higher m values in layer A were related to silt/sand storm laminae.

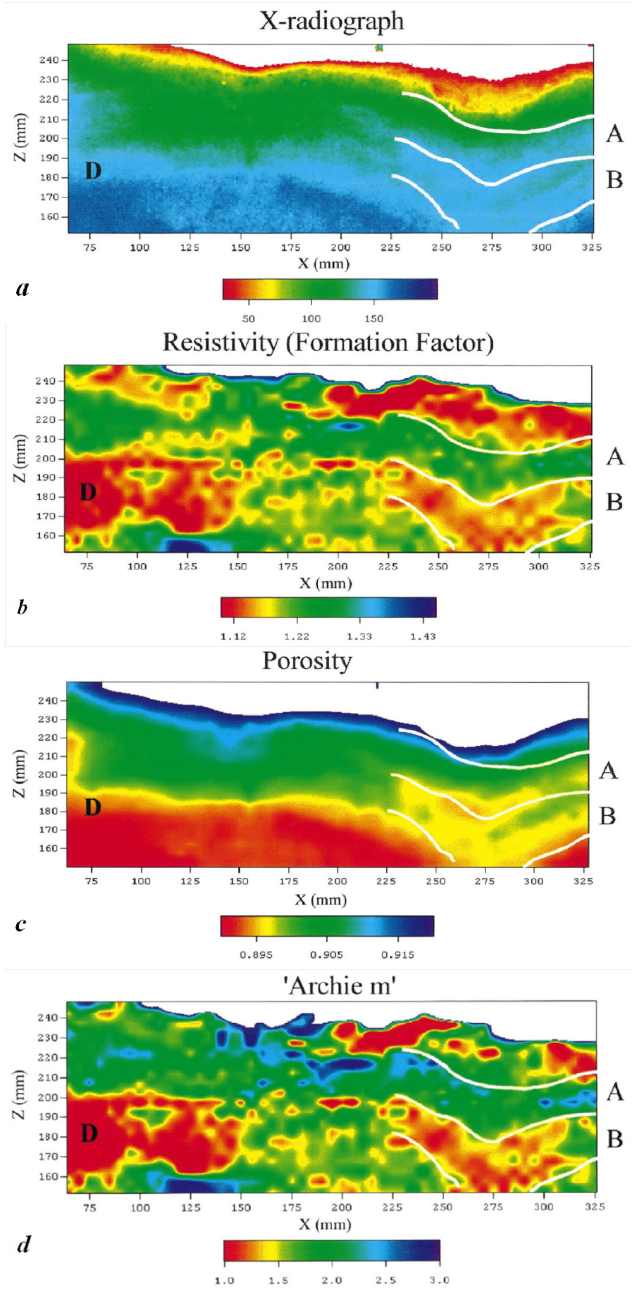

Figure 11: Joint use of X radiographs and microresistivity to characterise fabric and heterogeneity of sediment samples [Bri98].

ERT for porosity and mineralogy heterogeneity studies

In most studies related to hydrogeologic and geotechnics applications, ERT measurements had a resolution of around 10 mm. ERT has then been used to evidence porosity and mineralogy heterogeneities at higher scales, together with monitoring hydro chemical processes [Dam09, Com10]. Figure 12 refers to the experimental results of [Com05b] for the detection of clay fraction inclusions within a sand matrix. Areas where a clay fraction is present are evidenced as areas of higher conductivity. This higher conductivity is explained in terms of contribution of the surface conductivity to the electrical conductivity of clays, a contribution not present in sand.

Shape and position of the conductive inclusions are correctly evaluated and the accuracy of the geometric pattern is actually governed by the size of the element of the FEM mesh. Quantitative evaluation of the local electrical conductivity is not reliable in presence of sharp electrical gradients (as shown in Figure 12a and 12b). It can be noticed that in the reconstructions the sand portion around the kaolin cylinders seems to have a higher electrical conductivity than the remaining sand. This is clearly an artefact, since the sand was prepared homogeneously. Reason for this artefact comes mainly from the regularisation term in the inversion algorithm (Equation 13), that was chosen so to favour stability of the solution rather than its accuracy.

In practical terms, quantitative estimation can anyway be attempted, provided that gradients in the electrical conductivity of the investigated body are relatively modest. Figure 13 shows the interpretation of a test where Ticino sand was prepared at two different densities [Bor05]. Sand was compacted at porosity $n \approx 0.43$ within the cylinder (inclusion) evidenced as a dotted circle in Figure 13a and at porosity $n \approx 0.48$ outside that cylinder. Differences between local values of electrical conductivity appreciated in the ERT reconstruction are very small. Average porosities were then estimated on basis of reconstructed conductivity, since the electrical conductivity of the pore water was independently measured and Archie's exponent m was imposed equal to 1.5. Estimated values were $n \approx 0.42$ for the inclusion and $n \approx 0.46$ for the rest of the sample: such types of results pave the way for the quantitative use of ERT for local evaluations during hydro-chemo-mechanical tests.

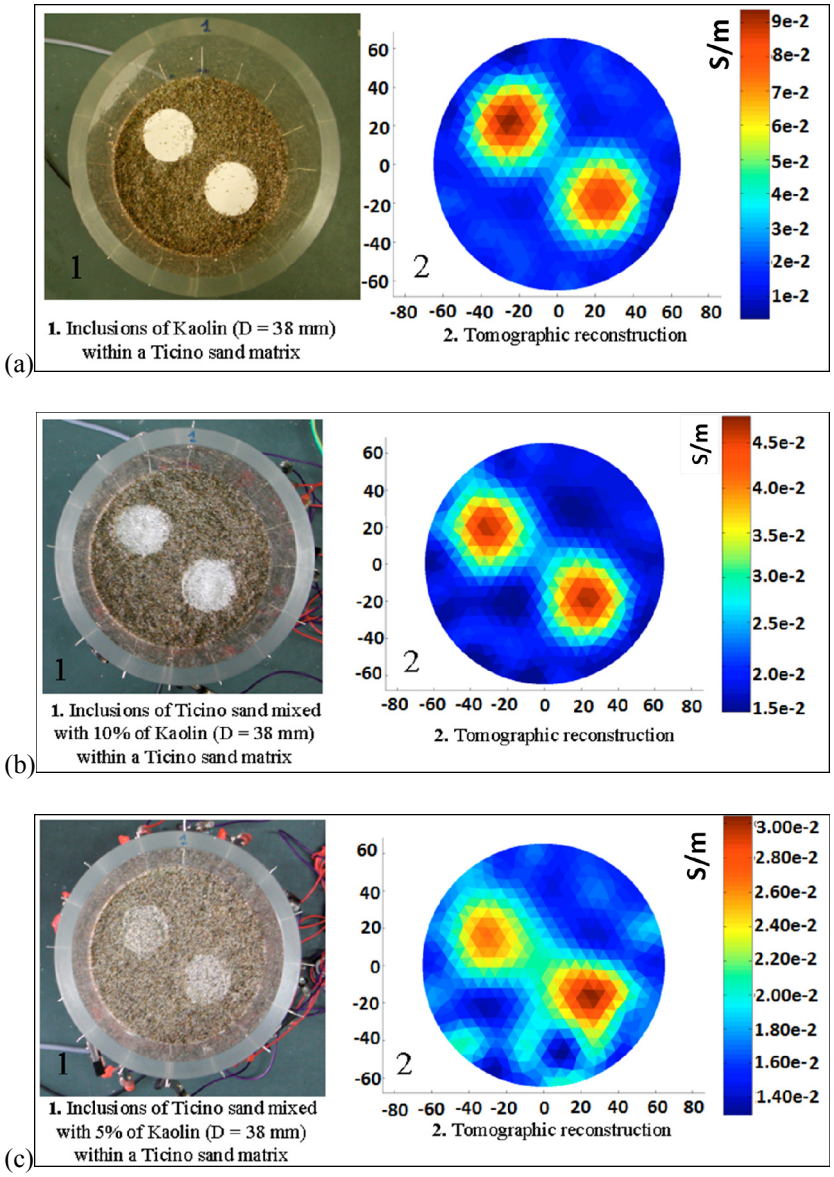

Figure 12: ERT maps of soil electrical conductivity of sand samples with inclusions of clay [Com05b] (axis units are mm).

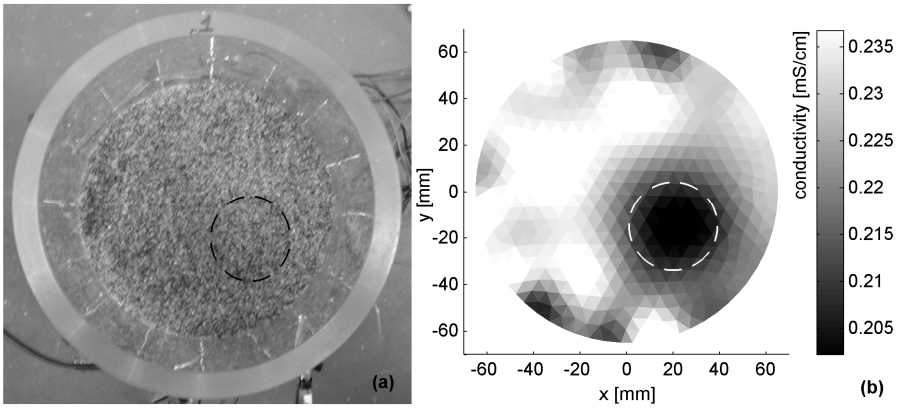

Figure 13: Cylindrical inclusion of compacted sand within a loose sand sample (a); ERT reconstruction (b) [Bor05].

4 Acknowledgements

Guido Musso thanks Cesare Comina (Università degli Studi di Torino) and Sebastiano Foti (Politecnico di Torino) for the joint work aimed at developing and performing ERT tests at laboratory scale at Politecnico di Torino.

5 References

[Abe99] Abell, A.B., Willis, K.L. & Lange, D.A. Mercury intrusion porosimetry and image analysis of cement-based materials. *Journal of Colloid and Interface Science*, *211, 39-44*, 1999.

[Abr04] Abramoff, M.D., Magalhaes, P.J., and Ram, S.J. Image processing with image. *J. Biophotonics International, 11(7), 36-41*, 2004.

[Ahm74] Ahmed, S., Lovell, C.W. & Diamond, S. Pore sizes and strength of compacted clay. *J. Geotech. Eng. Div., ASCE, 100(4), 407-425*, 1974.

[Air10] Airò Farulla, C., Ferrari, A. & Romero. Volume change behaviour of a compacted scaly clay during cyclic suction changes. *Canadian Geotechnical Journal, 47(6), 688-703*, 2010. DOI: 10.1139/T09-138

[Aït04] Aït-Mokhtar, A., Amiri, O., Dumargue, P. & Bouguerra, A. On the applicability of Washburn law: study of mercury and water flow properties in cement-based materials. *Materials and Structures*, *37, 107-113*, 2004.

[AlM96] Al-Mukhtar, M. Belanteur, N. Tessier D. & Vanapalli, S.K. The fabric of clay soil under controlled mechanical and hydraulic stresses. *Applied Clay Science, 11(2-4), 99-115,* 1996.

[And12] Andò, E., Hall, S.A., Viggiani, G., Desrues, J. & Bésuelle, P. Grain-scale experimental investigation of localised deformation in sand: a discrete particle tracking approach. *Acta Geotechnica, 7(1), 1-13,* 2012. DOI: 10.1007/s11440-011-0151-6.

[Aun01] Aung, K.K., Rahardjo, H., Leong, E.C. & Toll, D.G. Relationship between porosimetry measurement and soil-water characteristic curve for an unsaturated residual soil. *Geotechnical and Geological Engineering, 19, 401-416*, 2001.

[Bak90] Baker, J.M. & Allmaras, R.R. System for automating and multiplexing soil moisture measurement by time-domain reflectometry. *Soil Sci. Soc. Am. J., 54(1), 1-6*, 1990.

[Bak95] Baker, J.C., Grabowska-Olszewska, B. & Uwins, P.J.R. ESEM study of osmotic swelling of bentonite from Radzionkow (Poland). *Applied Clay Science, 9, 465-469,* 1995.

[Bar51] Barrett, E.P., Joyner, L.G. & Halenda, P.P. (1951). The determination of pore volume and area distributions in porous substances. I. Computations from nitrogen isotherms. J. Am. Chem. Soc. 1951, 73 (5), 373–380.

[Bés06] Bésuelle, P., Viggiani, G., Lenoir, N., Desrues, J. & Bornert, M. X-ray micro CT for studying strain localization in clay rocks under triaxial compression. *Advances in X-ray tomography for geomaterials*. J. Desrues, G. Viggiani & P. Bésuelle (eds.). ISTE Ltd, London, UK, 35-52, 2006.

[Bev91] Bevc, D., Morrison, H.F. Borehole-to-surface electrical resistivity monitoring of a salt water injection experiment. *Geophysic, 56, 769–777*, 1991.

[Bin96] Binley A., Henry-Poulter S. and Shaw B. Examination of solute transport in an undisturbed soil column using electrical resitance tomography. *Water Resources Research, 32(4), 763-769,* 1996.

[Bor02] Borsic A., Lionheart W. R. B. and McLeod C. N. Generation of anisotropic-smoothness regularisation filters for EIT. *IEEE Transactions on Medical Imaging, 21(6), 579-587*, 2002.

[Bor05] Borsic, A., Comina, C., Foti, S., Lancellotta, R. & Musso, G. Imaging heterogeneities with electrical impedance tomography: laboratory results. *Géotechnique, 55(7), 539-547*, 2005.

[Bre90] Breckon W. R. *Image Reconstruction in Electrical Impedance Tomography*, PhD thesis, Oxford Brookes Polytechnic, 1990.

[Bri98] Briggs, K.B., Jackson, P.D., Holyer R.J., Flint R.C., Sandidge, J.C. and Young, D.K. Two-dimensional variability in porosity, density, and electrical resistivity of Eckernförde Bay sediment. *Continental Shelf Research, 18, 1939-1964,* 1998.

[Car06] Carminati, A., Kaestner, A., Hassanein, R. & Koliji, A. Hydraulic properties of aggregate-aggregate contacts. *Advances in X-ray tomography for geomaterials.* J. Desrues, G. Viggiani & P. Bésuelle (eds.). ISTE Ltd, London, UK, 325-331, 2006.

[Cas92] Cases, J.M., Beraend, I., Besson, G., Francois, M., Uriot, J.P., Thomas, F. & Poirer, J.E. Mechanism of adsorption and desorption of water vapor by homoionic montmorillonite I. The sodium exchanged form. *Langmuir, 8, 2730–2739,* 1992.

[Com05a] Comina C. Imaging Heterogeneities and Diffusion in sand Samples - Electric and Seismic methods. Phd Thesis, Politecnico di Torino, Torino, 2005.

[Com05b] Comina C., Foti S, Lancellotta R, Musso G. and Borsic A. Imaging heterogeneities and diffusion in sand samples. *Proceedings of the XIth IACMAG,* Torin, 27-34, 2005.

[Com08] Comina, C., Foti, S., Musso, G. & Romero, E. EIT oedometer - an advanced cell to monitor spatial and time variability in soil with electrical and seismic measurements. *Geotechnical Testing Journal, 31(5), 404-412*, 2008. DOI: 10.1520/GTJ101367

[Com10] Comina C., Cosentini R.M., Foti S. and Musso, G. Electrical Tomography as laboratorymonitoring tool. *Rivista Italiana di Geotecnica, 1, 9-20,* 2010.

[Cos12] Cosentini, R.M., Della Vecchia, G., Foti, S. & Musso, G. Estimation of the hydraulic parameters of unsaturated samples by electrical resistivity tomography. *Géotechnique, 62(7), 583-594,* 2012. DOI: 10.1680/geot.10.P.0662012

[Dai92] Daily, W.D., Ramirez, A.L., LaBrecque, D.J., and Nitao, J. Electrical resistivity tomography of vadose water movement. *Water Resour. Res., 28, 1429–1442,* 1992.

[Dam09] Damasceno, V.M., Fratta, D. & Bosscher, P.J. Development and validation of a low-cost electrical tomographer for soil process monitoring. *Canadian Geotechnical Journal, 4, 842-854,* 2009.

[Dan93] Danilatos, G.D. Introduction to the ESEM instrument. *Microscopy Research and Technique, 25, 354-361,* 1993.

[Del82] Delage, P., Tessier, D. & Audiguier, M.M. Use of the cryoscan apparatus for observation of freeze-fractured planes of a sensitive Quebec clay in scanning electron microscopy. *Canadian Geotechnical Journal,19, 111-114*, 1982.

[Del84a] Delage, P. & Lefebvre, G. Study of the structure of a sensitive Champlain clay and of its evolution during consolidation. *Canadian Geotechnical Journal, 21, 21-35,* 1984.

[Del84b] Delage, P. & Pellerin, M. Influence de la lyophilisation sur la structure d'une argile sensible du Quebec. *Clay Minerals, 19, 151-160,* 1984.

[Del96] Delage, P., Audiguier M., Cui, Y.J. & Howatt, M.D. Microstructure of a compacted silt. *Canadian Geotechnical Journal, 33, 150-158,* 1996.

[Des06] Desrues, J., Viggiani, G. & Bésuelle, P. (Editors). *Advances in X-ray tomography for geomaterials.* ISTE Ltd, London, UK, 2006.

[Dia70] Diamond, S. Pore size distribution in clays. *Clays and clay minerals, 18, 7-23,* 1970.

[Fad96] Fadeev, A.Yu., Borisova, O.R. & Lisichkin, G.V. Fractality of porous silicas: a comparison of adsorption and porosimetry data. *Journal of Colloid and Interface Science, 183, 1-5,* 1996.

[Gar10] Garzón, E., Sánchez-Soto, P.J. & Romero, E. Physical and geotechnical properties of clay phyllites. *Applied Clay Science, 48, 307–318*, 2010.

[Geb06] Gebrenegus, T., Tuller, M- & Muhuthan, B. The application of X-ray computed tomography for characterisation of surface crack networks in bentonite-sand mixtures. *In: Advances in X-ray tomography for geomaterials*. J. Desrues, G. Viggiani & P. Bésuelle (eds.). ISTE Ltd, London, UK, 207-212, 2006.

[Gim97] Giménez, D., Perfect, E., Rawls, W.J. & Pachepsky, Ya. Fractal models for predicting soil hydraulic properties: a review. *Engineering Geology, 48, 161-183,* 1997.

[Hof75] Hoffman, R. A study of the advancing interface. Interface shape in liquid—gas systems. *Journal of Colloid and Interface Science, 50, 228-241,* 1975.

[Jac90] Jackson, P. D., Lovell, M. A., Pitcher, C., Green, C. A., Evans, C. J., Flint, R., and Forster, A. Electrical resistivity imaging of core samples. *In: Advances in core evaluation*. Worthington P.F. (ed.). Gordon and Breach Science Publishers, New York, 365-378, 1990.

[Jac02] Jackson P.D., Briggs. K. B., Flint, R.C., Holyer, R.J. and Sandidge, J.C. Two- and three-dimensional heterogeneity in carbonate sediments using resistivity imaging. *Marine Geology, 182, 55 – 76,* 2002.

[Jom03] Jommi, C. & Sciotti, A. A study of the microstructure to assess the reliability of laboratory compacted soils as reference material for earth constructions. *In: System-based Vision for Strategic and Creative Design*. F. Botempi (ed.). A.A. Balkema, Lisse, 3, 2409-2415, 2003.

[Jua86] Juang, C.H. & Holtz, R.D. A probabilistic permeability model and the pore size density function. *Int. J. Numer. Anal. Meth. Geomech., 10, 543-553,* 1986.

[Kar07] Karpyn, Z.T. & Piri, M. Prediction of fluid occupancy in fractures using network modeling and X-ray microtomography. Part 1: Data Conditioning and Model Description. *Physical Review E, 76, 016315*, 2007. DOI:10.1103/PhysRevE.76.016315.

[Kho12] Khoshbakht, F., Azizzadeh, M., Memarian, H., Nourozi, G. H. and Moallemi, S. A. Comparison of electrical image log with core in a fractured carbonate reservoir. *J. of Petroleum Science and Engineering, 86–87, 289-296,* 2012.

[Kol01] Kolehmainen V. *Novel Approaches to Image Reconstruction in Diffusion Tomography,* PhD thesis, Department of Applied Physics - Kuopio University, 2001.

[Kol06a] Koliji, A., Carminati, A., Kaestner, A., Vulliet, L., Laloui, L., Fluehler, H., Vontobel, P. & Hassanein, R. Experimental study of flow and deformation in aggregated soils using neutron tomography. *Advances in X-ray tomography for geomaterials.* J. Desrues, G. Viggiani & P. Bésuelle (eds.). ISTE Ltd, London, UK, 341-348, 2006.

[Kol06b] Koliji, A., Laloui, L., Cuisinier, O. & Vulliet, L. Suction induced effects on the fabric of a structured soil. *Transport in Porous Media, 64, 261-278*, 2006.

[Kom99] Komine, H., & Ogata, N. Experimental study on swelling characteristics of sand–bentonite mixture for nuclear waste disposal. *Soils and Foundations, 39(2), 83–97,* 1999.

[Kor92] Korvin, G. *Fractal models in the earth sciences*. Elsevier, Amsterdam, 1992.

[Law78] Lawrence, G.P. Stability of soil pores during mercury intrusion porosimetry. *J. Soil Science*, *29, 299-304*, 1978.

[Lee10] Lee, J. Y. and Santamarina, J. C. Electrical Resistivity Tomography in Cylindrical Cells—Guidelines for Hardware Pre-Design. *Geotechnical Testing Journal, 33(1), Paper ID GTJ102366,* 2010.

[Lov05] Lovell, M., Jackson, P., Flint, R. and Harvey, P.K. Fracture mapping with electrical core images. *Geological Society, London, Special Publications, (240), 107-115,* 2005. DOI:10.1144/GSL.SP.2005.240.01.09

[Low04] Lowell, S., Shields, J.E., Thomas, M.A. & Thommes, M. *Characterization of porous solids and powders: Surface area, pore Size and Density*. Springer Netherlands, 2004.

[Lyt78] Lytle, R.J. and Dines, K.A. *An impedance camera: a system for determining the spatial variation of electrical conductivity*. Report UCRL-52413. Lawrence Livermore Lab., Livermore, CA, 1978.

[Man12] Manahiloh, K.N. & Muhunthan, B. Characterizing liquid phase fabric of unsaturated specimens from X-ray Computed Tomography images. *Proc. 2nd European Conf. on Unsaturated Soils*, Napoli, Italy, 20-22 June 2012. Unsaturated Soils: Research and Applications. C. Mancuso, C. Jommi & F. D'Onza (eds.). Springer, Heidelberg, 1, 71-80, 2012.

[Mat95] Matthews, G.P., Ridgway, C.J. & Spearing, M.C. Void space modelling of mercury intrusion hysteresis in sandstone, paper coating, and other porous media. *Journal of Colloid and Interface Science, 171, 8-27,* 1995.

[Mey94] Meyer, K., Lorenz, P., Böhl-Kuhn, B. & Klobes, P. Porous solids and their characterization. Methods of investigation and application. *Cryst. Res. Technol., 29 (7), 903-930,* 1994.

[Mit05] Mitchell, J.K. & Soga, K. *Fundamentals of soil behaviour* (3rd edition). John Wiley & Sons, Inc. New Jersey, 2005.

[Mon03a] Montes-H, G., Duplay, J., Martinez, L. & Mendoza, C. Swelling-shrinkage kinetics of MX80 bentonite. *Applied Clay Science, 22, 279-293,* 2003.

[Mon03b] Montes-H, G., Duplay, J., Martinez, L., Geraud, Y. & Rousset-Tournier, B. Influence of interlayer cations on the water sorption and swelling-shrinkage of MX80 bentonite. *Applied Clay Science, 23, 309-321,* 2003.

[Mor02] Moro, F. & Böhni, H. Ink-bottle effect in mercury intrusion porosimetry of cement-based materials. *Journal of Colloid and Interface Science*, *246, 135-149*, 2002.

[Muk06] Mukunoki, T., Otani, J., Maekawa, A., Camp, S. & Gourc, J.P. Investigation of crack behaviour on cover soils at landfill using X-ray CT. *In: Advances in X-ray tomography for geomaterials*. J. Desrues, G. Viggiani & P. Bésuelle (eds.). ISTE Ltd, London, UK, 213-219, 2006.

[Mus03] Musso, G., Romero, E., Gens, A. & Castellanos, E. The role of structure in the chemically induced deformations of Febex bentonite. *Applied Clay Science, 23, 229-237*, 2003.

[Osi95] Osiensky, J.L., Donaldson, P.R. Electrical flow through an aquifer for contaminant source leak detection and delineation of plume evolution. *Journal of Hydrology, 169, 243–263*, 1995. DOI:10.1016/0022-1694(94)02610-N

[Pen00] Penumadu, D. & Dean J. Compressibility effect in evaluating the pore size distribution of kaolin clay using mercury intrusion porosimetry. *Canadian Geotechnical Journal, 37, 393-405*, 2000.

[Pir07] Piri, M. & Karpyn, Z.T. Prediction of fluid occupancy in fractures using network modeling and X-ray microtomography. Part 2: Results. *Physical Review E, 76, 016316*, 2007. DOI:10.1103/PhysRevE.76.016316

[Pol02] Polydorides N. and Lionheart W. R. B. A Matlab toolkit for three-dimensional electrical impedance tomography: a contribution to the Electrical Impedance and Diffuse Optical Reconstruction Software project. *Meas. Sci. Technol., 13(12), 1871-1883*, 2002.

[Pra85] Prapaharan, S., Altschaeffl, A.G. & Dempsey, B.J. Moisture curve of a compacted clay: mercury intrusion method. *J. Geotech. Engrg., ASCE, 111(9), 1139-1143*, 1985.

[Ree79] Reed, M.A., Lovell, C.W., Altschaeffl, A.G, & Wood, L.E. Frost-heaving rate predicted from pore-size distribution. *Canadian Geotechnical Journal*, *16, 463-472*, 1979.

[Rie12] Riedel, I., Andò, E., Salager, S., Bésuelle, P. & Viggiani, G. Water retention behaviour explored by X-ray CT analysis. *Proc. 2nd European Conf. on Unsaturated Soils*, Napoli, Italy, 20-22 June 2012. Unsaturated Soils: Research and Applications. C. Mancuso, C. Jommi & F. D'Onza (eds.). Springer, Heidelberg, 1, 81-88, 2012

[Rod06] Rodríguez-Rey, A., Ruiz de Argandoña, V.G., Calleja, L., Suárez del Río, L.M. & Velorio, C. Consolidants influence on sandstone capillarity. X-ray study. *Advances in X-ray tomography for geomaterials*. J. Desrues, G. Viggiani & P. Bésuelle (eds.). ISTE Ltd, London, UK, 381-387, 2006.

[Rol05] Rolland, S., Stemmelen, D., Moyne, C & Masrouri, F. Experimental hydraulic measurements in an unsaturated swelling soil using the dual-energy gamma-ray technique. *Proc. Int. Symposium on Advanced Experimental Unsaturated Soil Mechanics*, Trento, Italy, 27-29 June 2005. In: Advanced Experimental Unsaturated Soil Mechanics. A. Tarantino, E. Romero & Y.J. Cui (eds.). Taylor & Francis Group, London, 305-310. 2005.

[Rom99] Romero, E. Gens, A. & Lloret, A. Water permeability, water retention and microstructure of unsaturated Boom clay. *Engineering Geology, 54, 117-127*, 1999.

[Rom08] Romero, E. & Simms, P.H. Microstructure investigation in unsaturated soils: a review with special attention to contribution of mercury intrusion porosimetry and environmental scanning electron microscopy. *Geotechnical and Geological engineering, 26(6), 705-727*, 2008. DOI: 10.1007/s10706-008-9204-5.

[Rom11] Romero, E., Della Vecchia, G. & Jommi, C. An insight into the water retention properties of compacted clayey soils. *Géotechnique, 61(4), 313-328*, 2011. Doi: 10.1680/geot.2011.61.4.313

[Rom12] Romero, E., Senger, R., Marschall, P. & Gómez, R. Air tests on low-permeability claystone formations. Experimental results and simulations. Theme lecture. *Int. Workshop 'AMTSS - Advances in Multiphysical Testing of Soils and Shales'*, EPFL Lausanne (Switzerland), 3 - 5 September 2012.

[Sen09] Sentenac, P. and Zielinski, M. Clay fine fissuring monitoring using miniature geo-electrical resistivity arrays. *Journal Environmental Earth Sciences, 59(1), 205-214*, 2009. DOI:10.1007/s12665-009-0017-5.

[Sil73] Sills, I.D., Aylmore, L.A.G. & Quirk, J.P. A comparison between mercury injection and nitrogen sorption as methods of determining pore size distribution. *Proceedings of the Soil Science Society of America, 37, 535-537,* 1973.

[Sim01] Simms, P.H. & Yanful, E.K. Measurement and estimation of pore shrinkage and pore distribution in a clayey till during soil-water characteristic curve tests. *Canadian Geotechnical Journal, 38, 741-754*, 2001.

[Sim02] Simms, P.H. & Yanful, E.K. Predicting soil-water characteristic curves of compacted plastic soils from measured pore-size distributions. *Géotechnique, 52(4), 269-278*, 2002.

[Sim04] Simms, P.H. & Yanful, E.K. A discussion of the application of mercury intrusion porosimetry for the investigation of soils, including an evaluation of its use to estimate volume change in compacted clayey soils. *Géotechnique, 54(6), 421-426,* 2004.

[Sim05] Simms, P.H. & Yanful, E.K. A pore-network model for hydromechanical coupling in unsaturated compacted clayey soils. *Canadian Geotechnical Journal, 42, 499-514*, 2005.

[Sla97] Slater, L., Binley, A. and Brown, D. Electrical imaging of fractures using ground-water salinity change. *Groundwater 35, 436–442, 1997.*

[Som92] Somersalo, E., Cheney, M. and Isaacson, D. Existence and uniqueness for electrode models for electric current computed tomography. *SIAM J. Appl. Math. 52(4), 1023–1040*, 1992.

[Syl87] Sylvester, J. and Uhlman, G.. A global uniqueness theorem for an inverse boundary value problem. *Ann. Math., 125, 153 – 169,* 1987.

[Tak06] Takahashi, M., Takemura, T., Hirai, H., Murakoshi, A. & Kato, M. Spatial and density resolution in microfocus X-ray CT applied to studies of microstructural changes in rocks with increasing hydrostatic pressure. *In: Advances in X-ray tomography for geomaterials*. J. Desrues, G. Viggiani & P. Bésuelle (eds.). ISTE Ltd, London, UK, 421-427, 2006.

[Vau97] Vauhkonen M. *Electrical Impedance Tomography and Prior Information*. PhD thesis, Kuopio University, 1997.

[Van05] Van Geet, M., Volckaert, G. & Roels, S. The use of microfocus X-ray computed tomography in characterising the hydration of a clay pellet / powder mixture. *Applied Clay Science, 29, 73– 87,* 2005.

[Web97] Webb, P.A. & Orr, C. *Analytical methods in fine particle technology.* Micromeritics Instrument Corp, Norcross, 1997.

[Whi94] White, P.A.. Electrode arrays for measuring groundwater flow direction and velocity. *Geophysics, 59, 192–201,* 1994.

Experimental techniques for hydro-mechanical and electro-chemo-hydraulic processes

Enrique Romero*-Guido Musso-Cristina Jommi*****

** Universitat Politècnica de Catalunya*
Department of Geotechnical Engineering and Geosciences
c/ Jordi Girona, 1-3, Campus Nord UPC, Building D-2
08034 Barcelona - Spain
enrique.romero-morales@upc.edu

***Politecnico di Torino*
Dipartimento di Ingegneria Strutturale, Edile e Geotecnica
Corso Duca degli Abruzzi, 24
10129 Torino, Italy

****Politecnico di Milano*
Dipartimento di Ingegneria Strutturale
piazza Leonardo da Vinci, 32
20133 Milano, Italy

This chapter presents the fundamentals behind selected experimental techniques used to control and monitor some coupled multi-physics processes. The starting point is the review of the experimental techniques for coupled hydro-mechanical testing (liquid and vapour transfer techniques). Then, fundamentals of physical processes related to electrical techniques for the characterisation of geomaterials and for the induction of coupled electro-chemo-hydraulic processes are provided. Complementary aspects concerning the application of these techniques and some of their limitations are also discussed. Selected data from tests on a clayey silt in an electrokinetic oedometer are finally shown, to provide evidence of some effects of the coupled electro-chemo-hydraulic response of soils.

1 Introduction

The extension of geotechnical engineering applications and the research interest in multi-physics processes are becoming wider in recent years, mainly within the context of geoenvironmental, energy production, and geosciences areas. Topics such as crystal growth in geomechanics, natural risk analyses (fast sliding processes along faults and landslide surfaces), biological soil improvement, geothermal energy exploitation, waste confinement (at surface or at great depths using engineered barriers or host geological formations), soil pollution and remediation, carbon dioxide sequestration in geological formations, oil field subsidence phenomena and assessment of seals in hydrocarbon production, to cite but a few of them, are increasingly coming into prominence. These new fields of application require the incorporation of relevant and coupled thermo-hydro-chemo-bio-electro-mechanical phenomena, the evolution of which must be examined over important periods of time, and the introduction of new constitutive variables for a deeper understanding of the behaviour of geomaterials. Progress in these areas requires advanced experimental techniques, fundamental developments and numerical modelling, as well as detailed examination of well documented field cases. Within this context, the present chapter introduces selected experimental techniques to investigate hydro-mechanical and electro-chemo-hydraulic processes. The fundamental bases are first introduced, followed by descriptions on how these techniques are implemented. Complementary aspects concerning some of their limitations are also presented.

2 Hydro-mechanical processes

2.1 Introduction

This section focuses on the description of two widely used techniques to transfer and control the amount of water inside a porous medium; namely

- Axis translation technique that predominantly transfers (and controls) liquid phase through an interface permeable to dissolved salts, and that is related to the control of matric suction (i.e., difference between the gas and liquid phases); and
- Vapour equilibrium technique to transfer vapour through the gas phase, which is associated with the control of the relative humidity or total suction.

2.2 Axis translation technique for controlling liquid transfer

Axis translation is one of the most commonly used techniques for controlling matric suction, together with osmotic technique. The reader interested in osmotic technique is referred to [Del08a, Del08b, Tan11 and Bla08]. The pressure plate outflow technique is an early example of the use of axis translation technique [Ric41, Gar56].

This technique is associated with the matric suction component, in which water potential is controlled by liquid phase transfer through a saturated interface –usually saturated high air-entry value (HAEV) ceramic disk or saturated symmetric cellulose acetate membrane– that is permeable to dissolved salts. The procedure involves the translation of the reference pore air pressure, through an artificial increase of the atmospheric pressure Δu_a in which the soil is immersed. The procedure is described in Figure 1 for a setup corresponding to an isotropic cell with HAEV ceramic disk at the bottom and coarse porous disk at the top. Consequently, the negative pore water pressure increases by an equal amount if incompressibility of soil particles and water is assumed –i.e., if the curvature of the menisci is not greatly affected–. This translation of the pore water pressure into the positive range allows its measurement [Hil56], and consequently, its control if water pressure is regulated through a saturated interface in contact with the sample. To cover a wide matric suction range, the soil should preferably present a lower air-entry value than the corresponding one of the ceramic disk. To ensure that the top boundary presents no water flow condition, the top coarse porous disk should display a very low air-entry value (this ensures that no water is stored when applying matric suction), as indicated in Figure 1. Alternative combinations of porous disks can be used in a single cap; for example by surrounding the ceramic disk by a coarse porous ring through which air pressure is applied. Axis translation technique has been experimentally evaluated with soils having a continuous air phase and a degree of saturation varying between 0.76 and 0.95 by [Fre77] and by [Tar00] for degrees of saturation between 0.56 and 0.77. Further details of the physical fundamentals and implementation of the technique can be found in [Del08a, Hoy08, Mar08, Mas08 and Van08].

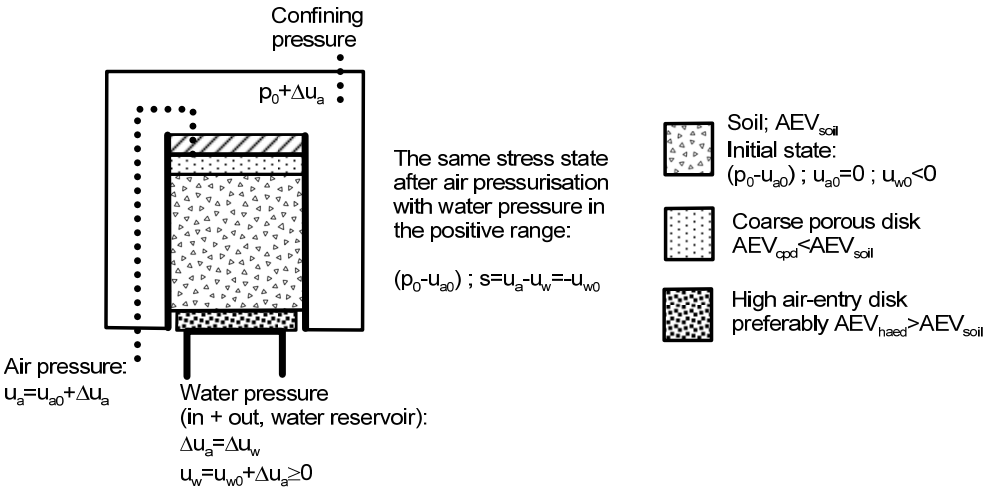

Figure 1: Axis translation application in an isotropic cell with bottom HAEV ceramic disk and top coarse porous disk.

Axis translation technique has been criticised concerning the following aspects: a) it

is not representative of field conditions, where air pressure is usually under atmospheric conditions (some authors have argued that axis translation alters soil behaviour by preventing cavitation; see for instance [Bak09]); b) there are some doubts in how the air pressurisation process affects the water pressure when water is held by adsorption mechanisms; and, finally c) it is not clear its application at nearly saturated states in the absence of a continuous gaseous phase. Nevertheless, axis translation technique has proved to provide reasonable results and a good continuity between vapour equilibrium results at elevated suctions and nearly saturated states. An example can be found in Figure 2, in which the overall picture of water retention results under constant volume conditions of an artificially prepared expansive clay (with pellets of Febex bentonite) were obtained by combining different techniques (transistor psychrometers and vapour control technique) jointly with axis translation [Hof05]. A recent benchmark aimed at comparing different experimental techniques for controlling/measuring suction (axis translation, osmotic technique, high-capacity tensiometer and dew-point psychrometer) on a mixture of kaolinite, bentonite and sand (reference soil), was presented by [Tar11]. The same techniques were tested by different laboratories and similar results were obtained for the water retention curves of the reference soil, which gives further confidence on the use of this technique.

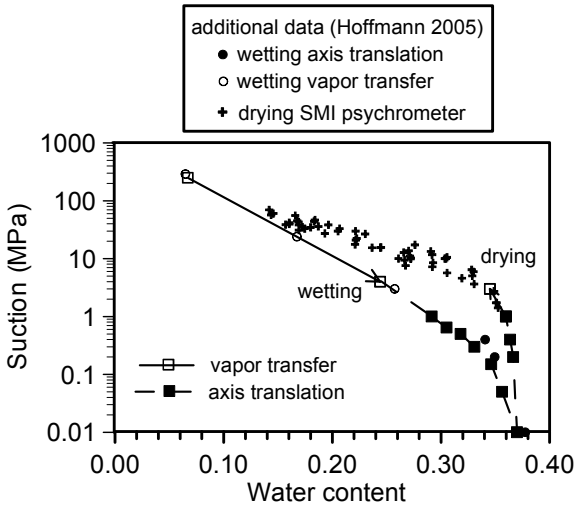

Figure 2: Water retention curves obtained by combining axis translation with other techniques [Hof05].

Main experimental difficulties concerning axis translation application are associated with the accumulation of diffused air beneath the HAEV ceramic disk, the control of the relative humidity of the air chamber to minimise evaporation or condensation effects on the sample, the application of the air pressurisation process at elevated degrees of saturation, and the estimation of the equalisation time.

In relation to air diffusion problems through the saturated porous network of the interface, it can induce the progressive loss of continuity between the pore water and the water in the control system. In addition, the accumulation of air can lead to water volume change errors in drained tests and pore-water pressure measurement errors in undrained tests. Consequently, an auxiliary device is required to flush periodically air bubbles accumulated below the HAEV ceramic. The following expression describes the rate of accumulation of dissolved air beneath the ceramic disk, which is based on the gradient of air concentration being the driving mechanism [Fre93, Rom99]:

$$\frac{dV_d}{dt} = \frac{n\,A\,D\,h\,(u_a - u_w)}{(u_w + u_{atm})\,t_c} \tag{1}$$

where n, A and t_c, represent the porosity (usually between 0.32 and 0.38 for commercial ceramics), the cross-sectional area and the disk thickness, respectively. h, is the volumetric coefficient of solubility of dissolved air in water (h=0.018 at 22°C), and D, the diffusion coefficient through the saturated interface. u_{atm}, represents the absolute atmospheric pressure; u_a and u_w refer to air and water gauge pressures. The quantification of air diffusion has been recently carried out by [Rom01a, DeG02, Air05 and Pad06]. Lawrence et al. [Law05] presented a pressure pulse technique for measuring diffused air volume using pressure/volume controllers. Figure 3a presents values of the coefficient of diffusion of air through a saturated ceramic disk with a nominal air-entry value of 1.5 MPa as a function of applied matric suction. Typical values are in the range between 3×10^{-11} and 2×10^{-10} m^2/s (for suctions < 0.7 MPa), lower than the values of diffusion of air in water (around 2.2×10^{-9} m^2/s at 20°C). Factors such as tortuosity of the paths and breakdown of Henry's law in a curved air-water interface can be associated with this reduction [Bar67]. The figure shows how this coefficient tends to increase as suction increases over 0.7 MPa and gets closer to the air-entry value of the ceramic (the value at which the gas convection transport is initiated). Figure 3b shows the pore size density function of a HAEV ceramic (nominal air-entry value 1.5 MPa and porosity 0.324) obtained by mercury intrusion porosimetry, in which a dominant pore size mode of 81 nm is obtained. The water retention curve obtained by mercury intrusion porosimetry of the ceramic is shown in Figure 3c. An air-entry value between 1.6 and 2 MPa is detected, which is slightly larger than the nominal value. Despite this higher value, the important air diffusion rates at suctions > 1 MPa indicate that the technique has some practical limitations when commercial ceramics are used. As deduced from Equation (1), increasing the water pressure is an efficient way to reduce air diffusion rates for a given geometry of the interface element and for specified matric suction. The conventional technique of the pressure plate apparatus, in which the pressure of water is maintained under atmospheric conditions, is the less efficient configuration to control the diffusion of air.

Concerning the second phenomenon of vapour transfer between the soil and the surrounding air, it can be controlled by maintaining an adequate relative humidity in

the air chamber (around 95%). Evaporative fluxes are originated due to the difference in vapour pressure between the soil surface and the air chamber. Volumetric evaporative fluxes can be detected in the water volume change device as a non-stop inflow to the soil under steady-state conditions. Condensation of vapour in the internal walls of the pressure chamber due to temperature variations has also been reported by [Oli06].

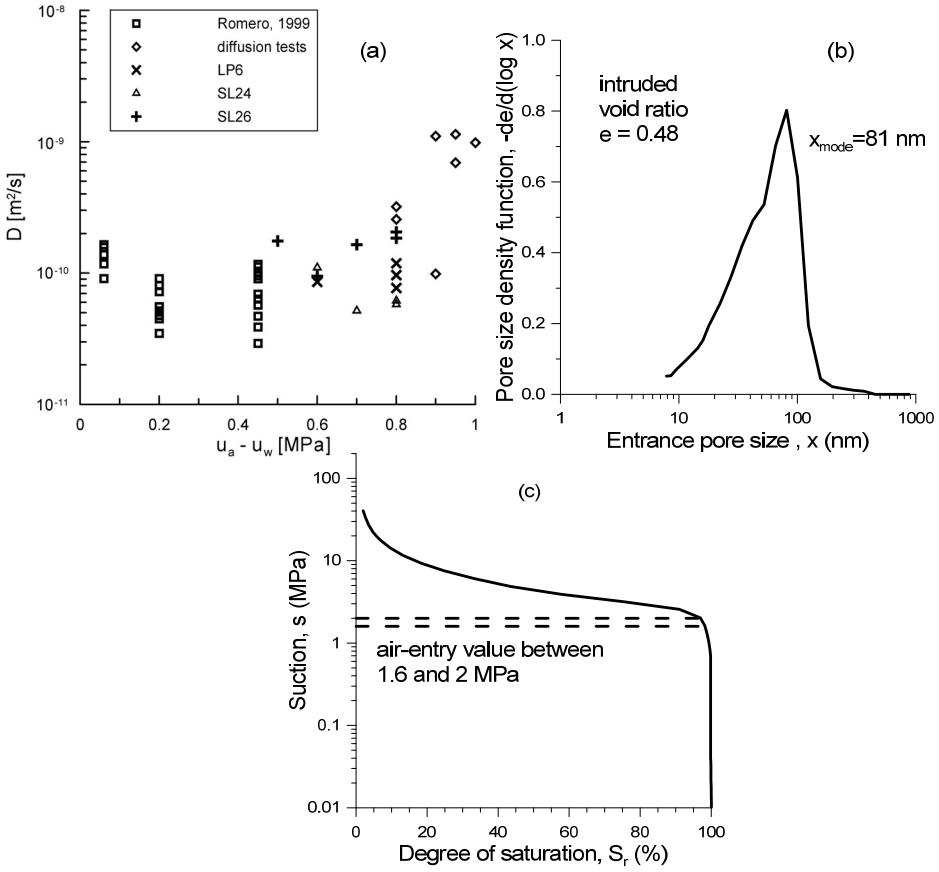

Figure 3: a) Diffusion coefficients for air through saturated ceramic disk (nominal air-entry value 1.5 MPa) for different matric suctions [Air05]. b) Pore size density function of HAEV ceramic disk (nominal air-entry value 1.5 MPa). c) Water retention curve of HAEV ceramic disk obtained by mercury intrusion porosimetry (nominal air-entry value 1.5 MPa).

Measured volumetric evaporative fluxes at different porosities are presented in Figure 4 for compacted clay inside an air chamber at an initial relative humidity h_{r0}=0.50. As shown in the scheme, two different water fluxes are involved in the process: a) an evaporative flux that dries the clay surface (dependent on soil proper-

ties –mainly vapour diffusivity– and on boundary conditions –h_r of air chamber above the evaporating surface–), and b) a liquid flux through the ceramic disk that regulates the applied matric suction and depends on soil and ceramic disk water permeability.

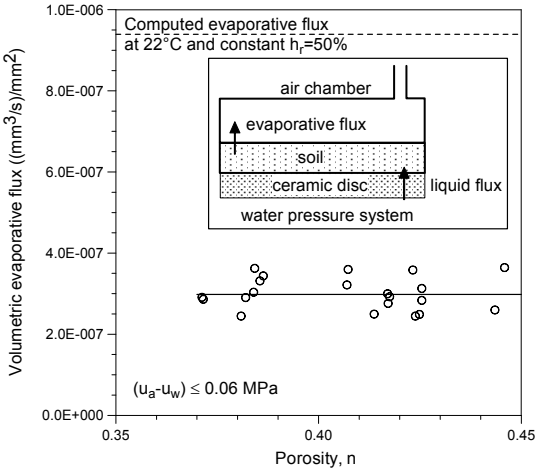

Figure 4: Measured volumetric evaporative fluxes [Rom99].

A series of 1-D numerical analyses using Code_Bright [Oli96] was carried out by [Rom99] to simulate evaporative fluxes and matric suction evolution during a wetting path performed on compacted clay. The analysis took into account liquid phase flow by Darcy's law and vapour diffusion according to Fick's law. The clay saturated permeability was 8.3×10^{-12} m/s, with the following power expression for the liquid relative permeability: $k_{rl} = S_e^{2.89}$ (the effective saturation is computed as $S_e = (S_r - 0.087)/0.913$, where S_r is the degree of saturation). S_e is computed as a function of matric suction: $S_e = [1+((u_a-u_w)/P)^{1/(1-\lambda)}]^{-\lambda}$, where $\lambda = 0.156$ and $P = 0.03$ MPa. The ceramic disk displayed a saturated permeability of 1.3×10^{-10} m/s. A tortuosity factor of 0.30 was considered, which accounts for complexities in pore geometry affecting vapour diffusion in air. Figure 5 shows the time evolution of matric suction during the wetting path for three representative points of the 10-mm sample (top in contact with coarse porous disk, mid-height and bottom in contact with ceramic disk), starting from an initial value $(u_a-u_w)_0$=1.9 MPa to $(u_a-u_w)_f$=0.45 MPa. An initial relative humidity of the air chamber h_{r0}=0.50 was assumed in accordance to the relative humidity of the laboratory. Two different systems were analysed. In the open system, a constant relative humidity of h_r=0.50 was prescribed along the wetting stage at the top surface of the sample in contact with the air chamber (refer to the scheme shown in Figure 4). On the other hand, in the closed system simulation the relative humidity progressively increased towards a final value h_r= 0.996. According to Figure 5, water evaporation will cause an initial drying on the clay upper surface. This drying progressively slows down and reverses as liquid water flows into the sample. On the contrary, a monotonic suction decrease is detected at the bottom

boundary of the sample. As observed in the figure, at the end of the wetting path, full matric suction equalisation throughout the sample height is not attained in the open system (matric suction at the top of the sample presents a value of 0.50 MPa under steady-state conditions). This is why it is important to ensure a high h_r in the air pressure system or alternatively control the volumetric evaporative flux measured under steady-state conditions. A maximum volumetric evaporative flux of 9.4×10^{-7} $(mm^3/s)/mm^2$ was computed, when h_r=0.5 was imposed in the air chamber. For measured volumetric evaporative fluxes lower than this value, no important consequences are expected and a relatively uniform matric suction distribution is expected throughout the sample height [Rom99,01a,b] (refer to Figure 4).

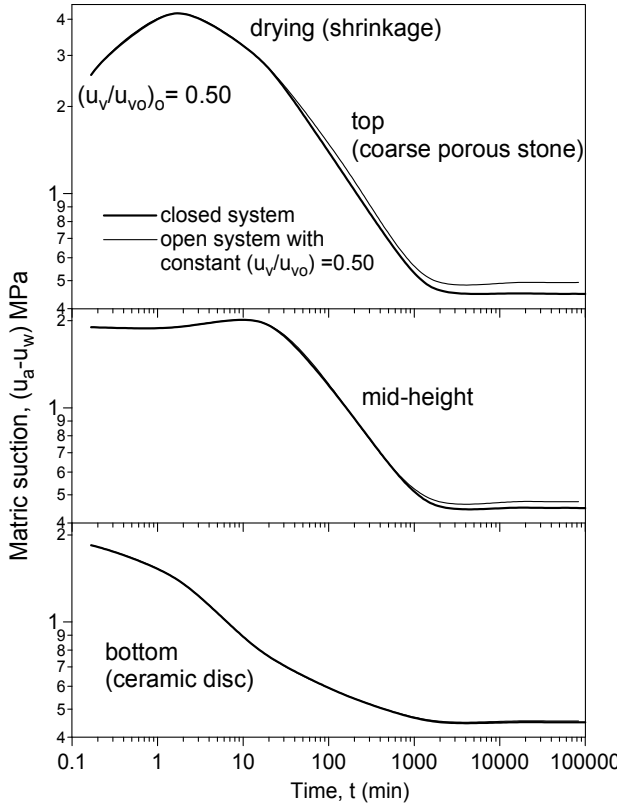

Figure 5: Numerical results of matric suction evolution at three different elevations during a wetting stage from s=1.9 MPa to 0.45 MPa [Rom99].

The application of air pressure at elevated degrees of saturation can induce irreversible arrangements in soil skeleton due to pore fluid compression (occluded air bubbles). Bocking and Fredlund [Boc80] studied the effect of occluded air during the use of axis translation technique. If nearly saturated states are expected to be reached

during the hydraulic paths, it is preferable to increase air pressure when the continuity of air is ensured (degrees of saturation < 0.85), and then maintain the continuous air phase at constant pressure. This can be observed in Figure 2, in which the drying path followed a wetting path that attained very low matric suctions (10 kPa). Throughout this hydraulic process, air pressure was maintained constant and suction was changed by manipulating water pressure.

One important difficulty when using axis translation technique is the estimation of the time required to reach suction equalisation. Water volume measurements are usually affected by the relative humidity of the air chamber and the diffusion of air. Although these phenomena can be minimised as previously suggested, the estimation of the equalisation time in oedometer and triaxial cells has been conventionally determined based on overall soil volume change measurements that are independently determined. Oliveira and Marinho [Oli06] studied the equilibration time in the pressure plate and recommended around three days for increments from 50 kPa to 100 kPa for gneissic soils. From the analytical solution proposed by [Kun62], which considers the ceramic disk impedance and the soil permeability to determine the time evolution of the water volume change in a soil with a rigid matrix, it is possible to estimate an equalisation time t_{95} for which 95% of the water outflow or inflow has occurred (for simplicity only one term of the Fourier series has been considered):

$$
\begin{aligned}
& t_{95} \approx -\frac{L^2}{\alpha_1{}^2 D} \ln\left[\frac{\alpha_1{}^2}{40}(a+\csc^2\alpha_1)\right]; \\
& a\alpha_1 = \cot\alpha_1 \quad \text{with} \quad 0 < \alpha_1 \le \frac{\pi}{2}; \\
& D = -\frac{k_w}{n\gamma_w}\frac{\delta s}{\delta S_r}
\end{aligned}
\tag{2}
$$

where L is the soil height (longest drainage path); D the capillary diffusivity that is assumed constant and is dependent on water permeability, k_w, and soil water capacity, $\delta s/\delta S_r$ (s is the matric suction, S_r the degree of saturation, n the porosity, and γ_w the unit weight of water); a the ratio of impedance of the ceramic disk to the impedance of the soil $a = k_w t_c/(Lk_d)$ (t_c is the ceramic disk thickness and k_d its water permeability), and α_1 the solution of the equation in the indicated range. For low disk impedance, $a \approx 0$ and $\alpha_1 \approx \pi/2$, the minimum equalisation time can be approximately estimated as:

$$
t_{95} \approx 1.129\frac{L^2}{D} \tag{3}
$$

For a clayey soil with L = 20 mm, $n = 0.48$, $k_w = 5\times10^{-12}$ m/s and $\delta s/\delta S_r \approx -2.8$ MPa in the suction range $0.1\,\text{MPa} < s < 0.5\,\text{MPa}$, and disk properties t_c = 7 mm and $k_d = 10^{-10}$ m/s, then $a \approx 0.018$, $\alpha_1 \approx 1.543$, $D \approx 3.0\times10^{-9}$ m^2/s and t_{95}

≈ 2615 min. It is important to remark that this estimation is based on a constant soil volume consideration, which is not exactly the case of a clayey soil. Nevertheless, it gives an approximate estimation of the minimum time required to reach suction equalisation.

2.3 Vapour transfer technique

Vapour equilibrium technique is implemented by controlling the relative humidity h_r of a closed system. Soil water potential is controlled by means of the migration of water molecules through the vapour phase from a reference system of known potential to the soil pores, until equilibrium is achieved. The thermodynamic relation between total suction ψ of soil moisture and the h_r of the reference system is given by the psychrometric law [Fre93]. The h_r of the reference system can be controlled by varying the chemical potential of different types of aqueous solutions [Lid97, Del98, Tan05]. Figure 6 shows the relationship between ψ and the concentration of NaCl aqueous solution (molality, m, mol of NaCl / kg of pure water). The upper limit is controlled by the salt solubility that restricts h_r=0.75 at 20°C.

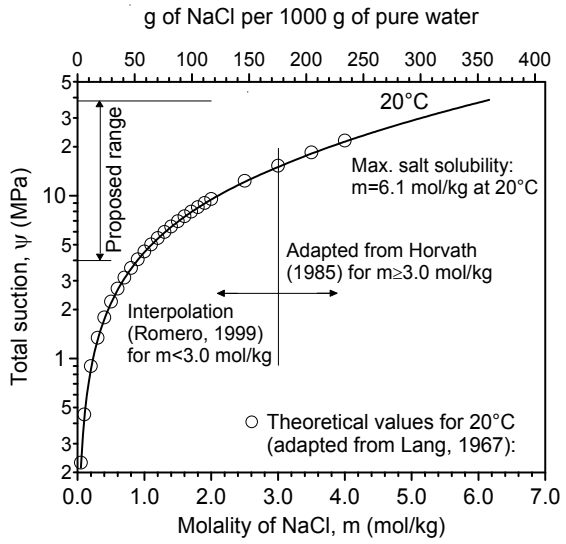

$$h_r = 1 - 0.035m - \chi m(m-3)$$
$$\chi = 1.739\times10^{-3} \text{ for } m \geq 3 \text{ mol/kg}$$
$$\chi = 1.142\times10^{-3} \text{ for } m < 3 \text{ mol/kg}$$

Figure 6: Total suction application with partially saturated NaCl solutions [Hor85, Rom99].

Oedometer cells installed inside a chamber with relative humidity control were used by [Est90, Ber97, Vil99, Cui05]. The main drawback of this experimental setup is that the time to reach moisture equalisation is extremely long due to the fact that vapour transfer depends on diffusion (several weeks are required for each suction step in the case of high-density clays as observed in Figure 7). In order to speed up

the process, vapour transfer –through the sample or along the boundaries of the sample– can be forced by a convection circuit driven by an air pump [Yah99, Bla00, Pin02, Llo03, Old04, Due04, Alo05, Due07, Pin09a]. Figure 7 shows the evolution of vertical strains (expansive deformations are positive) of compacted bentonite subjected to a reduction in suction (from 150 MPa to 4 MPa) under oedometer conditions (vertical net stress of 10 kPa), using both relative humidity controlled chamber (pure diffusion of vapour) and forced flow of humid air on both ends of the sample. As observed, the forced flow speeds up the process of suction change.

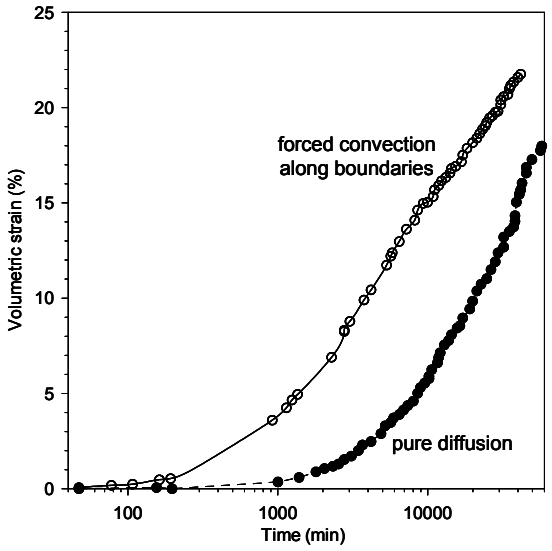

Figure 7: Evolution of volumetric strain (expansion is positive) on compacted bentonite using humid air flow along the boundaries of the sample (forced convection) or controlling the air relative humidity inside a closed chamber (pure diffusion) [Pin09a].

The mass rate transfer of vapour by convection (assuming isothermal conditions and constant dry air pressure u_{da}) can be expressed in terms of vapour density or mixing ratio differences between the reference vessel with aqueous solution (superscript r) and the soil (superscript s) [a: Old04, b: Jot07]

$$\begin{aligned} &\text{a)}\ M_{dry}\frac{\mathrm{d}w}{\mathrm{d}t} = q(\rho_v^r - \rho_v^s) = \frac{q\,M_{mw}}{RT}u_{v0}(h_r^r - h_r^s) \\ &\text{b)}\ M_{dry}\frac{\mathrm{d}w}{\mathrm{d}t} = q_{da}(x^r - x^s) = q_{da}\,x_0(h_r^r - h_r^s) \end{aligned} \qquad (4)$$

where M_{dry} is the soil dry mass, w the gravimetric water content, q the volumetric air flow rate, ρ_v the vapour density in air (water mass per unit volume of air), q_{da} the flow rate of dry air mass, and x the mixing ratio (mass of water vapour per unit mass

of dry air; x_0 represents the saturated mixing ratio). Assuming vapour an ideal gas, the vapour density can be expressed as $\rho_v = M_{mw} u_{v0} h_r / (RT)$, where u_{v0} is the saturated vapour pressure at absolute temperature T, M_{mw} is the molecular mass of water, R is the gas constant, and h_r the relative humidity. Based on the same assumption and that dry air is also an ideal gas, the following expression is obtained $x = M_{mw} u_v / (M_{mda}\, u_{da}) = 0.622\, u_v / u_{da}$, in which M_{mda} is the molecular mass of dry air mixture, u_{da} the dry air pressure and u_v the vapour pressure.

One of the difficulties in using the vapour equilibrium technique is associated with maintaining thermal equilibrium between the reference system (vessel with aqueous solution) and the sample. Assuming that the vapour pressure set by the reference saline solution is also present in the sample, the following correction is proposed, in which h_r is the relative humidity and u_{v0} the saturation vapour pressure at temperature T:

$$h_{r\,sample} = h_{r\,reference} \frac{u_{v0}(T_{reference})}{u_{v0}(T_{sample})} \tag{5}$$

A way to minimise this thermal effect is achieved by disconnecting the reference system that regulates the relative humidity, and allow the equalisation of vapour in the remaining circuit and the soil. This way, the mass of water being transferred from or to the soil is drastically reduced (there is no contribution in water transfer between the vessel and the soil). An equivalent testing procedure was used by [Old04] to overcome the long equalisation periods of the conventional vapour equilibrium technique.

Another problem that comes up when using the forced convection system is associated with air pressure differences created along the circuit. This fact makes that the intended relative humidity applied by the reference vessel cannot be assigned to the remaining circuit and the soil [Pin09a,b]. Dueck [Due04] studied the influence of air pressure changes in a forced convection circuit of vapour –driven by an air pump– and their consequences on the applied relative humidity. Figure 8 shows the experimental setup and the evolution of differential air pressures between two points of the circuit (upstream and downstream the filter stones that transfer vapour to or from the soil). The point upstream the filter is near the reference reservoir ('*ref*' in the figure). On the other hand, the point downstream the filter is close to the aspiration branch of the air pump ('*p*' in the figure) and is subjected to a pressure drop. After vapour equalisation, the pump is turned on and air forced through the circuit. At 67 min the speed of the pump is rapidly increased, and finally reduced from 78 min on. The consequences on the evolution of the relative humidity at the same two points of the circuit are shown in Figure 9. As observed, downstream point '*p*' near the pump undergoes important relative humidity changes due to air pressure drop, while upstream point '*ref*' is buffered by the reference salt solution reservoir. An expression to account for the effects of air pressure variations

on the relative humidity can be proposed based on the assumption that the mixing ratio $x = 0.622\ u_v / u_{da}$ set by the reference salt solution is also set in another point of the constant mass circuit. The following expressions are obtained between the relative humidity reference reservoir $h_{r\,ref}$ set by the salt solution, and another point of the circuit $h_{r\,p}$:

$$u_{v\,p} = u_{vref}\frac{u_{da\,p}}{u_{da\,ref}}$$
$$h_{r\,p} = h_{r\,ref}\frac{u_{da\,p}}{u_{da\,ref}} \tag{6}$$

in which $h_r = u_v / u_{v0}$ is the relative humidity, and u_{v0} is the common saturated vapour pressure.

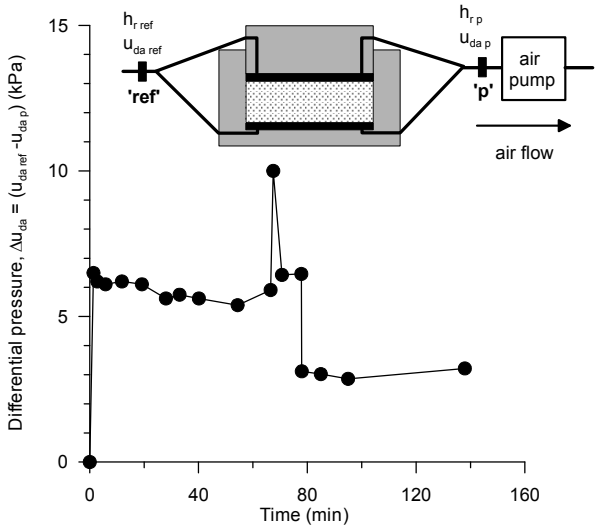

Figure 8: Experimental setup and time evolution of differential air pressures between upstream point 'ref' and downstream point 'p' ([Pin09b], experimental data from [Due04]).

Equation (6) is used to simulate the variations of h_r at downstream point '*p*', $h_{r\,p}$, which are plotted in Figure 9. The absolute pressure at point '*ref*' is fixed at $u_{da\,ref}$ = 101.3 kPa, while absolute pressure changes at point '*p*', $u_{da\,p}$, are estimated from Figure 8: $u_{da\,p}$ = 101.3 kPa-Δu_{da}. If both upstream and downstream absolute pressures are affected: for example, $u_{da\ ref}$ = (101.3+Δu_{da}/2) kPa and $u_{da\,p}$ = (101.3–Δu_{da}/2), equivalent results are obtained. As observed in Figure 9, the simulated points follow the general trend of the measured variations in $h_{r\,p}$, although

they display slightly larger values. An equivalent simulation is used to estimate the relative humidity at upstream point '*ref*', $h_{r\,ref}$, using $h_{r\,p}$ data. In this case, the simulated points do not follow the stable tendency of the relative humidity experimental data, which are buffered by the proximity of the reference salt solution reservoir. Nevertheless, the initial small drop, the next small increase at around 33 min and the smooth peak detected at 67 min are captured in their trend.

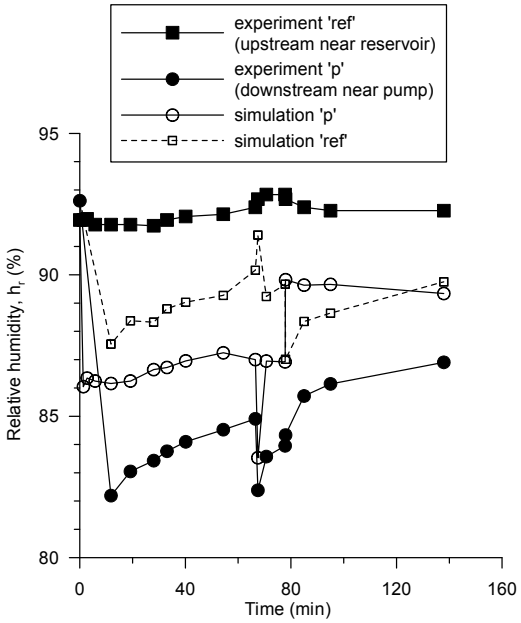

Figure 9. Time evolution of measured and simulated relative humidity at two points of the forced convection circuit: upstream point '*ref*' near the reservoir and downstream point '*p*' close to the pump ([Pin09b, experimental data from [Due04]).

Pintado et al. [Pin09a] performed numerical simulations using Code_Bright [Oli96] to study the physical processes that occur when forcing humid air to flow through a partially saturated sample. It was observed that forcing humid air reduced the equalisation time, but the results from the numerical simulations again highlighted that this flow must be carefully applied to avoid reaching, under steady state conditions, a different total suction than that intended. Gas advective flux followed a generalised Darcy's law with a relative permeability dependent on the degree of saturation. In the numerical analysis, the relationship between the intrinsic permeability for air flow under dry conditions k_{ia} and for water flow under saturated conditions k_{iw} was expressed as $k_{ia} = A k_{iw}$, where A is a material parameter. Due to the uncertainty in the value of parameter A, a back-analysis was done to match the axial deformation measured on densely compacted Febex bentonite during wetting under oedometer conditions (total suction change from 128 MPa to 84 MPa at a constant vertical stress of 0.15 MPa; height of the sample 12 mm). The estimated $A = 3.85\times10^{9}$ was

one order of magnitude higher than the mean value measured in complementary air and water permeability tests, but still within the range of variation of admissible values. As an additional information, the pressure difference between air inlet and outlet ΔP_g=4 kPa was measured when vapour was forced to flow through the specimen. The transient results (time evolution of vertical strains) of the numerical simulations and the fitted experimental results are presented in Figure 10. As clearly observed in the figure, equalisations develop faster at higher pressure differences and higher intrinsic air permeability. An important observation is that final vertical strains are not the same for the four simulations due to the fact that the suction reached at equilibrium is different for all the cases considered. This can be seen in Figure 11, which summarises the different total suctions reached under steady state conditions at the mid-height node of the specimen for the four different cases indicated in Figure 10. If the air pressure difference between the ends of the sample is high, the total suction in the soil under steady state conditions will be different from the expected suction applied by pure diffusion transfer (static test in the figure), as also measured by [Due04, Mer11]. Figure 12 shows that the vapour inflow into the sample decreases with elapsed time because the air permeability becomes lower as the degree of saturation increases during the wetting stage. The mass of vapour that flows into the sample is larger than the mass of vapour that flows out during the transient wetting stage because a percentage of this water is stored in the sample. The steady state is reached after two days, which provides evidence of the efficiency of this experimental method.

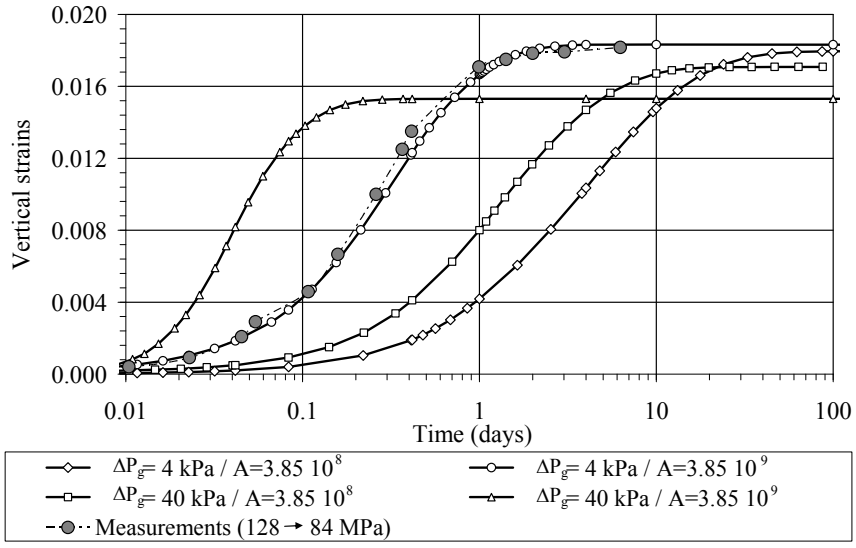

Figure 10: Laboratory measurements and model fitting the evolution of axial strain (swelling is positive) during a wetting path (128 MPa to 84 MPa) at constant vertical net stress (0.15 MPa). Simulations for different A and ΔP_g values [Pin09a].

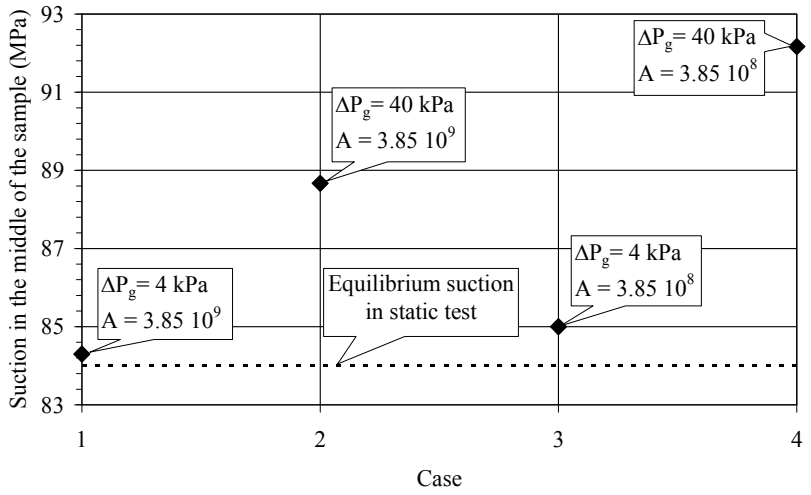

Figure 11: Total suction reached under steady state conditions at the central node of the specimen after the wetting path at constant vertical net stress for the four different cases indicated in Figure 10 [Pin09a].

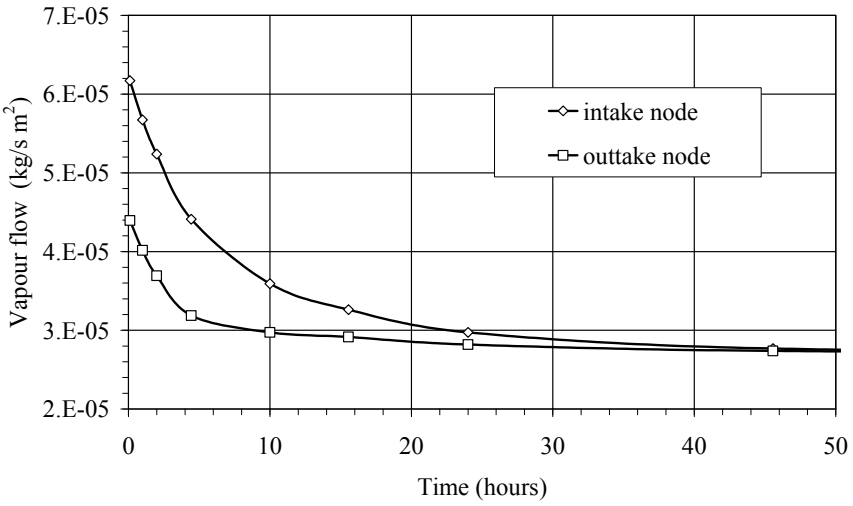

Figure 12: Time evolution of vapour flow during the transient wetting stage. Simulation for A=3.85×109 and ΔP_g=4 kPa [Pin09a].

2.4 Simulation assisted study of the equalisation period when using vapour equilibrium

To analyse the time required for equilibrating homogeneously a deformable sample under oedometer conditions –of major experimental concern when applying a total suction step–, simulation aided techniques (Code_Bright [Oli96]) are presented in this section to study the progression of total suction at local scale and along a drying path (for further details refer to [Mer11]). The usual experimental criterion to define the hydraulic equalisation period under oedometer conditions is based on measuring axial strains and controlling axial strain rates below a specified value (typically below 0.1%/day), due to the experimental difficulty in knowing the precise hydraulic status of the sample during vapour transfer (usually the evolution of vapour transferred to or from the sample is not measured). The two main challenges of the simulations are the correct computation of the evolution of axial strains of the sample during total suction application and to verify if suction stabilises at the elapsed time indicated by the mechanistic approach used conventionally in the experimental procedure (< 0.1%/day).

In the simulation of the results, the flux of water in the gas phase is governed essentially by the non-advective flux, since the gas pressure is maintained under atmospheric conditions. The non-advective component is a function of the diffusion-dispersion tensor and the gradient of mass fraction of water in the gas phase. The water volumetric advective flux is defined by Darcy's law. This flux is affected by the liquid degree of saturation through a relative permeability. The application of the relative humidity at the sample boundaries is set by Equation (7), similar to that used by [Wil94]. In this equation, evaporation arises from the difference between the vapour density at the soil surface ($\rho_g \varpi_g^w$), and the vapour density in the environment $\left(\rho_g \varpi_g^w\right)^0$. Parameter β_g is associated with the turbulent exchange function and depends on the movement of the air above the evaporating surface.

$$j_g^w = \beta_g \left[\rho_g \varpi_g^w - \left(\rho_g \varpi_g^w \right)^0 \right] \tag{7}$$

Values of parameter β_g were obtained by [Pin09a] for conditions prevailing in laboratory with relative humidity control (β_g=2×10^{-3} m/s) and for a closed oedometer cell with circulating vapour (β_g=4×10^{-4} m/s). In the case of the simulation reported by [Mer11], the parameter was obtained by back-analysis leading to a value of β_g=7×10^{-4} m/s, which is of the same order of magnitude than the values found experimentally. This factor can be considered as an impedance factor affecting the efficiency of the system to release the water from the soil.

As previously indicated, the drying path develops volumetric changes on the sample. Therefore, it is necessary to perform the coupled analysis with a simple constitutive model, which takes into account volumetric changes due to total suction or relative

humidity changes besides net vertical stress changes. The selected mechanical constitutive model on monotonic drying was the nonlinear state surface model for partially saturated soils proposed by [Llo85], together with the shear modulus or the Poisson's ratio to define the increments of shear strain.

Figure 13 presents suction equalisation curves (compression is negative) for clayey samples initially prepared at initial water content w_o=34 % and subjected to three different target suctions under oedometer conditions (4.75 mm is the sample height after vertical stress application: 0.1 MPa). These curves show that the rate of shrinkage depends on the total suction change applied to both top and bottom evaporating surfaces. The sample at s=14 MPa (h_r=90%) requires 266 hours to equilibrate, according to the mechanistic criterion (axial strain rate: 0.1%/day). Samples subjected to total suctions of s=58 MPa (h_r=65%) and s=85 MPa (h_r=54%), require 192 and 169 hours, respectively. It is interesting to remark that the sample subjected to the lowest total suction change requires more time to stabilise compared to the remaining ones, despite being closer to the initial saturated state. In this case, suction equalisation time is controlled by the flux of vapour interaction between the sample and the environment, which mainly depends on the vapour density gradient and the exchange properties between the evaporating surface and the glass chamber atmosphere. Results of the simulated curves compared with the experimental ones are plotted in Figure 13.

In Figure 14 the evolutions of total suction at mid-height of the sample for the three simulations are presented. The figure indicates that suction takes around 120 hours to equilibrate for the simulation at s=85 MPa, 168 hours for the simulation at s=58 MPa and 312 hours for the simulation at s=14 MPa. Again and consistent with the mechanistic approach, systematically longer times are required for lower total suctions values. When comparing these simulated equalisation times with the ones based on vertical strain rates, the results indicate that for the lowest suction the experimental time of 266 hours is lower than that given by the simulation. This fact indicates that an additional period of at least 48 hours has to be considered to ensure suction equalisation throughout the sample height. On the other hand, for the remaining applied suctions, the experimental equalisation time given by the mechanistic criterion gives somewhat higher values compared with the numerical observations. Based on these simulations, it appears that the equalisation period based on a mechanical stabilisation criterion (time required to attain vertical strain rates lower than 0.1%/day) is an appropriate way to estimate the suction equalisation period.

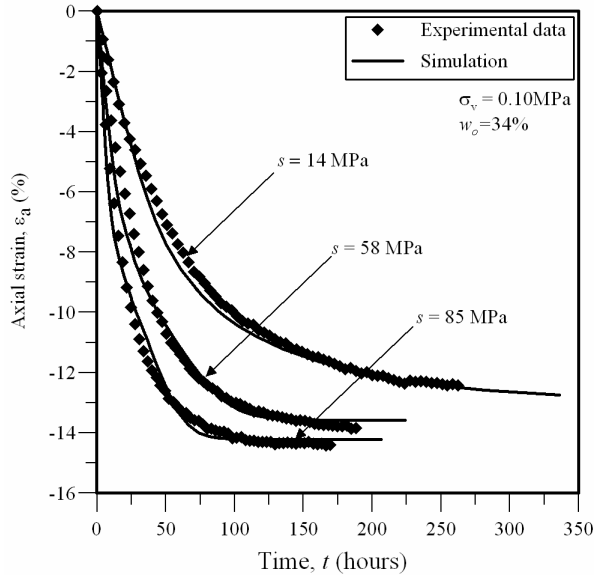

Figure 13: Experimental and simulated axial strain evolutions (compression is negative) for clayey samples subjected to drying at three different target total suctions [Mer11].

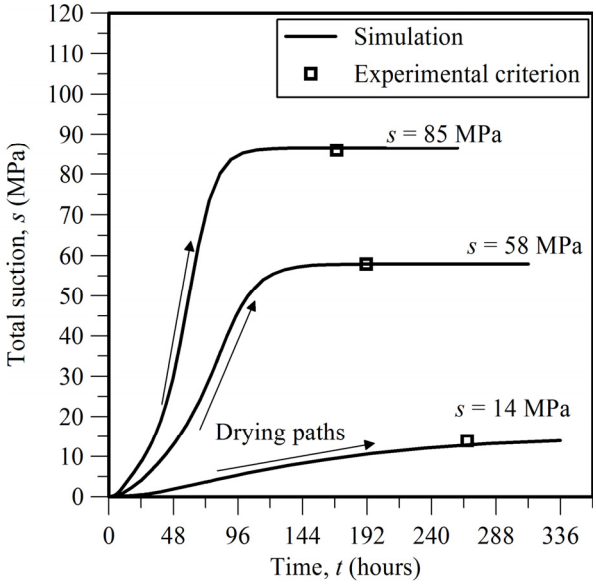

Figure 14: Simulated total suction evolution at mid-height of the sample and comparison with the equalisation time estimated experimentally based on a mechanistic criterion [Mer11].

3 Electro-chemo-hydraulic processes

3.1 Introduction

In the following, electrical and electrochemical processes in geomaterials will be reviewed in light of two possible classes of applications. The first one is electrical characterisation, or the determination of the electrical characteristics (electrical conductivity and impedance) of the medium. Electrical characteristics can be related to the porosity, fabric and saturation degree of the geomaterial and to the properties of the constituent phases, so that the electrical characterisation can contribute to indirect evaluation of porosity, degree of saturation and water salinity. The second class of applications is the induction of transport processes, which can be both direct (such as electromigration, or transport of ions under an electrical field) and coupled (such as electroosmosis, or transport of water within a porous medium under an electrical field). Transport processes induced by an electrical field can be used both for mechanical purposes (consolidation and slope stabilisation) or environmental purposes (remediation of contaminated sites).

3.2 Electrical conductivity of soils and rocks

Electrical flux in geomaterials could be both a direct flux or coupled flux (streaming current, heat current and diffusion current, see following paragraph and [Mit05]). When no hydraulic, thermal and chemical gradients are acting, or for negligible coupling coefficients, electrical current density i is proportional to the gradient of the electrical potential ϕ as according to Ohm's law:

$$i = -\chi_t \nabla \phi \tag{8}$$

where χ_t [1] is the electrical conductivity of the soil and ϕ is the electrical potential.

In theory, electrical charges could travel through the solid phase, the water phase and at the interface between water and solid phase (surface conduction), while practically no electrical flux occurs in air or hydrocarbons. Most minerals are insulators (although the electrical conductivity of metals can be as high as $10^5 - 10^8$ S/m) and their contribution to the electrical conductivity of the geomaterial is usually neglected: readers interested in the analysis and interpretation of the electrical behaviour of dry rocks can refer to the book of [Par67].

Several theoretical and empirical relationships have been proposed to model the electrical conductivity of geomaterials. These relationships take into account the

[1] The usual symbol for electrical conductivity is σ. Here χ is used instead to avoid confusion with stress.

effects of tortuosity, particle shape, degree of saturation, microstructure and surface conductivity in different ways[2].

Among the relationships that do not consider surface conductivity, Archie's law [Arc42] is the most widely used. It has been derived for oil reservoir sands, and accounts for the effects of porosity and saturation as follows:

$$\chi_t = \chi_w n^m S_r^{\ p} \tag{9}$$

where χ_w is the electrical conductivity of the water phase, n is the porosity, m is an exponent that accounts for the tortuosity of the porous medium, S_r is the degree of saturation and p is an empirical exponent that also depends on the fabric of the material (particularly on its pore size distribution, see e.g. [Sen97]). The formation factor F^*:

$$F^* = n^{-m} \tag{10}$$

often used in oil engineering represents the ratio of the resistivity of the saturated material to the resistivity of the saturating water.

Archie's law in saturated conditions has been extended to account for surface conductivity by [Wax68]:

$$\chi_t = X\left(\chi_w + \chi_s\right) \tag{11}$$

where X is a constant analogous to $(F^*)^{-1}$ and χ_s is a surface conductivity term. A limitation of Waxman and Smits expression (11) is that it assumes that the surface conductivity is affected by the geometry of the porous medium in the same way as the water conductivity term. This expression should be used with caution also because surface conductivity is not constant for a given material, but depends on the characteristics of the solid phase surface groups, on the pore fluid pH and on its concentration (for a detailed discussion see [Del05]). As a matter of fact, surface conductivity is an important contribution for clayey soils with a high specific surface: its value is greater the lower the salinity of the pore water. In these particular soils, attention must be paid to the fact that chemistry also influences the dimensions of pores [e.g. Mus03] and then affects the soil electrical conductivity by altering the formation factor. A discussion on aspects related to surface conductivity, including simple theoretical models to evaluate surface conductivity starting from the Diffuse Double Layer theory, can be found in [Kle03].

[2] For a list of theoretical models, the book of [San01] is suggested.

3.3 Electrolytic conduction

In water the electrical current is carried by ions, dragged towards the electrodes of opposite polarity. Ionic mobility u is the drift velocity of an ion under an unit electric field. According to the Nernst-Einstein equation, at infinite dilution the ionic mobility is proportional to the diffusion coefficient D:

$$u = \frac{D\nu F}{RT} \tag{12}$$

where ν is stoichiometric coefficient of the ion, F is Faraday's constant (F = 96485 C/mol of electrons), R is universal gas constant (8.314 Joule mol^{-1} K^{-1}) and T is absolute temperature. Contribution of ions of a given specie i to the electrical conductivity of a solution is:

$$\chi_i = c_i u_i \nu_i F = c_i \Lambda_i \tag{13}$$

where c_i is concentration (expressed in mol/m^3) and Λ_i is molar conductivity (electrical conductivity of a mole) of the specie i (expressed in $S\,m^2$/mol). The overall electrical conductivity of a water solution is then given by the sum of the contributions of the n species in solution:

$$\chi_w = F \sum_{i=1}^{n} c_i \nu_i u_i \tag{14}$$

Equation (14) shows that χ_w is related to the concentration of dissolved species. The actual relationship depends on concentration. At high concentrations, ionic mobility and molar conductivity decrease, and the linearity between concentration and electrical conductivity is lost. Figure 15 shows experimental results and interpretation of measurements of electrical conductivity at increasing concentrations of NaCl electrolyte (see also [Kle03]).

3.4 Electrolytic cells and electrode reactions

It is of interest to understand how electrical current is transmitted to a water solution, since this process involves electrode reactions, *electrolysis,* that can change the chemical composition of the pore water at the points of injection.

An electrolyte, or a ionic conductor, is a substance where ions are the main charge carriers. Two electrodes injecting a current and the electrolyte between them constitute an *electrolytic cell.* The interface between the electrodes and the electrolyte is the seat of chemical reactions necessary to exchange electrons between the metallic part of the circuit (where electrons are the charge carriers) and the electrolyte (where

ions are the charge carriers). A conceptual scheme of transport and reactions processes occurring is given in Figure 16.

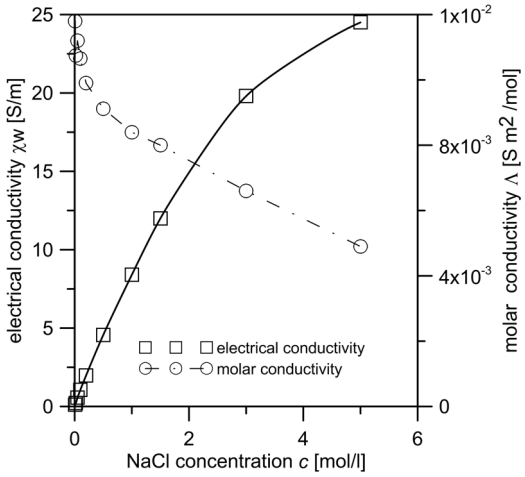

Figure 15: Electrical conductivity and molar conductivity of NaCl solutions (modified from [Mus05]).

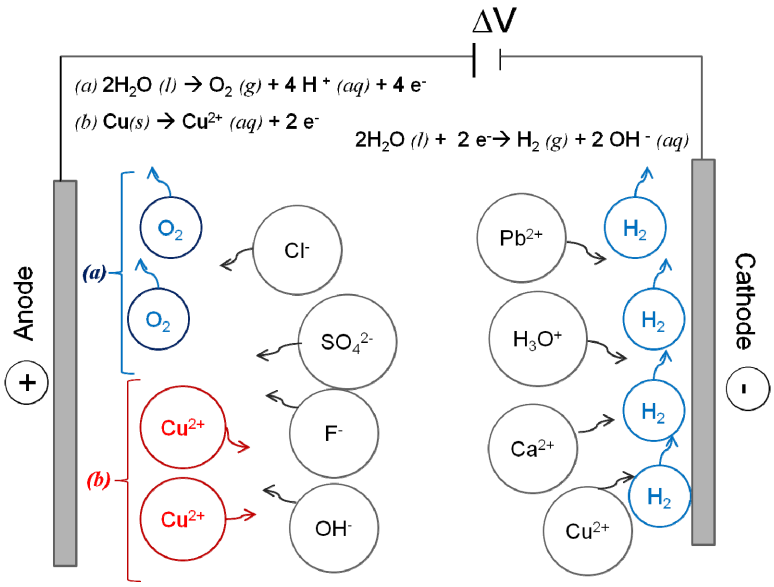

Figure 16: Conceptual scheme of transport and reactions within an electrolytic cell.

Electrons are removed from the electrolyte through an oxidation reaction. One or more species in the electrolyte serve as electron donor (*reductant*) and the electrode as a receiver of electrons. Oxidation reactions are written as follows:

$$\mathrm{Red}_1 \rightarrow \mathrm{Ox}_1 + \nu \mathrm{e}^- \tag{15}$$

where *Red* is the reductant specie, *Ox* the oxidant and ν is the stoichiometric coefficient of the electrons e^- involved in the reaction. The electrode at which oxidation occurs is the *anode*: in an electrolytic cell this is the positive electrode (the one towards which are attracted ions with negative charge, *anions*).

Electrons travel through the external metallic circuit and re-enter the cell at the opposite electrode, the *cathode* by means of a reduction reaction:

$$\mathrm{Ox}_2 + \nu \mathrm{e}^- \rightarrow \mathrm{Red}_2 \tag{16}$$

In an electrolytic cell the cathode is the negative electrode: it attracts *cations* (species with positive charge).

Considering that many species are dissolved in the pore water of a soil, one could imagine several different possible redox reactions. Actually, only a few of them (ideally one oxidation and one reduction reaction) do occur. If the material constituting the electrodes and the species in solution are known, it is possible to foresee which reactions will take place on basis of the electrochemical potential *E*. This is evaluated on basis of the Nernst equation (17), and it is a function of the standard potential of the reaction E^0, of absolute temperature and of stoichiometric coefficient:

$$E = E^0 - \frac{RT}{\nu F} \ln \frac{a_{red}}{a_{ox}} \tag{17}$$

where a_{red} and a_{ox} are the activities of the reduced and oxidised specie.

Standard potentials can be found in chemistry textbooks [Atk10]. The reference reaction is reduction of protons, whose standard potential E^0 is conventionally zero:

$$2H^+ + 2e^- \rightarrow H_2 \tag{18}$$

At the anode the reaction with the most negative (or least positive) potential is favoured until the species involved are used up and/or until a high voltage stimulates competing reactions. Depending on the material used to build the electrode, M_A, the oxidation reaction (15) can either be oxidation of water [Loc83]:

$$2H_2O(l) \rightarrow O_2(g) + 4H^+(aq) + 4e^- \tag{19a}$$

which has a standard potential $E^0 = +1.23\ V$ ($E = +0.82\ V$ when pH = 7), or oxidation of the electrode:

$$M_A \rightarrow M_A^{v+} + ve^- \tag{19b}$$

As it can be appreciated in Table 1, the standard electrode potential of the reaction (19a) is higher than that of some typical metals that could be used to build the electrodes (Aluminium, Iron or Copper), but is smaller than that of noble metals (Platinum or Gold).

Table 1: Selected standard potentials of reduction reactions.

Reaction	**Standard Electrode Potential E^0 (V)**	**Reaction**	**Standard Electrode Potential E^0 (V)**
$Al^{3+} + 3e^- \rightleftharpoons Al(s)$	−1.660	$2H_2O\ (l) \rightleftharpoons O_2(g) + 4H^+(aq) + 4e^-$	+1.230 +0.82 (pH = 7)
$Zn^{2+} + 2e^- \rightleftharpoons Zn(s)$	−0.762	$Hg^{2+} + 2e^- \rightleftharpoons Hg(l)$	+0.850
$Fe^{2+} + 2e^- \rightleftharpoons Fe(s)$	−0.440	$Pt^{2+} + 2e^- \rightleftharpoons Pt(s)$	+1.188
$Cu^{2+} + 2e^- \rightleftharpoons Cu(s)$	+0.340	$Au^+ + e^- \rightleftharpoons Au(s)$	+1.690

Anodes made of Aluminium, Zinc, Iron or Copper in a neutral water environment release the metallic cation into the electrolyte (e.g. a Copper electrodes will enrich the electrolyte with Cu^{2+} ions) and corrode (case *(b)* in Figure 16). Anodes made of inert materials (e.g. graphite) or made of noble metals do not corrode, and reaction (19a) takes place since potential E is lower than the metal's one. In this case, water next to the anode acidifies and oxygen is released in gaseous form (case *(a)* in Figure 16).

At the cathode the reaction with the most positive potential is favoured. Water reduction:

$$2H_2O(l) + 2e^- \rightarrow H_2(g) + 2OH^- \tag{20}$$

often occurs since its electrochemical potential at pH = 7 is E = + 0.41 V, which is higher than most potentials of reactions involving metal cations.

The mass q of elements altered by electrolytic reactions (e.g. the mass of H^+ or OH^- ions developed when using inert electrodes) can be calculated through Faraday's laws of electrolysis:

$$q = \frac{Q}{F} \cdot \frac{M}{\nu} \tag{21}$$

where Q is cumulate electrical charge passing through the cell (expressed in Coulombs, C) and M is molar mass of the substance.

3.5 Electrode polarisation and overpotential phenomena

Compensation of electrical charges at the electrode – electrolyte interface causes polarisation, which is the development of an electrical double layer consisting of a sheet of positive charge at the surface of the electrode and a sheet of negative charge next to it in the solution (or vice versa). The electrical double layer makes the electrical potential of the solution different from the electrical potential of the electrode. Theoretical models have been formulated describing the concentration of counterions in the solution and the associated voltage profile (Helmholtz layer model, Gouy-Chapman model, Stern model) (see [Mit05]).

The difference between the electrical potential of the electrode and the electrical potential of the solution next to it does not only depend on polarisation, but also on metal deposition, gas development and on the intensity of the electrical current. Altogether, this difference is called *overpotential* η. The exact value of the overpotential is difficult to predict theoretically, although significant deposition / gas development is expected to occur only when $\eta > 0.6$ V [Atk10].

3.6 Electrical conductivity measurements

The simplest way to determine the electrical conductivity χ of a specimen in laboratory is by measuring the electrical resistance R in a given geometrical arrangement. R is obtained through Ohm's law:

$$\Delta\phi = R \cdot I \tag{22}$$

where $\Delta\phi$ is electrical potential drop between two points and I is electrical current. Once that R is known, χ is derived through a shape factor α:

$$\chi = \frac{1}{\rho} = \frac{\alpha}{R} \tag{23}$$

For instance, if R is the resistance of a parallelepiped under one dimensional flux condition, it is:

$$\chi = \frac{1}{\rho} = \frac{l}{RA} \tag{24}$$

where ρ is the resistivity (inverse of conductivity), l is the distance between the points where the electrical potential is measured and A is the section of the sample. From Equation (24) it follows that the shape factor in one dimensional flow conditions is $\alpha = l/A$.

Two different types of experimental setup are used to determine the electrical conductivity of soil and rock samples: the two terminal electrodes and the four terminal electrodes systems (Figure 17). In the two terminal electrodes system, the anode and the cathode are used both to inject the electrical current I and to measure the electrical potential drop $\Delta\phi$.

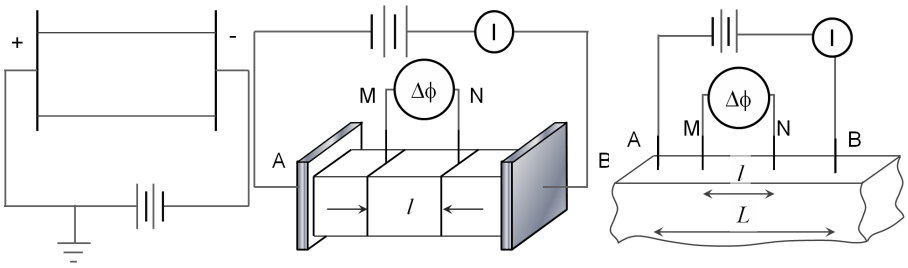

Figure 17: Two electrodes terminal (left) and four electrodes terminal (center and right) systems (modified from [Par67])

Although very simple to build, this system presents the disadvantage that the potential drop measured between the cathode and the anode necessarily includes the overpotential η, whose value is in principle unknown. Very high η are expected when inert electrodes are used, since O_2 and H_2 bubbles produced by electrolysis of water accumulate at the electrode – specimen interface, acting as very powerful insulators. Overpotential is expected to reduce at increasing frequency of the electrical signal: electrical potential drops measured with a two electrodes system at relatively high frequencies are in principle related only to the resistance of the soil specimen. Measurements performed by a two electrodes system are anyway difficult to interpret, since the frequency above which polarisation effects becomes negligible (limiting frequency) depends on conductivity, permittivity, and length of the specimen [Kle97]. On basis of permittivity measurements, Klein and Santamarina [Kle97] found that the limiting frequency of sands and kaolinite specimens at different water

contents and water salinity ranged between 10^2 and 10^4 Hz, although real conductivity values appeared to be insensitive of frequency above 100 Hz. More critical evidences were obtained for bentonite samples, where the limiting frequency in terms of permittivity ranged as high as 1 MHz and conductivity values were frequency dependent for $f < 1$ kHz.

In the four electrodes measurement system, two electrodes (A and B) are devoted to inject the electrical current and two other electrodes (M and N) are devoted to measure the potential drop: this excludes overpotential effects. Anyway, since also these electrodes work over a metal – electrolyte interface, they measure an overall electrochemical potential difference $\Delta\psi$ and not simply the electrical potential difference, $\Delta\phi$. Their readings can then be partially affected by differences in concentration of the species in solution. To keep errors to a minimum, it is suggested to use well referenced electrodes jointly with solutions whose composition and expected concentration is, although broadly, anticipated. For instance, [Mus00] used silver chloride electrodes (Figure 18) to monitor the local evolution of the electrical conductivity within clay samples during bench scale electrokinetic tests. The working principle is the silver – silver chloride redox reaction:

$$Ag_{(s)} + Cl^- \rightleftarrows AgCl_{(s)} + e^- \tag{25}$$

AgCl salt deposits at the interface between silver and the electrolyte (Figure 18), centre): since the only species in solution is the chloride anion, the Nernst equation (17) of reaction (25) is:

$$E = E^0 - \frac{RT}{F} \ln a_{Cl^-} \tag{26}$$

When two silver chloride electrodes are used (M and N) the measured potential difference is then:

$$\Delta\psi = \Delta\phi - \frac{RT}{F} \ln\left(\frac{a_{cl^-}^M}{a_{cl^-}^N}\right) \tag{27}$$

where $a_{Cl^-}{}^{(M)}$ and $a_{Cl^-}{}^{(N)}$ are activity of the chloride in the proximity of electrode M and N. By using silver electrode measurements without corrections (then using $\Delta\psi$ instead of $\Delta\phi$), the error made is 0.06 V when $a_{Cl^-}{}^{(M)} / a_{Cl^-}{}^{(N)} = 10$, and is 0.12 V when $a_{Cl^-}{}^{(M)} / a_{Cl^-}{}^{(N)} = 100$.

3.7 Review of laboratory experiments involving electrical conductivity measurements

Most two electrodes terminal systems described in the literature have two cylindrical electrodes laying on top and bottom of soil samples. Samples are inserted into cylinders of non-conductive materials. Some of these cells allow a vertical load to be applied, so they also work as oedometer cells. Materials used for the electrodes include rigid metals (e.g. copper, aluminium, steel), noble metals that do not oxidize (platinum, gold) and graphite (when porous, it can also work as a porous stone).

Table 2 presents a schematic review of selected studies taken from the geomechanical literature where two electrodes terminal systems were used.

Table 2: Selected studies with two electrodes terminal systems.

Study	Electrodes/ Geometry	Mechanical	Hydraulic / Chemical	Objective / Results
[Fuk99]	Stainless steel mesh 1D vertical meas.	Oedometer	-	Evolution of microstructure with load in undisturbed and reconstituted clay specimens
[McC05]	Stainless steel. 1D horizontal and vertical measurement	Oedometer	-	Evaluation of anisotropy upon loading of undisturbed and reconstituted samples
[Lee08]	Stainless steel. Quasi spherical (Needle probe)	Oedometer	-	Evolution of resistance evolution upon loading: evidences of anisotropy and load history effects
[Fuk01]	Stainless steel mesh 1D vertical measurements	Oedometer	Imposed saturation degree / pore water salinity	Preliminary characterisation of soil electrical behaviour aimed at using a four electrodes electrical CPT for the detection of contaminated layers.
[Ble03]	Stainless steel. 1D radial and vertical measurements	-	1 D diffusion in column and oedometer	Evaluation of the effective diffusion parameter of NaCl in kaolin specimens
[Bez09]	Stainless steel. 1D radial measurements	-	1 D diffusion in column	Evaluation of the effective diffusion parameter of NaCl in kaolin specimens
[Att08]	Silver Paint. 1D vertical measurements	-	Evaporation	Evidencing differences between water retention and electrical conductivity in the unsaturated range
[Cho04]	Quasi spherical (Needle probe)	-	-	Evaluation of specimen heterogeneity through electrical resistance profiles
[Fes07]	Stainless steel. Quasi spherical (Needle probe)	-	-	Evaluation of specimen heterogeneity through electrical resistance profiles
[Mus09]	Stainless steel. Quasi spherical (Needle probe)	-	Evaporation	Evaluation of local saturation degree through electrical resistance profiles

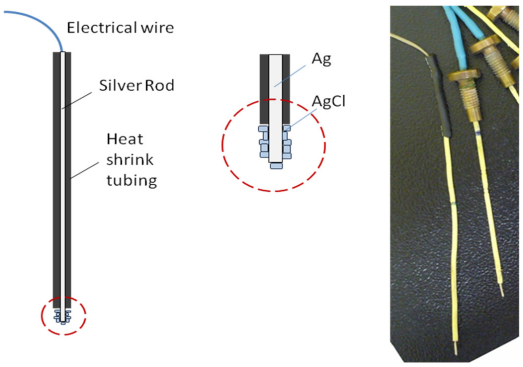

Figure 18: Scheme of a silver chloride electrode for voltage measurements (left), detail of the Ag/AgCl interface (centre), picture of two silver chloride electrodes (right).

Results of two electrode terminals systems were checked against four electrodes terminal systems by [Kle97], suggesting the possibility of explicitly taking into account overpotential effects in the circuit analysis of the experimental results. They proposed a 'simple circuit', introducing an electrode capacitance C_e (Figure 19, left), and an 'enhanced circuit', introducing an electrode capacitance C_e in parallel with an electrode resistance R_e and a ionic diffusion term Q (Figure 19 right).

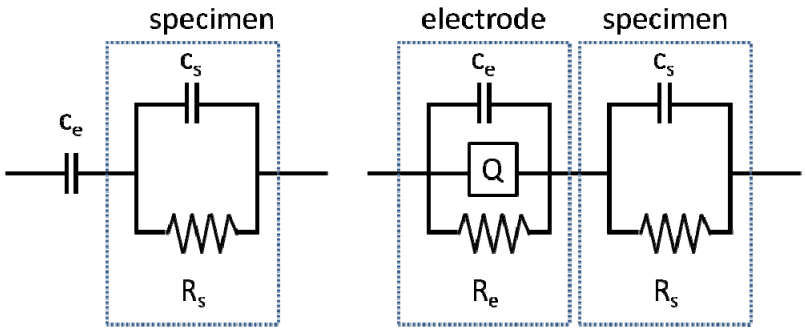

Figure 19: Simple (left) and enhanced (right) circuits for the interpretation of 2 electrode terminals systems. Modified from [Kle97].

Four electrodes terminal systems have been implemented in different geometries. In some studies (e.g. [Abu96a,b]) electrodes A and B are plates at the sample top and bottom and electrodes M and N are punctual electrodes (rods) between A and B, so that one dimensional electrical flow occurs (as in the centre of Figure 17). In many other studies all electrodes are punctual and disposed in different geometries at the sample boundaries, as in the right side of Figure 17 (e.g. [Mou67, Kal93]).

Table 3: Selected studies with four electrodes terminal systems.

Study	Eletrodes / Geometry	Mechanical	Hydraulic / Chemical	Objective / Results
[Mou67]	6 punctual platinum electrodes / 2 pairs of injecting electrodes at the base, 1 pair of voltage electrodes at the top	Oedometer	-	Evaluation of transversally isotropic parameters for electrical anisotropy. 1.10 (a) < χ_h / χ_v < 25.5 (b) a): packed dry bentonite, σ_v = 55 kPa b): bentonite slurry, distilled water, σ_v =165 kPa
[Ana95]	4 punctual circular electrodes / 3 on the base and 1 on the top	Oedometer	-	Evaluation of electrical anisotropy during oedometer loading.
[Kug96]	4 punctual circular electrodes / 3 on the base and 1 on the top	Triaxial	-	Evaluation of electrical anisotropy during triaxial shearing of kaolinite samples
[Kal93]	8 punctual electrodes/ work in turn 4 at a time: 2 external inject current, 2 internal measure potential	-	Water content imposed with pressure plate	Evaluation of relationship between water content and electrical conductivity. Estimation of surface conductivity.
[Abu96a]	2 copper plates and 2 copper rods / vertical measurements: plates inject current, rods measure potential	-	water content imposed upon standard proctor compaction	Evaluation of relationship between water content and electrical conductivity of compacted samples. Loose agreement between electrical conductivity and hydraulic permeability
[Abu96b]	2 copper plates and 2 copper rods / vertical measurements: plates inject current, rods measure potential			Evaluation of bentonite content in sand - bentonite mixtures

As it can be appreciated in Tables 2 and 3, electrical measurements have been associated to an equal number of hydro-chemical and mechanical studies. In studies related to mechanical processes, electrical measurements mostly provided semi quantitative information, such as the anisotropy ratio $A = \chi_h / \chi_v$ used in [Ana95] and [Kug96] to provide an insight on microstructure evolution and on its effects during loading of clay samples in oedometer and triaxial conditions (where χ_h is the horizontal component and χ_v is the vertical component of the electrical conductivity tensor). In other studies, good results were obtained in terms of indirect evaluation of transport parameters ([Ble03]). To allow this interpretation, electrical measurements have to be interpreted in terms of evolution of concentration of a species in space and time. Transport models are then used to simulate the hydro-chemical processes, and transport parameters are sought by means of optimisation through back analyses. Several measurements have to be taken: a limitation of most of the experimental set ups presented in Tables 2 and 3 is that they consider the volume of soil between the measuring electrodes as homogeneous, limiting the possibility of studying transport processes.

A way to relax the assumption of homogeneity comes from performing an high number of electrical measurements with different electrodes in different parts of the

specimen, to be integrated by means of tomography reconstructions (ERT technique, discussed in the previous chapter). Another possibility is moving the measuring electrodes along the specimen. This has been implemented as an electrical needle probe in [Cho04]. The probe is a two terminal electrode system made of two coaxial electrodes: the first one (internal) is a rod, the second one (external) is a metallic hollow cylinder (Figure 20a). The two electrodes are separated by a dielectric material and the electrical signal between them must travel entirely in the soil. The needle probe can be inserted and moved into the soil sample to gather an electrical profile. To be effective, electrical profiling must be done without locally affecting porosity (e.g. in undrained conditions).

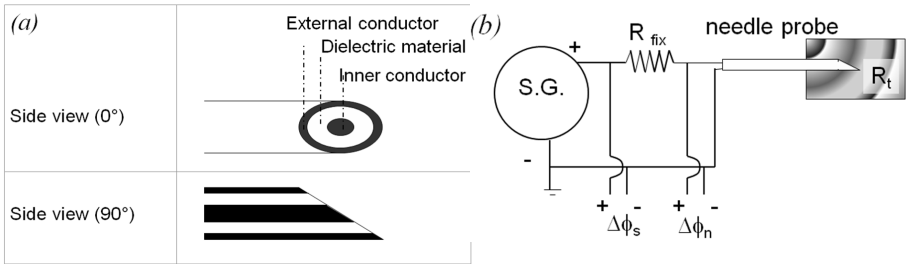

Figure 20: Scheme of the needle probe: arrangement of the electrodes (left), simplified electrical circuit with signal generator and needle probe (right) (modified from [Cho04]).

A scheme of the electrical circuit of [Cho04] is given in Figure 20b. A known fixed resistance R_{fix} is in series with the probe and the electrical current in the circuit is:

$$I = \frac{\Delta\phi_s - \Delta\phi_n}{R_{fix}} \tag{28}$$

where $\Delta\phi_s$ is the potential drop imposed by the signal generator over the whole circuit and $\Delta\phi_n$. is the potential drop in correspondence of the probe. The electrical resistance R of the investigated soil volume is then:

$$R = \frac{\Delta\phi_n}{I} \tag{29}$$

Calibration requires that the effects of frequency on measurements are taken into account. First an operating frequency, higher than the limiting one, is chosen. Then resistance measurements are taken at known medium resistivity, a procedure that is implemented by measuring R values immersing the probe into different solutions having known values of ρ. Experimental (R, ρ) couples are then fitted to determine

the shape factor α of Equation (23): Figure 21a shows a calibration of a needle probe taken from [Fes07]. This relationship is then inverted when interpreting experimental data to evaluate the soil electrical conductivity on base of resistance measurements.

Figure 21b, modified from [Fes07], shows an application of electrical profiles provided by the needle probe, interpreted in terms of porosity. It refers to measurements taken along a column after sedimentation of a dry clay material (Beaucaire clay) had occurred in water. First the electrical conductivity of the water, χ_w, was measured in the supernatant. Local values of soil conductivity χ_t were then estimated based on resistance measurements, through the calibration of Figure 21a. The profile of porosity was then obtained inverting Archie's relationship (9) for the saturated case:

$$n = \left(\frac{\chi_t}{\chi_w} \right)^{1/m} \tag{30}$$

where it was assumed that m = 1.8. Estimated porosities were consistent with direct measurements, based on local mass measurements, proving the potentialities of this approach.

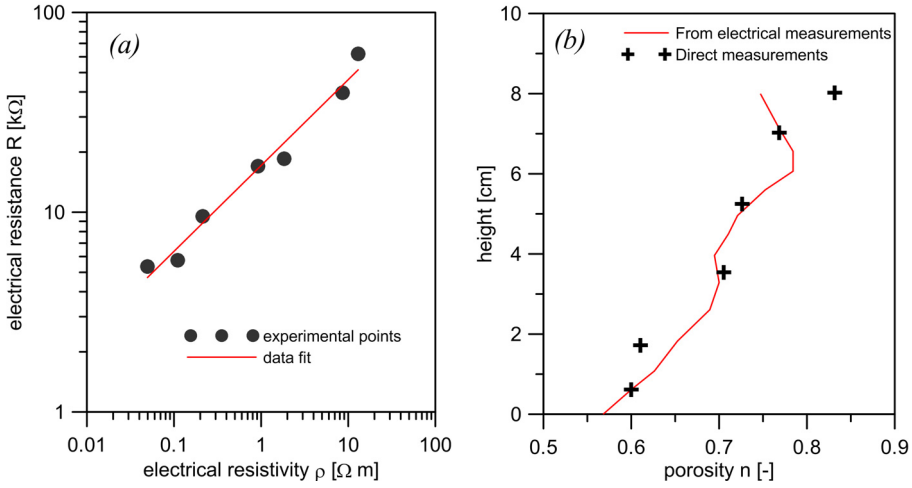

Figure 21: Calibration curve of an electrical needle probe (a) and porosity profile of a column of a sedimented clay obtained with needle probe measurements (b) (modified from [Fes07]).

3.8 Coupled effects of electro-hydraulic fields: electroosmosis

Direct flows discussed in detail in the previous sections are not exhaustive of the processes which are promoted in the presence of field gradients. To close this chapter it is worth mentioning, although briefly, electroosmosis (already introduced in Section 3), which is the transport of water induced by an electric field.

Electroosmosis is an inherently coupled electro-hydraulic process, promoted by the unbalanced surface charge of the solid grains [Spo84]. This coupled flow has been described by means of a number of chemo-physically based models at the pore scale, which justify the formulation of phenomenological laws adopted in geotechnical engineering.

With reference to saturated conditions, the simplest phenomenological formulation for coupled hydro-electrical fluxes in saturated soils is given by the linear system [Mit05]:

$$\begin{bmatrix} i \\ j_w \end{bmatrix} = -\begin{bmatrix} \chi_t & \varepsilon^* \\ k_{eo} & k_w \end{bmatrix} \begin{bmatrix} \nabla\phi \\ \nabla h_w \end{bmatrix} \tag{31}$$

where i is the current density, j_w is the volumetric discharge of water per unit area, $\nabla\phi$ is the electrical potential gradient, ∇h_w is the hydraulic head gradient. The electrical conductivity, χ_t, and the hydraulic conductivity, k_w, account for direct fluxes. The out-of-diagonal coefficients respectively quantify mass flow promoted by the electric field, through the electroosmotic permeability, k_{eo}, and for electric current arising as a consequence of mass flow of water, through the coefficient ε^*. The latter coefficient, describing the so-called *streaming potential* can be derived from the electroosmotic permeability by means of the Onsager's reciprocity principle, and it will not be further taken into consideration in the following. It is worth noting that, for practical applications, which will be briefly discussed in another chapter, the streaming potential can be usually disregarded.

Here the attention is focused on the limits of this linear formulation in the light of the considerations made in the previous sections on the chemical processes which accompany an electric field in the soil.

Relying on the linear formulation given by Equation (31), the electroosmotic permeability could be determined in principle by a very simple experimental setup. A cylindrical cell with insulating and water tight lateral walls could be equipped with a top and bottom plates acting as a pair of electrodes in contact with the sample and allowing for drainage. By imposing the same hydraulic head (and chemical composition) at the boundaries of the sample and constant electrical potential difference between the two plates, a one-dimensional, constant water discharge should be in-

duced. A constant electrical current density is expected in this one-dimensional constant electrical field:

$$\begin{aligned} j_w &= -k_{eo}\,\nabla\phi \\ i &= -\chi_t\,\nabla\phi \end{aligned} \tag{32}$$

Similar experimental arrangement has been adopted extensively in the past to determine the electroosmotic premeability of soils, sometimes in conjunction with uniaxial loading ram to impose vertical stress. In the latter case, the equipment is commonly named *electroosmotic oedometer*. From the electrical point of view, this kind of apparatus belongs to the class of the two electrodes terminal systems, summarised in Table 2. An ideal scheme of such an experimental setup is reported in Figure 22, where the theoretical distributions of pore water pressure and of the electrical potential are indicated.

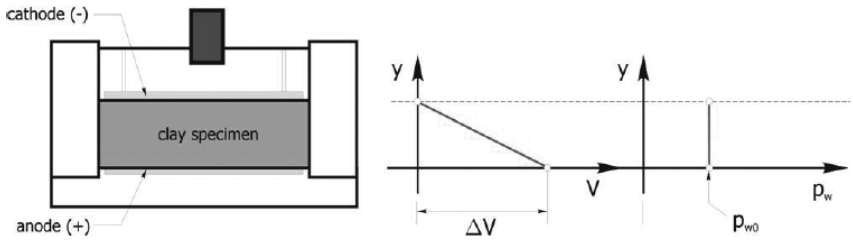

Figure 22: Ideal scheme of electroosmotic oedometer [Tam10].

Selected results from electroosmotic tests performed in a similar equipment are presented in Figures 23 and 24. The comprehensive set of experimental data, together with a detailed description of the equipment developed, and of the material tested are reported in [Gab08a,b] and [Tam10].

In Figure 23 data of water discharge in time are reported of tests lasting not more of 20 minutes at constant applied electric gradient. Water outflow is fairly linear in time although a slight tendency to decrease can be appreciated, even in this short duration tests. If the outflow rate is reported as a function of the applied electrical gradient (Figure 24), a linear relationship between voltage and water flow rate can be drawn and a representative value of the short-term electroosmotic conductivity can be determined.

The data presented in Figure 24 also show the evidence of the energy consumed at the electrodes for water oxidation (section 3.4) and the occurrence of an overpotential η (section 3.5). The outflow rate of water leaving the sample is in fact found to grow linearly with the applied potential drop, if an offset of 1.44 V is applied. This offset can be associated to overpotential effects: since it *consumes* a portion of the

electrical potential, not all the gross potential applied is available as a source for coupled fluxes, and only a part of it being actually imposed on the soil sample. As already discussed in section 3.6, the electrical overpotential, may be due to different and concurrent causes.

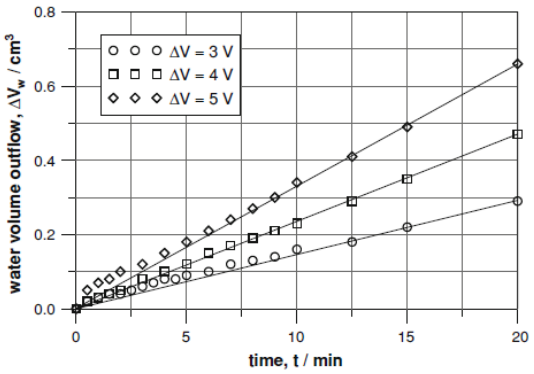

Figure 23: Water discharge data of short term electroosmotic test on a clayey silt [Gab08a].

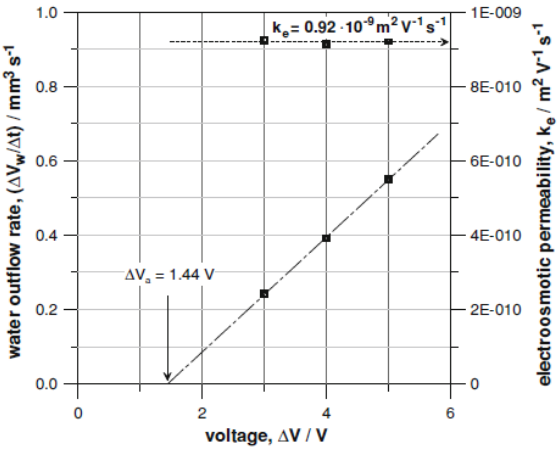

Figure 24: Electroosmotic permeability from data of short term electrokinetic filtration test on a clayey silt [Gab08a].

Results of a similar test, but having longer duration, run on a silty clay of comparable chemical composition as the previous clayey silt, are reported in Figure 25. The test lasted about 15 days, and it was run by imposing a constant current density through the soil, while measuring the voltage at the two extremes of the sample. Dramatic decrease of the average electroosmotic permeability may be observed in

time in the long duration test, which suggests that different coupled phenomena, other than those already described, start to occur in time. Many of these phenomena, discussed in detail in a following section, are actually triggered by local variations of electrical conductivity, due both to variation in the chemical composition of the pore fluid (for example caused by redox reactions, equations (19) and (20)) and by desaturation processes.

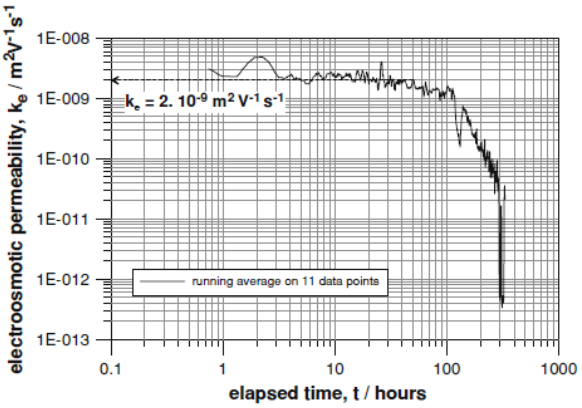

Figure 25: Time evolution of the average electroosmotic permeability of a silty clay in a controlled current density one-dimensional test [Gab08b].

A relevant role has been recognised to be played by penetration into the sample of the gas front generated at the anode [Tam10, Gab08a, Air09], which cannot escape easily from the soil, as it remains entrapped by the water flow towards the cathode. Penetration of the gas front partly desaturates the soil, lowering the electrical conductivity (section 3.2), as well as the electroosmotic permeability.

Little experimental information is available in the literature to quantify the influence of the water degree of saturation on the electroosmotic permeability. The few data collected allow inferring that the electroosmotic permeability of an unsaturated soil might follow a law conceptually similar to that proposed by Archie [Arc42], depending on a power of the water degree of saturation:

$$k_{eo}\left(S_w\right) = k_{eo}^{\ sat}\ k_{eo}^{\ rel} = k_{eo}^{\ sat}\ S_w^{\ \alpha} \tag{33}$$

Data reported in Figure 26 suggest that the electroosmotic permeability decreases with water degree of saturation to a power of about 3, which is intermediate between electric conductivity and hydraulic conductivity.

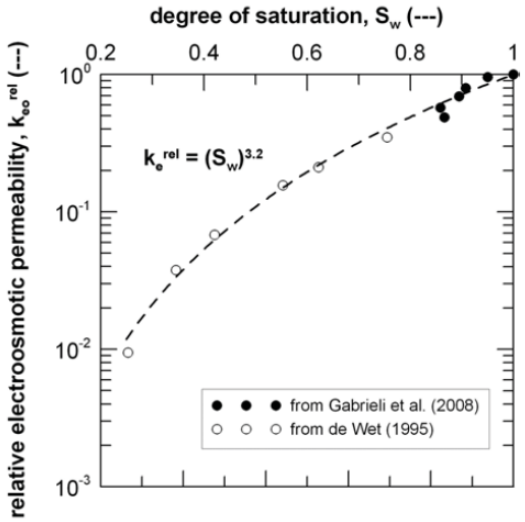

Figure 26: Relative electroosmotic permeability as a function of the water degree of saturation [Tam10].

Ions transport, change in pH, chemical reactions in the aqueous phase and with soil grain constituents may further complicate the simple initial scheme proposed for electroosmotic transport which in reality seldom may be considered a simple and linear coupled water – electric charge transport in porous medium (see, for instance, [Air09]). The merit of Equation (31) is to provide a linearised reference description of this coupled flow around a current equilibrium state.

4 References

[Abu96a] Abu-Hassanein, Z. S., Benson, C. H. and Blotz, L. R. Electrical resistivity of compacted clays. *Journal of Geotechnical Engineering, 122 (5), 397-406*, 1996.

[Abu96b] Abu-Hassanein, Z. S., Benson, C. H., Wang, X., and Blotz, L. R. Determining bentonite content in soil-bentonite mixtures using electrical conductivity. *Geotechnical Testing Journal, 19(1), 51–57*, 1996.

[Air05] Airò Farulla, C. and Ferrari, A. Controlled suction oedometric tests: analysis of some experimental aspects. *Proc. Int. Symposium on Advanced Experimental Unsaturated Soil Mechanics*, Trento, Italy, June 27-29, 2005. Advanced Experimental Unsaturated Soil Mechanics EXPERUS

2005. A. Tarantino, E. Romero and Y.J. Cui (eds.). A.A. Balkema Publishers, Leiden: 43-48, 2005.

[Air09] Airoldi, F., Jommi, C., Musso G., Paglino, E. Influence of calcite on the electrokinetic treatment of a natural clay. *J. Appl. Electrochemistry, 39, 2227-2237*, 2009.

[Alo05] Alonso, E.E., Romero, E., Hoffmann, C. and García-Escudero, E. Expansive bentonite-sand mixtures in cyclic controlled-suction drying and wetting. *Engineering Geology, 81 (3), 213-226*, 2005.

[Ana95] Anandarajah A. and Kuganenthira, N. Some aspects of fabric anisotropy of soil. *Géotechnique, 45(1), 69 –81*, 1995.

[Arc42] Archie, G.E. The electrical resistivity log as an aid to determining some reservoir characteristics. *Trans AIME, 146, 54-63*, 1942.

[Atk10] Atkins P. and De Paula J. *Physical Chemistry*. Oxford University Press, Oxford, 9th ed, 2010.

[Att08] Attia A.M., Fratta D. and Bassiouni Z. Irreducible Water Saturation from Capillary Pressure and Electrical Resistivity Measurements. *Oil & Gas Science and Technology – Rev. IFP, 63(2), 203-217*, 2008. DOI: 10.2516/ogst:2007066.

[Bak09] Baker, R. & Frydman, S. Unsaturated soil mechanics: Critical review of physical foundations. *Engineering Geology, 106(1-2), 26-39*, 2009.

[Bar67] Barden, L. and Sides, G.R. The diffusion of air through the pore water of soils. *Proc. 3rd Asian Reg. Conf. on Soil Mechanics Foundation Engineering*, Israel, 1, 135-138, 1967.

[Ber97] Bernier, F., Volckaert, G., Alonso, E.E. and Villar, M.V. Suction-controlled experiments on Boom clay. *Engineering Geology, 47, 325-338*, 1997.

[Bez09] Bezzar, A. and Ghomari, F. Nondestructive test to track pollutant transport into landfill liners. *Environmental Geology, 57(2), 285–290*, 2009. DOI: 10.1007/s00254-008-1265-5.

[Bla00] Blatz, J. & Graham, J. A system for controlled suction in triaxial tests. *Géotechnique, 50 (4), 465-469*, 2000.

[Bla08] Blatz, J., Cui, Y.J. and Oldecop, L. Vapour equilibrium and osmotic technique for suction control. *Geotechnical and Geological Engineering, 26(6), 661-673,* 2008. DOI: 10.1007/s10706-008-9196-1.

[Ble03] Blewett, J., McCarter, W. J., Chrisp, T. M. and Starrs G. An experimental study on ionic migration through saturated clay. *Engineering Geology, 70, 281-291*, 2003.

[Boc80] Bocking, K.A. and Fredlund, D.G. Limitations of the axis translation technique. *Proc. 4th Int. Conf. on Expansive Soils*, Denver, Colorado: 117-135, 1980.

[Cho04] Cho, G. C.; Lee, J-S. and Santamarina, J.C. Spatial Variability in Soils: High Resolution Assessment with Electrical Needle Probe. *Journal of Geotechnical and Geoenvironmental Engineering, 130 (8), 843-850*, 2004.

[Cui05] Cuisinier, O. and Masrouri, F. Influence de sollicitations hydriques et mécaniques complexes sur le comportement d'un sol gonflant compacté. *Canadian Geotechnical Journal, 42(3), 731–741*, 2005.

[DeG02] De Gennaro, V., Cui, Y.J., Delage, P. and De Laure, E. On the use of high air entry value porous stones for suction control and related problems. *Proc. 3rd Int. Conf. on Unsaturated Soils,* Recife, Brasil, March 10-13, 2002. Unsaturated Soils. J.F.T. Jucá, T.M.P. de Campos and F.A.M. Marinho (eds.). A.A. Balkema Publishers, Lisse, 1: 435-440, 2002.

[Del98] Delage, P., Howat, M.D. and Cui, Y.J. The relationship between suction and swelling properties in a heavily compacted unsaturated clay. *Engineering Geology, 50, 31-48*, 1998.

[Del08a] Delage, P., Romero, E. & Tarantino, A. Recent developments in the techniques of controlling and measuring suction in unsaturated soils. *Unsaturated Soils: Advances in Geo-Engineering, Proc. 1st European Conf. on Unsaturated Soils,* Durham, UK. D.G. Toll, C.E. Augarde, D. Gallipoli and S.J. Wheeler (eds.). CRC Press/Balkema, Leiden: 33-52, 2008.

[Del08b] Delage, P. & Cui, Y.J. An evaluation of the osmotic method of controlling suction. *Geomechanics and Geoengineering: An International Journal, 3(1), 1-11*, 2008. DOI: 10.1080/17486020701868379

[Del05] Delgado A.V., Gonzalez-Caballero F., Hunter R.J., Koopal L.K. and Lyklema J. Measurement and interpretation of electrokinetic phenomena (IUPAC Technical Report). *Pure Appl. Chem., 77 (10), 1753–1805*, 2005. DOI: 10.1351/pac200577101753.

[Due04] Dueck, A. *Hydro-mechanical properties of a water unsaturated sodium bentonite. Laboratory study and theoretical interpretation*. Ph. D. Thesis, Lund University, Sweden, 2004.

[Due07] Dueck, A. Results from suction controlled laboratory tests on unsaturated bentonite – Verification of a model. *Proc. 2nd Int. Conf. Mechanics of*

Unsaturated Soils, Weimar, Germany, March 7-9, 2007. Experimental Unsaturated Soil Mechanics. T. Schanz (ed.). Springer Proceedings in Physics, 112. Springer-Verlag, Berlin: 329-335, 2007.

[Est90] Esteban, F. *Caracterización experimental de la expansividad de una roca evaporítica.* Ph. D. Thesis, Universidad de Cantabria. Spain (in Spanish), 1990.

[Fes07] Festa, C. *Resistivity and seismic methods applied to laboratory soil testing*. PhD Thesis. Politecnico di Torino, 2007.

[Fre77] Fredlund, D.G. and Morgenstern, N.R. Stress state variables for unsaturated soils. *J. Geotech. Engrg. Div., ASCE, 103(5), 447-466*, 1977.

[Fre93] Fredlund, D.G. and Rahardjo, H. *Soil mechanics for unsaturated soils.* John Wiley & Sons, Inc. New York, 1993.

[Fuk99] Fukue, M., Minato, T., Horibe, H. and Taya N. The micro-structures of clay given by resistivity measurements. *Engineering Geology, 54, 43-53*, 1999.

[Fuk01] Fukue M., Minato T., Horibe H. and Taya N. Use of a resistivity cone for detecting contaminated soil layers. *Engineering Geology, 60, 361 – 369*, 2001.

[Gab08a] Gabrieli, L., Jommi, C., Musso G., Romero, E. Influence of electroosmotic treatment on the hydro-mechanical behaviour of clayey silts: preliminary experimental results. *J. Appl. Electrochemistry, 38, 1043-1051*, 2008.

[Gab08b] Gabrieli, L., Jommi, C., Musso G., Romero, E. Electrokinetic treatment of a natural silt in saturated and unsaturated conditions. *Proc. 3rd Int. Symposium GeoProc'2008*. Thermo-Hydromechanical and Chemical Coupling in Geomaterials and Applications. J.-F. Shao and N. Burlion (eds.). ISTE Ltd, London: 203-210, 2008.

[Gar56] Gardner, W.R. Calculation of capillary conductivity from pressure plate outflow data. *Soil Sci. Soc. Am. Proc., 20, 317-320*, 1956.

[Hil56] Hilf, J.W. *An investigation of pore-water pressure in compacted cohesive soils.* PhD Thesis. Technical Memo No.654, United States Bureau of Reclamation, Denver, 1956.

[Hof05] Hoffmann, C., Romero, E. and Alonso, E.E. Combining different controlled-suction techniques to study expansive clays. *Proc. Int. Symposium on Advanced Experimental Unsaturated Soil Mechanics*, Trento, Italy, June 27-29, 2005. Advanced Experimental Unsaturated Soil Mechanics

EXPERUS 2005. A. Tarantino, E. Romero and Y.J. Cui (eds.). A.A. Balkema Publishers, Leiden: 61-67, 2005.

[Hor85] Horvath, A.L. *Handbook of aqueous electrolyte solutions: physical properties, estimation and correlation methods*. Ellis Horword Limited, John Wiley & Sons, New York, 1985.

[Hoy08] Hoyos, L.R., Laloui, L. ad Vassallo, R. Mechanical testing in unsaturated soils. *Geotechnical and Geological Engineering, 26(6), 675-689*, 2008. DOI: 10.1007/s10706-008-9200-9.

[Jot07] Jotisankasa, A., Coop, M. and Ridley, A. The development of a suction control system for a triaxial apparatus. *Geotechnical Testing Journal, 30(1), 1-7*, 2007.

[Kal93] Kalinski, R.J. and Kelly, W. E. Estimating water content of soils from electrical resistivity . *Geotechnical Testing Journal, 16(3), 323-329*, 1993.

[Kle97] Klein, K. and Santamarina, J. C. Methods for Broad-Band Dielectric Permittivity Measurements (Soil-Water Mixtures, 5 Hz to 1.3 GHz), *Geotechnical Testing Journal, 20(2), 168-178*, 1997.

[Kle03] Klein, K. and Santamarina, J. C. Electrical Conductivity in Soils: Underlying Phenomena. *J. Environ. Eng. Geophys., 8(4), 263–273*, 2003.

[Kug96] Kuganenthira, N., Zhao, D. & Anandarajah, A. Measurement of fabric anisotropy in triaxial shearing. *Géotechnique 46(4), 657-670* , 1996.

[Kun62] Kunze, R.J. and Kirkham, D. Simplified accounting for membrane impedance in capillary conductivity determinations. *Soil Sci. Soc. Am. Proc., 26, 421-426*, 1962.

[Law05] Lawrence, C.A., Houston, W.N., Houston, S.L. and Harraz, A.M. Pressure pulse technique for measuring diffused air volume. *Proc. Int. Symposium on Advanced Experimental Unsaturated Soil Mechanics*, Trento, Italy, June 27-29, 2005. Advanced Experimental Unsaturated Soil Mechanics EXPERUS 2005. A. Tarantino, E. Romero and Y.J. Cui (eds.). A.A. Balkema Publishers, Leiden: 9-13, 2005.

[Lid97] Lide, D.R. & Frederikse, H.P.R. CRC *Handbook of chemistry and physics. A ready-reference book of chemical and physical data.* CRC Press, New York, 1997.

[Lee08] Lee, C., Lee, J-S., Lee, W. and Cho T.H. Experiment Setup for Shear Wave and Electrical Resistance Measurements in an Oedometer. *Geotechnical Testing Journal, 31(2), 1 – 7,* 2008.

[Llo85] Lloret, A. & Alonso, E.E. State surfaces for partially saturated soils. *Proc. 11th Int. Conf. on Soil Mechanics and Foundation Engineering,* San Francisco, 2, 557 – 562, 1985.

[Llo03] Lloret, A., Villar, M. V., Sánchez, M., Gens, A., Pintado, X. and Alonso, E. E. Mechanical behaviour of heavily compacted bentonite under high suction changes. *Géotechnique, 53(1), 27–40*, 2003.

[Loc83] Lockhart N.C. Electroosmotic dewatering of clays, III. Influence of clay type, exchangeable cations and electrode materials. *Colloids and Surfaces, 6, 253-269,* 1983.

[Mar08] Marinho, F.A.M., Take, W.A. and Tarantino, A. Measurement of matric suction using tensiometric and axis translation techniques. *Geotechnical and Geological Engineering*, *26(6), 615-631,* 2008. DOI: 10.1007/s10706-008-9201-8.

[Mas08] Masrouri, F., Bicalho, K.V. and Kawai, K. Laboratory hydraulic testing in unsaturated soils. *Geotechnical and Geological Engineering, 26 (6), 691-704*, 2008. DOI: 10.1007/s10706-008-9202-7.

[McC05] McCarter, W J., Blewett, J, Chrisp, T M., Starrs, G. Electrical property measurements using a modified hydraulic oedometer. *Canadian Geotechnical Journal, 42 (2), 655-662(8)*, 2005.

[Mer11] Merchán, V., Romero, E. & Vaunat, J. An adapted ring shear apparatus for testing partly saturated soils in the high suction range. *Geotechnical Testing Journal, 34 (5), 1-12*, 2011.

[Mit05] Mitchell, J.K. and Soga, K. Fundamentals of soil behavior. *John Wiley & Sons*, Hoboken, New Jersey, 2005.

[Mou67] Mousseau, R.J., and R.P. Trump. Measurement of electrical models anisotropy of clay-like materials. *J. Appl. Phys. 38:4375–4379*, 1967.

[Mus00] Musso, G. *Electrokineti phenomena in soils*. Ph.D Thesis, Politecnico di Torino, 2000.

[Mus03] Musso, G., Romero, E., Gens, A. & Castellanos, E. The role of structure in the chemically induced deformations of FEBEX bentonite. *Applied Clay Science, 23, 229-237*, 2003.

[Mus05] Musso, G. and Romero, E. Chemo – mechanical behaviour of high density bentonites. Imbibition and diffusion tests. *Proc. of the Int. Symp. on Large Scale Field Tests in Granite Sitges,* Barcelona, Spain 12-14 Nov. 2003. E.E. Alonso and A. Ledesma (eds.). Balkema, Leiden, The Netherlands, 283-291, 2005.

[Mus09] Musso, G., Casini, F., Colombo, L., Jommi, C. and Springmann, S. Impiego di un ago elettrico per la misura indiretta del contenuto in acqua di campioni non saturi. *Incontro annuale dei ricercatori di Geotecnica, IARG 2009*, Roma, Italy, (in Italian), 2009.

[Old04] Oldecop, L. and Alonso, E.E. Testing rockfill under relative humidity control. *Geotechnical Testing Journal, 27(3), 1-10*, 2004.

[Oli96] Olivella, S., Gens, A., Carrera, J. & Alonso, E.E. Numerical formulation for a simulator (CODE_BRIGHT) for the coupled analysis of saline media. *Engineering computations, 13 (7), 87-112*, 1996.

[Oli06] Oliveira, O.M. and Marinho, F.A.M. Study of equilibration time in the pressure plate. *Proc. 4th Int. Conf. on Unsaturated Soils, Carefree,* Arizona, April 2-6, 2006. Unsaturated Soils. Geotechnical Special Publication No. 147. G.A. Miller, C.E. Zapata, S.L. Houston and D.G. Fredlund (eds.). ASCE, Reston, Virginia, 2, 1864-1874, 2006.

[Pad06] Padilla, J.M., Perera, Y.Y., Houston, W.N., Perez, N. and Fredlund, D.G. Quantification of air diffusion through high air-entry ceramic disks. *Proc. 4th Int. Conf. on Unsaturated Soils, Carefree, Arizona, April 2-6, 2006.* Unsaturated Soils. Geotechnical Special Publication No. 147. G.A. Miller, C.E. Zapata, S.L. Houston and D.G. Fredlund (eds.). ASCE, Reston, Virginia, 2, 1852-1863, 2006.

[Par67] Parkhomenko E.I. *Electrical Properties of Rocks*. Plenum, New York, 1967.

[Pin02] Pintado, X. *Caracterización del comportamiento termo-hidro-mecánico de arcillas expansivas*. Ph. D. Thesis, Universitat Politècnica de Catalunya, Spain (in Spanish), 2002.

[Pin09a] Pintado, X., Lloret, A. & Romero, E. Assessment of the use of the vapour equilibrium technique in controlled-suction tests. *Canadian Geotechnical Journal, 46 (4), 411-423*, 2009. DOI: 10.1139/T08-130

[Pin09b] Pintado, X., Lloret, A. & Romero, E. Reply to the discussion by Leong et al. on 'Assessment of the use of the vapour equilibrium technique in controlled-suction tests'. *Canadian Geotechnical Journal, 46(12), 1485-1486*, 2009. DOI: 10.1139/T09-131

[Ric41] Richards, L.A. A pressure membrane extraction apparatus for soil suction. *Soil Science, 51(5), 377-386*, 1941.

[Rom99] Romero, E. *Characterisation and thermo-hydro-mechanical behaviour of unsaturated boom clay: an experimental study*. PhD Thesis, Universitat Politècnica de Catalunya, Barcelona, Spain, 1999.

[Rom01a] Romero, E. Controlled-suction techniques. *Proc. 4º Simpósio Brasileiro de Solos Nâo Saturados Ñ SAT'2001*. W.Y.Y. Gehling & F. Schnaid (eds.). Porto Alegre, Brasil, 535-542, 2001.

[Rom01b] Romero, E., Gens, A. & Lloret, A. Laboratory testing of unsaturated soils under simultaneous suction and temperature control. *Proc. 15th Int. Conf. on Soil Mechanics and Geotechnical Engineering,* Istanbul, August 27-31, 2001. A.A. Balkema, Rotterdam, 1, 619-622, 2001.

[San01] Santamarina, J.C., Klein, K.A., and Fam, M.A. *Soils and waves*. John Wiley & Sons, Toronto, 2001.

[Sen97] Sen P. N. Resistivity of partially saturated carbonate rocks with microporosity. *Geophysics, 62(2), 415–425*, 1997.

[Spo84] Sposito, G. *The surface chemistry of soils* Oxford University Press, New York, 1984.

[Tam10] Tamagnini, C., Jommi, C., Cattaneo F. A model for coupled electro-hydro-mechanical processes in fine grained soils accounting for gas generation and transport. *Annuals of the Brazilian Academy of Science, 82, 169-193*, 2010.

[Tan05] Tang, A.M., and Cui, Y.J. Controlling suction by the vapour equilibrium technique at different temperatures and its application in determining the water retention properties of MX80 clay. *Canadian Geotechnical Journal, 42, 287-296*, 2005.

[Tan11] Tang, A.M., Cui, Y.J., Qian, L.X., Delage, P. & Ye, W.M. Calibration of the osmotic technique of controlling suction using a miniature tensiometer. *Proc. 5th Asia-Pacific Conf. on Unsaturated Soils,* 29 February – 2 March 2012, Dusit Thani Pattaya, Thailand. Unsaturated Soils: Theory and Practice. A. Jotisankasa, A. Sawangsuriya, S. Soralump and and W. Mairaing (eds.). Kasetsart University, Thailand, 1, 423-427, 2011.

[Tar00] Tarantino, A., Mongiovì, L. and Bosco, G. An experimental investigation on the independent isotropic stress variables for unsaturated soils. *Géotechnique, 50(3), 275-282*, 2000.

[Tar11] Tarantino, A., Gallipoli, D., Augarde, C.E., De Gennaro, V., Gómez, R., Laloui, L., Mancuso, C., El Mountassir, G., Muñoz, J.J., Pereira, J.-M., Peron, H., Pisoni, G., Romero, E., Raveendiraraj, A., Rojas, J.C., Toll, D.G., Tombolato, S. & Wheeler, S. Benchmark of experimental techniques for measuring and controlling suction. *Géotechnique, 61(4), 303–312*, 2011. DOI: 10.1680/geot.2011.61.4.303

[Van08] Vanapalli, S.K., Nicotera, M-V. and Sharma, R.S. Axis translation and negative water column techniques for suction control. *Geotechnical and*

Geological Engineering, *26(6), 645-660*, 2008. DOI: 10.1007/s10706-008-9206-3.

[Vil99] Villar, M.V. Investigation of the behaviour of the bentonite by means of suction-controlled oedometer tests. *Engineering Geology, 54, 67-73*, 1999.

[Wax68] Waxman, M. H., and Smits, L. J. M. Electrical Conductivities in Oil-Bearing Shaly Sands. *Soc. Pet. Eng. J, 8, 107-122*, 1968.

[Wil94] Wilson, G.W., Fredlund, D.G. & Barbour, S.L. Coupled soil - atmosphere modeling for soil evaporation. *Canadian Geotechnical Journal, 31(2), 151-161*, 1994. DOI: 10.1139/t94-021

[Yah99] Yahia-Aissa, M. *Comportement hydromécanique d'une argile gonflante fortement compactée.* Ph. D. Thesis, Ecole Nationale des Ponts et Chaussées, France, 1999.

Physical models at increasing scale and role of theoretical / numerical back-analyses

Enrique Romero*-Guido Musso-Cristina Jommi*****

** Universitat Politècnica de Catalunya*
Department of Geotechnical Engineering and Geosciences
c/ Jordi Girona, 1-3, Campus Nord UPC, Building D-2
08034 Barcelona, Spain
enrique.romero-morales@upc.edu

***Politecnico di Torino*
Dipartimento di Ingegneria Strutturale, Edile e Geotecnica
Corso Duca degli Abruzzi, 24
10129 Torino, Italy

****Politecnico di Milano*
Dipartimento di Ingegneria Strutturale
piazza Leonardo da Vinci, 32
20133 Milano, Italy

In spite of advancements in the techniques for the study of thermo-hydro-chemo-mechanical behaviour of geomaterials at the REV scale, the latter might not provide an exhaustive picture of transport processes in soil, when non-linear coupling terms arise, and when scale effects are expected. To overcome the difficulties associated with this issue, physical models, in which relevant coupled fields may be tracked in time, can be developed. Most often, theoretical and / or numerical models must accompany the interpretation of the physical test, to exploit all the information provided by measurements. In this chapter a few examples of increasing complexity are briefly presented to discuss this viewpoint and to show the potentialities provided by physical models aided by theoretical and numerical interpretation in the comprehension of coupled behaviour.

1 Introduction

Geomechanics and geo-environmental engineering problems, such as earth constructions, waste confinement at surface or at great depths, soil pollution and remediation, often involve heat, mass and contaminant transport. These processes cannot be fully understood unless a clear picture of coupled thermo-hydro-chemo-mechanical behaviour of geomaterials is drawn. Despite advancements in experimental techniques developed to study these processes (refer to the previous chapters), and despite the development of refined control techniques, issues remain regarding the effects promoted by the coupling terms and their interpretation.

On the one hand, control conditions may be imposed only on the boundary of the specimen at the macroscopic, or phenomenological, scale. Homogeneity of the relevant fields inside the specimen is not guaranteed when transport processes occur. On the other hand, control may be applied only to direct fields, but indirect processes, arising as a consequence of primary gradients, evolve independently from any external control. Non-linearity, which almost always characterise the behaviour of soils under any coupled field, further complicate full understanding of the soil response.

As a consequence, detailed experimental information on the local distribution of the relevant field quantities usually remains unknown, unless local/tomographic experimental data are provided (see, for instance, the previous chapter on experimental techniques for multi-scale description of soil fabric). If not, theoretical back-analysis or numerical simulation aided techniques seem to be mandatory to interpret the experimental information and better define the soil response to external loading.

In this chapter a few examples, from previous physical models of the authors, are presented to contribute to this discussion. Firstly, experimental setup of cells at laboratory scale (bench/mock-up scale) equipped with different combinations of chemo-thermo-hydro-mechanical controlled conditions at the boundary are presented. The cells were developed and used in the study of a number of multi-physics processes in geomaterials, within the context of different investigations:

- soil-atmosphere interaction for the prediction of local water balance in upper unsaturated soils [Car11a, b];
- thermal loads effects on saturated geomaterials in the performance of low-permeability argillaceous formations proposed as potential radioactive waste repository [Muñ09, Lim10, Lim11];
- air migration and air pressure breakthrough processes in low permeability argillaceous formations and their role in the onset of air pathways [Rom10, Rom12a,b];
- electrical resistivity tomography in the study of salt transport, wetting processes and water retention properties at the bench scale [Com11, Cos12].

The examples are accompanied by comments on the use of theoretical back-analysis and numerical simulation tools for the understanding of the evolutionary processes at the local scale. Theoretical and numerical models are useful to evidence which, among several possible coupled / multiscale phenomena, have a significant role on

the investigation of concern. Then they provide complementary information on the evolution of local variables, due to coupled interaction mechanisms, and also offer a possible interpretation tool for checking reliability of experimental results.

In the numerical modelling of all these coupled problems a huge amount of information on the material behaviour is usually needed. Given also simple models, a large number of material parameters are usually involved, which, in some cases, can be evaluated directly from purportedly designed laboratory tests. However, in most cases, when coupled processes are involved, back-analysis of laboratory experiments specifically designed to highlight the relevant processes associated with the unknown parameters are necessary. Carrying out a back-analysis of the boundary value test allows better identification of some model parameters which cannot be easily derived from direct experimental information on a homogeneous REV, by means of the definition and the minimisation of an objective function, which depends on the differences between measured and computed variables. The suggested procedure is not free of drawbacks, it may admit more than one solution, and a certain degree of judgment must be always put in interpreting the data, as the following examples help in showing.

2 Hydraulic boundary value model column for soil-atmosphere interaction

2.1 Introduction

Water balance resulting from the transport processes taking place in the unsaturated zone is a key factor in the hydrological and mechanical processes responsible for slope instability and shallow landslides. Infiltration and evaporation affect shallow water-table fluctuations, groundwater recharge, and groundwater contamination. Spatial and temporal distribution of rain and evaporation are the forcing climatic conditions at the boundary of the soil system. Infiltration and evaporation hydrologic models, based on climatic forcing conditions only, are most often adopted to predict the water balance in the subsoil, while scarce information on the soil water retention and transport properties are introduced in these models. This approach has two obvious drawbacks. Firstly the soil properties contribute to determine infiltration and evaporation capacity of the soil in a different way as a function of the seasonal conditions. Secondly, these purely hydrologic models can reproduce quite well the water content evolution in the upper soil layers, if properly trained on some historical data, but they will lose their predictive capabilities, when changes should intervene in the climatic conditions or in the soil properties.

To overcome these drawbacks, and provide predictive tools which could account for changing scenarios, numerical models can be developed. Accurate description of the actual physical processes requires the solution of a non-isothermal problem account-

ing for two-phase liquid and vapour transport (e.g. [Phi57, Mil84]). When models of the latter class are designed, concerns may arise on the best way to translate meteorological data into forcing boundary conditions, on the one hand, and on the experimental verification of the predictive capabilities of these numerical models, on the other.

In this section, selected results from a prototype soil column, set up at the Structural Engineering Department of the Politecnico di Milano, and left in the environmental uncontrolled atmospheric conditions, starting from the end of October 2009, are presented. The prototype was designed to obtain direct experimental information on soil-atmosphere water exchanges, based on a simple measurement technology, which could be easily replicated in situ, when a true scale monitoring programme were planned. More details on the equipment and assessment of standard hydrologic models are provided by [Car11a, b].

2.2 Experimental Setup

The soil prototype cell (Figure 1) is a 1200 mm high transparent tube, made of acrylic to avoid any electrical interference with capacitive probes, with a 5 mm thick wall and an internal diameter of 290 mm. The column is fastened at its bottom into an acrylic base plate, by insertion in a 5 mm wide annular hole sealed with a couple of o-rings, to avoid evaporation or outflow of liquid water. The base plate internally allows for the allocation of a porous stone, eventually connected to an external water level regulation device and pressure measurement system. The diameter was chosen to ensure that the sensors response was not influenced by the wall of the acrylic tube. Previous experimental data had shown that the capacitive probes measurements are affected by the water content in a cylindrical volume of soil of about 160 mm diameter and 150 mm height, centred on the probe. At the centre of the base plate a 25 mm depth circular hole was designed, to ensure correct centred positioning of the capacitance probes PVC access tube.

To provide information on soil-atmosphere water exchange, capacitive probes were chosen. Suction was not controlled, nor measured, contrarily to what laboratory tests at the REV scale may suggest. This choice was dictated by the following reasons: (a) water content is the information needed for water balance evaluation, and (b) suction measurement in situ can be reliable only in a limited suction range, depending on the suction probes air entry-value, and on their response time.

Basically, the chosen probe provides the resonance frequency of an inductive-capacitive circuit, in which the soil participates as a resistive and capacitive element, depending on its water content. The sensor accuracy is ± 0.06% of the readout soil water content. A smaller-scale chamber had been previously designed to provide the reference data in water and in air, and to verify the calibration of the sensors inserted in a soil representative volume [Ava12].

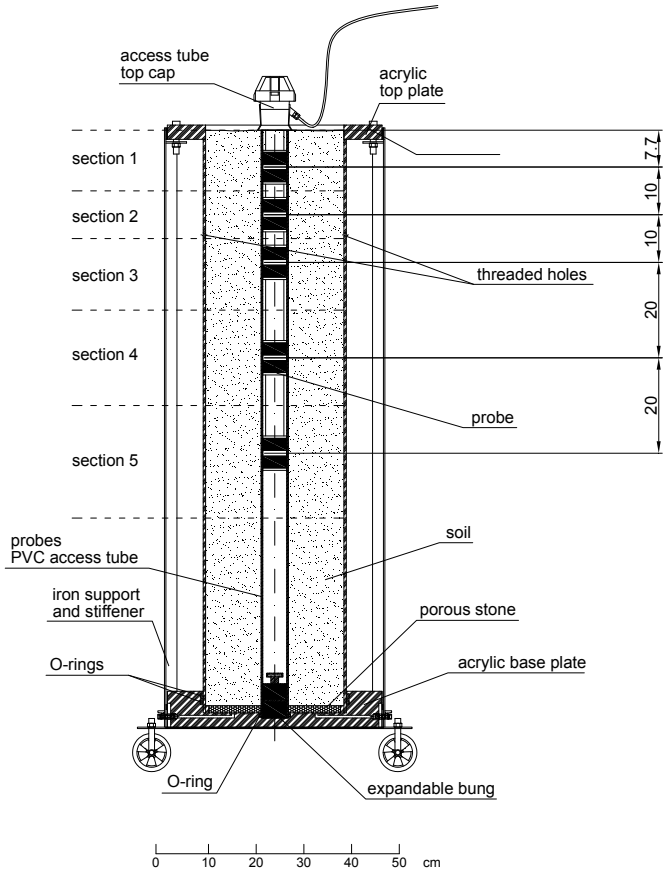

Figure 1: Schematic layout of the prototype column apparatus [Car11a].

A meteorological station, consisting of a rain gauge, a thermo hygrometer with an anti-radiant shield, a combined wind speed-direction sensor and a global radiometer was mounted nearby the prototype column, to provide actual meteorological information. The rain gauge has a resolution of 0.2 mm, with accuracy of ±0.2 mm/min in the range between 0 and 1 mm/min, and of ± 1% in the range 1-10 mm/min. The thermo hygrometer has accuracy of ± 0.1 °C for temperature, and of ± 1.5% for humidity. The wind sensor has a speed resolution of 0.05 m/s and a resolution of 4° for direction, a speed accuracy of 0.1 m/s ± 1% and a direction accuracy of 1% of the respective readout values. The global radiometer has an uncertainty of ±10% over a day measurement.

The installation depth of the five probes used in the prototype is indicated in Figure 1, and it was chosen in such a way that sharp gradients expected close to the soil-atmosphere boundary could be accurately tracked.

2.3 Experimental results

Data refer to a sandy silt, having a liquid limit of $w_L = 0.33$ and a plastic limit of $w_P = 0.20$. The soil was mixed with tap water, left to homogenise in a humid chamber for 24 hours, and then compacted as uniformly as possible in layers of 10 cm thickness. The as compacted mean void ratio was $e_0 = 0.55$ at an initial degree of saturation $S_{r0} = 0.50$.

Meteorological data measured in the first two months, from 20/10/2009 to 20/12/2009 are reported in Figure 2, while the response of the soil water probes is collected in Figure 3. In the figure, the probes data are already processed to give the volumetric water content time evolution at the various depths. Soil water content was registered any 5 min, while the weather parameters were collected every 20 min.

The data allow for distinguishing clearly the response of the soil to the forcing meteorological conditions, and to highlight the role played by the soil hydraulic properties and by the previous hydraulic history. The progression of infiltration fronts following rainy events may be appreciated by the sudden increase of the water content, with a time lag increasing from the top to the bottom of the soil column. Equally, the evaporation rate tends to decrease with depth, and can hardly be appreciated below the first 50 cm depth.

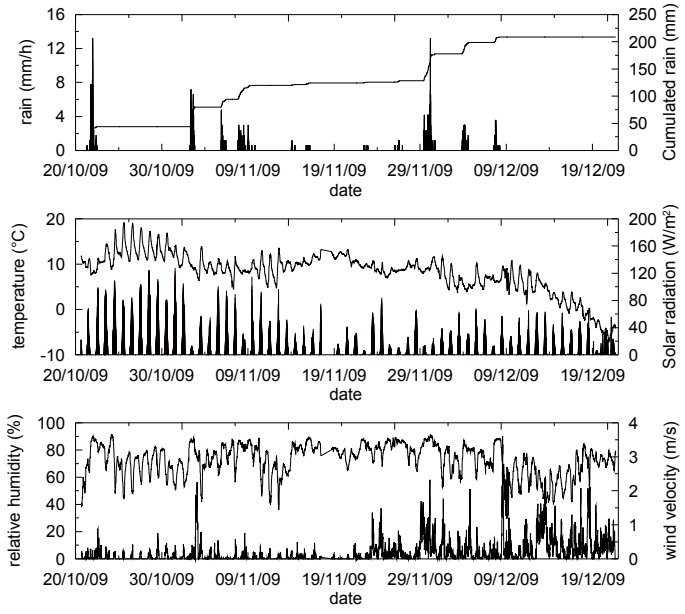

Figure 2: Meteorological data [Car11a].

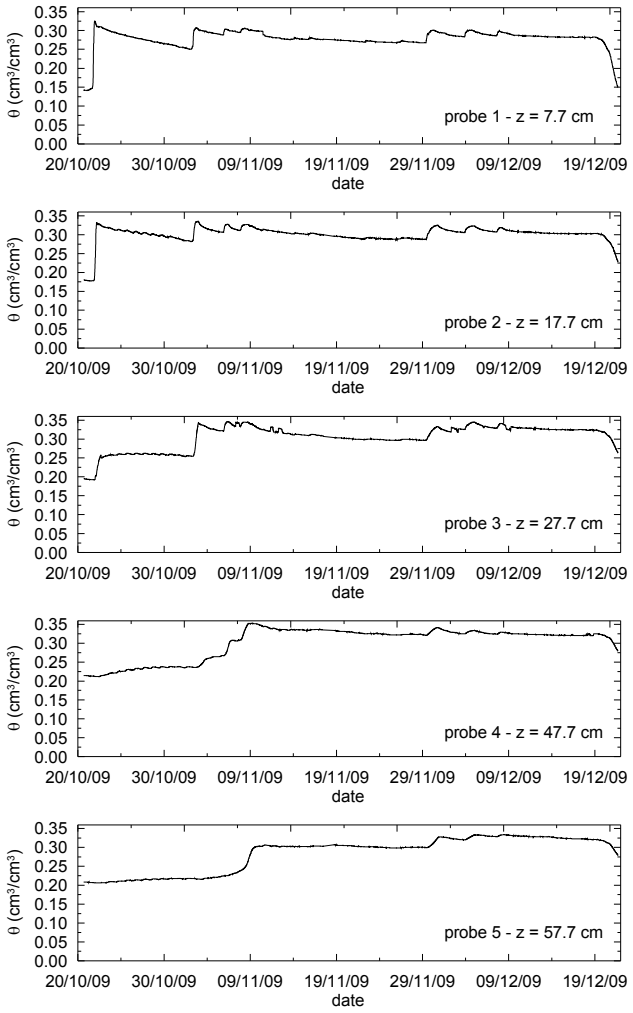

Figure 3: Evolution of soil volumetric water content at increasing depths [Car11a].

Immediately after rain stops, in the upper portions of the soil the water content starts to decrease at a rate which seems to be independent from the actual temperature or relative humidity. The datum suggests that, for this soil, the dominating process just after a rainy event is downward infiltration, at least for a short time interval. Afterwards, the water content variation tends to stabilise to a constant decreasing rate, which is interpreted as the effect of evaporation towards the upper surface. Only the first 50 cm topsoil seem to contribute significantly to the evaporation process, although a slight decrease in the water content at a depth of 57.7 cm begins to be appreciated when the actual saturation degree is close to one.

To provide deeper insight into the soil water mass balance, three rainy events are analysed in more detail. The first one had a cumulated rain of 43.8 mm in about 11 hours (Figure 4), the second one 36 mm over a 14 hour period (Figure 5) and the last one 47.6 mm over 22 hours (Figure 6). In each figure, the probe readings and the rainfall event description (intensity and cumulated values) are reported, together with diagrams which help in the analysis of water balance. To perform the balance, the column was subdivided into five sections, starting from the top soil-atmosphere interface (Figure 1). Volumetric water content measured by each probe was assumed to be representative of the whole section. The incremental and the cumulative mass variations were then calculated starting from the top section and adding progressively the underlying layers.

The data referring to the first event (Figure 3) clearly show the advancing front starting from the first section and reaching the third section after few hours. Sections 4 and 5, below the first 30 cm, are not affected directly by the rain event. The amount of water which can be stored in the upper layers correspond to the difference between the water content at the beginning of rain and the water content corresponding to saturation. Once saturation is reached, the probe reading remains constant until rain stops. Constant readings in the upper soil layers at increasing water content at greater depths denote a continuing infiltration process downwards. The cumulative mass variations in the first sections show that all the rain infiltrates into the soil, due to the initial low water content.

Infiltration following the second rainy event analysed (02/11/09, Figure 4) reaches more rapidly the third section and starts to affect also the lower section 4. Nonetheless, the amount of water stored into the soil layers is still measured by the water content variation in the first three sections. In fact, when the fourth probe reading starts to increase (at the beginning of the day after the rain), in the upper layers the water content is already decreasing, denoting that a downward redistribution process is taking place. The amount of water that infiltrates into the soil is less than that available from rainfall, even if the cumulated rain is lower than in the previous event and its duration is longer, which is a clear consequence of the role played by the initial soil water distribution.

The influence of the initial water content distribution is even more evident with reference to the third rainy event (Figure 5), characterised by a cumulate similar to the first one analysed, albeit distributed over a longer time period. In this case, the infiltration front clearly reaches quickly the last monitored section, as the upper layers were close to saturation already at the beginning of the rainfall. Nonetheless, only one third of the total amount of water available from rainfall infiltrates into the soil, as the peak in the cumulative water mass shows, just at the end of the rainfall. In this case, water ponding was clearly evident at the top surface.

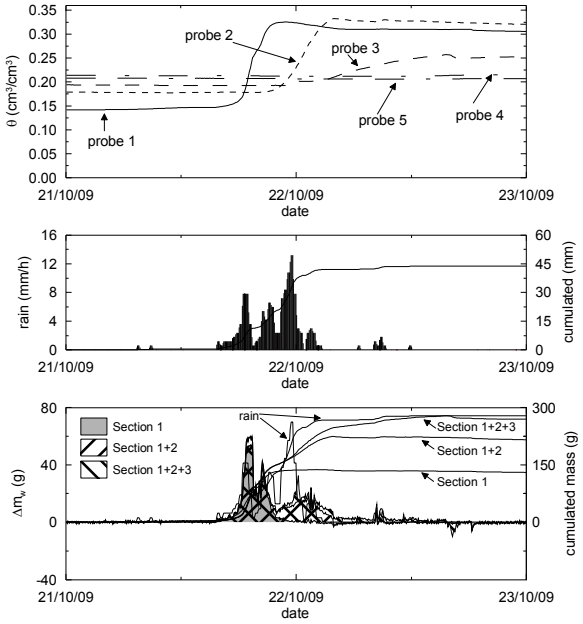

Figure 4: Data and elaborations for rainfall event on 22/10/2009 [Car11a].

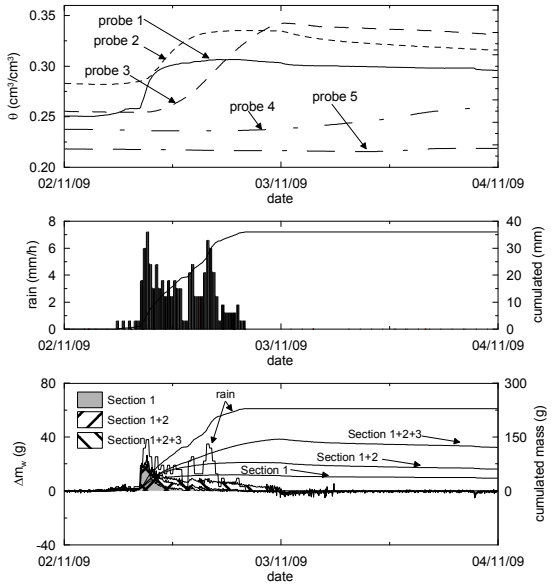

Figure 5: Data and elaborations for rainfall event on 2/11/2009 [Car11a].

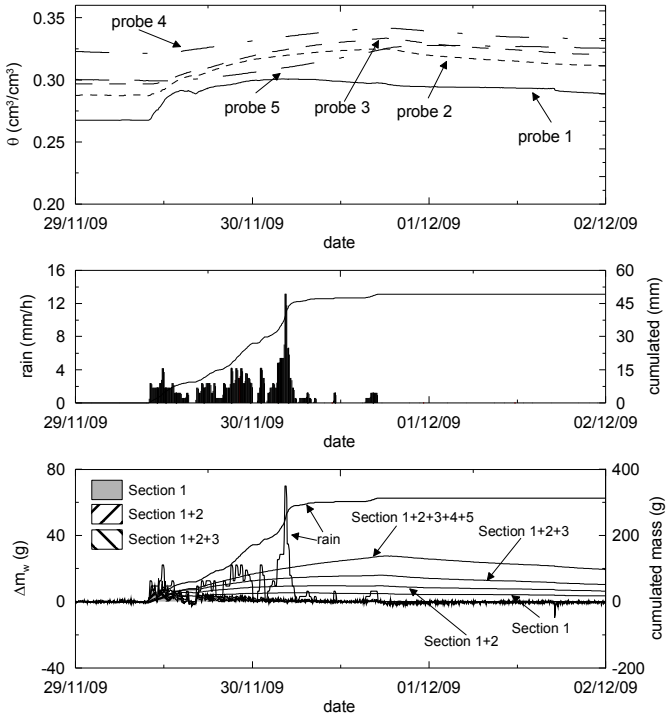

Figure 6: Data and elaborations for rainfall event on 29/11-30/12/2009 [Car11a].

The previous three comparisons highlight that in real problems, when coupled transport processes occur in the field – which is simulated in the prototype column – different aspects concur to determine the soil response, which is not homogeneous at all, in spite of possible homogeneity of soil properties. Not only non-linear coupling affects the behaviour of the soil at the REV scale, as already discussed in the previous chapters, but also the local actual state of the soil at the beginning of any event largely determine the soil response. Here, water saturation distribution at the beginning of rainfall events clearly emerged as the key factor in the water balance, given the soil properties and the forcing boundary conditions. Internal redistribution takes place continuously and affects increasing depths as the average water content increases.

In practical applications, not only the boundary conditions cannot be controlled, but also the response of the soil is dynamically evolving as a function of the actual boundary conditions and of the previous loading history, which cannot be completely reproduced at the scale of a laboratory test. The prototype soil column apparatus, developed for the analysis of soil-atmosphere interaction, allows for tracking water balance depending on rain infiltration, evaporation outflow and moisture movements inside the soil, but only by careful post processing of the soil water content data.

The soil column was instrumented with capacitive probes only, in view of the field applications, where the installation of other measuring instruments would be more difficult or less significant. Although suction probes would provide a more complete picture of the hydraulic state of the soil, their response time is much higher than that of water content probes, whenever installed in soils finer than sands.

3 Thermo-hydraulic boundary value experiments

3.1 Thermo-hydraulic properties using simple setups. Back-analysis of parameters

A simple testing setup was developed by [Pin02a,b] to determine selected thermo-hydraulic parameters on heavily compacted Febex bentonite under partially saturated states. Tests were designed to apply a controlled flux of heat at one of the ends of a cylindrical specimen (38 mm diameter, 76 mm high) and to maintain the other end at constant temperature. A latex membrane allowed soil deformation while keeping constant the overall water content. Since coupled phenomena could induce flow of water either because of pressure gradients (liquid flow) or because of vapour diffusion, local water contents were expected to change inside the sample. An additional external layer (55 mm thick) of heat insulating deformable foam surrounded the specimen, to limit lateral loss of heat. To ensure well reproducible boundary conditions and a controlled heat flux at the sample ends, two identical parts of specimen were placed symmetrically to the heater, as shown in Figure 7. The heater is a copper cylinder (38 mm diameter, 50 mm high) with five small electrical resistances housed inside. In the tests, a constant power of 2.6 W was used, which allowed reaching steady state temperatures in the range of 70-80ºC at the hotter end of the specimen. At the colder end, a constant temperature of 30ºC was maintained by circulating water through the stainless steel head in contact with the soil (Figure 7).

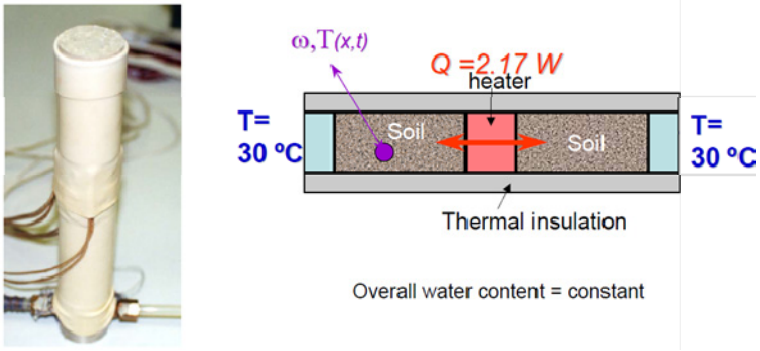

Figure 7: Photograph of the simple experimental setup (without external thermal insulation and upper head) and scheme of the experimental device [Pin02a,b].

During the tests, temperatures at both ends and at three internal points of the specimen, located at regular intervals, were monitored. At the end of the tests, the soil samples were cut into six small cylinders and the water content of each one determined.

Three specimens of bentonite statically compacted at a dry density of 1.68 Mg/m^3 and with initial water content of 15.3, 16.9 and 17.1%, respectively, were tested. Temperatures measured during the heating period for one of the specimens (w=17.1%) are shown in Figure 8. Temperature reached a quasi-steady state regime after 10 hours.

A back-analysis procedure was used for the identification of some thermal and hydraulic parameters [Pin02a]. The fully coupled finite element program Code_Bright [Oli96] was used to model the thermo-hydraulic behaviour of the clay. Axisymmetric analyses allowed evaluating the effect of loss of heat at the lateral boundary of the sample –around 60% of total heater power–, which highlighted the importance of performing 2D analyses of the experiment, instead of more simple 1D simulations.

Temperatures obtained at four different elapsed times and at four points of the sample, as well as water contents measured at the end of the test, were considered as data vector for the inverse problem. Optimisation aimed at reducing the value of an objective function, expressing the difference between values predicted by a forward model of the test and data vector. For each test, optimisation was achieved by changing the value of three model parameters. Among these, one corresponded to the thermal problem –the thermal conductivity of bentonite under saturated condition, λ_{sat}–; and two corresponded to the hydraulic problem –the tortuosity factor τ affecting the diffusion of vapour [Oli94], and the exponent β of the unsaturated relative permeability law (k_r=S_r^{β}). The remaining model parameters were obtained directly from complementary tests [Llo07]. The values of β, τ and λ_{sat} found are summarised in Table 1.

Table 1: Exponent in relative permeability law obtained for the different tests.

Test	Water content (%)	β in $k_r = S_r^{\beta}$	Tortuosity factor τ for diffusion of vapour	Saturated thermal conductivity λ_{sat} ($Wm^{-1}K^{-1}$)
1	15.5	3.06	0.56	1.19
2	16.9	1.10	0.74	1.31
3	17.1	1.68	0.90	1.38

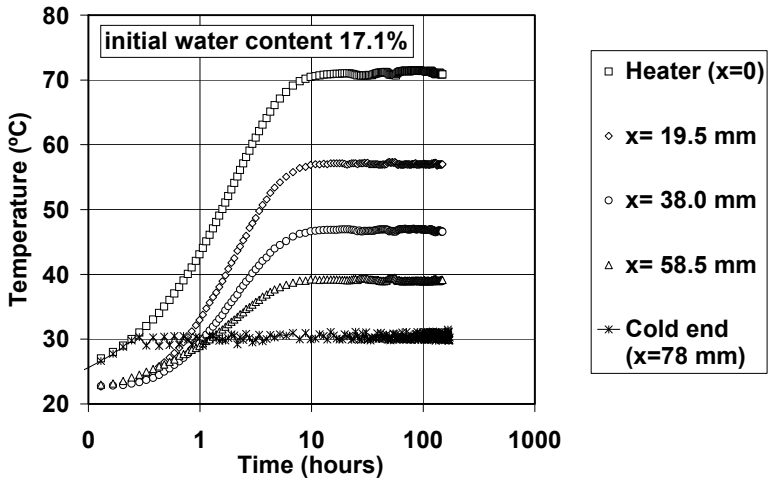

Figure 8: Evolution of temperature in a prescribed heat flow test [Pin02b].

The optimisation procedure showed that there were different combinations of parameters giving equivalent results in terms of the objective function. This was expected, since in the measured water content it was difficult to distinguish between water transported by liquid flow (controlled by β) and by vapour diffusion (controlled by τ). Taking into account all the tests together, the following set of parameters and laws was selected:

$$k_r = S_r^3 \;;\quad \tau = 0.8 \;;\quad \lambda\,(\mathrm{Wm^{-1}K^{-1}}) = 0.47 + 0.68 S_r \tag{1}$$

This set of parameters was used to solve the direct problem and simulate all the heat flow tests, which are plotted in Figures 9 and 10. The error between measured and computed values was of the order of magnitude of the measurement error [Pin02b]. As observed in the figures, the inverse method provided a systematic and consistent procedure to find the best parameters that reproduced the measurements for the selected model. The method also gave further insight into the model by allowing capturing the dependence and coupling between parameters [Pin02b].

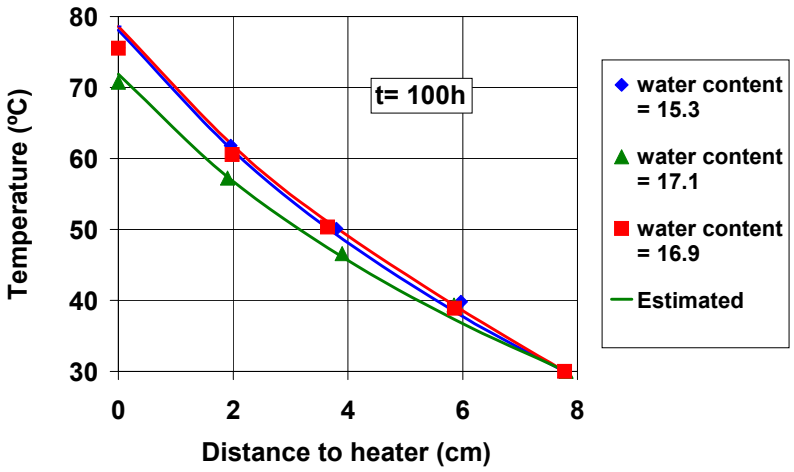

Figure 9: Measured and computed temperatures in the prescribed heat flow tests, using the final selected parameters [Pin02b].

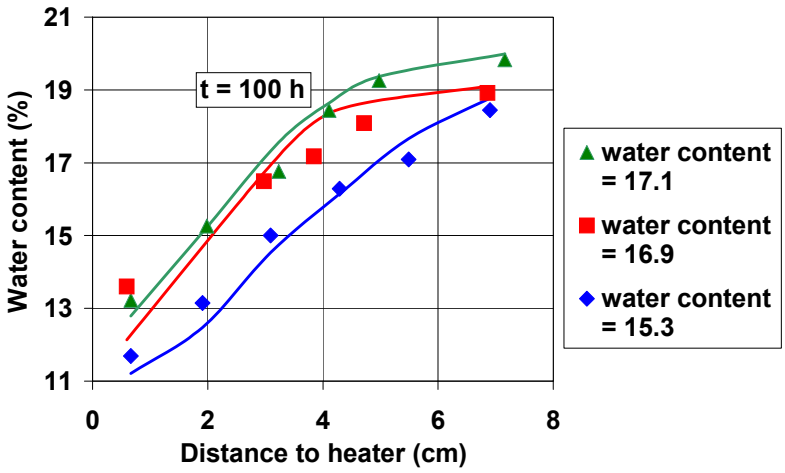

Figure 10: Measured and computed water contents in the prescribed heat flow tests, using the final selected parameters [Pin02b].

3.2 Constant volume cell for heating pulse tests. Experimental setup, back-analysis of thermal parameters and simulation of results

Thermal impact may play an important role on the behaviour of low-permeability saturated clayey formations in connection with the design of a repository for 'High-Level Radioactive Waste'. This impact can be studied through back-analysis of heating pulse tests.

Figure 11 shows a scheme of a constant volume (isochoric) and axi-symmetric heating cell [Muñ09, Lim10, Lim11], which is used to study heating pulse tests with controlled power supply and controlled hydraulic boundary conditions. Soil sample size is 75 mm in diameter and 100 mm high. A controlled-power heater is installed along the axis of the sample in the lower part of the cell. Different transducers monitor the sample response, as shown in the figure: two miniature pore water pressure transducers (Pw_1 and Pw_2 in Figure 11), and three thermocouples (T_1, T_2 and T_3). The cell is equipped with top and bottom valves to apply controlled hydraulic boundary conditions (u_u and u_b).

Heating tests at (nearly) constant volume and different target temperatures (maximum 85°C) were performed under controlled hydraulic boundary conditions on natural and saturated Boom clay [Lim10, Lim11]. Attention is focused on the time evolution of temperature and pore water pressure changes during heating and cooling paths –i.e., pore pressure build-up during quasi-undrained heating and later dissipation to the applied hydraulic boundary conditions–. Throughout the course of the heating/cooling paths, the bottom drainage is maintained open at constant water backpressure using an automatic pressure / volume controller, while the upper valve is kept closed. This backpressure is important since it allows measuring the pore pressure drop during the cooling phase without invading the negative range (below atmospheric conditions). The initial and external temperatures are regulated by submerging the cell inside a temperature controlled water bath at temperature T_4 (Figure 11). Figure 12a shows the time evolutions of temperature for different locations and along a heating and cooling cycle. Figure 12b presents the corresponding time evolutions of pore water pressures.

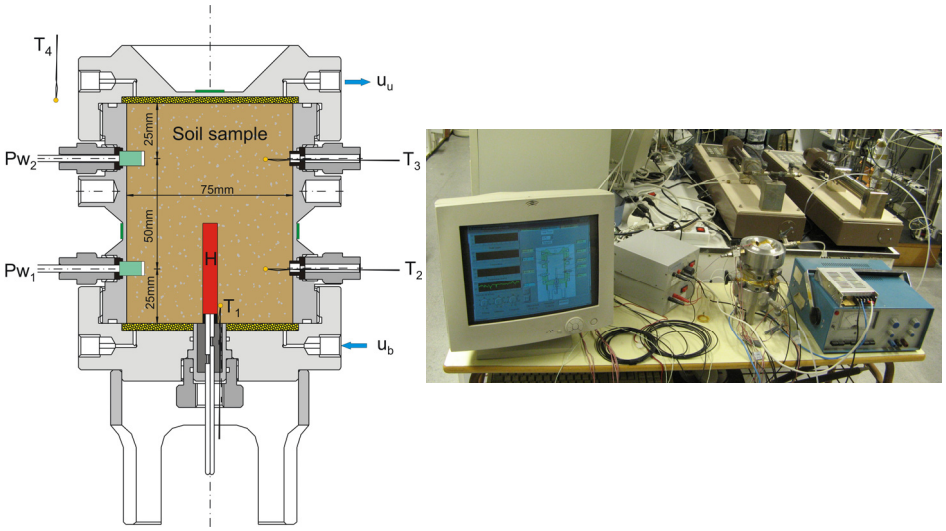

Figure 11: Quasi-isochoric axi-symmetric heating cell and components [Lim10, Lim11].

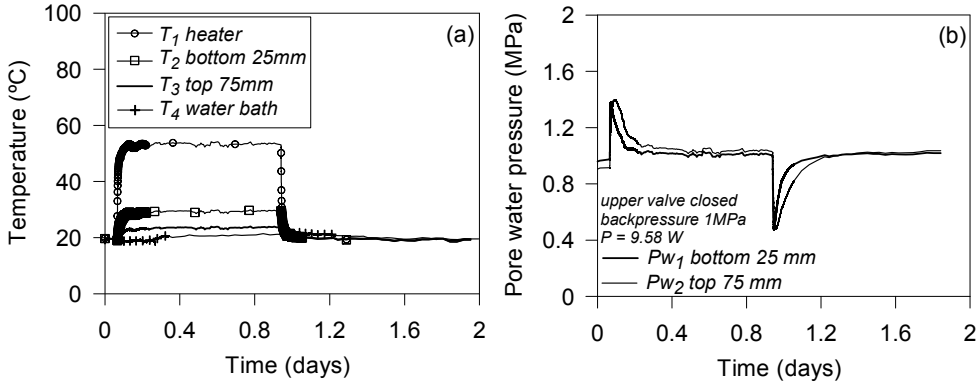

Figure 12: Temperature and pore water pressure evolutions during heating and cooling paths on saturated Boom clay [Lim10, Lim11].

In the interpretation of the test results, it was assumed that temperatures and heat flux were not influenced by water pressure and flow, which means that heat convection was assumed to be negligible. The driving process for temperature change during the test is thus conduction only. This assumption is justified by the condition of constant overall volume prevailing in the heating cell that makes the change in porosity and the velocities of the solid phase very small. Moreover, the low permeability of the material prevents the existence of high velocities for the liquid phase. The flux of heat convected by the solid and liquid phases is, therefore, extremely low.

On the contrary, water pressure and flow were assumed to be influenced also by temperature: as a consequence, while the thermal problem was decoupled from the hydraulic one, the hydraulic problem was coupled to the thermal one.

The test was then interpreted in two separated stages. First, a back-analysis of temperature measurements was carried out by performing uncoupled thermal simulations using the finite element program Code_Bright [Oli96]: only the balance equation for energy was solved. Heat exchanged by the highly conductive stainless steel cell with the controlled water bath was accounted for as a convection-type boundary condition of the problem. This heat flux was assumed to be proportional to the difference between the temperature of the cell and the temperature of the water bath (around 19ºC) at each boundary node, through a convection coefficient h. Thermal optimisation was then aimed at identifying the values of the saturated thermal conductivity λ and the convection coefficient h. Calculations were performed for different combinations of λ and h. For each of them, a measure of the discrepancy between temperature simulation results and temperature experimental measurements ε was computed for different elapsed times. The three-dimensional plot in Figure 13 shows the differences ε between simulation results and experimental observations. The best agreement was obtained for $\lambda = 1.6$ $Wm^{-1}K^{-1}$ and $h = 24$ $Wm^{-2}K^{-1}$. Figure 14 (at the bottom) displays the temperature field inside the cell at the maximum temperature of the heater (85ºC) and under steady state conditions and using the previously back-analysed parameters.

Thermal parameters were then further used to calibrate selected hydraulic parameters by analysing joint thermal and hydraulic results. Figure 15 displays the time evolutions of temperature and pore water pressure (experimental and simulated results) of Boom clay during heating and cooling paths. The water permeability values determined by back-analysis were in agreement with direct measurements performed with controlled-gradient tests.

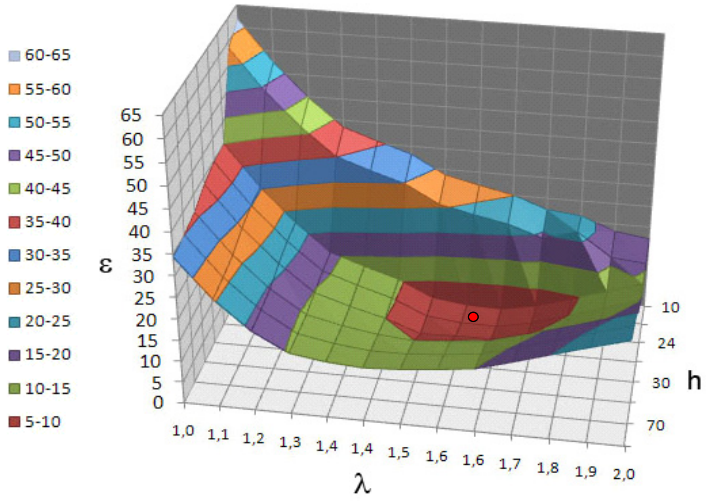

Figure 13: Three-dimensional graph showing the differences in temperature between observations and calculations in the back-analysis of the heating pulse test. Determination of thermal conductivity λ and convection coefficient h [Lim11].

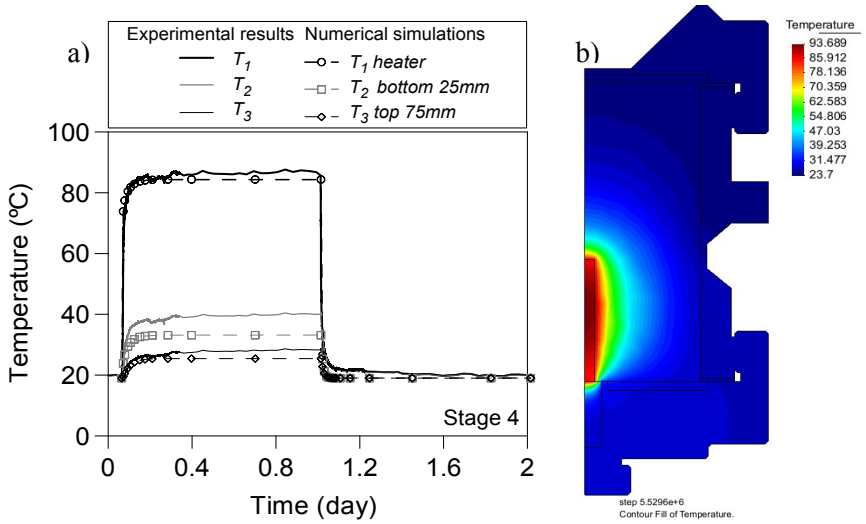

Figure 14: (a) Time evolution of temperature: experimental and simulated results. (b) Temperature field inside the cell at maximum heater temperature [Lim11].

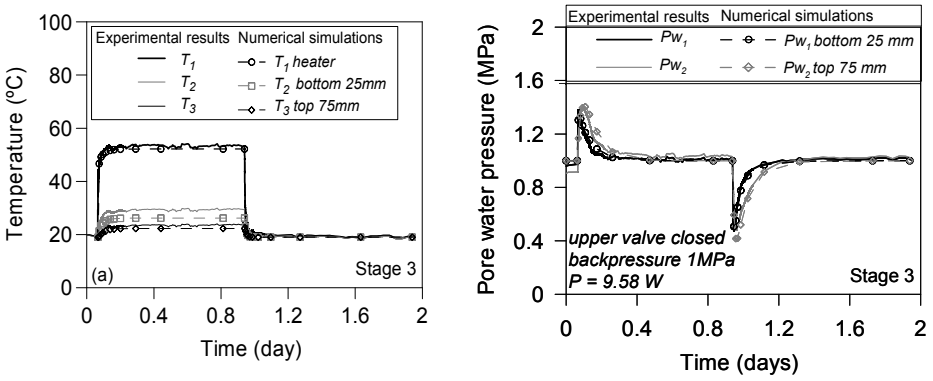

Figure 15: Heating and cooling paths on Boom clay. Experimental and numerical results [Lim11].

4 Air tests on low-permeability claystone formations

Understanding the phenomena and processes associated with release of gases from the disposal systems of a geological repository for radioactive waste is one of the key issues in the assessment of repository performance [Hor99, Har03, Arn08]. The actual gas migration mechanisms may entail standard two-phase flow conditions (partially displacing water) or more complex mechanisms involving coupled two-phase geomechanical phenomena –in all cases, preferential gas pathways will develop taking advantage of the material heterogeneity and anisotropy, rock discontinuities or interfaces–. These gas transport mechanisms are sensitive to the stress state. In fact, two-phase flow is affected by porosity changes and pathway transmissivity is sensitive to fracture aperture variations (see for instance, [Oli08]). Laboratory scale experiments under controlled pneumatic, hydraulic and mechanical boundary conditions are important within this context to provide quantitative data for model validation (applicability of two-phase flow models) and for parameter estimation (calibration of hydraulic and two-phase flow properties).

Figure 16 shows a scheme of the high-pressure triaxial cell jointly with the test set-up, which was specifically designed to apply isotropic/anisotropic stress states up to a maximum of 40 MPa, while injecting air at controlled volume rate [Rom10, Rom12a,b]. Axial strain of small-height specimens –confined by several neoprene membranes and aluminium foils– is registered by an external LVDT transducer. Each cap of the triaxial cell has inlet and outlet lines, prepared for gas and liquid connections. The equipment uses four automatic pressure / volume controllers (P/V in the figure), two for gas (injection and extraction at downstream point), and two for water, which can be used in combination (for example, air injection and water pressure at downstream). The gas injection pressure / volume controller has a maxi-

mum range of 20 MPa (maximum volume 500 mL), and is able to control volume rates between 10^{-4} mL/min and 100 mL/min (volume resolution < 5 mm^3). The 2 MPa P/V controllers for air and water at downstream present a volumetric resolution of 1 mm^3 (pressure resolution 1 kPa).

Before the air injection tests, saturation of the samples was ensured, and water permeability was measured using different hydraulic gradients at different isotropic confining stresses. Figure 17 displays a scheme of this type of hydraulic test (test A in the figure), in which upstream / downstream volume changes and axial strains are recorded. For the air injection test B in the figure, the upstream water line was rapidly drained to inject air pressure at 0.5 MPa and the recovery system maintained with water at 0.5 MPa to better ensure sample saturation. The sample was let to equalise under an initial pore water pressure of 0.5 MPa and at the target total stress (typically between 15 and 19 MPa). Fast air injection at controlled volume rates (typically at 100 mL/min) started from an initial air pressure value of 3 MPa. After reaching maximum air pressure (lower than the confining stress), the upstream piston was stopped and air pressure was let to decay at constant volume. Fitting the constant mass system for different injection periods allowed estimating the initial injection volume of air (injection piston and air lines). Pressure deviations from the perfect gas law for a constant mass system in the injection point allowed estimating the injected mass of air and mass inflow rates into the sample. Information on outflow rates was recorded and used to define the breakthrough pressures.

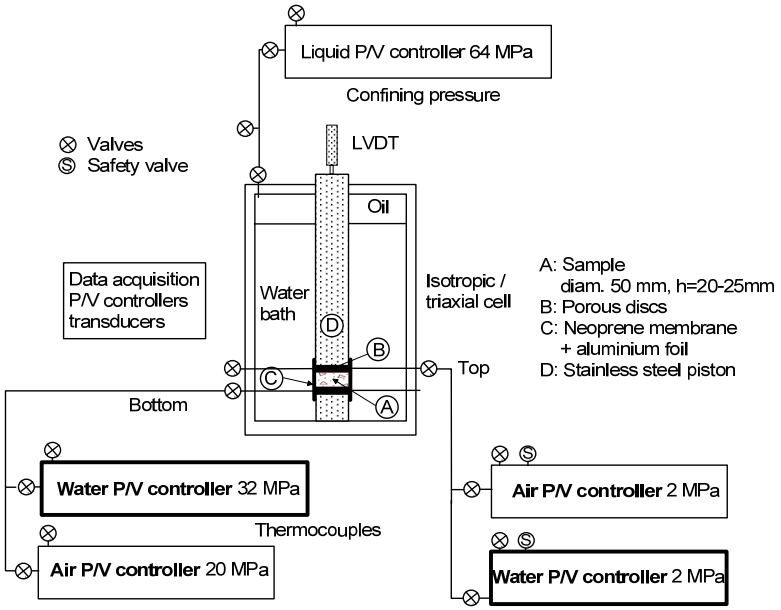

Figure 16: Scheme of the air injection and water permeability setup with high-pressure triaxial cell and four pressure/volume controllers (two for air and two for water) [Rom12a,b].

Figure 18 shows the time evolution of air injection pressure during a fast controlled volume-rate test at 15 MPa isotropic confining stress on a low-porosity claystone sample. V_0 in the figure represents the initial injection volume of air (injection piston and air lines). As observed in the figure, the injection pressure increased up to 13 MPa, followed by a shut-in and recovery period at constant volume. Outflow response was immediately observed after shut-in corresponding to a small drop in the injection pressure, followed by a subsequent gradual decline. After the apparent air breakthrough process –corresponding to an increase in the outflow pressure–, the injection pressure showed a steep decline. The constant downstream pressure condition of 0.5 MPa was not possible to maintain due to the high outflow volume rates detected (the downstream pressure increased until reaching 2 MPa, where a constant pressure was again prescribed by the pressure release valve). With regard to the axial displacement response (negative axial displacement corresponds to expansion), the sample at constant isotropic total stress displayed quasi-reversible features with expansion at the early fast air injection stage and progressive compression towards approximately the initial volume on air pressure dissipation.

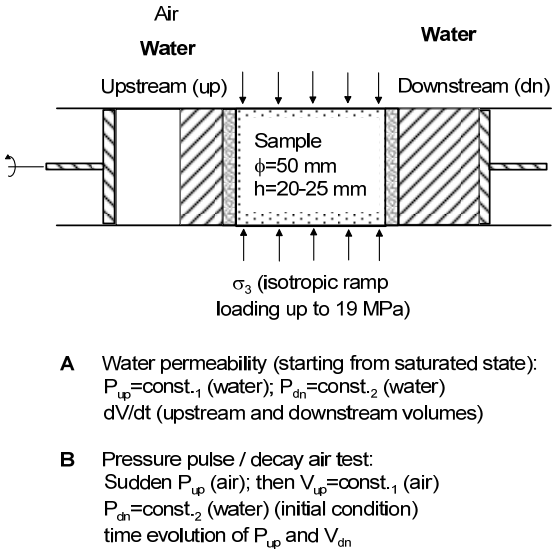

Figure 17: Type of tests performed during controlled-gradient water permeability tests and fast air injection tests followed by recovery period at constant volume [Rom12b].

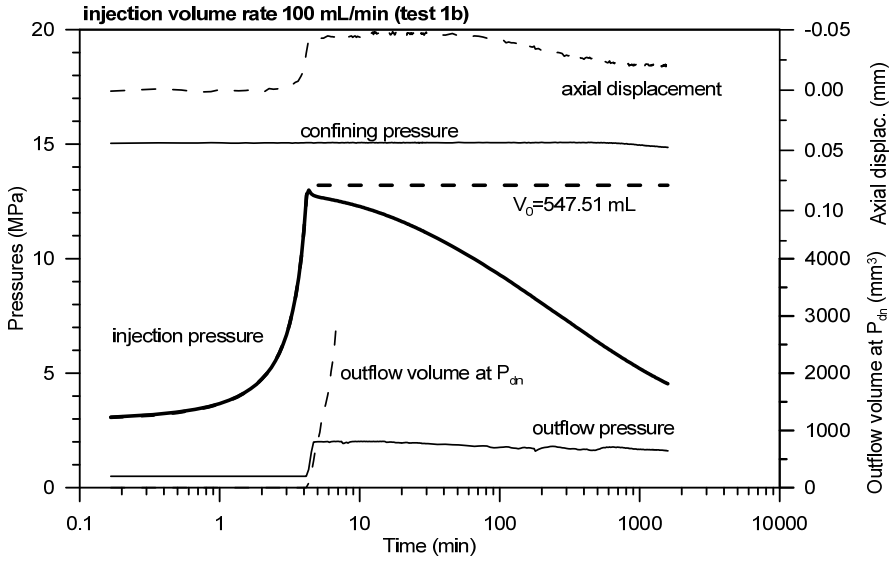

Figure 18: Measured time evolution of pressures at the injection and outflow sides together with outflow volume and axial displacement [Rom12a,b].

To help with the interpretation of the results and for the investigation of the measured responses in terms of injection and outflow pressures, as well as outflow volumes, numerical models were used implementing the geometry of the sample and the corresponding boundary conditions on the injection and outflow sides. For the analyses, standard two-phase flow processes were considered in the numerical model in an attempt to reproduce the observed measurements. The two-phase flow code TOUGH2 [Pru99] was used, which takes into account fluid flow in both liquid and gas phases occurring under pressure, viscous, and gravity forces according to Darcy's law. Pressures in the liquid and gaseous phases are related by the capillary pressure functions and interference between the phases is represented by relative permeability functions. Standard two-phase flow model parameters were calibrated based on the experimental data, as well as by inverse modelling of the air injection / outflow responses using ITOUGH2 code [Fin07]. Results of the numerical modelling are shown in Figure 19, together with some of the estimated two-flow phase parameters (intrinsic permeability K, and parameters p_0 –associated with air-entry process– and n of the van Genuchten model used for the water retention curve [van80]).

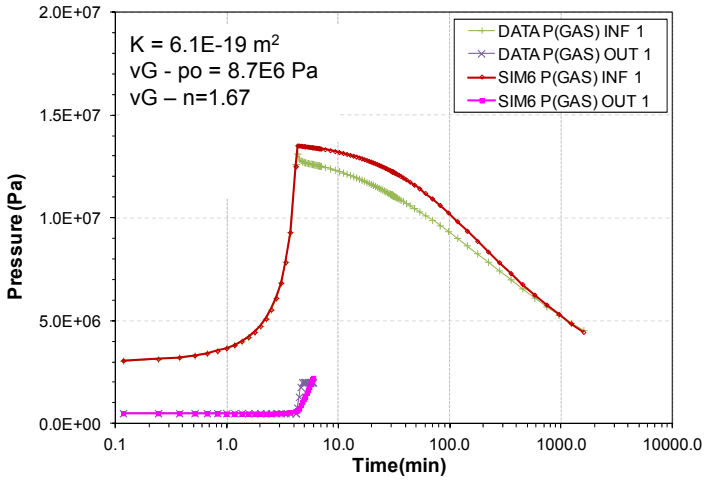

Figure 19: Simulation (sim) and measured (data) results in terms of injection pressure and outflow pressures [Rom12b].

As observed in Figure 19, the analysis using standard two-phase flow model provided insight into the overall air flow mechanisms and showed a good agreement between the measured pressures at the injection and outflow sides of the sample. However, no consistent parameter set could be determined, in agreement with the complementary characterisation tests performed on the material, which can be attributed to the compressibility of the sample and the resulting non-linear phenomena (changes in porosity along the sample). Changes in porosity associated with changes in constitutive stress and corresponding changes in intrinsic permeability have not been considered in the present study. Numerical analyses are currently being performed [Sen12] that include the coupled changes in porosity and intrinsic permeability under changing stress states, hence accounting for coupling between pore compressibility, porosity, intrinsic permeability and capillary pressure.

5 Monitoring processes with ERT

5.1 Introduction

Although ERT has a lower resolution than other techniques (e.g. X-ray tomography, [Ols99]), it can be convenient since it is relatively easy to implement, flexible and economic. ERT has been used to monitor: transport of saline tracers [Bin96, Dam09, Com11, Pol12], mechanical consolidation [Com10] and unsaturated flow [LaB04, Cos12, Bre12], in both two dimensional and three dimensional conditions.

Monitoring is made through of a sequence of maps of electrical conductivity obtained through ERT reconstructions. Transport phenomena can be visualised as a

series of 'electrical pictures'. The effects of material or pore network heterogeneities on transport can be appreciated. For instance, by plotting electrical conductivity histories at selected points, [Bin96] showed areas of preferential flow on a planar section of a flow column.

3D ERT analysis of hydro-chemo-mechanical processes can be done with experimental cells such as the 'EIToedometer' described in [Com08], an oedometer cell whose sidewall and top and bottom plates are covered with a plastic insulating material (Figure 20). Electrodes are both on the sidewall of the cell and on the top and bottom plates. Measurement protocol can then include 'horizontal' measurements, in which the pairs of electrodes that apply electrical current and those that measure electrical potential are on the sidewall; 'vertical' measurements, in which both types of electrodes are on the base and top plates; and 'mixed' measurements, in which the electrodes that apply electrical current are on the sidewall and the measuring electrodes are on the plates. Other 3 D cells such as those of [Ols99, Koe08] have electrodes only on the sidewalls, but at different heights.

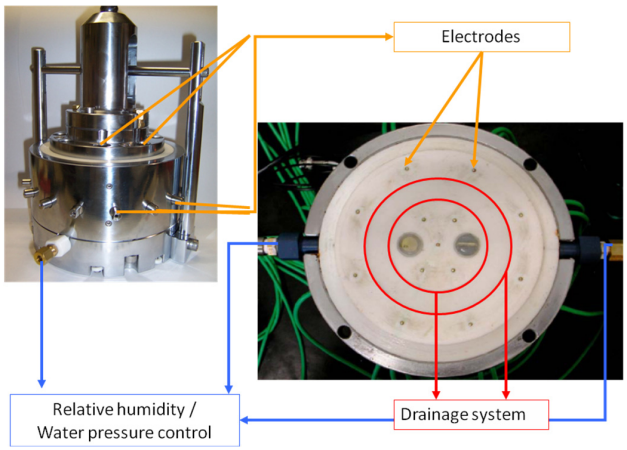

Figure 20: Pictures of the EIToedometer described in [Com08] evidencing the position of the electrodes and the drainage system. The cell diameter is D=130 mm while the cell height can range from H = 40 mm to H = 60 mm.

Time needed to run a complete set of measurements necessary for a single 3D ERT image is highly dependent on the system used (number of electrodes, number of measurements, operating frequency). Anyway it is generally short compared to characteristic times of most hydro-chemo-mechanical processes studied in the laboratory. As an outcome, for monitoring and back-analysis purposes, it is legitimate to associate each image with a well defined time instant.

Transient processes can be imaged as local changes of electrical conductivity. Due to intrinsic heterogeneity of samples, when the perturbation caused by transient

processes is small, appreciating small electrical changes caused by testing can be difficult. Visualisation in terms of differential images can be convenient. In differential images the difference between the electrical conductivity at two given moments is plotted, so that the effects of transient processes are emphasised.

Figure 21a refer to the analysis of a consolidation process occurring in the EIToedometer [Com10]. The difference between the electrical conductivity immediately before imposing a load and the electrical conductivity while consolidation is ongoing is plotted here. A threshold in the representation ($\Delta\chi$ = 0.001 mS/ cm) has been set to evidence the zones of the sample where larger electrical conductivity changes have taken place. Since chemical composition was maintained constant throughout the test, detected conductivity changes are related only to porosity reduction. Actually, volumes where this phenomenon is more relevant merge towards the drainage lines.

Figure 21b is an example of detection of flow patterns [Com11]. It refers to a sample where a layer of kaolin (10 mm thick) was placed between two layers of sand (15 mm thick each). NaCl grains were placed on top of the upper sand layer and wetted to induce dissolution and transport through the cell. The electrical conductivity increase, plotted in Figure 21b, can then be interpreted as an increase of NaCl concentration within the pore water. The differential image shows the difference between the electrical conductivity 60 minutes after the beginning of the test and the initial one. Salt concentration increased in the upper sand layer and also at the interface between kaolin and the cell walls. Thus, the image testifies a weak contact between the kaolin layer and the cell and a preferential flow path for salt.

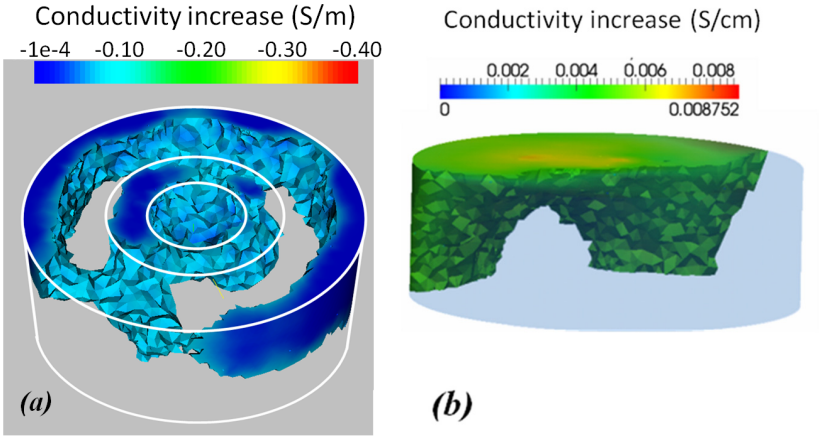

Figure 21: (a) 3D ERT differential image of mechanical consolidation. Porosity reduction (conductivity loss) close to the drainage lines is evident; (b) 3D ERT differential image of salt transport. Zones of increased salt concentration (higher conductivity increase) show migration of salt through a weak contact zone between kaolin and cell wall.

5.2 Back-analysis of transport processes with ERT

Use of ERT reconstructions for back analysis of transport processes and parameter estimation has been developed firstly for in situ geophysical applications [Mic03, Sin05] and then for laboratory experiments [Koe08, Cos12, Pol12]. Several field tests showed so called 'mass balance problems', i.e. significant differences between the total mass of water (or salt) actually present in the monitored domain and the mass estimated via ERT reconstruction. For instance while monitoring an infiltration test [Bin02] found that the increase in the amount of water estimated by the ERT was consistently lower than the real amount, with errors up to 50%. Errors such as this have generally been attributed to poor resolution of the electrical measurements in areas far from the electrodes and to smoothing, together with the fact that boundary conditions associated with the hydro-electrical problem are not univocally established during field tests [Koe08]. Mass balance problems, that can prejudice success of back-analyses, have not been detected in recent laboratory experiences [Koe08, Cos12] (Figure 22).

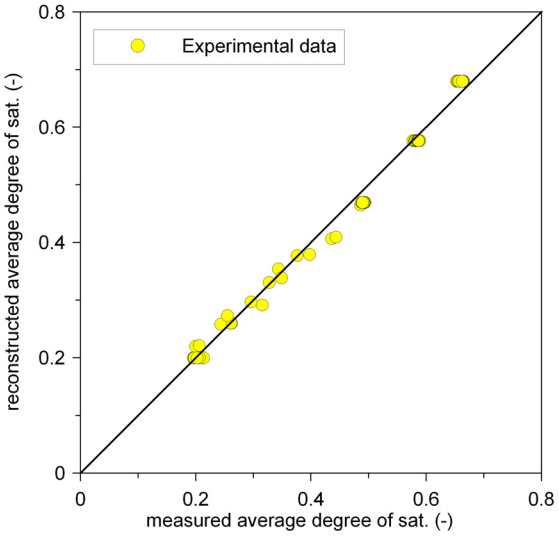

Figure 22: Mass of water detected through ERT inversion (expressed in terms of saturation degree) compared with mass of water actually present in the sample [Cos12]. The sample had an initial saturation S_r=0.2 and was then wetted under controlled flow conditions.

Both *decoupled inversion* and *coupled inversion* strategies have been implemented for back analysis. *Decoupled inversion* requires two different reconstruction stages. The first reconstruction refers to the electrical problem: electrode measurements at the boundaries are the data vector and reconstruction provides a map of estimated local conductivities. These conductivities are converted into water content / water concentration. In the second reconstruction the water content / salt concentration

maps obtained through the first inversion are used as data vector. The forward model is the hydro-chemo-mechanical model of the problem of concern and optimisation is obtained by changing its parameters.

Coupled inversion requires a single inversion process. Archie's law, the mass balance equation(s) of the hydro-chemo-mechanical problem and the electrical charge balance equation are coupled together since the beginning. Data vector is populated by the electrode measurements, while minimisation is done directly on the hydro-chemo-mechanical parameters. Decoupled inversion can suffer from the presence of artefacts and smoothing effects of ERT inversion, while coupled inversion can be computationally demanding and then strategies can be introduced to reduce the complexity of the problem (e.g. [Pol12]).

Decoupled inversion has been used by [Cos12] to estimate the parameters of the water retention curve (wetting branch) of sand and silt samples. Samples were placed in the EIToedometer (moist tamping) at an initial saturation degree Sr=0.20 and wetted by imposing a constant water pressure at the bottom end of the sample. Fast (type 1) and slow (type 2) wetting tests were run on both materials. In the type 1 tests, the imposed water pressure was 50 kPa : after about 1 minute of water inflow, drains were closed and electrical measurements were performed at a constant global water content for 3000 minutes to assess the local redistribution of water (homogenisation). In the type 2 tests water pressure at the boundaries was 5 kPa, applied for about 40 minutes. Electrical measurements were performed during wetting and homogenisation.

Figure 23 shows the evolution of electrical conductivity over time in a longitudinal section of the sand sample, under 'fast' wetting conditions. Time t=0 (Figure 23a) corresponds to the initial condition, consisting of a homogenous electrical conductivity field. Water inflow took place after the ERT reconstruction shown in Figure 23a and was already completed by the time of occurrence of the ERT reconstructions presented in Figures 23b, c and d.

Changes in shape and tone of darker areas in Figure 23 are associated with movement of water. Since wetting was 'fast', in Figure 23b the water content close to the drainage system is higher than elsewhere and significant water content differences exist over the sample. Water content tends to homogenise progressively in time, although it is not yet completely homogeneous when t=3000 min.

Test sequences have been simulated with a commercial Finite Element Method code (Comsol) by introducing the mass balance equations for water and air phase,

$$\frac{\partial\left(\phi S_r \rho_w\right)}{\partial t} + \nabla \cdot \left(\rho_w \mathbf{q}_w\right) = 0$$
$$\frac{\partial\left(\phi\left(1-S_r\right)\rho_a\right)}{\partial t} + \nabla \cdot \left(\rho_a \mathbf{q}_a\right) = 0 \quad ; \quad (2)$$

where ρ_i and u_i are density and pressure of the i-th phase, $\mathbf{q}_i$ is specific discharge and ϕ is porosity. Generalised Darcy laws were used to model the flow of both water and air:

$$\mathbf{q}_w = -k_w(S_r)\nabla\left(z + \frac{u_w}{\rho_w g}\right)$$
$$\mathbf{q}_a = -k_w(S_r)\nabla\left(z + \frac{u_a}{\rho_a g}\right) \quad (3)$$

air and water conductivities were then related to the degree of saturation [Bro64, Cor54]:

$$k_w = k_w^{sat} S_r^{\beta}$$
$$k_a = k_a^{dry}(1-S_r^2)(1-S_r)^2 \quad (4)$$

where k_w^{sat} is water conductivity in saturated conditions and k_a^{dry} is air conductivity in dry conditions. The water retention curve was modelled with the relationship [van80]:

$$S_e = \frac{S_r - S_r^{RES}}{1 - S_r^{RES}} = \left(\frac{1}{1+(\alpha s)^n}\right)^{(1-1/n)} \quad (5)$$

where α and n are experimental parameters and $s=u_a-u_w$ is the matric suction.

Decoupled inversion was run to find the values of β (Equation 4) and of the α and n (Equation 5) that minimise the scatter between ERT reconstructions and hydro-mechanical simulations. Figure 24 shows the water retention curves drawn on basis of the inversions, compared with reference experimental points obtained on analogous samples tested in a controlled suction oedometer with axis translation technique (wetting branch).

The agreement with the reference is very good, considering that water retention curve based on the inversions are obtained through back-analysis of a flow process,

and then are ‘dynamic’ water retention curves (since the water content correspondent to a given suction reflects a dynamic condition).

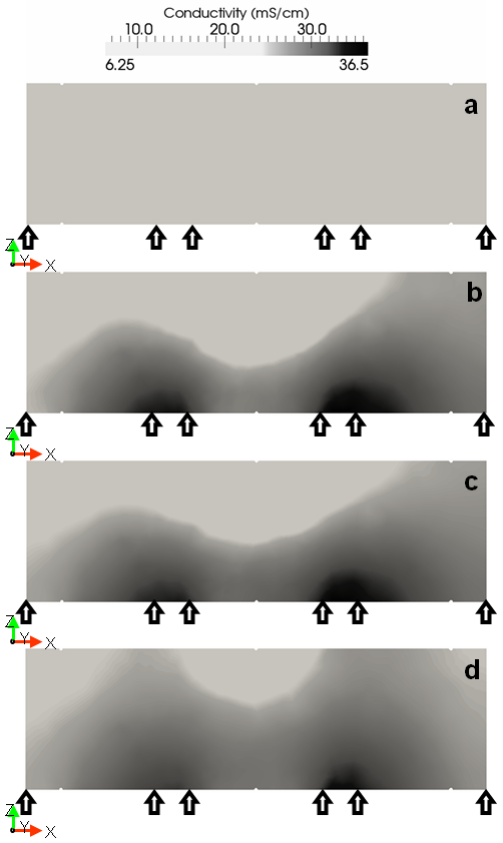

Figure 23: Fast wetting test on a sand sample [Cos12]: time evolution of electrical conductivity over a longitudinal cross-section: a) t=0, b) t=10 min, c) t=110 min, d) t=3000 min (arrows indicate drain positions).

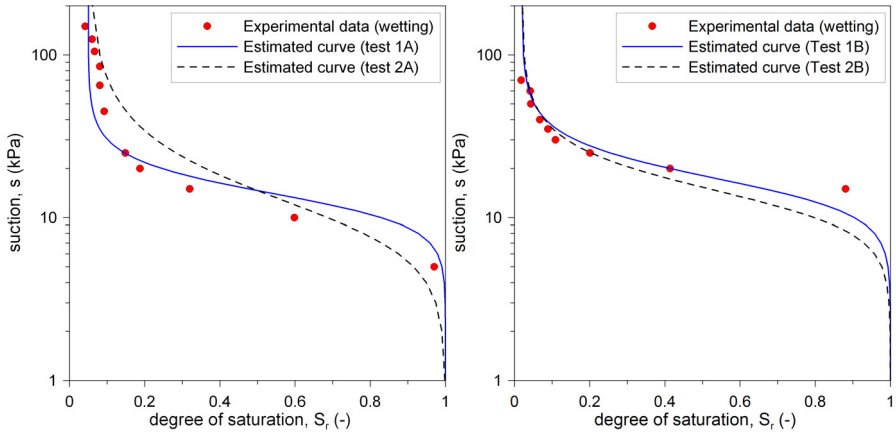

Figure 24: Water retention curves obtained through decoupled inversion of wetting events monitored by means of 3D ERT: (test A) sand sample; (test B) silt sample. 'Experimental data' have been obtained through axis translation technique in a suction controlled oedometer.

6 Acknowledgements

The first author acknowledges the financial support provided by EIG-EURIDICE / SCK.CEN and ONDRAF/NIRAS (Belgium) through a PhD collaboration project for section 3.2, and by NAGRA (Switzerland) through different research projects with CIMNE (Spain) for section 4. The contributions of Dr Marco Caruso (section 2) Prof Antonio Lloret (section 3.1), Dr Analice Lima (section 3.2), Dr Renato Cosentini and Dr Gabriele Della Vecchia (section 5) and Dr Juliana Knobelsdorf are greatly acknowledged.

7 References

[Arn08] Arnedo D., Alonso E.E., Olivella S. and Romero, E. Gas injection tests on sand/bentonite mixtures in the laboratory. Experimental results and numerical modelling. *Physics and Chemistry of the Earth 33, S237-S247*, 2008.

[Ava12] Avanzi F., Caruso M. and Jommi, C. Calibration in the laboratory of capacitance sensors. Submitted for publication to 1st *Pan-American Conf. on Unsaturated Soils 2013, Cartagena, Colombia,* 1-8, 2012.

[Bin96] Binley A., Henry-Poulter S. and Shaw B. Examination of solute transport in an undisturbed soil column using electrical resistance tomography. *Water Resources Research, 32(4), 763-769*, 1996.

[Bin02] Binley, A., Cassiani, G., Middleton, R. and Winship, P. Vadose zone flow model parameterisation using cross-borehole radar and resistivity imaging. *Journal of Hydrology, 267, 147–159*, 2002.

[Bre12] Breen S.J., Carrigan C.R., LaBreque D.J. and Detwiler, R.L. Bench-scale experiments to evaluate electrical resistivity tomography as a monitoring tool for geologic CO2 sequestration. *Int. Jour. Of Greenhouse Gas Control 9, 484 – 494*, 2012.

[Bro64] Brooks, R.H. and Corey, A.J. Hydraulic properties of porous media. *Hydrol., Paper 3*, Colorado State University, Fort Collins, CO, 1964.

[Car11a] Caruso, M. and Jommi, C. A prototype soil column to calibrate numerical models accounting for soil–atmosphere interaction. *In: Unsaturated Soils* E. Alonso & A. Gens (eds.). Taylor & Francis Group, London, UK, Vol. 2, 1121-1132, 2011.

[Car11b] Caruso, M. and Jommi, C. Infiltration and evaporation from bare soil: a comparison between experimental data and predictive models. *In: Unsaturated Soils: Theory and Practice.* A. Jotisankasa, a. Sawangsuriya, S. Soralump & W. Mairaing (eds.). Kasetsart University, Thailand, Vol. II, 791-796, 2011.

[Com08] Comina, C., Foti, S., Musso, G. and Romero, E. EIT oedometer – an advanced cell to monitor spatial and time variability in soil. *Geotechnical Testing Journal ASTM, 31(5), 404-412*, 2008. DOI: 10.1520/GTJ101367

[Com10] Comina, C., Cosentini, R.M., Foti, S. and Musso, G. Electrical Tomography as laboratory monitoring tool. *Rivista Italiana di Geotecnica, 1, 9-20*, 2010.

[Com11] Comina C., Cosentini, R.M., Della Vecchia, G., Foti, S. and Musso G. 3D-electrical resistivity tomography monitoring of salt transport in homogeneous and layered soil samples. *Acta Geotechnica, 6 (4), 195-203*, 2011.

[Cor54] Corey, A.T. The interrelations between gas and oil relative permeabilities. *Producers Monthly, 19, 38-41*, 1954.

[Cos12] Cosentini, R.M., Della Vecchia, G., Foti, S. and Musso, G. Estimation of the hydraulic parameters of unsaturated samples by electrical resistivity tomography. *Géotechnique, 62(7), 583-594*, 2012. DOI:10.1680/geot.10.P.0662012

[Dam09] Damasceno, V.M., Fratta, D. and Bosscher, P.J. Development and validation of a low-cost electrical tomographer for soil process monitoring. *Canadian Geotechnical Journal, 4, 842-854*, 2009.

[Fin07] Finsterle, S. ITOUGH2 User's Guide, Report LBNL-40040, Lawrence Berkeley National Laboratory, Berkeley, CA, USA, 2007.

[Har03] Harrington, J.F. and Horseman, S.T. Gas migration in KBS-3 buffer bentonite. Sensitivity of test parameters to experimental boundary conditions. SKB Technical Report TR-03-02, Stockholm, Sweden, 2003.

[Hor99] Horseman, S.T., Harrington, J.F. and Sellin, P. Gas migration in clay barriers. *Engineering Geology 54, 139-149*, 1999.

[Koe08] Koestel, J., Kemna, A., Javaux, M., Binley, A. and Vereecken H. Quantitative imaging of solute transport in an unsaturated and undisturbed soil monolith with 3-D ERT and TDR. *Water Resources Research, 44, W12411, 17,* 2008. DOI:10.1029/2007WR006755

[LaB04] LaBreque, D.J., Sharpe, R., Wood, T. and Heath, G. Small scale electrical resistivity tomography of wet fractured rocks. *Ground Water, 42(1), 111-118*, 2004.

[Lim10] Lima, A., Romero, E., Gens, A., Muñoz, J. and Li, X.L. Heating pulse tests under constant volume on Boom clay. *Journal of Rock Mechanics and Geotechnical Engineering, 2(2), 124–128,* 2010.

[Lim11] Lima, A. *Thermo-hydro-mechanical behaviour of two deep Belgian clay formations: Boom and Ypresian clays.* PhD Thesis. Universitat Politècnica de Catalunya, Spain, 2011.

[Llo07] Lloret, A. and Villar, M.V. Advances on the knowledge of the thermo-hydro-mechanical behaviour of heavily compacted ''FEBEX'' bentonite. *Physics and Chemistry of the Earth, 32, 701–715*, 2007.

[Mic03] Michot, D., Benderitter, Y., Dorigny, A., Nicoullaud, B., King, D. and Tabbagh, A. Spatial and temporal monitoring of soil water content with an irrigated corn crop cover using surface electrical resistivity tomography. *Water Resources Research*, *39(5), 1138,* 2003. DOI:10.1029/2002WR001581.

[Mil84] Milly P. C. D.. A simulation analysis of thermal effects on evaporation from soil. *Water Resources Research*, *20(8), 1087-1098,* 1984.

[Muñ09] Muñoz, J.J., Alonso, E.E. and Lloret, A. Thermo-hydraulic characterisation of soft rock by means of heating pulse tests. *Géotechnique, 59 (4), 293-306*, 2009.

[Oli94] Olivella, S., Carrera, J., Gens, A. and Alonso, E.E. Nonisothermal multiphase flow of brine and gas through saline media. *Transport in Porous Media, 15, 271-293*, 1994.

[Oli96] Olivella, S., Gens, A., Carrera, J. and Alonso, E.E. Numerical formulation for a simulator (CODE_BRIGHT) for the coupled analysis of saline media. *Engineering Computations, 13(7), 87-112*, 1996.

[Oli08] Olivella, S. and Alonso, E.E. Gas flow through clay barriers. *Géotechnique 58(3),157–176*, 2008.

[Ols99] Olsen, P.A., Binley, A., Henry-Poultier, S. and Tych W. Characterizing solute transport in undisturbed soil cores using electrical and X-ray tomographic methods. *Hydrol. Process. 13, 211-221*, 1999.

[Phi57] Philip J. R. and de Vries D. A. Moisture movement in porous materials under temperature gradients. *EOS Trans. AGU, 38, 222-232,* 1957.

[Pin02a] Pintado, X. *Caracterización termo-hidro-mecánica de arcillas expansivas*. PhD Thesis, Universitat Politècnica de Catalunya, Spain (in Spanish), 2002. http://www.tdx.cat/bitstream/handle/10803/6227/TESIS.pdf

[Pin02b] Pintado, X., Ledesma, A. and Lloret, A. Backanalysis of thermohydraulic bentonite properties from laboratory tests. *Engineering Geology, 64, 91–115*, 2002.

[Pol12] Pollock, D. and Cirpka, O.A. Fully coupled hydrogeophysical inversion of a laboratory salt tracer experiment monitored by electrical resistivity tomography. *Water Resources Research, 48, W01505, 13,* 2012. DOI:10.1029/2011WR010779.

[Pru99] Pruess, K., Oldenburg, C. and Moridis, G. TOUGH2 User's Guide, Version 2.0, Lawrence Berkeley National Laboratory, LBNL-43134, 1999.

[Rom10] Romero, E., Arnedo, D., Gómez, R., Alonso, E.E. and Marschall, P. Gas injection laboratory experiments on Opalinus clay (preliminary results). Book of abstracts *Clays in Natural and Engineered Barriers for Radioactive Waste Confinement*, Nantes, France, March 29–April 1 2010. 4th International Meeting Andra (France), in cooperation with Nagra (Switzerland), Ondraf/Niras (Belgium) and SKB (Sweden). O/05/4: 113-114, 2010.

[Rom12a] Romero, E., Senger, R. and Marschall, P. Air Injection laboratory experiments on Opalinus clay. Experimental techniques, results and analyses. *Proceedings Shale Workshop EAGE Conferences*, Barcelona, Spain, January 23-25, 2012. C07: 96-100, 2012.

[Rom12b] Romero, E., Senger, R., Marschall, P. and Gómez, R. Air tests on low-permeability claystone formations. Experimental results and simulations. Theme lecture. *Int. Workshop 'AMTSS - Advances in Multiphysical Testing of Soils and Shales'*, EPFL Lausanne (Switzerland), 3 - 5 September, 2012.

[Sin05] Singha, K. and Gorelick, S. M. Saline tracer visualized with three-dimensional electrical resistivity tomography: Field-scale spatial moment analysis. *Water Resources Research, 41, W05023*, *17,* 2005, DOI:10.1029/2004WR003460.

[Sen12] Senger R., Romero E., Ferrari A. and Marschall P. Characterization of gas flow through low-permeability claystone. Laboratory experiments and two-phase flow analyses. Extended abstract submitted to *Clays in Natural and Engineered Barriers for Radioactive Waste Confinement*, *4th International Meeting Andra* (France), Montpellier, France, 22-25 October, 2012.

[van80] van Genuchten, M.Th. A closed-form equation for predicting the hydraulic conductivity of unsaturated soils. *Soil Sci. Soc. Am. J. 44, 892-898*, 1980.

Soils and Waves – A Preview

J. Carlos Santamarina

Georgia Institute of Technology

Soils are granular materials. Their characterization faces inherent difficulties related to the effect of the "measurement on the measurand". Low-energy geophysical measurements offer unique opportunities for soil characterization and process monitoring. In particular, elastic and electromagnetic waves provide complementary information about the soil mass in the near-surface. Data interpretation requires proper understanding of physical phenomena involved.

1 Introduction[1]

The near-surface is covered with soil in most onshore and offshore locations. Soil characterization by sampling and in situ testing techniques (e.g., cone penetration and pressuremeters) faces unavoidable perturbation effects. Near-surface site characterization using elastic and electromagnetic perturbations cause no appreciable perturbation and yields important sediment information, including the spatial distribution of materials, small-strain elastic properties and electromagnetic characteristics. In turn, geophysical measurements can be associated with soil parameters relevant to geotechnical engineering analysis and design.

This chapter presents information about elastic (small-strain) and electromagnetic properties of soils and their relations to soil parameters. The goal is to explain physical links between geophysical measurements and soil properties, emphasize global trends, and highlight variables that exert first-order effects. The chapter includes simple, yet robust, concepts and relations that can be readily used in designing measurement procedures and in data interpretation.

[1] This chapter is extracted from (see original source for references): Santamarina, J.C., Rinaldi, V., Fratta, D., Klein, K., Wang, Y.H., Cho, G.C., Cascante, G. (2005). A Survey of Elastic and Electromagnetic Properties of Near-Surface Soils, in Near-Surface Geophysics, Chapter 4, Ed. D. Buttler, SEG, pp. 71-87.

2 Soil Properties

Soils are composed of mineral grains and pore fluid (e.g., air, water, organics). The particulate nature of soils determines most soil characteristics. The constituents, grain size distribution, and spatial variability of a near-surface soil formation reflect its formation history. For example, glacial deposits are heterogeneous and are composed of a wide range of particle sizes. On the other hand, eolian and deltaic formations have narrow grain size distributions. Residual soils form in situ (are not transported), are coarser with depth and may exhibit some degree of cementation. Some soils present clear records of climatic fluctuations, such as varved clays which are composed of successive seasonal thin layers of silt and clay, rendering a soil with high anisotropy in its mechanical, conduction and diffusion properties. Diagenetic effects after deposition can severely alter the properties of granular materials. In particular, light cementation can drastically increase the small-strain shear stiffness (increases more than two orders of magnitude are possible), even when changes in strength remain relatively small.

Particle size is a critical soil parameter: the smaller the particle size, the higher the surface area of the grain relative to its volume, and the more important surface-related forces (electrical, capillary and drag) become relative to self-weight and skeletal forces. For near-surface conditions, surface-related forces gain relevance in sub-millimetric sized particles, and a clear transition in behavior occurs between 10 μm and 100 μm size particles.

The particle shape in coarse silts and sands tends to be rotund, i.e., the short, intermediate and long axes are approximately the same length. However, micro and submicron size particles become increasingly more platy or rod-like.

The range in packing density and porosity of a soil is intimately related to the grain size distribution of the soil (e.g., well-graded materials render higher maximum densities) and the particle shape (e.g., platy particles produce a wider range of densities). For example, the porosity in mono-size spherical particles can range between n=0.476, corresponding to cubic packing, and n=0.260 for a face centered cubic packing. On the other hand, the porosity of kaolinite can range from n=0.91 at the slurry-to-sediment transition (i.e., suspended to interacting particles), to n~0.02 in shales (hence, density and porosity in clays are affected by stress history). Typical values for near-surface soil conditions, phase diagrams and relations among gravimetric and volumetric parameters are summarized in Table 1.

Three distinct mechanisms contribute to anisotropy in soils. First, inherent depositional fabric anisotropy results from the sedimentation of non-spherical grains (geometrical eccentricity as low as 1.1:1 is sufficient to cause significant elastic anisotropy). Second, stress anisotropy alters inter-particle forces and contacts, and produces global fabric anisotropy. Third, soil layering, as in the case of varved clays. The first two components alone can render shear stiffness anisotropy in excess of 1.7:1.

Table 1: Phase Relations, Porosity and Threshold Strain

Phase Relations

Unit weight	$\gamma = \rho g = \frac{W}{V_t}$	Saturation	$S_w = \frac{V_w}{V_v}$
Mass density	$\rho = \frac{M}{V_t}$	Grav. water cont.	$w = \frac{W_w}{W_s}$
Specific gravity	$G_s = \frac{\rho_g}{\rho_w}$	Vol. water cont.	$\theta = \frac{V_w}{V_t}$
Void ratio	$e = \frac{V_v}{V_s} = \frac{n}{1-n}$	Relationship	$\theta = nS_w = \frac{G_s\, w_g}{1+e}$
Porosity	$n = \frac{V_v}{V_t} = \frac{e}{1+e}$	Specific surface	$SS = \frac{\text{surface area}}{\text{mass}}$
Useful equation	$S_w e = G_s\, w$	Adsorbed water	$w = SS\ t_{ads}\ \rho_w$

Typical porosity and specific surface values for near surface soils

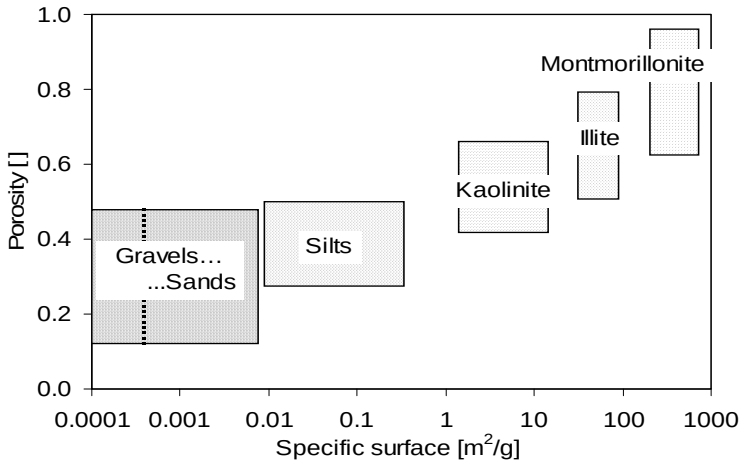

Elastic threshold shear strain γ_{elas}

Increases with effective confinement and with soil plasticity (fineness)

Low end: $\gamma_{elas} = 5 \times 10^{-6}$ (e.g., sand at 20 kPa confinement)

High end: $\gamma_{elas} = 1 \times 10^{-4}$ (e.g., kaolinite at 200 kPa confinement)

Note on sub-indices: t=total, g=grain, w=water, v=voids, s=solids

The mechanical response of the granular skeleton is intimately related to the strain level. The transition between small and medium strains is the "elastic threshold strain". When shear strains are smaller than the elastic threshold strain, the behavior of the soil is considered quasi-elastic, the skeletal stiffness is maximum, and the energy loss is minimum. The elastic threshold strain increases as the confining stress acting on the skeleton increases, decreases with increasing stiffness of the mineral that makes the particles, and increases with increasing specific surface of the soil (Table 1). Geophysical studies involve small-strain phenomena.

The small-strain stiffness of the granular skeleton is determined by the flatness of interparticle contacts. Flatter contacts result from elastic, viscous and/or plastic deformation of contacts in relation to interparticle forces (skeletal as well as capillary), and the precipitation of cementing species (including solution/precipitation of the grain mineral itself). Angular and rough particles lead to lower small-strain skeletal stiffness.

The most common pore fluids in near-surface soils are air and water. Organic fluids may be present as well, and are most often considered contaminants. The distinct properties of these fluids play a critical role in the application of elastic and electromagnetic waves for the characterization of near-surface formations:

- Air: low mass and high compressibility (yet, both effects combine to render a high sound velocity, V_P=343 m/s, which is higher than the velocity of elastic waves in most near-surface soils), dielectric permittivity similar to free space, and very limited electrical conductivity.
- Water: high bulk stiffness; composed of polar water molecules, thus, it hydrates salts forming electrolytes, and hydrates ions adsorbed on mineral surfaces rendering double layers; high interfacial tension with either air or immiscible organic fluids.
- Organic fluids (contaminants): high bulk stiffness, mostly non-polar.
- De-aired liquids are characterized by a high bulk stiffness, which exceeds the bulk stiffness of the granular skeleton for near-surface soils. The presence of air causes a drastic drop in the bulk stiffness of fluids and creates mixed-fluid conditions.

In the presence of fluids, the total boundary stress σ applied to a soil mass is shared by the granular skeleton and the fluid. The portion carried by the skeleton is the effective stress σ'. For near-surface soils, the bulk stiffness of the skeleton B_{sk} is much smaller than the bulk stiffness of the mineral that makes the grains B_g; in this case, the effective stress $\sigma'=\sigma-u$ is equal to the total stress σ minus the pore fluid pressure u. The effective stress determines shear strength τ_{ult} (e.g., Coulomb's failure criterion: $\tau_{ult}=\sigma'\tan\phi$ where ϕ is the friction angle of the soil), stiffness (e.g., Hertzian behavior), and dilatancy (i.e., the volume change upon shear may be either positive or negative).

The presence of two non-miscible fluids adds interfacial tension and capillary forces between particles. This is typically the case between air and water, or water and organic fluids. One or both fluids may percolate; the one that percolates controls the global electrical conductivity. Saturation conditions often vary in the near-surface. Typically, the formation is water-saturated below the water table; above the water table, the degree of saturation S_w decreases towards the free surface. The effect of capillary forces on soil behavior increases as particle size decreases, and should be taken into consideration in clayey or silty soils.

Given the dipolar nature of water molecules and their thermal vibration, water effectively dissolves excess salts present in the soil, hydrates ions adsorbed on mineral surfaces, and may dissolve the mineral itself depending on pH and the type and concentration of hydrated ions. The immediate consequences of these phenomena include:

- The pore water in any soil is an aqueous electrolyte, that is, it consists of free water molecules and hydrated cations and anions that can move relative to each other.
- Hydrated counter-ions around mineral surfaces gain mobility, yet they remain in the vicinity of the particle surface due to Coulombian attraction (i.e., to satisfy electroneutrality), forming a diffuse layer.
- The resulting counter-ion cloud interacts with the cloud around neighboring particles leading to the development of interparticle electrical forces. These forces can affect the mechanical behavior of near-surface clayey soils.

3. Wave Phenomena and Soils

Near-surface soil characterization using elastic and electromagnetic waves involves long-wavelength conditions, whereby the wavelength is much longer than the particle size. The two types of waves experience similar wave phenomena, including time delay, attenuation, dispersion, reflection, refraction, diffraction, and interference. A list of salient wave phenomena and differences between elastic and electromagnetic waves are presented in Table 2.

The propagation velocity and attenuation of mechanical and electromagnetic perturbations in soils depend on distinct soil properties. Elastic wave propagation is affected by soil parameters that determine mass density ρ, and the complex bulk stiffness B and shear stiffness G. On the other hand, the propagation of electromagnetic waves is affected by soil properties that determine polarizability, electrical conductivity, and magnetizability. These interrelations are explored in the following sections.

Table 2: Wave Phenomena in the Near Surface

Medium	**Phenomena (both waves)**	**Special Manifestations in Elastic or Electromagnetic Waves**
Interfaces and boundaries	Reflection Refraction Dispersion	Mec Mode conversion Rayleigh, Love, Stonley waves EM Polarization-dependent reflection Brewster's angles of total transmision
Anisotropy	Bi-refringence	Mec S-wave splitting Quasi-propagation EM Bi-refringence
Gradual variation in depth (velocity gradient)	Ray bending	Mec R-wave dispersion
Inclusions - anomalies (e.g., λ vs. size)	Diffraction Scattering Low-pass filtering	
Material spatial scales (e.g., λ vs. layer thickness)	Low-pass filtering Multiple layer reflections	
Material time scales (e.g., ω vs. relaxation time)	Attenuation Dispersion Resonance	
Multi-phase	Attenuation Dispersion	Mec Relaxation Biot Slow P-wave EM Multiple relaxations
Non-linear behavior (i.e., excitation exceeds linear threshold)	High loss	Mec Shock-waves EM Heating, sparks
Inherent coupling between electrical, mechanical, chemical and thermal energies	Dynamic energy coupling	Mec Seismo-electric EM Electro-seismic

Note: Elastic ("Mec") or Electromagnetic ("EM") waves.

Such a multiplicity of possible wave phenomena hints at the complexity of wave-based studies. More importantly, it also highlights the potential for gaining detailed information about the medium by explicitly targeting these phenomena. In general, properly designed test procedures and adequate signal processing are required.

4 Salient Observations

The previous discussion introduced the multiple microscale phenomena that coexist in soils and the ensuing macroscale properties. The principal observations in view of elastic and electromagnetic properties follow:

- A sediment is a granular skeleton made of interacting mineral particles.
- The soil mass is not inert and its properties are not constant.
- The granular skeleton is inherently porous and pervious.
- The pore volume is filled with the fluid phase, which can be air, water, organic contaminants, or mixtures thereof.
- The mechanical response (stiffness, shear strength, volume change) of the granular skeleton that makes the soil is determined by the effective stress.
- When particles are small, the specific surface is high and surface related forces gain relevance relative to interparticle forces transmitted through the granular skeleton.
- In particular, electrical and capillary forces should be considered when particles are smaller than ~10 μm. In this case, changes in the state of stress, degree of saturation and/or fluid chemistry cause changes in the soil response.

Elastic Wave Propagation in Soils

J. Carlos Santamarina

Georgia Institute of Technology

Soils are granular materials. The propagation of low-energy mechanical perturbations provides information about the elastic properties of the soil and can be used to characterize on-going processes. There are several propagation modes. Velocity is determined by stiffness and mass density. P-waves can be effectively used to verify saturation, and if the soil is saturated, the P-wave velocity can be used to estimate porosity. The S-wave velocity (and the P-wave velocity if the soil is unsaturated, S_w<99%) reflects the stiffness of the skeleton, which depends on the state of stress, cementation, capillary forces, and soil mass density. Attenuation results from internal loss mechanisms.

1 Elastic Wave Propagation[1]

Near-surface characterization using elastic waves is conducted at frequencies that vary between a few Hz to the kHz. In this frequency range, the wavelength in soils ranges between tens of centimeters to tens of meters, therefore, the wavelength is much greater than the grain size, and the perturbation propagates through the soil mass as in a continuum.

The propagation of elastic waves in geophysical studies involves strain levels that are lower than the threshold strain of the soil (Exception: sources of mechanical waves tend to cause large local amplitude, and emitted waves experience high attenuation in the near field of the source). Then, relevant equations for velocity, attenuation and dispersion in soils can be obtained by presuming visco-elastic wave propagation conditions. These concepts and relations are summarized next.

[1] This chapter is extracted from (references listed in this manuscript):
Santamarina, J.C., Rinaldi, V., Fratta, D., Klein, K., Wang, Y.H., Cho, G.C., Cascante, G. (2005). A Survey of Elastic and Electromagnetic Properties of Near-Surface Soils, in Near-Surface Geophysics, Chapter 4, Ed. D. Buttler, SEG, pp. 71-87.

2 Wave velocity

There are three important propagation modes in the near-surface: longitudinal P-waves, transverse S-waves, and retrograde elliptical Rayleigh R-waves. The propagation velocity in each mode and the controlling soil variables are discussed next.

P-waves and S-waves. The shear modulus of the soil G_{soil} only depends on the skeleton shear stiffness, $G_{soil}=G_{sk}$, and it is not affected by the bulk stiffness of the pore fluid. For this reason, S-waves are preferred for the characterization of near-surface deposits when the soil mass is saturated. The shear wave velocity V_S is

$$V_S = \sqrt{\frac{G_{soil}}{\rho_{soil}}} \tag{2}$$

where ρ_{soil} is the mass density of the soil. The shear modulus of soils is determined by the state of stress, the degree of cementation, and by processes that alter interparticle contacts such as capillary forces and electrical forces. Shear wave velocity values can be lower than 1 m/s for soils near the suspension-to-skeleton transition, and can reach 300 m/s to 400 m/s at depths of about 40 m. Cementation, even when light, can drastically increase the shear wave velocity, reaching and exceeding 700 m/s. High suction in unsaturated fine grained soils can have a similar effect. Table 1 presents additional guidelines for the estimation of shear wave velocity.

The propagation velocity of longitudinal P-waves is proportional to the constraint modulus M and the mass density ρ of the soil mass

$$V_P = \sqrt{\frac{M_{soil}}{\rho_{soil}}} = \sqrt{\frac{B_{soil} + \frac{4}{3}G_{soil}}{\rho_{soil}}} \tag{3}$$

where B_{soil} is the bulk modulus and G_{soil} is the shear modulus of the soil. The bulk stiffness of the minerals that make the grains B_g is much greater than the bulk stiffness of the granular skeleton B_{sk} (in this case, Biot-Gassman relations can be simplified; in fact, the Biot relaxation in soils is small for most practical purposes). Furthermore, the bulk stiffness of de-aired fluids $B_{fl}= B_w$ is also greater than the bulk stiffness of the skeleton. However, even minute quantities of air in the fluid phase drastically reduce the bulk modulus of the fluid mixture. Expressions for the bulk modulus of the soil B_{soil} as a function of the bulk modulus of fluid B_{fl} and the particles B_g, the degree of water saturation S_w, and the porosity n of the soil are presented in Table 1.

Table 1: Wave Velocity in Soils

Shear wave velocity V_S (Saturated or dry soils)

$$V_S = \theta \left(\frac{\sigma'_{mean}}{1kPa} \right)^{\beta}$$

σ'_{mean} mean effective stress on polarization plane

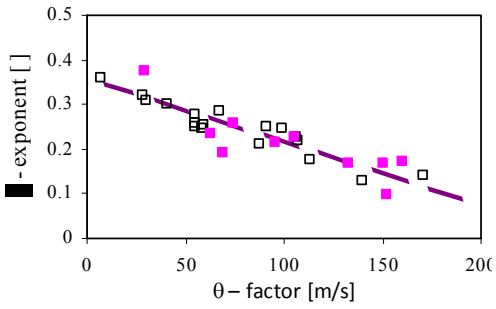

Unsaturated soils - Capillary effects on V_S

The finer the soil and the lower the water content, the higher the suction. At S_w=100% ➔ suction=0

$$V_S = V_S|_{Sw=1} \left(1 + \frac{suction \cdot S_w}{0.75\sigma'_z} \right)^{\beta}$$

Bulk modulus and mass density

Fluid Mixture	$B_{fl} = \left(\frac{S_w}{B_w} + \frac{1 - S_w}{B_a} \right)^{-1}$	$\rho_{fl} = (1 - S_w)\rho_a + S_w \rho_w$
Suspension (fluid + particles)	$B_{sus} = \left(\frac{n}{B_{fl}} + \frac{1 - n}{B_g} \right)^{-1}$	$\rho_{sus} = (1 - n)\rho_g + n\rho_{fl}$
Soil * (fluid + skeleton)	$B_{soil} = B_{sus} + B_{sk}$	$\rho_{soil} = \rho_{sus} = (1 - n)\rho_g + n\rho_{fl}$

Typical values in m/s (top 40 m)

V_P in water	1482		
V_P in air	343		
V_P in saturated soils	1450-1900	V_S in saturated soils	<50-400
V_P in unsaturated soils	<100-800	V_S in unsat. clayey soils	<100-500
V_P in lightly cemented	400-1000	V_S in lightly cemented	250-700

Note: (*) Assumes $B_{sk}/B_g \approx 0$ and low frequency limit

Rayleigh waves. The free soil-air or sediment-water boundary promotes the formation of surface R-waves. The Rayleigh wave velocity V_R is related to the S-wave and P-wave velocities, and can be estimated as (modified from Achenbach, 1975),

$$V_R \approx \frac{0.874+1.117\nu}{1+\nu} V_S \tag{4}$$

where ν is Poisson's ratio. For unsaturated soils, $V_R \approx 0.9V_S$. R-waves permit characterizing the near-surface without drilling boreholes. The depth probed by the perturbation is proportional to the wavelength $z_{probed} \approx \lambda = V_R/f$. R-wave propagation is non-dispersive in homogeneous materials. However, when the medium is heterogeneous, all layers within the probed depth z_{probed} affect the propagation velocity at a given frequency. Therefore, the velocity is not constant with frequency, and the measured velocity-frequency dispersion curve can be inverted to infer the variation of the medium with depth; the technique is known as Spectral Analysis of Surface Waves or SASW.

Poisson's ratio. The small-strain value of Poisson's ratio ν can be estimated from V_P and V_S velocities,

$$\nu = \frac{\frac{1}{2}\left(\frac{V_P}{V_S}\right)^2 - 1}{\left(\frac{V_P}{V_S}\right)^2 - 1} \tag{5}$$

The Poisson's ratio for saturated soft soils (S_r=100%) approaches $\nu \rightarrow 0.5$. The small-strain Poisson's ratio for unsaturated soils (S_r<99%) is lower than $\nu <\sim 0.15$.

3 Material attenuation

The amplitude of propagating waves decreases with distance. This is due to geometric spreading of the wave front, partial transmission at interfaces, and material losses. In the absence of geometric spreading, the amplitudes A_1 and A_2 of a plane wave at two locations Δl apart in a quasi-homogeneous medium, are related by the material attenuation coefficient α [m^{-1}], $A_2/A_1=\exp(-\alpha\Delta l)$. The attenuation coefficient α for elastic waves in soils can be related to other measures of energy loss, including the quality factor Q and the damping ratio D,

$$\frac{1}{Q} = \frac{V\alpha}{\pi f} = 2D \tag{6}$$

In terms of the damping ratio D, soils are highly under-damped materials (D<<100%). The small-strain damping ratio for oven-dry sands captures thermo-elastic effects and can be smaller than D<0.2% (Q>250). In moist and saturated soils, energy losses are governed by viscous effects, and the damping ratio can reach

values of D=2% to 5% (Q=25 to 10). The damping ratio D=1/(2Q) is constant in dry soils and it increases linearly with frequency in wet soils. Additional values and trends are summarized in Table 2.

Table 2: Elastic Wave Attenuation in Soils

Physical processes

Dry - small strain:	thermo-elastic relaxation
Moist/wet - small strain:	viscous loss prevails
Large strain:	frictional loss

Surface waves

$$\frac{Q_S}{Q_R} = \frac{\frac{Q_S}{Q_P}\left[4(1-a)\frac{b}{a}\right] + 4(1-b) - (2-a)^3}{\left[4(1-a)\frac{b}{a}\right] + 4(1-b) - (2-a)^3}$$

where $a=(V_R/V_S)^2$, $b=(V_R/V_P)^2$

Typical damping values at small strain

Gravelly Soils	D = 0.008 – 0.018	σ_0' = 100 - 400 kPa	$\gamma < 10^{-5}$	CT
Sand Air-dry	D = 0.002 – 0.01	σ_0' = 20 - 1800 kPa	$\gamma < 10^{-5}$	RC
Saturated	D = 0.003 – 0.021	σ_0' = 28 - 1800 kPa	$\gamma = 10^{-5}$	CT&RC
Clayey soils	D = 0.01 – 0.052	σ_0' = 15 - 500 kPa	$\gamma < 10^{-4}$	CT&RC
Residual soils	D = 0.009 – 0.054	σ_0' = 25 - 35 kPa	$\gamma < 10^{-5}$	RC
Peat ($w_g \approx 200\%$)	D ≈ 0.025	σ_0' = 66 - 135 kPa	$\gamma \approx 10^{-5}$	CT

Notes: γ is the strain, σ_0' is the effective confinement, w_g is the gravimetric water content, and PI is the plasticity index. RC: resonant column test (typical frequency range 50 Hz to 250 Hz). CT: cyclic triaxial test (typical frequency range <1 Hz).

The "skin depth" S_d is the distance the wave travels before its amplitude decays by 1/e. Therefore, the skin depth for a plane wave is $1/\alpha$. It follows from Equation 6 that the skin depth S_d is

$$S_d = \frac{1}{\alpha} = \lambda\frac{Q}{\pi} = \lambda\frac{1}{2\pi D} \tag{7}$$

Therefore, for the range of damping in soils, typically between D~0.1% (i.e., Q~500) and D<5% (i.e., Q>10), the skin depth for elastic waves is many times the wavelength. This is an important advantage for the characterization of near-surface soils.

4 Attenuation-dispersion

Nearly-constant and constant damping models predict an increase in velocity of about 1.5D for a ten-fold increase in frequency (e.g., Kjartansson, 1979). For example, given a soil with damping ratio D=1%, the velocity increase for a log-cycle in frequency is about 1.5%.

In the case of visco-elastic losses, the maximum attenuation takes place at the relaxation frequency, and it is related to the normalized change in velocity across the relaxation, $2D_{max}=\Delta V/Vo$. For example, if the velocity changes 6% across the relaxation, the maximum damping will be about $D_{max}=3\%$. Most of the change in velocity takes place within one log cycle before and after the relaxation frequency. (Note: high frequency excitation at kHz-frequencies are still much lower than Biot's critical frequency for most soils, which is estimated in the kHz for coarse clean sands and in the MHz for clays).

5 Example

The application of equations and trends introduced in this chapter is illustrated with the example summarized in Table 3.

6 Main observations

Equations, data and trends in this section and in Tables 1 and 2 support the following main observations about elastic wave propagation in near-surface soils:

- If the soil is saturated with de-aired water ($S_r=100\%$), the P-wave velocity of the soil varies between ~1450 m/s and about ~1900 m/s (depending on porosity n), Poisson's ratio approaches $\nu \rightarrow 0.5$, and the shear wave velocity is determined by the shear stiffness of the soil skeleton (and the mass density of the soil).
- If the soil is unsaturated ($S_r<99.0\%$), the bulk stiffness of the fluid is very low, the bulk and shear moduli of the soil mass are those of the soil skeleton, Poisson's ratio is low $\nu<0.15$, and the P-wave velocity is about 1.4 to 1.6 times higher than the shear wave velocity.
- The velocity of S-waves for any degree of saturation and the velocity of P-waves in unsaturated soils ($S_r<99\%$) are determined by: (1) cementation - even light cementation can increase velocity by several times; (2) state of effective stress in uncemented soils; (3) capillary forces in silty or clayey soils (depends on particle size and degree of saturation); and (4) other effects such as those that control mass density or that may alter interparticle electrical forces.
- The wave velocity is approximately constant for frequencies below a ~kHz. Velocity varies a few percentage per log cycle of frequency.
- The dispersion of surface waves captures the variability of the soil profile.

- Attenuation is low. Damping ratio values are between D~0.1% (i.e., Q~500) and D<5% (i.e., Q>10). The skin depth is many times greater than the wavelength.

Table 3: Elastic Wave Parameter Estimation

Consider a saturated (S_r = 1.0) sandy soil with porosity n = 0.35. The assumed specific gravity and bulk stiffness of the mineral that makes the grains are S_G= 2.65 and $B_g = 3.5 \cdot 10^{12}$ N/m^2. The water table is at a depth z_w = 2 m. Estimate elastic wave propagation conditions at a depth of z = 10 m for a high resolution near surface study conducted at a frequency f ~ 800 Hz.

Preliminary computations

$e = n/(1-n) = 0.54$

$\rho_g = S_G \cdot \rho_w = 2650$ kg/m^3

$\rho_{soil} = (1-n)\rho_g = 1722$ kg/m^3 above water table (assumed dry)

$\rho_{soil} = (1-n)\rho_g + n(S_r \cdot \rho_w) = 2072$ kg/m^3 below water table (assumed saturated)

State of stress σ' *at* z = 10 m (g = 9.81 m/s^2 is the acceleration of gravity)

$\sigma_v = \Sigma z \cdot \rho_{soil} \cdot g = 2\ (1722\ \text{kg/m}^3) \cdot g + 8\ (2072\ \text{kg/m}^3) \cdot g = 196.4$ kPa

$u = z \cdot \rho_w \cdot g = 8\ (1000\ \text{kg/m}^3) \cdot g = 78.5$ kPa

$\sigma'_v = \sigma_v - u = 196.4\ \text{kPa} - 78.5\ \text{kPa} = 117.9$ kPa

Ratio of effective stresses at rest $K_o \approx 0.5$ (estimated)

$\sigma'_h = K_o \cdot \sigma'_v = 0.5 \cdot 117.9\ \text{kPa} = 59$ kPa

$\sigma'_{mean} = (\sigma'_v + \sigma'_h)/2 = (117.9\ \text{kPa} + 59\ \text{kPa})/2 = 88.4$ kPa

S-wave velocity at z = 10 m (for S_{HV}, i.e., polarized on the vertical plane)

$\beta = 0.22$ and $\theta = 80$ m/s (for loose to dense sand)

$V_S = \theta(\sigma'_{mean}/1\ \text{kPa})^{\beta} = 80\ \text{m/s}\ (88.4\ \text{kPa}/1\ \text{kPa})^{0.22} = 214.5$ m/s

P-wave velocity at z=10 m

$G_{soil} = V_S^2 \cdot \rho_{soil} = (228.5\ \text{m/s})^2 \cdot 2072\ \text{kg/m}^3 = 1.1 \cdot 10^5$ kPa

$B_{sk} = (2/3)G_{soil}(1+\nu)/(1-2\nu) = 8.7 \cdot 10^4$ kPa

$B_{sus} = [n/B_w + (1-n)/B_g]^{-1} = 5.41 \cdot 10^6$ kPa

$B_{soil} = B_{sus} + B_{sk} = 5.5 \cdot 10^6$ kPa

$V_P = [(B_{soil} + 4/3 \cdot G_{soil})/\rho_{soil}]^{0.5} = 1648$ m/s

Velocity within range listed in Table 1

Damping: Expect damping D~0.01-0.02 (with some increase with frequency)

Wavelength and skin depth (considering D~0.02 for both P and S-waves)

S-wave	wavelength:	$\lambda = V_S/f = 214.5\ \text{m/s} / 800\ \text{Hz} = 0.27$ m
	skin depth:	$S_d = \lambda/(2\pi D) = 0.27\ \text{m} / (2\pi \cdot 0.02) = 2.13$ m
P-wave	wavelength:	$\lambda = V_P/f = 1648\ \text{m/s} / 800\ \text{Hz} = 2.06$ m
	skin depth:	$S_d = \lambda/(2\pi D) = 1080\ \text{m} / (2\pi \cdot 0.02) = 16.39$ m

Electromagnetic Wave Propagation in Soils

J. Carlos Santamarina

Georgia Institute of Technology

Soils are granular materials. The propagation of low-energy electromagnetic perturbations provides information about the electromagnetic properties of the soil, i.e., electrical conductivity, permittivity and magnetic permeability. These parameter reflect: volumetric water content (permittivity at high frequencies), the mobility and availability of ions (electrical conductivity), and the presence of ferromagnetic impurities (magnetic permeability). Attenuation combines magnetization, polarization and Ohmic losses

1 Electromagnetic Parameters[1]

The electromagnetic properties of geomaterials include the magnetic permeability μ (the ability of the medium to respond to a magnetic field), the dielectric permittivity κ (the ability of the soil to become polarized in response to an electric field), and the conductivity σ (the availability and mobility of charges). Both relative permittivity and relative permeability are complex quantities κ^* and μ^*

$$\mu^* = \mu' - j\mu'' \tag{1}$$

$$\kappa^* = \kappa' - j\kappa'' \tag{2}$$

The imaginary components μ'' and κ'' capture magnetization and polarization losses, respectively. These components are in phase with the conductivity, rendering an effective conductivity that increases with frequency.

[1] This chapter is extracted from (find all references in this manuscript):
Santamarina, J.C., Rinaldi, V., Fratta, D., Klein, K., Wang, Y.H., Cho, G.C., Cascante, G. (2005). A Survey of Elastic and Electromagnetic Properties of Near-Surface Soils, in Near-Surface Geophysics, Chapter 4, Ed. D. Buttler, SEG, pp. 71-87.

$$\sigma_{eff} = \kappa'\mu''\varepsilon_o\omega + (\sigma + \kappa''\varepsilon_o\omega)\mu' \tag{3}$$

A propagating electromagnetic wave travels through the soil with phase velocity V_{ph}

$$V_{ph} = \frac{c_o}{\mathrm{Im}\left[\sqrt{\left(-\kappa'\mu' + \kappa''\mu'' + \frac{\sigma\mu''}{\varepsilon_o\omega}\right) + j\left(\frac{\sigma_{eff}}{\varepsilon_o\omega}\right)}\right]} \tag{4}$$

where $c_o = 2.99 \times 10^8$ m/s is the speed of light in free space. The attenuation coefficient α is

$$\alpha = \frac{\omega}{c_o}\mathrm{Re}\left[\sqrt{\left(-\kappa'\mu' + \kappa''\mu'' + \frac{\sigma\mu''}{\varepsilon_o\omega}\right) + j\left(\frac{\sigma_{eff}}{\varepsilon_o\omega}\right)}\right] \tag{5}$$

Most soils in the near-surface are non-ferromagnetic ($\mu'=1$ and $\mu''=0$). In this case, the previous equations become,

$$\sigma_{eff} = \sigma + \kappa''\varepsilon_o\omega \tag{6}$$

$$V_{ph} = \frac{c_o}{\sqrt{\kappa'}} \cdot \frac{1}{\sqrt{\frac{1}{2}\left(\sqrt{1 + \left(\frac{\sigma_{eff}}{\varepsilon_o\omega\kappa'}\right)^2} + 1\right)}} \tag{7}$$

and

$$\alpha = \frac{\omega\sqrt{\kappa'}}{c_o}\sqrt{\frac{1}{2}\left(\sqrt{1 + \left(\frac{\sigma_{eff}}{\varepsilon_o\omega\kappa'}\right)^2} - 1\right)} \tag{8}$$

While elastic wave propagation in soils always involves low-loss conditions, this may not be the case for electromagnetic waves. In many cases, the effective conductivity of the soil is high and the skin depth $S_d=1/\alpha$ is smaller than the wavelength. When the effective conductivity is small $\sigma_{eff}/(\varepsilon_o\omega\kappa') \ll 1$, the skin depth is many times the wavelength and the phase velocity becomes $V_{ph}=c_o/\sqrt{\kappa'}$.

These equations show that velocity and attenuation vary with frequency for a given set of material properties. Furthermore, the electromagnetic properties of soils are frequency-dependent themselves. The following discussion of electromagnetic properties provides a physical explanation in the case of soils, and guidelines for their

estimation and interpretation. The discussion is centered on frequency ranges that are compatible with the operating frequencies of the most common geophysical techniques for near-surface characterization as listed next.

Device	*Operating Frequency*	*Main electromagnetic parameter*
TDR	~ 1 GHz	κ'
GPR	10 MHz to 1 GHz	κ'
EM Induction	0.5 kHz to 20 kHz	σ
Resistivity	< 60 Hz	σ

2 Magnetic permeability

Water and most soil-forming minerals are non-ferromagnetic (i.e., the real relative magnetic permeability is about $\mu' \approx 1$). When ferromagnetic impurities are present, the magnetic permeability of the soil mass is proportional to the volume fraction of impurities. Such mixtures may present relaxation spectra in the kHz range. Typical values of magnetic permeability and an expression for the mixture of clay and a low volume fraction of iron-filings are presented in Table 1.

Table 1: Magnetic Permeability

Magnetization		
Magnetization mechanisms in ferromagnetic materials: no magnetic field H=0; rotation of spins within domains H>0; and translation of domain walls H>0.		
Single materials		
water, quartz, kaolinite	~0.9999 (diamagnetic)	
montmorillonite, illite, granite, hematite	1.00002-1.0005 (paramagnetic)	
nickel, iron	> 300 (ferromagnetic)	
Predictive relations		
Wagner's model for spherical particles	$\mu' = 1 + 3\theta_{Fe}$	for $\theta_{Fe}<0.2$
Kaolinite with iron filings (at 10 kHz)	$\mu' = 1 + 4\theta_{Fe} + 7\theta_{Fe}^2$	for $\theta_{Fe}<0.3$

Note: θ_{Fe} is the volume fraction of ferromagnetic inclusions

3 Dielectric permittivity

Soils are electrically neutral overall; however, negative charges (electrons and anions) and positive charges (protons and cations) can be displaced by applying an electric field. When charges are displaced from their equilibrium position, the medium becomes polarized. The permittivity of a material increases from high frequencies to low frequencies, gradually accumulating polarizations as the frequency decreases and larger scales become involved. The following observations and trends apply to geomaterials at MHz frequencies:

- The permittivity of most soil-forming minerals ranges between 3 and 10. The permittivity of free water below f<10 GHz is about 80.
- Given the high porosity of near-surface soils, the measured permittivity in soils at f >200 MHz is dominated by the orientation polarization of free water (water beyond the adsorbed water layer around particles of thickness $t_{ads} \approx$ 2-3 monolayers). In this frequency range, the permittivity is controlled by the volumetric water content. Hence, if the soil is saturated, the porosity can be determined.
- The displacement of hydrated ions in the pore fluid and in double layers is restricted by interfaces (e.g., the particles themselves); this adds interfacial polarization at low MHz frequencies. Therefore, the permittivity at frequencies lower than ~100 MHz depends not only on volumetric water content, but also on the ionic concentration of the pore fluid, the specific surface of the soil, and the interparticle arrangement.
- The prevalence of Ohmic losses at frequencies lower than ~10 MHz causes high attenuation in wave propagation and the skin depth is shorter than the wavelength.

Table 2 provides typical values and convenient trends for soils.

4 Electrical conductivity

The electrical conductivity of most soil-forming minerals as well as the conductivity of de-ionized water are very low ($\sigma < 10^{-4}$ S/m). However, the mixture of water and soils can exhibit high electrical conductivity. There are two participating phenomena:

- Water hydrates excess salts and the pore fluid becomes an electrolyte, that is, a mixture of free water molecules, hydrated cations and hydrated anions.
- Water also hydrates counter-ions adsorbed onto dry particles, thereby forming a counter-ion cloud around the particle.

Therefore, the electrical conductivity in soils is ionic in nature and includes contributions from (1) the pore fluid electrolyte (but reduced by the porosity, saturation and tortuosity); and (2) the conduction along the particle surfaces, which is proportional to the specific surface of the soil. The contribution of surface conduction to the global conduction gains relevance in clays filled with a low-conductivity electrolyte. Trends and characteristic values are presented in Table 3.

Table 2: Permittivity (Relevant frequency range 1 MHz-1 GHz)

Polarization

Note: Permittivity increases as frequency decreases

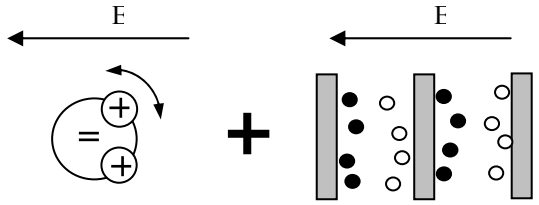

orientation of polar molecules | *interfacial polarization*

Permittivity of single-phase soil components (radio frequencies)

water	78.5	quartz	4.2 - 5
methanol	32.6	calcite	7.7 - 8.5
most organic fluids	2 to 6	most minerals	6 - 10

Permittivity of wet soils ($\theta_w=S_r \cdot n$)	**Frequency**	**Author**
$\kappa' = 1.40 + 87.6\,\theta_w - 18.7\,\theta_w^2$	50 MHz	Wensink
$\kappa' = 3.03 + 9.3\theta_w + 146\,\theta_w^2 - 76.7\,\theta_w^3$	MHz to GHz	Topp et al.
$\kappa' = 3.3 + 41.4\theta_w + 16\,\theta_w^2$	~ 1GHz	Wensink
$\kappa' = 3.14 + 23.8\theta_w + 16.0\theta_w^2$		Wang
$\kappa' = 40\theta_w \quad 3.9 + \sqrt{44.8 \quad 392\theta_w + 1600\theta_w^2}$		Selig and Mansukhani
$\kappa' = (2.6 \quad 1.6n + 7.9\theta_w)^2$		Based on CRI mixture model

Trend for soils

(f~1 GHz)

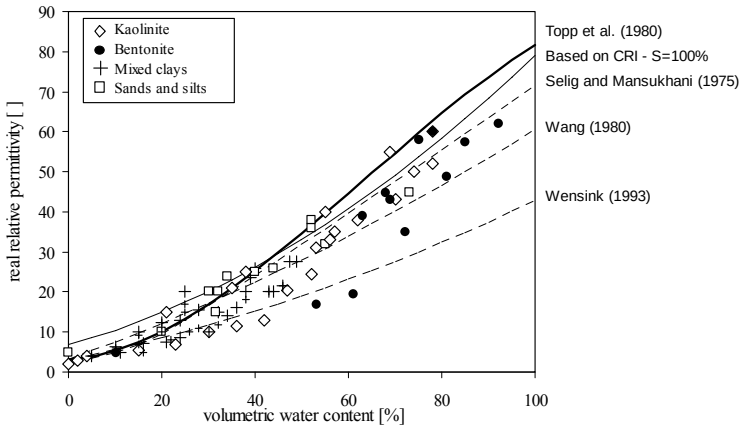

Table 3: Electrical Conductivity

Availability and mobility of hydrated ions

Note: The effective conductivity increases as frequency increases

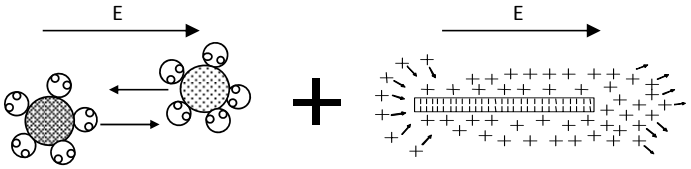

Conductivity of single-phase soil components (σ in S/m)

de-ionized water	10^{-6}	organic fluids	$\sim 10^{-11}$
fresh water	10^{-3}	most soil-forming minerals	10^{-15}-10^{-7}
sea water	4	(Note: some minerals are conductive)	

Medium	Value - Trend	Comments
water + salt = electrolyte	$\sigma_{el} = 0.15\,\mathrm{TDS}$	σ_{el} in mS/m; TDS: total dissolved salts in mg/L (Annan, 1992)
wet soils	$\sigma_{soil} = n\sigma_{el} + (1-n)\Theta\rho_g S_s$	Θ is surface conduction. Needs correction for tortuosity and saturation
	$\sigma_{soil} = a\sigma_{el}\, S_r^c\, n^m$	a≈1 m~1-2.4 c~4-5 (Archie, 1942)

Trend for soils

(σ in S/m)

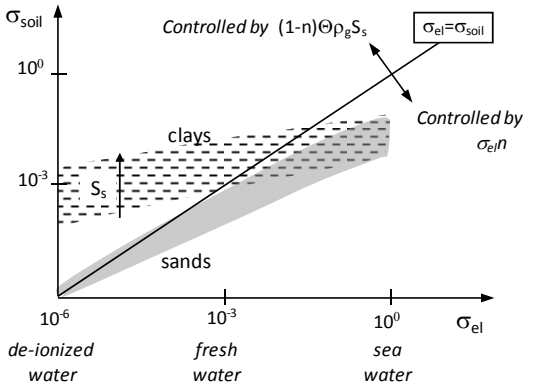

Notes: The surface conduction for kaolinite is about $\Theta \approx 10^{-9}$ Siemens. Tortuosity may reduce the electrical conductivity in clays more than in sands. Hence, the conductivity of marine clays may be lower than the conductivity of marine sands, at the same void ratio.

5 Example

The application of equations and trends introduced in this chapter is illustrated with the example summarized in Table 4.

Table 4: Electromagnetic Wave Parameter Estimation.

Consider the same formation as in the example presented for elastic wave properties (sandy soil, saturated S_r=1.0, porosity n=0.35). The saturating fluid is fresh water and the total dissolved salts is TDS=8 mg/l. Estimate the electromagnetic wave parameters relevant for site characterization with GPR operating with 100 MHz antennae.

Relative magnetic permeability μ

It is assumed that there are no ferromagnetic impurities present

$\mu' = 1.0 \qquad \mu'' = 0.0$

Relative permittivity κ

$\theta_w = n \cdot S_r = 0.35$

$\kappa' = 15$ (between 10-to-20) $\kappa'' << \sigma/\omega \cdot \varepsilon_o$ (assumed)

Effective electrical conductivity σ

$\sigma_{el} = 0.15\ TDS = 1.2 \cdot 10^{-3}$ S/m

$\sigma_{soil} \cong 0.3 \cdot 10^{-4}$ S/m (estimated with both expressions in the table for n = 0.35)

$\sigma_{eff} = \sigma + \kappa'' \cdot \omega \cdot \varepsilon_o = 0.3 \cdot 10^{-4}$ S/m

Wave velocity V_{ph} *and wavelength* λ

$V_{ph} = 7.75 \cdot 10^7$ m/s

$\lambda = V_{ph}/f = 0.775$ m

Attenuation α *and skin depth* S_d

$\alpha = 0.077\ m^{-1}$

$S_d = 1/\alpha = 13.0$ m

6 Main observations

Three material properties that affect the propagation of electromagnetic waves in soils: magnetic permeability, permittivity, and electrical conductivity. The information presented in this section and in Tables 1, 2, and 3 permit extracting the following main conclusions:

- The magnetic permeability increases as the amount of ferromagnetic impurities increases. Most near-surface soils are non-ferromagnetic.
- The permittivity at frequencies above f>200 MHz is proportional to volumetric water content, and can be used to determine porosity in saturated soils.
- The higher the permittivity, the lower the wave phase velocity.
- The conductivity reflects the availability of hydrated ions. High surface area soils (i.e., clayey soils) and excess salts increase the conductivity of the soil.
- High conductivity reduces the skin depth, which can become shorter than the wavelength.
- The wave velocity is approximately constant in all soils for frequencies below a few kHz. Velocity variations are on the order of a few percentage per log cycle of frequency.
- The dispersion of surface waves captures the variability of the soil profile.
- Attenuation is low, rendering damping ratio values between D~0.1% (i.e., Q~500) and D<5% (i.e., Q>10). The skin depth is many times greater than the wavelength.

Thermal Properties of Soils

J. Carlos Santamarina

Georgia Institute of Technology

Soils are granular materials. Thermal conduction in soils takes place through contacts. The quality of contacts for thermal conduction depends on effective stress and the presence of liquids at interparticle contacts. At the macroscale, the thermal conductivity of sediments is determined by volumetric fractions, the properties of the phases, the spatial arrangement of grains and their connectivity. Bounds and the selection of predictive models must recognize the role of contacts on thermal conductivity in sediments.

1 Introduction[1]

More than 98% of the earth's volume is at a temperature higher than 1000°C, and the temperature of the earth core may exceed 5000°C. This great geothermal dynamo has determined the geological history of the earth. Heat flux in oceans and climate change are macro-scale manifestations of geothermal phenomena.

Several geotechnical engineering problems involve the thermal properties of geomaterials; examples include thermal stabilization, foundation effects in permafrost regions, thermo-piles, geomechanics of geothermal energy resource recovery, thermal storage, radioactive waste disposal, pavement performance in extreme climates, and the formation-destabilization of methane hydrates in sub-seafloor sediments.

[1] This chapter is extracted from (references listed in these sources):
- Cortes, D.D., Martin, A.I., Yun, T.S., Francisca, F.M., Santamarina, J.C. and Ruppel, C. (2009), Thermal Conductivity of Hydrate-Bearing Sediments, J. Geophysical Research. vol. 114. DOI 10.1029/2008JB006235.
- Yun, T.S. and Santamarina, J.C. (2008). Fundamental Study of Thermal Conduction in Dry Soils, Granular Matter, vol. 10, no. 3, pp. 197-207. DOI 10.1007/s10035-007-0051-5

2 Heat Transfer in Granular Media

Heat transfer takes place through convection, radiation, and conduction. In granular media, the relative contribution of convective heat transport gains relevance in coarse grained soils characterized by a mean grain size greater than 6 mm. On the other hand, radiative heat transport occurs through photon emissions and electromagnetic wave propagation and is only significant at temperatures above ~500°C. Therefore, heat transport in fine sands and clays at low temperatures is conductive, and the thermal conductivity is the key parameter governing heat transfer.

The thermal conductivities of sediment components vary across several orders of magnitude: mineral grains (order of $10 Wm^{-1}K^{-1}$), water (order of $1 Wm^{-1}K^{-1}$), and air (order of $0.01 Wm^{-1}K^{-1}$). Such a contrast in thermal conductivities leads to preferential particle-level heat transport processes in granular materials (Figure 1): Conduction in the solid particle, Solid-to-solid conduction through the contact area, Solid-fluid-solid conduction (this conduction path is especially relevant in partially saturated soils with pendular water), Conduction through the fluid within the porous network, convection (relevant when $D_{50} \geq 6mm$), radiation at interparticle contacts: heat propagation takes place by radiation across the gap between contacting particles. and radiation from the particle surface into the surrounding medium (the penetration depth is inversely proportional to the material density (e.g., cm in water; meters in air).

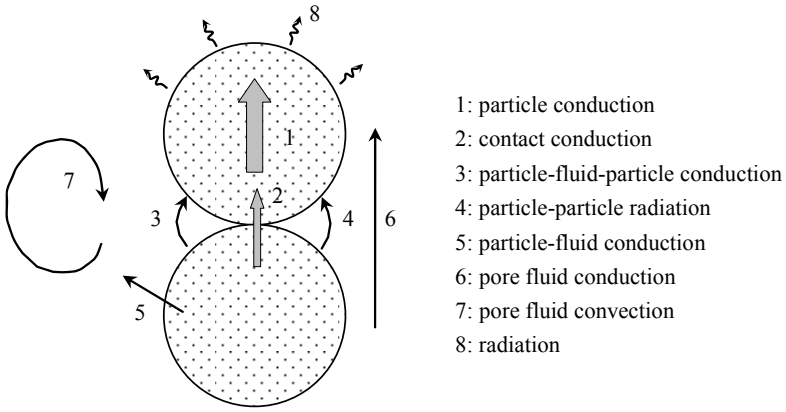

Figure 1: Thermal conduction paths in sediments.

Heat flux through contacts plays a preponderant role on the effective thermal conductivity in dry soils. The contact area A_c is a non-linear function of the contact normal force N (e.g., Hertzian contact). This explains the role of effective stress on thermal conductivity in granular materials at constant packing. Furthermore, experimental results suggest that contact level conduction increases not only by loading

but any other mechanism that enhances the effective contact area, including flattening of surface roughness, cementation, creep/diagenesis and pendular water.

3. Data - Bounds

Dry Soils. Data in Figure 2 show the increase in thermal conductivity with decreasing porosity in dry soils. These trends reflect the increase in interparticle coordination and possible improvements in conduction efficiency. Particle shape affects thermal conductivity through the packing density: particle irregularity leads to increased porosity, and lower interparticle coordination. In turn, lower porosity correlates with higher thermal conductivity. Therefore, a correlation between porosity in dry soils and thermal conductivity already captures the effect of particle shape on coordination number. Note, however, that particle irregularity makes the stiffness of the granular skeleton more sensitive to the state of the stress due to enhancement in contact quality. A similar trend is anticipated for thermal conduction.

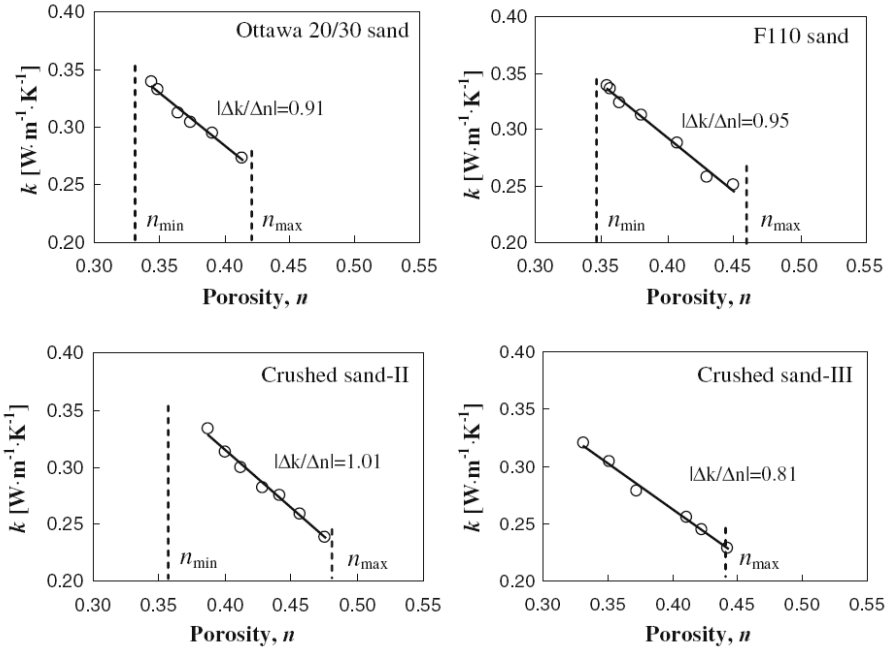

Figure 2. Changes in thermal conductivity with porosity. Maximum and minimum porosities shown for reference in each case. The thermal conductivity increases linearly with decreasing porosity in all cases.

Wet Soils. Data for water saturated specimens are shown in Figure 3. Thermal conductivity values are much higher than for air dry conditions, highlighting the role of water in heat transport across contacts. The saturated sand shows no measurable

sensitivity of thermal conductivity to changing effective stress. Saturated kaolinite exhibits an increase in thermal conductivity (λ= 2.1Wm^{-1}K^{-1} to 2.8Wm^{-1}K^{-1}) for increasing effective stress (σ'= 50kPa to 1000kPa) as a consequence of changes in porosity (n= 0.67 to 0.51).

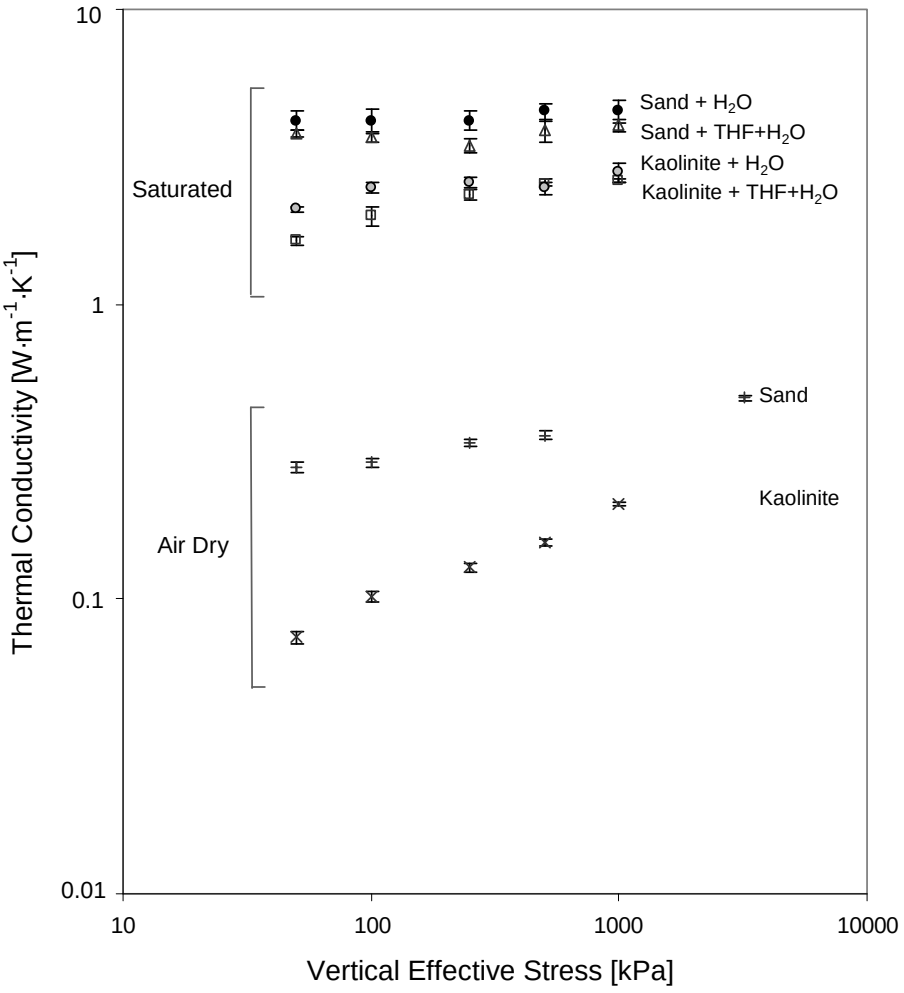

Figure 3. Dry vs. water saturated sand and clay. Changes in thermal conductivity with effective stress.

Theoretical bounds are summarized in Table 1. Analytical predictions of thermal conductivity are based on the mixture geometry, the properties of each phase and the volumetric fractions.

Table 1. Theoretical thermal conductivity mixture models - Bounds

Series	$k_{eff} = \left(\sum_i \frac{\theta_i}{k_i} \right)^{-1}$	
Parallel	$k_{eff} = \sum_i \theta_i k_i$	
Geometric Mean	$k_{eff} = \prod_i k_i^{\theta_i}$	
Hashin & Shtrikman Bounds	$k_{eff} = k_1 \left[1 + \frac{3\theta_2 (k_2 - k_1)}{3k_1 + \theta_1 (k_2 - k_1)} \right]$	lower bound: 1=solid, 2=pore upper bound: 1=pore, 2=solid

4 Main Observations

There are several heat transport processes in granular materials. The quality of interparticle contacts and coordination number govern thermal conduction in dry soils. The presence of liquids or cementing agents at contacts, and larger contact areas (due to either loading, creep, or diagenesis) enhance thermal conduction.

- *General:* The particle-level analysis of heat transfer explains the ordered sequence of thermal conductivity values: $k_{air} < k_{dry\ soil} < k_{water} < k_{saturated\ soil} < k_{mineral}$.
- *Mineralogy:* The thermal conductivity of quartz is higher than other common soil forming minerals. Thus, the thermal conductivity of sediments is proportional to the volumetric fraction of quartz.
- *Particle size:* Interparticle conductive heat transfer is proportional to the particle radius and inversely proportional to the inter-contact distance. Larger particles lead to higher thermal conductivity.
- *Packing density and coordination number:* Interparticle contacts play an important role in heat transfer processes. The higher the packing density and coordination number, the higher the thermal conductivity of the sediment. Round particles and well-graded soils tend to attain denser packing, higher coordination and higher thermal conductivity than angular particles.
- *Water content:* Water acts as a relatively high conductivity bridge between particles. Therefore the thermal conductivity of unsaturated soils increases with the degree of saturation
- *Effective stress:* The increase in packing density, coordination number, and contact quality with increasing effective stress leads to higher thermal conductivity. Load-bearing granular chains within the soil skeleton facilitate heat transfer.

In summary, the thermal conductivity of sediments is determined by volumetric fractions, the properties of the phases, the spatial arrangement of grains and their connectivity.

INPG – 3SR
46 avenue Félix Viallet
BP 53
38041 GRENOBLE CEDEX 9
FRANCE

ISBN 978-3-00-039683-0

Fon: +33 (0) 456 528 621
Fax: +33 (0) 476 827 043
president@alertgeomaterials.eu
http://alertgeomaterials.eu

ALERT Doctoral School 2012

Advanced experimental techniques in geomechanics

Editors: G. Viggiani, S. A. Hall, E. Romero

ISBN 978-3-00-039683-0